Reconstruction of cortical activity from MEG data using brain networks and transmission delays estimated from dMRI

Ivana Kojčić

▶ **To cite this version:**

Ivana Kojčić. Reconstruction of cortical activity from MEG data using brain networks and transmission delays estimated from dMRI. Medical Imaging. Université Côte d'Azur, 2022. English. NNT : . tel-03944354v1

HAL Id: tel-03944354

https://inria.hal.science/tel-03944354v1

Submitted on 18 Jan 2023 (v1), last revised 13 Mar 2023 (v3)

HAL is a multi-disciplinary open access archive for the deposit and dissemination of scientific research documents, whether they are published or not. The documents may come from teaching and research institutions in France or abroad, or from public or private research centers.

L'archive ouverte pluridisciplinaire **HAL**, est destinée au dépôt et à la diffusion de documents scientifiques de niveau recherche, publiés ou non, émanant des établissements d'enseignement et de recherche français ou étrangers, des laboratoires publics ou privés.

UNIVERSITÉ CÔTE D'AZUR

ÉCOLE DOCTORALE
SCIENCES ET TECHNOLOGIES DE L'INFORMATION ET DE LA COMMUNICATION

THÈSE DE DOCTORAT

Reconstruction de l'activité corticale

à partir de données MEG à l'aide de réseaux cérébraux et de délais de transmission estimés à partir d'IRMd

Ivana KOJČIĆ

Centre Inria d'Université Côte d'Azur, Équipe-Projet Athena

Présentée en vue de l'obtention du grade de docteur en
Automatique et Traitement du Signal et des Images
d'Université Côte d'Azur

Dirigée par : *Théodore Papadopoulo*
Co-encadrée par : *Samuel Deslauriers-Gauthier*

Date de soutenance:
18/11/2022

Devant le jury, composé de :

Christian Bénar, Directeur de Recherche, Institut de Neurosciences des Systèmes, Inserm – Rapporteur

Rachid Deriche, Directeur de Recherche, Inria d'Université Côte d'Azur – Examinateur

Samuel Deslauriers-Gauthier, Chargé de Recherche, Inria d'Université Côte d'Azur – Co-Encadrant

Gloria Menegaz, Professeur titulaire, Université de Vérone – Rapporteuse

Théodore Papadopoulo, Directeur de Recherche, Inria d'Université Côte d'Azur – Directeur de thèse

Benoît Scherrer, Professeur assistant, Harvard Medical School - Examinateur

PhD thesis

Reconstruction of cortical activity from MEG data using brain networks and transmission delays estimated from dMRI

Ivana Kojčić

Centre Inria d'Université Côte d'Azur
Athena Project Team

Date of defense
November 18th 2022

To my mother
for her ceaseless support
& everlasting love.

Funding

This doctoral project was funded by the European Research Council (ERC) under the European Union's Horizon 2020 research and innovation program (ERC Advanced Grant agreement No 694665: CoBCoM - Computational Brain Connectivity Mapping).
Data were provided by the Human Connectome Project, WU-Minn Consortium (Principal Investigators: David Van Essen and Kamil Ugurbil; 1U54MH091657) funded by the 16 NIH Institutes and Centers that support the NIH Blueprint for Neuroscience Research; and by the McDonnell Center for Systems Neuroscience at Washington University.
The authors would like to thank to Inria Sophia Antipolis - Méditerranée "Nef" computation cluster for providing resources and support.

Abstract

White matter fibers transfer information between brain regions with delays that are observable with magnetoencephalography and electroencephalography (M/EEG) due to their millisecond temporal resolution. We can represent the brain as a graph where nodes are the cortical sources or areas and edges are the physical connections between them: either local (between adjacent vertices on the cortical mesh) or non-local (long-range white matter fibers). Long-range anatomical connections can be obtained with diffusion MRI (dMRI) tractography which yields a set of streamlines representing white matter fiber bundles. Given the streamlines' lengths and the information conduction speed, transmission delays can be estimated for each connection. dMRI can thus give an insight into interaction delays of the macroscopic brain network.

Localizing and recovering electrical activity of the brain from M/EEG measurements is known as the M/EEG inverse problem. Generally, there are more unknowns (brain sources) than the number of sensors, so the solution is non-unique and the problem ill-posed. To obtain a unique solution, prior constraints on the characteristics of source distributions are needed. Traditional linear inverse methods deploy different constraints which can favour solutions with minimum norm, impose smoothness constraints in space and/or time along the cortical surface, etc. Yet, structural connectivity is rarely considered and transmission delays almost always neglected.

The first contribution of this thesis consists of a multimodal preprocessing pipeline used to integrate structural MRI, dMRI and MEG data into a same framework, and of a simulation procedure of source-level brain activity that was used as a synthetic dataset to validate the proposed reconstruction approaches.

In the second contribution, we proposed a new framework to solve the M/EEG inverse problem called Connectivity-Informed M/EEG Inverse Problem (CIMIP), where prior transmission delays supported by dMRI were included to enforce temporal smoothness between time courses of connected sources. This was done by incorporating a Laplacian operator into the regularization, that operates on a time-dependent connectivity graph. Nonetheless, some limitations of the CIMIP approach arised, mainly due to the nature of the Laplacian, which acts on the whole graph, favours smooth solutions across all connections, for all delays, and it is agnostic to directionality.

In this thesis, we aimed to investigate patterns of brain activity during visuomotor tasks, during which only a few regions typically get significantly activated, as shown by previous studies. This led us to our third contribution, an extension of the CIMIP approach that addresses the aforementioned limitations, named CIMIP_OML ("Optimal Masked Laplacian"). We restricted the full source space network (the whole cortical mesh) to a network of regions of interest and tried to find how the information is transferred between its nodes. To describe the interactions between nodes in a directed graph, we used the concept of *network motifs*. We proposed an algorithm that (1) searches for an optimal network motif – an optimal pattern of interaction between different regions and (2) reconstructs source activity given the found motif.

Promising results are shown for both simulated and real MEG data for a visuomotor task and compared with 3 different state-of-the-art reconstruction methods.
To conclude, we tackled a difficult problem of exploiting delays supported by dMRI for the reconstruction of brain activity, while also considering the directionality in the information transfer, and provided new insights into the complex patterns of brain activity.

Keywords: M/EEG, source localization, inverse problems, diffusion MRI, structural and functional brain connectivity, network neuroscience

Résumé

Les fibres de la matière blanche permettent le transfert d'information dans le cerveau avec des délais observables en Magnétoencéphalographie et Électroencéphalographie (M/EEG) grâce à leur haute résolution temporelle. Le cerveau peut être représenté comme un graphe où les nœuds sont les régions corticales et les liens sont les connexions physiques entre celles-ci: soit locales (entre sommets adjacents sur le maillage cortical), soit non locales (fibres de la matière blanche).
Les connexions non-locales peuvent être reconstruites avec la tractographie de l'IRM de diffusion (IRMd) qui génère un ensemble de courbes («streamlines») représentant des fibres de la matière blanche. Sachant les longueurs des fibres et la vitesse de conduction de l'information, les délais de transmission peuvent être estimés. L'IRMd peut donc donner un aperçu des délais d'interaction du réseau cérébral macroscopique.
La localisation et la reconstruction de l'activité électrique cérébrale à partir des mesures M/EEG est un problème inverse. En général, il y a plus d'inconnues (sources cérébrales) que de capteurs. La solution n'est donc pas unique et le problème est dit mal posé. Pour obtenir une solution unique, des hypothèses sur les caractéristiques des distributions de sources sont requises. Les méthodes inverses linéaires traditionnelles utilisent différentes hypothèses qui peuvent favoriser des solutions de norme minimale, imposer des contraintes de lissage dans l'espace et/ou dans le temps, etc. Pourtant, la connectivité structurelle est rarement prise en compte et les délais de transmission sont presque toujours négligés.
La première contribution de cette thèse est un pipeline de prétraitement multimodal utilisé pour l'intégration des données d'IRM, IRMd et MEG dans un même cadre, et d'une méthode de simulation de l'activité corticale qui a été utilisée comme jeu de données synthétiques pour valider les approches de reconstruction proposées.
Nous proposons également une nouvelle approche pour résoudre le problème inverse M/EEG appelée «Problème Inverse M/EEG Informé par la Connectivité» (CIMIP pour Connectivity-Informed M/EEG Inverse Problem), où des délais de transmission provenant de l'IRMd sont inclus pour renforcer le lissage temporel entre les décours des sources connectées. Pour cela, un opérateur Laplacien, basé sur un graphe de connectivité en fonction du temps, a été intégré dans la régularisation. Cependant, certaines limites de l'approche CIMIP sont apparues en raison de la nature du Laplacien qui agit sur le graphe entier et favorise les solutions lisses sur toutes les connexions, pour tous les délais, et indépendamment de la directionnalité. Lors de tâches visuo-motrices, seules quelques régions sont généralement activées significativement. Notre troisième contribution est une extension de CIMIP pour ce type de tâches qui répond aux limitations susmentionnées, nommée CIMIP_OML («Optimal Masked Laplacian») ou Laplacien Masqué Optimal. Nous essayons de trouver comment l'information est transférée entre les nœuds d'un sous-réseau de régions d'intérêt du réseau complet de l'espace des sources. Pour décrire les interactions entre nœuds dans un graphe orienté, nous utilisons le concept de *motifs de réseau*. Nous proposons un algorithme qui 1) cherche un motif de réseau optimal

- un modèle optimal d'interaction entre régions et 2) reconstruit l'activité corticale avec le motif trouvé.
Des résultats prometteurs sont présentés pour des données MEG simulées et réelles (tâche visuo-motrice) et comparés avec 3 méthodes de l'état de l'art.
Pour conclure, nous avons abordé un problème difficile d'exploitation des délais de l'IRMd lors l'estimation de l'activité corticale en tenant compte de la directionalité du transfert d'information, fournissant ainsi de nouvelles perspectives sur les patterns complexes de l'activité cérébrale.

Mots clés: M/EEG, localisation de sources, problèmes inverses, IRM de diffusion, connectivité cérébrale structurelle et fonctionnelle, neurosciences des réseaux

Acknowledgments

This thesis has been both a challenging and a wonderful journey. Doing my PhD in Inria and moving to Côte d'Azur was one of the greatest priviledges of my lifetime.

First and foremost, I would like to thank Rachid Deriche for his warm welcome in the Athena team and for giving me the opportunity to, first, do an internship and then to continue with a PhD in this great environment. Rachid, I will be forever grateful for all your support, both scientific and personal. Thank you for believing in me before you even met me and throughout my whole PhD. Especially in my low periods when my progress was slow and I did not believe too much in myself. Thank you for reassuring me in those several critical moments that..."If it's not good, it's not the end." And lastly... thank you for keeping your door always wide open.
Secondly, I would like to thank Théodore Papadopoulo for accepting to be my supervisor. Théo thank you for all your support in the process, with interesting scientific parts, but also with the boring administrative ones which we both hate but France apparently loves. Thank you for all the "15 min" brainstorming sessions that turned into 1h or more. Your thorough feedback and insightful comments reassured me greatly that my manuscript is ready to be sent.
A special thanks goes to the person I owe this thesis to, Samuel Deslauriers-Gauthier. Sam, I could not imagine what this journey would have been like without you. Firstly, thank you for being a programming guru who taught me how to code properly from the very beginning. Secondly, thank you for your pragmatic approach to science and work in general... and for putting me back on track every time I would diverge. And I diverged a lot. Thank you for tolerating my indecisiveness and for reminding me that "Done is better than perfect". Moreover, thank you for your ceaseless patience and availability (despite my underestimate of time)... and for answering 1 million of my questions. Lastly, thank you for your time. I would have never done this much without you, I am extremely grateful I have had you as a mentor. All this work is also yours.

I am very grateful to Gloria Menegaz and Christian Bénar for putting their time to review this manuscript. I would also like to thank Benoît Scherrer for accepting to the member of my jury and for setting the ground for my work.

I would also want to thank all the past, and present members of the Athena team. Thank you Abib, Amandine, Antonia, Aymane, Côme, Etienne, Federica, Guillermo, Isa, Igor, Joan, Kostia, Lars, Lavinia, Ludovic, Matteo, Maureen, Max, Nathalie, Océane, Patryk, Paul-Emmanuel, Petru, Pierre, Rebecca, Romain, Sandra, Sara S., Sara M. and Sofiane. It has been an honour and pleasure to share these years with you in Inria during lunch and coffe breaks, but also outside of work on apéros, beach parties and other activities. I learned a lot from you and hope our careers will lead us to cross again in the future and, perhaps, share another part of our roads together. A big, big thanks goes to all my office mates (who tolerated me and

my love for working in the dark so well) Etienne, Isa, Patryk, Océane, Sandra, Igor & Petru. Thank you for the warm & friendly atmosphere and for all the laughs & stories we shared together. It has truly been a pleasure.

Next, I'd like to thank my friends from Serbia. First and foremost, Maja Vujić (ex Lončarski) & Marija Van Hecke (ex Cvijetinović), for being such wonderful friends and for sharing some of our most joyful & brightest moments of our lives, as well as some of the darkest ones, especially throughout this PhD journey. A special thanks goes as well to Marija Bojanić, Anastazia Žunić, Ivana Pavićević and Anica Milovanović for their friendship throughout the years, for being my travel buddies & for the perpetual festive spirit between us.
I also want to dedicate a few words to my friends I met here in Inria & in Nice, since 2018. until now: Marco Benzi, Milica Tomašević, Siddharth Pritam, Selma Souihel, Pawel Mlynarski, Vu Hai Nguyen, Fiammetta Di Pasquale, Domenico Laco, Francesco Soranna, Carolina Arana, Mriko Bartolo... & other friends from Casa del Pueblo. It is indispensable to thank some the members of the Mountain Gang such as Lara, Sandra, Geremia, Michal, Minh, Luigi, Kerwin, Achilleas, Léo, Mariam, Martina, Lucilla, Lala... for our great hiking adventures and beach parties. Thank you for making my social life in Nice absolutely wonderful & rich in joy and a lifetime of great memories. I am beyond grateful I met you.
Thank you all for your support, friendship & love...and for never letting me feel alone, even if some of you are thousands kilometers apart.

Finally, I'd like to thank my family for believing in me, especially my grandparents and my father who are cheering for me from above.
Last but not the least, I'd like to thank my mom Božica for being my anchor and for giving me a firm ground to stand on. Thank you for your infinite support and unconditional love throughout my life. Without you, all of this would be impossible. This is yours just as much as it is mine.

Contents

Notation

x	scalar variable
$\boldsymbol{x} = [x_0, ...x_{n-1}]^T$	vector $\in \mathbb{R}^n$
$\boldsymbol{X}$	matrix
$\boldsymbol{x}_i$	i^{th} element of vector $\boldsymbol{x}$
$\boldsymbol{X}_{ij}$	the element of the i^{th} row and j^{th} column of matrix $\boldsymbol{X}$
$\hat{\boldsymbol{x}}$	estimated vector
$\hat{\boldsymbol{X}}$	estimated matrix
$\nabla_{\boldsymbol{X}}$	the gradient with respect to (w.r.t.) $\boldsymbol{X}$
$\|\|\boldsymbol{x}\|\|_1 = \sum_i^n \|x_i\|$	l_1-norm of a vector $\boldsymbol{x}$
$\|\|\boldsymbol{x}\|\|_2 = \sqrt{x_1^2 + ... + x_n^2}$	Euclidean or l_2-norm of a vector $\boldsymbol{x}$
$\|\|\boldsymbol{x}\|\|_p = (\sum_i^n \|x_i\|^p)^{\frac{1}{p}}$	l_p norm of a vector $\boldsymbol{x}$ for $1 \leq p \leq \infty$
$\|\|\boldsymbol{X}\|\|_F = \sqrt{\sum_{ij} \|\boldsymbol{X}_{ij}\|^2} = \sqrt{tr\left(\boldsymbol{X}\boldsymbol{X}^T\right)}$	Frobenius norm of a matrix $\boldsymbol{X}$

List of Acronyms

AP	Action Potential
BEM	Boundary Element Method
CNS	Central Nervous System
CSD	Constrained Spherical Deconvolution
CSF	CerebroSpinal Fluid
DAG	Directed Acyclic Graph
dMRI	Diffusion Magnetic Resonance Imaging
dWI	Diffusion Weighted Imaging
EEG	ElectroEncephaloGraphy
ERP	Event Related Potential
FC	Functional Connectivity
fMRI	Functional Magnetic Resonance Imaging
fODF	Fiber Orientation Distribution Function
GCV	Generalized Cross Validation
GM	Gray Matter
HARDI	High Angular Resolution Diffusion Imaging
HCP	Human Connectome Project
LASSO	Least Absolute Shrinkage and Selection Operator
LCMV	Linearly Constrained Minimum Variance
LORETA	LOw Resolution Electrical TomogrAphy
MEG	MagnetoEncephaloGraphy
MEM	Maximum Entropy on the Mean
MNE	Minimum Norm Estimates
MRI	Magnetic Resonance Imaging
MSMT-CSD	Multi-Shell Multi-Tissue Constrained Spherical Deconvolution
MUSIC	MUltiple SIgnal Classification
PNS	Peripheral Nervous System
PSP	PostSynaptic Potential
SC	Structural Connectivity
SNR	Signal to Noise Ratio
SVD	Singular Value Decomposition
SQUID	Superconducting QUantum Interference Device
WM	White Matter

”All that is gold does not glitter,
Not all those who wander are lost;
The old that is strong does not wither,
Deep roots are not reached by the frost.”

J.R.R. Tolkien, *The Fellowship of the Ring*

Introduction

Context

The human brain with its $\sim$ 86 billion neurons [Herculano-Houzel 2009] is the most complex organ in the body and one of the most complex systems on Earth. It has been perplexing scientists in their endeavours to elucidate its structure and function for more than a century. It will for sure continue to bewilder in the years to come, yet, to a lesser extent, owing to the development of brain imaging technologies. During the last decade, immense progress has been made with neuroimaging technologies such as functional and diffusion magnetic resonance imaging (fMRI, dMRI) as well as magnetoencephalography and electroencephalography (M/EEG). They provide new insights into the understanding of the human brain by allowing us to reconstruct the complex structural and functional network organization of the brain *in vivo* and non-invasively. Integration of structural (dMRI) with functional (fMRI, M/EEG) modalities has the potential to identify and characterize the connections between different brain regions and yield a detailed picture of brain architecture and dynamics [Deriche 2016].

Still, mapping the human brain structure and function remains a daunting challenge in neuroscience due to its complexity and multi-scale nature. The first level of complexity is due to the colossal number of neurons, which would make the mapping on the neuronal level unfeasible. Moreover, studying a network of billions of neurons would be complicated and impractical. In order to reduce this high dimensionality, neurons can be aggregated into groups of neural assemblies or parcellated into a smaller number of brain regions.
This leads us to the second level of complexity, the **spatial scale**. The brain can be represented on 3 different spatial scales: (1) microscale (nm to μm) at the level of individual neurons, (2) mesoscale (μm to mm) at the level of neural assemblies and (3) macroscale (mm to cm) at the level of brain regions, which is the scale we are interested to explore in this thesis. Brain can be modelled as a graph of nodes which represent certain neural elements (e.g. neural assemblies/brain regions), connected by edges representing some measure of physical, functional or causal interaction between them [Meunier *et al.* 2010]. This graph-like representation of brain networks is called a *connectome* [Sporns *et al.* 2005].
The third level of complexity originates from the different **temporal scales** on which the brain can be studied and analyzed, due to the differences in time resolutions across functional modalities. The temporal resolution of metabolic imaging methods such as positron emission tomography (PET) and fMRI is at level of *seconds*, while in modalities such as M/EEG it is at the *millisecond* scale. Hence, PET and fMRI lack the temporal resolution to track fast perceptual and cognitive processes in the brain on the millisecond scale, while M/EEG allow such assessments.

Yet, some common grounds observations emerged through the insights obtained with these different modalities. Two complementary organizational principles of the brain represent the hallmark of its complex neural dynamics: *functional segregation* and *functional integration* [Tononi *et al.* 1994]. Functional segregation pertains to the brain's ability for specialized information processing to occur within locally clustered and densely interconnected neural populations. Functional integration refers to the coordinated activation and interaction of specialized brain regions distributed across different cortical areas. The structural wiring of the brain defines its possible internal dynamic states and its range of responses to external perturbations. Structural connectivity places constraints on which functional interactions occur in the network [Tononi *et al.* 1994] and shapes the rich and dynamic set of functional interactions of neural elements that underlie human cognition and behavior [Sporns 2011].

Invisible to the naked eye, at the spatial scale of micrometers, action potentials represent the most basic form of neuronal communication. They propagate with a finite velocity due to their physical properties, leading to the unavoidable fact that neural signal transmission *cannot* be instantaneous. This scales up to the dynamic functional interactions in the macroscopic brain networks. The union of specialized brain areas is mediated by functional integration, which happens in part through the **information transfer** in the long-range white matter fibers, whose properties introduce communication delays. These **delays** are measurable with M/EEG due to its high temporal resolution. Long-range anatomical connections can be obtained by dMRI tractography on a macroscopic scale, which yields a set of streamlines representing white matter fiber bundles. Given the streamlines' lengths and the signal propagation speed, transmission delays can be estimated for each connection. dMRI can thus give an insight into interaction delays of the macroscopic brain network.
Recovering electrical activity of the brain from M/EEG measurements is known as the M/EEG inverse problem. Since there are more unknowns (brain sources) than sensors, the solution is non-unique and the problem ill-posed. Prior constraints on the characteristics of source distributions are needed to obtain a unique solution. Traditional linear inverse methods deploy different constraints which can favour solutions with minimum norm [Hämäläinen & Ilmoniemi 1994], impose smoothness constraints in space along the cortical surface [Pascual-Marqui *et al.* 1994], or time [Baillet & Garnero 1997]. While structural connectivity was exploited in several methods [Hammond *et al.* 2013, Phillips *et al.* 2002], temporal dynamics of the data was not considered.
Only few approaches include **transmission delays supported by dMRI** as prior structural information, like [Fukushima *et al.* 2015, Belaoucha & Papadopoulo 2020] where source intensities are modeled with multivariate autoregressive models whose elements are constrained by dMRI-derived anatomical connections, or [Deslauriers-Gauthier *et al.* 2019, Belaoucha *et al.* 2015] based on a probabilistic technique called maximum entropy on the mean (MEM), which explicitly use delays inferred from dMRI.

Contributions of the thesis

The joint use of dMRI and M/EEG is an attractive avenue for exploring brain activity in terms of large-scale neural dynamics. This was at heart of what we were trying to exploit in this thesis: to resonstruct cortical activity from M/EEG data using transmission delays estimated from dMRI in a network-based framework.
Integrating multimodal data is a cumbersome task due to the various coordinate systems and units the data are acquired and expressed. Yet, it was an important process that lead us to one part of the **first contribution** of this thesis, a multimodal preprocessing pipeline used to integrate structural MRI, dMRI and MEG data into a same framework. The source-level brain activity lacks the ground truth, since currently no non-invasive functional modality can directly assess it. Therefore, it needs to be simulated in order to validate the accuracy of reconstruction methods. That is why we developed a simulation procedure that we used as a synthetic dataset to validate the proposed reconstruction approaches.

The **second contribution** of this thesis consists of a novel framework for solving the M/EEG inverse problem named Connectivity-Informed M/EEG Inverse Problem (CIMIP), where prior transmission delays supported by dMRI are included to enforce temporal smoothness between time courses of anatomically connected sources. We incorporated the Laplacian operator into the regularization, that operates on a time-dependent connectivity graph, as well as some of its variants. Nonetheless, certain limitations of the CIMIP approach emerged, mainly due to the nature of the Laplacian, that acts on the whole graph, favours smooth solutions across all connections, for all delays, and it is agnostic to directionality.

Even though the functional properties of different brain areas are expressed locally, they are the outcome of an interactive network working as an integrated system. We wanted to explore patterns of brain activity during visuomotor tasks, during which only a few regions usually get significantly activated. This led us to our **third contribution**, an extension of the CIMIP approach that addressed some of the CIMIP limitations, named CIMIP_OML ("Optimal Masked Laplacian"). We restricted the full source space network (the whole cortical mesh) to a network of regions of interest and tried to find how the information is transferred between its nodes. We used the concept of *network motifs* to describe the interactions between nodes in a directed graph. We proposed an algorithm which (1) searches for an optimal network motif i.e. an optimal interaction pattern between different brain regions and (2) reconstructs the source activity given the found motif. We show promising results for both simulated and real MEG data for a visuo-motor task and compare it quantitatively and qualitatively with 3 different state-of-the-art reconstruction methods.

Organization of the manuscript

Chapter 1: Background

This Chapter introduces the reader with the basic concepts in neuroscience and neuroimaging methods used in this thesis. We start with a brief overview of the nervous system and neuroanatomy. Secondly, we explain the basics of brain function in general and point out the functions of brain regions involved in visuomotor tasks, since we aim to recover brain activity during such task paradigms. Thirdly, we explain the origins of neural activity measured with EEG and MEG. Moreover, we compare and contrast EEG and MEG as functional imaging modalities. In addition, we describe different brain atlases. Further, we define the M/EEG forward problem and the theory and mathematical framework behind its solution (the leadfield matrix). On top of that, we introduce basic concepts in diffusion MRI: the information its signal captures, the representaton of fiber orientations and diffusion tractography. The output of a tractography pipeline is a set of streamlines representing the white matter fiber bundles, which is at the essence of this thesis. Finally, we introduce the reader to the main concepts and ideas in *network neuroscience*.

Chapter 2: State of the art: M/EEG inverse problem

In this Chapter, we start by introducing different approaches to solve the M/EEG inverse problem, the main hypotheses behind them and mathematical frameworks used to obtain the source estimates. We start by explaining the general formulation and why the problem is ill-posed. Then, we describe the three main families of approaches (1) the dipole fitting approaches, (2) the scanning methods and (3) distributed source models. We focus in more details on the last one, since our work falls into this category. Furthermore, we present a taxonomy of the algorithms in the group of distributed inverse solvers according to the priors they deploy and we also elaborate the theoretical and practical aspects behind each prior.

Chapter 3: Data preprocessing and simulation

In this Chapter, we first show our multimodal preprocessing pipeling used for integration of structural MRI, diffusion MRI and MEG data into a same framework. Several preprocessing steps such as the extraction of the cortical surfaces and parcellation and source space creation are explained in details. Secondly, we describe the head conduction model and the computation of the leadfield matrix. Thirdly, we specify the processing of MEG data, dMRI data (notably dMRI tractography) used in the thesis. Fourthly, we clarify and illustrate the 5 different coordinate systems in which the used data were acquired and expressed, along with the transforms that bring the data from one system to another. Fiftly, we outline the 3 spatial scales for brain's surface representation, their mapping to the underlying streamlines and explain the computation of the structural connectivity matrix and the delay matrix. Lastly, we define the simulation of source-level brain activity that was used as a

synthetic dataset to validate the reconstruction approaches presented in Chapter 4 and 5.

Chapter 4: Connectivity-informed M/EEG inverse problem

In this Chapter, we first highlight the importance of including the delays in the M/EEG inverse problem. Then, we mention some of the current methods used for the choice of regularization parameters. Moreover, we describe the evaluation error metrics used for performance assessment of different reconstruction methods. Basic concepts in graph theory are described, as well as the role of the Laplacian operator as a smoothness constraint in inverse problems. We propose Connectivity-Informed M/EEG Inverse Problem (CIMIP) to solve the M/EEG inverse problem, where prior transmission delays supported by dMRI are included to enforce temporal smoothness. In addition, we show 3 different variations of the CIMIP regularization matrix and the assumptions behind them. Furthermore, we show results for simulated and real data and compare with 3 different state-of-the-art reconstruction methods. Lastly, we highlight the limitations and open questions regarding the proposed approach.

Chapter 5: Optimal Masked Laplacian

This Chapter presents our last contribution. We first mention some limitations of the Laplacian operator and how we try to alleviate its impacts on the reconstructions. We address the following: (1) the impact of restraining the source space to a network of interest, (2) the impact of directionality in the information transfer and (3) the impact of estimation of transmission speed. In addition, we reflect back on the brain areas involved in visuomotor tasks and the networks they belong to, needed to integrate the processing of visual information, motor planning and execution. We introduce our last contribution, CIMIP_OML which is an algorithm that (1) searches for an optimal network motif, i.e. an optimal pattern of interaction between different regions and (2) reconstructs the source activity given the found motif. Moreover, we show the found optimal motifs and the source estimates obtained with them, for both simulated and real data. We again compare reconstruction results with 3 different state-of-the-art methods and the CIMIP approach proposed in Chapter 4. Finally, we mention some limitations of CIMIP_OML and highlight some future perspectives.

Chapter 6: Conclusion

The last Chapter contains a discussion and a conclusion that summarizes the main contributions from Chapters 3,4 and 5 of this dissertation. We also discuss general limitations across the different aspects of the thesis, reflect on the open questions and give some perspectives for future work.

Chapter 1

Background

Contents

Overview

This Chapter introduces the reader with the basic aspects in neuroscience and neuroimaging methods used in this thesis. It is by no means an exhaustive presentation of each included topic, but rather a presentation of the main concepts needed for the following Chapters. We start with a brief overview of the nervous system and

neuroanatomy. Secondly, we explain the basics of brain function and point out the functions of brain regions involved in visuomotor tasks, since we aim to recover brain activity during such task paradigms. Thirdly, we describe different brain atlases. Fourthly, we describe the origins of neural activity measured with EEG and MEG, and compare and contrast these two functional imaging modalities. Further, we define the M/EEG forward problem, the theory and mathematical framework behind its solution (the leadfield matrix). On top of that, we introduce the basic concepts in diffusion MRI: the information its signal captures, the representation of fiber orientations and diffusion tractography. The output of a tractography pipeline is a set of streamlines representing white matter fiber bundles, which is at the core of this thesis. Lastly, we introduce the main concepts and ideas in *network neuroscience*.

1.1 The nervous system

The nervous system is the most complex of all the different systems which constitute the human body. It is highly organized, with the role to coordinate body's conscious and unconscious functions. It constantly receives information coming from the internal and external environment, integrates and analyses them, and determines appropriate action(s) to be performed by different body parts. Anatomically, it is divided into the central nervous system (CNS) and the peripheral nervous system (PNS) (See Figure 1.1). The CNS is comprised of the brain and the spinal cord,

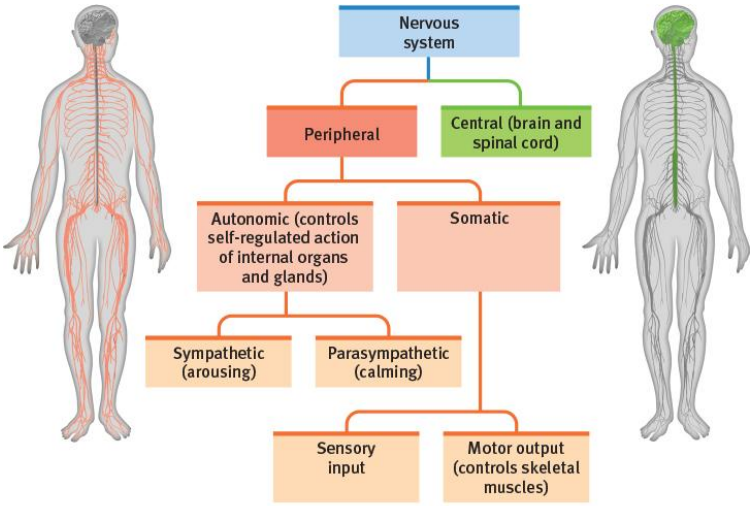

Figure 1.1: The central nervous system (CNS) and the peripheral nervous system (PNS). Taken from [Myers 2011]

while the PNS is comprised of a myriad of nerves that link receptors on the body with the CNS [Gray 1878]. These nerves enable the functions of different senses, as well as with the movements of the body. The PNS delivers stimuli from body surfaces and skeletal muscles, but also from internal organs to the circuits within the spinal cord and the brain, where they are integrated in order to produce a response.

This response is transfered back trough the PNS and is translated either into motor commands that enable body movement(s) or the regulation and adjustment of internal organs. Functionally, the PNS can be divided into two parts: somatic nervous system (SNS) and autonomic nervous system (ANS). The SNS is responsible for transmitting the sensation information from the sensory organs to the CNS, as well as for controlling skeletal muscles. The ANS is responsible for the unconscious control and regulation of the internal organs. The PNS is mediated by the brain– the central information processing and decision-making unit, which is also in the spotlight of this thesis.

1.2 The human brain

The brain is the most complex organ in the human body. On average, it comprises of around 86.06 ± 8.12 billion neurons and 84.61 ± 2.17 billion non-neuronal cells [Azevedo *et al.* 2009]. It marks supremacy over all mammalian brains: it is the most cognitively competent, the largest-than-expected from body size, enriched with an overdeveloped cerebral cortex. While it weights only around 1.5 kg, it forms just 2% of the total body mass and it receives 14% of the cardiac output and accounts for nearly 20% of resting O_2 consumption [Herculano-Houzel 2009]. The 3 main parts of the brain are cerebrum, cerebellum, and brainstem. In this thesis the focus is on the cerebrum (and refer to it as the *brain*), which is divided in two hemispheres occupying the left and the right part of the cranial cavity. The 2 hemispheres are divided by a prominent central fissure, and they are joined by a bundle of white matter fibers called the corpus callosum, that transmit messages from one side to the other. The hemispheres, as well as different cortical and subcortical structures that constitute them, are comprised of 2 main tissues: the gray matter (GM) and the white matter (WM) (See Figure 1.2). The gray matter is mainly comprised of cell bodies and relatively few myelinated axons, while white matter contains mainly long-range myelinated axons and relatively few cell bodies [Gray 1878]. Brain's surface can be observed from different points of view as illustrated in Figure 1.3 A), which are: from the front (frontal or anterior view), from the side (lateral view), from the back (occipital or posterior view) and from the middle (medial view). When viewing sections through the brain, three mutually perpendicular planes are commonly considered, as shown in Figure 1.3 B). The coronal or frontal plane is a vertical plane dividing the brain into front (anterior) and back (posterior) sections. The sagittal plane is a vertical plane dividing the brain into left and right sections. Finally, the axial or horizontal plane divides the brain into an upper (superior) and a lower (inferior) section.

1.2.1 Gray matter

As already mentioned, the gray matter is mainly comprised of cell bodies. It constitutes the cerebral cortex (on the surface of the hemispheres), the cerebellum, and the cortical structures within the white matter (such as thalamus, hypothalamus,

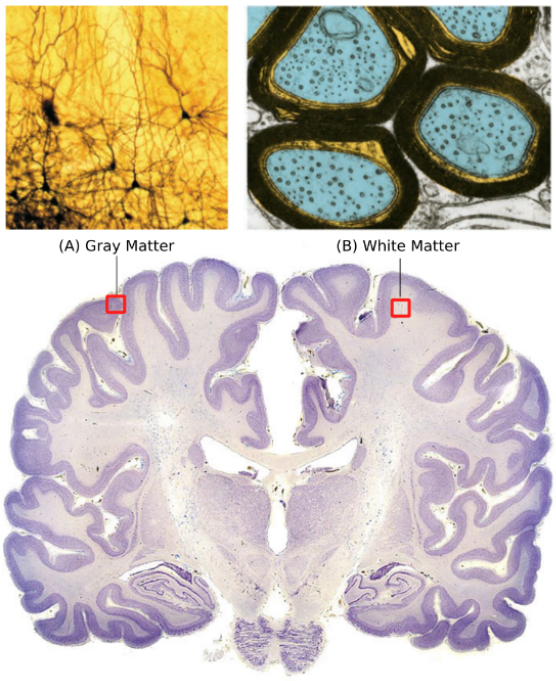

Figure 1.2: Division of brain tissue into gray and white matter. (A) gray matter is mainly comprised of cell bodies. (B) White matter comprises mostly of packed axons. Image taken from [Gallardo Diez 2018], as adapted from the brain museum (www.brainmuseum.org) and [Purves *et al.* 2019].

basal ganglia etc.) and the gray column within the spinal cord. The cerebral cortex is the most important GM structure since its involved in higher-level processes of the human brain such as thought, reasoning, learning, memory, decision-making, language, emotion, intelligence and personality. It is $\sim$ 2–4 mm thick and covers a surface area of $\sim$1600 cm^2, which is a rather large area within the available cranial volume. This is possible because the brain surface is highly folded. It's hypothesized that major driving force of these folds is the mechanical tension created by neuronal connections during development [Essen 1997]. This folding process creates ridges and fissures, which are called *gury* and *sulci*, respectively.

1.2.2 White matter

The white matter is comprised of long-range myelinated axons that originate from the neurons in the gray matter. These axons are gathered into bundles of different diameter and multiple bundles form larger pathways called fasciculi, or tracts [Catani & De Schotten 2012]. Most white matter fibers connect different regions of the cerebral cortex. Others link cortical areas with the PNS or subcortical structures, while a smaller number of them links only subcortical structures.

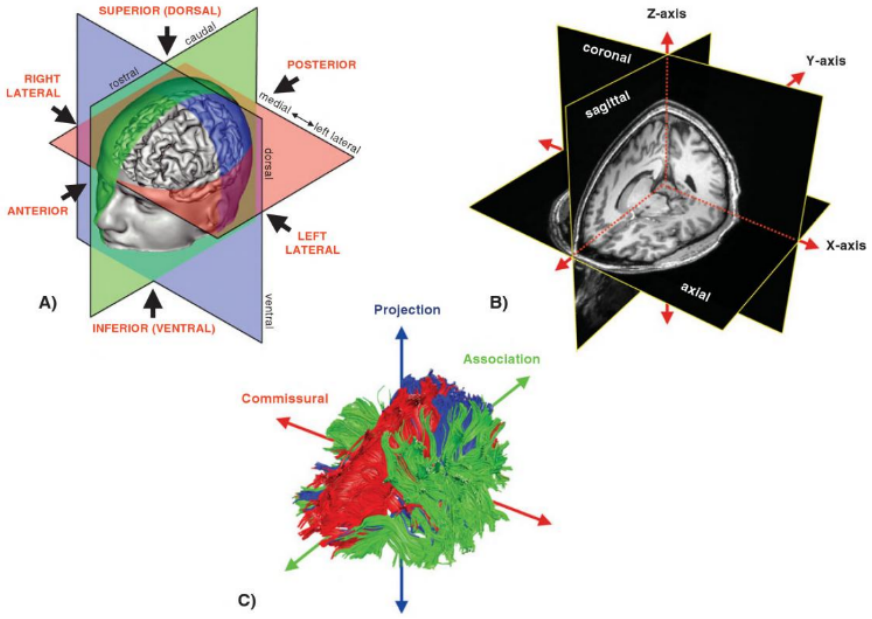

Figure 1.3: Terminology indicating the different orientations representing the different brain views: (A) stereotaxic or surface views, (B) anatomical planes and (C) connectional neuroanatomy (according to the 3 major groups of white matter tracts). Taken from [Catani & De Schotten 2012])

These fiber bundles can be divided into 3 categories [Gray 1878] (see Figure 1.3 on the bottom):

- **Association fibers** connect different cortical areas within the same hemisphere. They can be divided into 2 groups:
  - U-shape fibers (or short association fibers) connect adjacent gyri and lie directly beneath the gray matter.
  - Long association fibers connect more distant brain regions. Some of the most prominent ones are the uncinate fasciculus, cingulum, superior longitudinal fasciculus, inferior longitudinal fasciculus, ventrical occipital fasciculus, occipitofrontal fasciculus and arcuate fasciculus.
- **Projection fibers** connect the cortex with the lower parts of the brain, such as the spinal cord, subcortical areas (like the thalamus) or cerebellum. They can be ascending (afferent) or the descending (efferent). Functionally, the ascending fibers carry mainly input sensory information while the descending pathways are motor fibers transmitting the output information responsible for movements.
- **Commisural fibers** connect the two hemispheres of the brain. The largest and the most important one is called the corpus callosum (CC) comprising of around ∼200-300 million axons, while the other 2 most important parts are the anterior commissure (AC) and the posterior commisure (PC).

The main white matter fiber tracts are depicted in Figure 1.4. All these fibers form a complex network which represents the structural wiring of the brain.

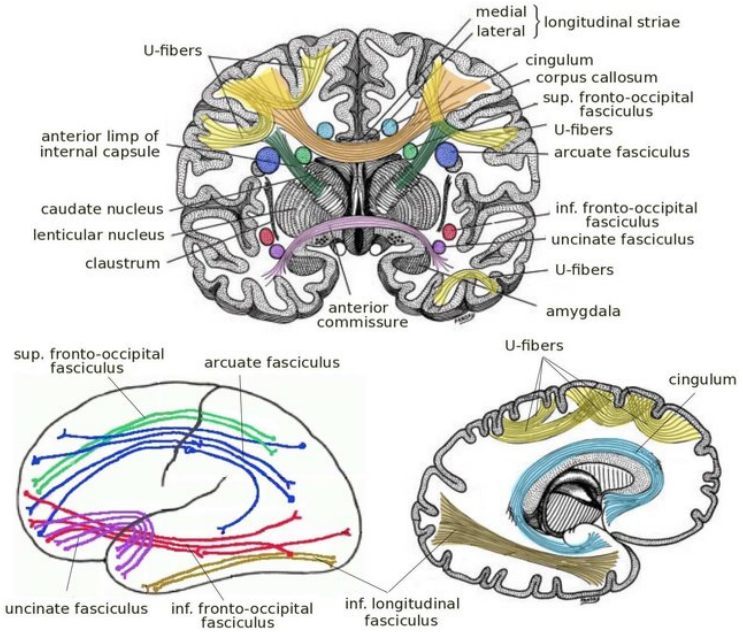

Figure 1.4: Illustration of the major white matter fiber tracts and their anatomic relationships. Image taken from [Guevara Alvez 2011].

1.2.3 Brain function

The brain function is regarded as the result of highly interconnected neurons arranged both laterally and hierarchically within the cerebral cortex and deep brain nuclei. The two hemispheres are divided into 4 main lobes: frontal, parietal, temporal, and occipital (see Figure 1.5). Each lobe is comprised of regions responsible for processing information coming from both internal and external stimuli. Main functionalities of different parts of the cortex are depicted in Figure 1.6.
Some of the main functional divisions and subdivisions associated to each lobe are the following:

- **Frontal lobe** is associated with motor functions, reasoning, planning, problem-solving, speech production, personality and emotions.
- **Parietal lobe** is associated with spatial orientation of the body and surroundings, perception, somatic senses, such as touch and temperature in addition to language comprehension.
- **Occipital lobe** is associated with visual processing and association.
- **Temporal lobe** is associated with recognition of auditory stimuli such as hearing, speech comprehension, as well as with visual recognition.

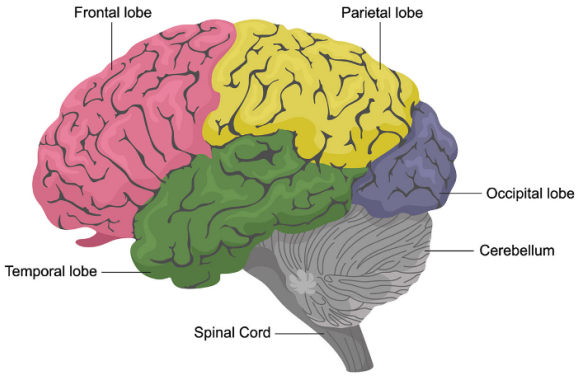

Figure 1.5: Division of the cerebral cortex into 4 main lobes: frontal, parietal, temporal and occipital. Image taken from
https://www.hopkinsmedicine.org/health/conditions-and-diseases/anatomy-of-the-brain

1.2.3.1 Visuomotor areas

In this thesis, we are interested in brain areas in charge of processing of visual information, motor planning and execution, as well as their interactions and integration into visuomotor networks. Areas in the brain in charge of visual processing are located in the occipital lobe, in the posterior part of the brain [Arthur & Guyton 1982] (see Figure 1.6). The primary sensory cortex is located in the postcentral gyrus. It handles signals coming from the thalamus while the thalamus receives the corresponding signals from the brain stem and the spinal cord [Marieb & Hoehn 2007]. The motor cortex is located in the rear portion of the frontal lobe, anterior to

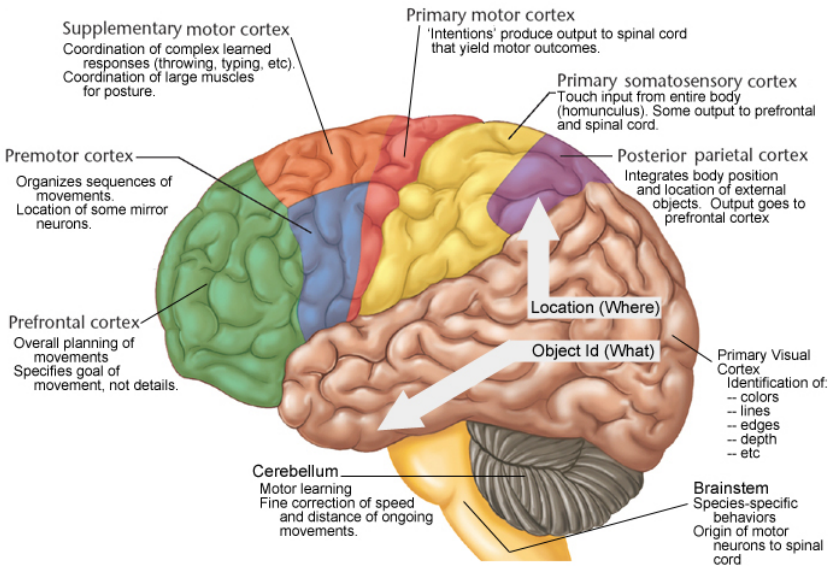

Figure 1.6: Image taken from
https://web.bvu.edu//faculty/ferguson/Course_Material/2011_Courses/Bio_2011/Ch8.pdf

the central sulcus which separates the frontal and parietal lobes [Arthur & Guyton 1982, Donoghue & Sanes 1994, Schieber 2001] (see Figures 1.6 and 1.7). The motor cortex is divided into three following subareas, where each has its own topographical representation of muscle groups and specific motor functions:

- The **primary motor area/cortex (M1)**. It lies in the frontal lobe, in the precentral gyrus (anterior to the central sulcus). This corresponds to area 4 in Brodmann's classification of cortical areas.
- The **premotor area/cortex (PMA)** lies 1-3 cm anterior to the primary motor cortex.
- The **supplementary motor area (SMA)** lies in the frontal lobe, in the superior frontal cortex.

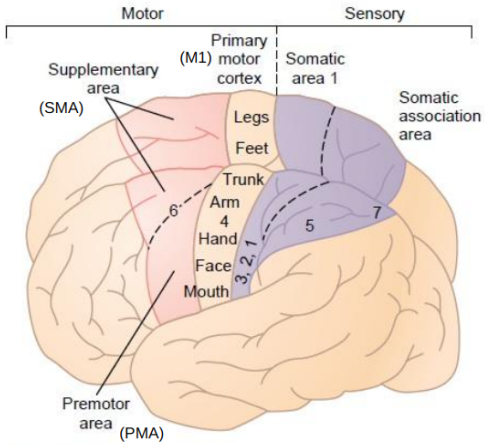

Figure 1.7: Somatosensory and motor functional areas of the cerebral cortex. The numbers 4-7 are Brodmann's cortical areas. Notice the topographical representations of the different muscle areas of the body in the primary motor cortex (M1), such as the face and mouth region the arm and hand area, the trunk, as well as the leg and feet areas Adapted from [Arthur & Guyton 1982].)

They also have different roles in the movement. For example, M1 handles signals coming from the premotor area of the frontal lobes, and it has been implicated in control of muscle force or length. PMA is involved in coupling arbitrary cues to motor acts and generates more complex "patterns" of movement than M1. SMA appears to participate more in internal guidance or planning of movement [Donoghue & Sanes 1994]. Regarding the activity, there are 3 different potentials preceding voluntary movement which can be recorded from the human scalp: 1. the readiness potential (RP), 2. the motor potential (MP), and 3. the premotion positivity (PMP) [Deecke *et al.* 1969]. The MP is generated by activity in the motor cortex associated with hand movement.

The cortical homunculus represents the motor or the sensory distribution map along the brain's cerebral cortex [Marieb & Hoehn 2007] (See Figure 1.8). The word "homunculus" is a Latin word that means "little man". It represents how the body is

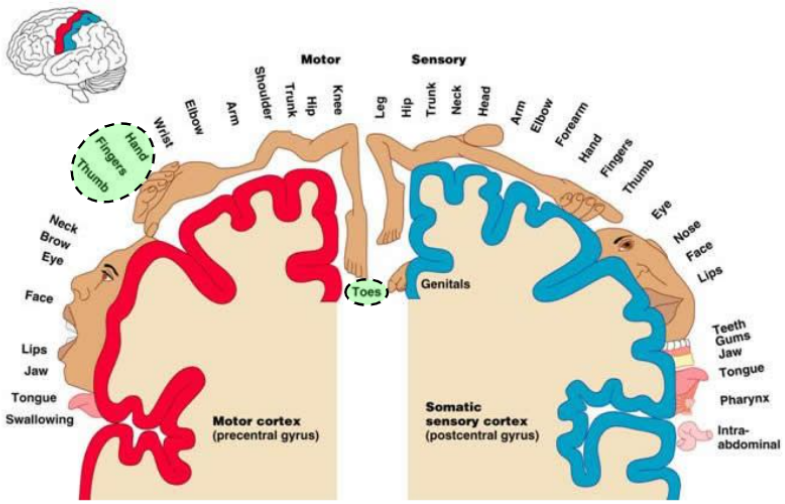

Figure 1.8: The cortical homunculus. We emphasize in green the ares associated with the hands and the feet, since the experimental paradigm of the real task MEG data we used consisted of those limb movements.

perceived within the brain and the distribution of neurons in these areas in order to create this perception. The motor homunculus is a topographic representation of the body parts and its correspondents along the precentral gyrus of the frontal lobe. Correspondingly, the sensory homunculus is a topographic representation of the body parts along the postcentral gyrus in the parietal lobe.

1.2.3.2 Visuomotor networks: state-of-the-art

In this thesis, we focused on visuomotor networks and the interactions among different brain regions needed to integrate the processing of visual information, as well as motor planning and execution. Several studies examinated brain activity during motor tasks, mostly in fMRI, and confirmed the activation of the aforementioned motor areas, M1, PMA and SMA [Martuzzi *et al.* 2006, Abe & Hanakawa 2009, Yeo *et al.* 2011, Frässle *et al.* 2021]. M1 and SMA ares have been shown to be mostly active (though not exclusively) contralateral to the hand movement [Martuzzi *et al.* 2006, Frässle *et al.* 2021] mostly due to the motor potential (MP), while the spatial distribution of the premotion positivity (PMP) is more widespread and bilaterally symmetrical [Deecke *et al.* 1969]. For example, in [Frässle *et al.* 2021] the authors assessed the validity of regression Dynamic Causal Modelling (rDCM) for inference of whole-brain effective connectivity patterns from fMRI data, using a dataset with a hand movement task. They showed that rDCM could infer plausible effective connectivity patterns in a brain network of 200 regions, and with graph-theoretical measures applied to the whole-brain effective connectivity patterns showed the important role of motor regions and the hemispheric asymmetries of the network (see Figure 1.9).

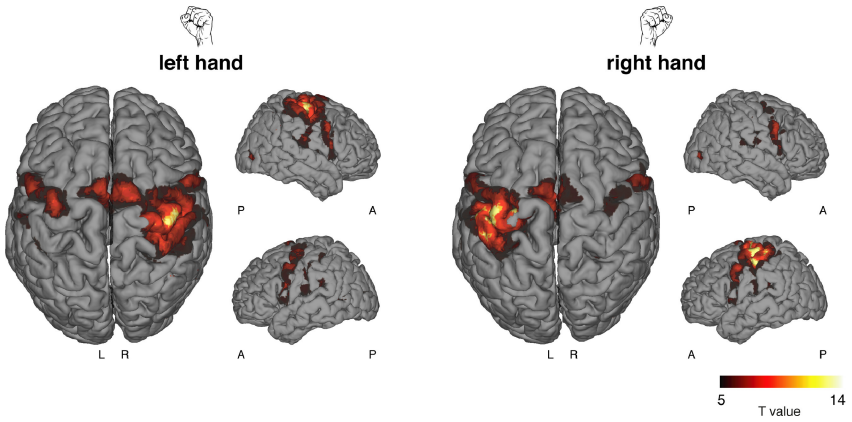

Figure 1.9: Image taken from [Frässle *et al.* 2021] showing BOLD activation during visually synchronized unilateral hand movements at the group level (25 subjects). Left-hand (left) and right-hand fist closings (right) evoked activation in a distributed network, mainly lateralized to the contralateral hemisphere.

Areas in the brain in charge of visual processing (V1-V5) are located in the occipital lobe, in the posterior part of the brain. Numerous fMRI studies have investigated the activation of these areas when subjects were presented with different visual stimuli, such as [Yeo *et al.* 2011, Napadow *et al.* 2013, Martuzzi *et al.* 2006]. Callosal fibers play an important role in the interhemispheric interactions both in visuo-visuo and visuo-motor interhemispheric interactions [Kust Küst 2003, Martuzzi *et al.* 2006]. An example of results of an fMRI study demonstrating the brain's response in visual areas to translating stripes stimulation is shown in Figure 1.10. Recent work of [Ionta 2021] presents a summarizing review of the available neuropsychological evidence on the development of visual competences, with a focus on the associated visuomotor integration has been proposed recently (See Figure 1.11 illustrating the main cortical areas involved in visual perception and visuomotor coordination). Experiments involving lateralized processes, such as unilateral limb movements, provide strong qualitative predictions [Stephan *et al.* 2007, Frässle *et al.* 2021] that concern both the location where processes should occur (or not occur) as well as the asymmetry (or mirror symmetry) of processes across hemispheres.
Currently, there are no means to assess *directly* and globally which white matter pathways were used for brain communication during a specific task, although some promising indirect approaches have been proposed [Deslauriers-Gauthier *et al.* 2019, Deslauriers-Gauthier *et al.* 2020]. Microelectrode arrays (MEAs) have a very high spatial resolution, at the level of individual neurons. However, they can only cover the brain area of a few mm^2. ECoG electrodes are placed directly onto the surface of the brain and can cover an area of several cm^2. They provide a richer spatial resolution because the electrical activity is recorded directly from the cortex, which bypasses the effects of the volume conduction caused by the skull and the scalp. Both MEAs and ECoG are invasive since they require a craniotomy for their implantation. Yet, at present, there is no existing technique, not even invasive, to measure the electrical activity at the axonal level for the whole human brain.

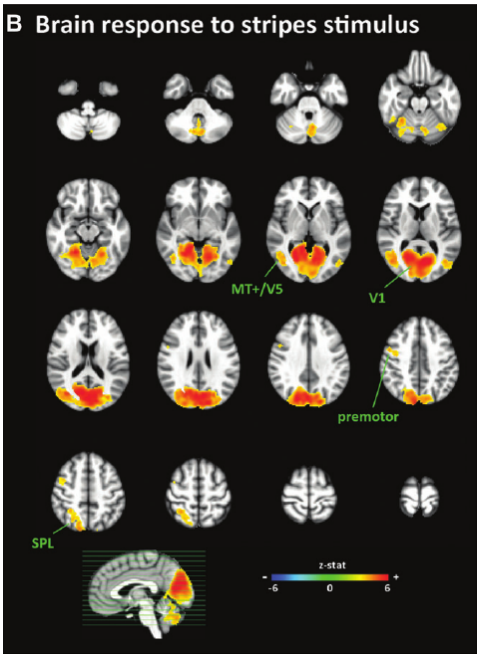

Figure 1.10: Image taken from [Napadow *et al.* 2013]. Brain fMRI response to visual stimulation with translating stripes. Robust fMRI activation was found in primary (V1) and secondary (motion-sensitive MT and V5) visual brain areas. Activation was also noted in SPL and premotor areas, as well as in the cerebellum.

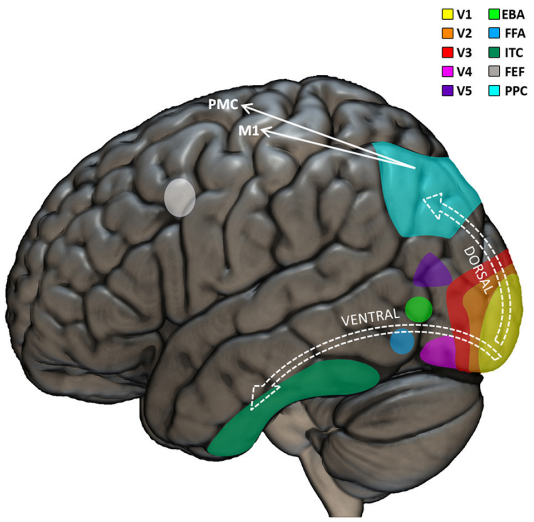

Figure 1.11: Image taken from [Ionta 2021]. Graphical representation of the main cortical regions involved in visual perception and visuomotor coordination. The visual input is first processed by the primary visual cortex (V1). Further processing is done by the extrastriate visual regions (V2-V5) that triggers the recruitment of the dorsal or ventral stream as a function of whether or not the visual input needs to be used to perceive or move in the environment, respectively. EBA, extrastriate body area; FFA, fusiform face area; ITC, inferior temporal cortex; FEF, frontal eye field; PPC, posterior parietal cortex; M1, primary motor cortex; PMC, premotor cortex.

1.2.4 Atlases of the human brain

The human brain contains almost 100 billions neurons [Herculano-Houzel 2009], a number that highlights the daunting challenge of mapping such a network. Numerous studies in cytoarchitecture, brain function, as well as neural tract tracing techniques show that neurons tend to organize and activate in spatially coherent groups [Schmahmann *et al.* 2009, Brodman 1909, Tzourio-Mazoyer *et al.* 2002, Desikan *et al.* 2006, Destrieux *et al.* 2010, Glasser *et al.* 2016, Gallardo *et al.* 2018]. Dividing the brain into distinct and spatially coherent groups (regions) according to a certain criteria is called *parcellation*. The aim of parcellating the brain is to reduce the dimensionality of the neuronal network of billions of neurons into a smaller, tractable number of regions. Parcellations that are consistent and reproducible across subjects allow us to elucidate various properties about the human brain. A large number of brain atlases has been proposed, notably in the last two decades. Each of them subdivides the cortex based on different assumptions about cytoarchitectonic, anatomical, functional and structural criteria (See Figure 1.12). The interested reader is referred to [Gallardo Diez 2018] for a detailed review on brain parcellations. Let us mention some of the most notable atlases and the criteria they are based upon.

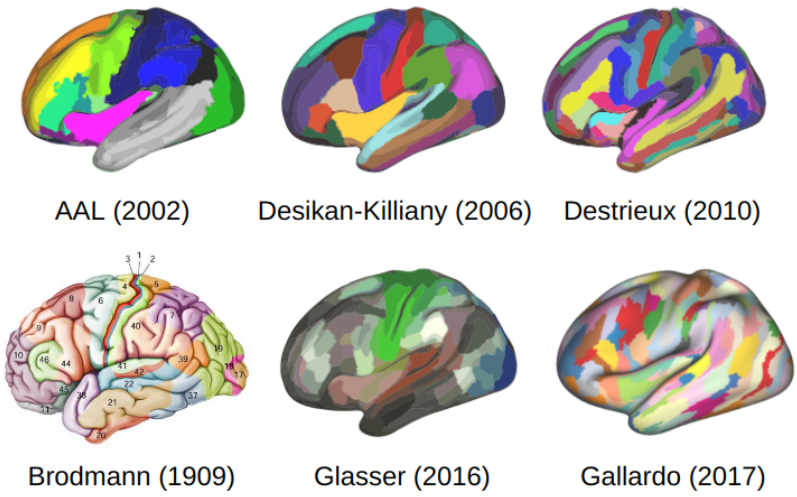

Figure 1.12: Different parcellations of the human brain. Top: AAL atlas [Tzourio-Mazoyer *et al.* 2002], Desikan-Killiany [Desikan *et al.* 2006], Destrieux [Destrieux *et al.* 2010]. Bottom: Brodmann [Brodman 1909], Glasser [Glasser *et al.* 2016] and Gallardo [Gallardo *et al.* 2018] atlas. Adapted from [Zhi *et al.* 2022] and [Gallardo *et al.* 2018].

Cytoarchitectonic atlases are based on the cellular composition of the cortex, taking into account the criteria such as thickness, neuronal type and their celular organization. The most famous atlas of this type dates more than a century, the Brodmann atlas [Brodman 1909].

Anatomical atlases characterise each region by its shape and location in the brain. The most famous examples in this category are the AAL atlas [Tzourio-Mazoyer *et al.* 2002], the Desikan-Killiany atlas [Desikan *et al.* 2006] and the Destrieux atlas [Destrieux *et al.* 2010]. All anatomical atlases divide the cortex in a different number of regions (generally smaller than 100), as the definition of the boundaries of each region is done manually. In this thesis we used the Desikan-Killiany atlas, which is based on the manual segmentation of a template brain accounting for morphological consistencies of healthy human brains. This atlas contains 68 cortical regions and it is one of the most widely used in the brain imaging community due to its high accuracy when defined on new subjects.
Functional atlases aim to divide the brain into regions involved in different functions of the brain. They are usually defined with imaging techniques such as functional Magnetic Resonance Imaging (fMRI).
Structural atlases rely upon axonal connectivity patterns in different cortical areas, with respect to a predefined set of regions of interest. The development of in-vivo techniques such as diffusion MRI-based tractography for tracking the axonal fiber bundles allowed several of such atlases to appear. In structural and functional atlases, the typical way to generate a parcellation is by first computing a connectivity matrix between regions and then parcellate it using some clustering technique.
State-of-the-art parcellations exploit multiple imaging modalities and methodologies, resulting in atlases which are coherent with more than one of the aforementioned criteria. Some notable examples in this category are the Glasser atlas [Glasser *et al.* 2016] and the Gallardo atlas [Gallardo *et al.* 2018].

1.3 The origin of neural activity

Neurons (or nerve cells) are cells within the nervous system that interact and communicate with each other using a combination of electrical and chemical signals, by means of specialized contacts called synapses [Purves *et al.* 2019]. Supporting cells (called neuroglia) do not have the property of electrical signaling. Yet, they have multiple vital functions in the developing and adult brain like maintaining the ionic surrounding of nerve or modulating the rate of nerve signal propagation. Most neurons comprise of a cell body, an axon and dendrites (see Figure 1.13). The cell body (or soma) is where the metabolic activity of a neuron takes place and where neurotransmitters get synthesized. The cell body generally has two types of extensions: multiple short **dendrites** and one long, tubular **axon**. The dendrites morphology resembles a tree and they are responsible for receiving incoming signals from other nerve cells. The complexity of the dendritic arbor determines the number of neurons with whom a neuron can communicate, ranging from one or few, to a rather larger number of other neurons. The axons are the transmitting elements of neurons that can convey electrical impulses over distances in range from 0.1 mm to even 2 m. Most axons are insulated by a fatty sheath called **myelin**, that is regularly interrupted with gaps called the nodes of Ranvier. Myelin serves as a separating layer for

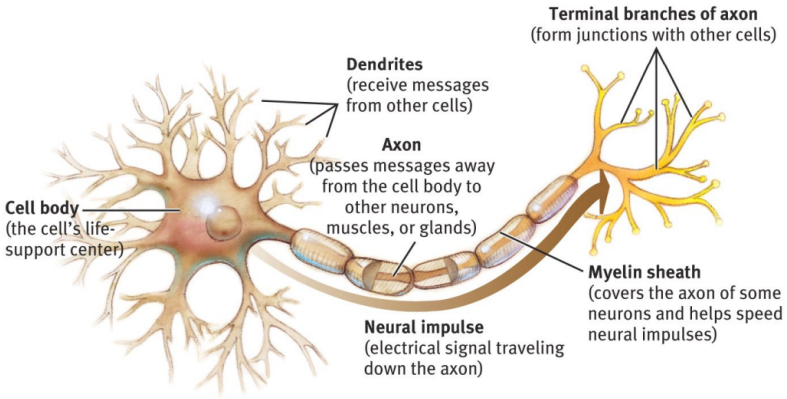

Figure 1.13: The structure of a neuron and its connections. Image taken from [Weiten 2021].

the axon from the extracellular components. Yet, it is mainly involved in increasing the velocity of nerve impulse transmission for a quick response. Unmyelinated axons also exist and they conduct nerve impulses at a low velocity.
Morphologically, neurons can be divided in two major groups: granule neurons and pyramidal neurons. Granule cells are star-shaped neurons, typically $< 20\mu m$ in diameter, while pyramidal neurons have large, pyramid-shape bodies in range $20 - 120\mu m$. Pyramidal neurons are multipolar (with a single axon and many dendrites) excitatory neurons, and they comprise of $\sim 2/3$ of all neurons in the mammalian cerebral cortex.
Functionally, neurons can be divided into **excitatory** and **inhibitory**. Excitatory neurons release the neurotransmitter glutamate to send signals to other cells, while inhibitory neurons release gamma-Aminobutryc acid, to reduce neuronal excitability throughout the nervous system.
Another neuronal classification can be done based on their role in a neuronal circuit. Neurons that transmit information towards the circuit are called **afferent** neurons, while the ones that transmit information away from the circuit are called **efferent** neurons. As mentioned above, the axons transmit electrical signals between the soma and synapses that are called Action Potentials (AP) (see Figure 1.14).
A neuron receives several input signals (postsynaptic potentials (PSPs)) through its dendrites from the neurons it is connected to. Then, the neuron will spike (transmit an AP to other neurons) or not, depending on its membrane potential. At rest, the neuron's voltage is around -70 mV. This is called the resting membrane potential and it is the difference in the electrical potential on either side of the membrane, when the cell is at rest. Activation of an excitatory synapse causes the flow of positive ions into the cell, resulting in a local change of membrane potential (this is called depolarization). If this potential change i.e. the depolarization threshold is higher than 20 mV, AP is triggered. When an input signal (synaptic potential) depolarizes the neuronal membrane, the local change in membrane potential opens local N_a^+ channels which allow N_a^+ ions to flow down its concentration gradient, from outside of the cell where the N_a^+ concentration is high towards inside where

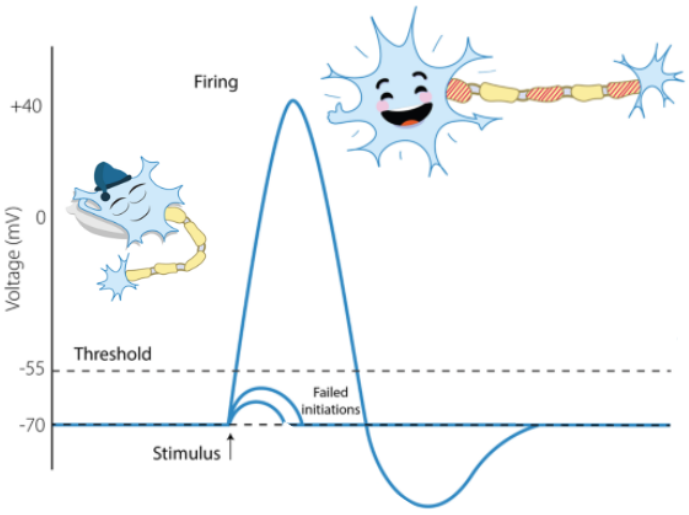

Figure 1.14: A charming illustration of an Action Potential (AP). Image adapted from [Khrennikov *et al.* 2018]

it is low. This makes the membrane's potential jump to approximately +40 mV. When N_a^+ ions' gates close, K^+ ions' gates open due to concentration and voltage gradient and K^+ ions leave the cell. Due to this outflow of positive ions from the cell, the membrane potential begins to repolarize back towards its rest potential. During repolarization, the potential first decreases below the resting value (this is called hyperpolarization). Lastly, the membrane's potential comes back to its rest value. The AP is conducted down the axon, to the axon's terminal, where it initiates a chemical communication with other neurons. The most famous mathematical model that describes how action potentials in neurons are initiated and propagated is the Hodgkin and Huxley model [Hodgkin & Huxley 1952].

The current flowing from the soma to the dendrites is called the **intracellular** or the **primary current**. Due to electrical charge concervation principles, **extracellular** (**secondary**, return or volume) **currents** are generated as well. Both primary and secondary currents contribute to creating an electric and magnetic field that can be measured on the scalp or outside the head [Hämäläinen *et al.* 1993, Baillet *et al.* 2001].

The primary current is more dense than the secondary current since the extracellular current is more dispersed. The *main* primary currents which give rise to measurable M/EEG signals are the postsynaptic PSPs in the large cortical pyramidal neurons, oriented perpendicularly to the cortical surface. Synchronous activation of each macro-column of thousands of such neurons behaves as an electrical dipole [Niedermeyer & Lopes da Silva 1995] (See Figure 1.15). The orientations of dendritic trunks of these neurons are coherent and perpendicular to the cortical mantle. At least 50,000 of such neurons are needed to generate a measurable signal [Clerc & Papadopoulo 2008]. Each PSP can contribute to as little as 20 fAm current dipole, which is too small to be detected with M/EEG. The minimal amplitude of current

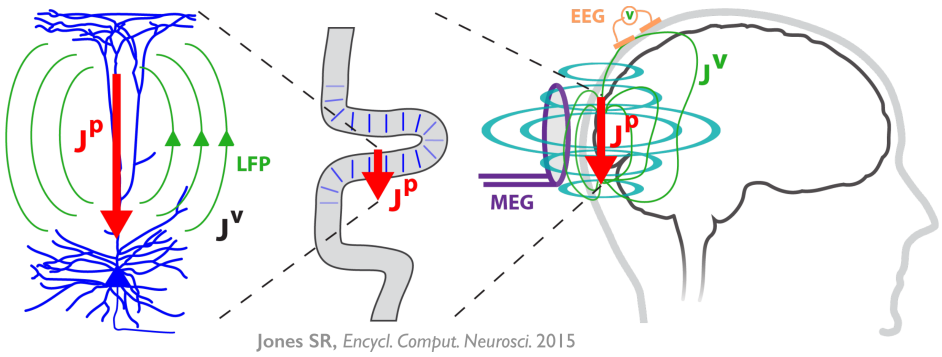

Figure 1.15: Schematic representation of electric and magnetic fields generated by the primary current, which behaves as an electrical dipole (red arrow). Image taken from [Jaeger & Jung 2015].

dipole moments required to generate a measureable signal is∼10 nAm, which corresponds to around a million of synapses being simultaneously active. Therefore, what is actually measured is the cumulative summation of activity of millions of synapses that are spatially close. Given the thickness of the cortex of about 4 mm, a net current expected to be yielded by a 5mm x 5mm patch is around 10 nAm [Baillet *et al.* 2001]. For great reviews on the origins of extracellular fields and currents see [Niedermeyer & Lopes da Silva 1995] and [Cohen 2017].

1.4 Fundamentals of EEG and MEG

Electroencephalography (EEG) and magnetoencepalography (MEG) are functional neuroimaging modalities which provide information about the brain activity non-invasively and almost instantaneously. They have high temporal resolution which allows to track fast perceptual and cognitive processes in the human brain on the millisecond scale [Niedermeyer & Lopes da Silva 1995, Hämäläinen *et al.* 1993, Sarvas 1987]. EEG and MEG can be measured simultaneously and reveal complementary properties of the electromagnetic fields of the brain [Malmivuo *et al.* 1997, Darvas *et al.* 2004].

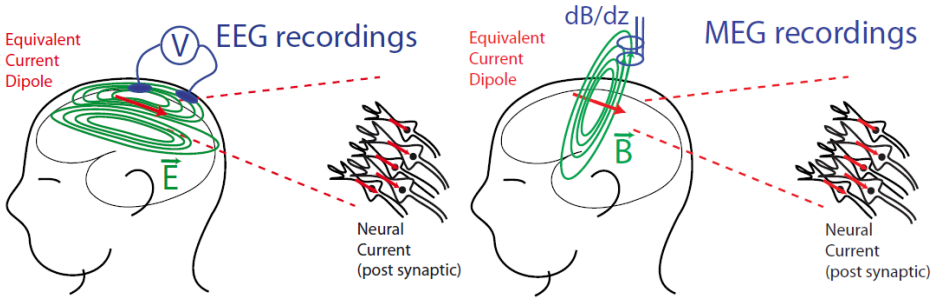

Figure 1.16: EEG and MEG recordings. Adapted from [Gramfort 2009].

1.4.1 Principles of EEG

Electroencephalography was developed by a German physicist Hans Berger in 1929. It records brain activity by measuring generated electrical signals with the help of electrodes. It produces measurements that are a set of potential differences between pair of electrodes, when these electrodes are placed on the scalp [Tudor *et al.* 2005, Bazil *et al.* 2007]. The EEG recordings can be used for direct, real time, monitoring of spontaneous and evoked brain activity allowing spatiotemporal localization of neuronal activity. It is widely used in the clinical context, principally to localize epileptogenic zones, which can be useful in for surgical planning for patients with partial seizures [Alarcon *et al.* 1994, Huppertz *et al.* 2001, Bénar *et al.* 2006, Jatoi *et al.* 2014] Further, it is also used to diagnose/analyze different neural disorders (epilepsy, tumors, locating head damages, schizophrenia, depression, Parkinson's and Alzheimer's diseases,...) but also for Brain-Computer interfaces (BCI), in the gaming industry etc.

1.4.2 Principles of MEG

Magnetoencephalography was developed in 1972. by David Cohen (See Figure 1.17). Fundamentally, any electrical current produces magnetic induction, whose strength can be measured remotely from the current source – for example, with a pick-up coil. The magnetic flux across the coil surface induces an electrical current in the coil wiring material, whose amplitude is proportional to the magnetic induction [Baillet 2017]. Magnetic signal produced by neural currents is in the nanoampere (10^{-9} A) range, so extracranial magnetic inductions are typically measured on a scale of femtoteslas (10^{-15} T). For comparison, the Earth's magnetic field strength is from 25 to 65 μT. This is why MEG measurements are performed in a magnetically shielded room.

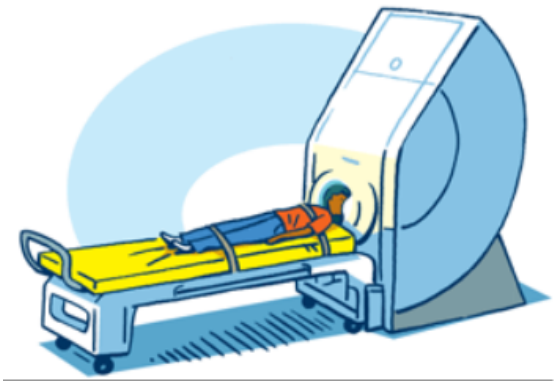

Figure 1.17: Schematic illustration of a MEG system. Modern MEG systems comprise of a helmet-shaped dewar that houses hundreds of sensors and that fits the subject's head. Image taken from https://www.chp.edu/our-services/brain/neurosurgery/epilepsy-surgery/diagnostic-evaluation/meg.

The present industry standards rely on pick-up coils coupled with superconducting interference devices (SQUIDs) [Hämäläinen *et al.* 1993, Baillet 2017]. SQUIDs exploit the principles of quantum physics for the detection of small electrical currents, like those induced by weak magnetic signals, with high sensitivity and large dynamic ranges. Two different types of such sensors exist, gradiometers and magnetometers. Clinical applications of MEG are manifold. Apart from epilepsy where it is used for localizing epileptogenic brain regions, a substantial body of work in autism spectrum disorder demonstrates that simple MEG measures of delayed early auditory responses (easily implementable in the clinic) are indicative of the syndrome's severity. MEG is clinically prescribed and reimbursed in a few countries for specific indications like pharmacologically intractable epilepsy and presurgical functional mapping of brain tumors [Baillet 2017]. Nevertheless, its use in brain tumor cases remains limited since MEG analysis pipelines remain time-consuming, which is usually incompatible with the time pressures of clinical decision-making and surgical interventions in neuro-oncology. For more details see a comprehensive review on MEG in [Baillet 2017].

1.4.3 EEG versus MEG

As we mentioned above, EEG and MEG can reveal complementary properties of the electromagnetic fields of the brain. Although EEG and MEG signals originate from the same neurophysiological processes, there are important differences.
EEG signals are strongly affected by the difference in electrical conductivity between the scalp, skull and other biological tissues. On the other hand, magnetic permittivity (magnetic equivalent of conductivity) is homogeneous and identical across all compartments (including the air between the scalp and sensors) [Malmivuo *et al.* 1997, Darvas *et al.* 2004].
Since magnetic fields are less distorted than electric fields by the skull and scalp, this results in a better spatial resolution of the MEG. Spatial topography of MEG sensor data is visually and quantitatively less smeared and distorted than that of EEG. This results in clearer interpretation of MEG sensor topography in terms of the anatomical locations of its underlying brain sources. Typically, the number of electrodes in EEG is $N_{EEG} \approx 60 - 100$, while in MEG the number of gradiometers or magnetometers is $N_{MEG} \approx 300$.
Concerning the influence of current flow direction, brain regions in sulcal walls (tangential current flow) produce MEG signals that are stronger than sources along gyral crowns (radial current flow) [Baillet 2017]. Scalp EEG can, thus, detect activity both in the sulci and at the top of the cortical gyri, whereas MEG is most sensitive to activity originating in sulci. The EEG is sensitive to all components of the electric field, while MEG is sensitive only to the tangential components. (See Figure 1.18). Hence, EEG is sensitive to activity in more brain areas, but activity visible in MEG can be localized with more accuracy. The decay of magnetic fields as a function of distance is more pronounced than for electric fields. Therefore, MEG is more sensitive to superficial cortical activity, which makes it useful for the study

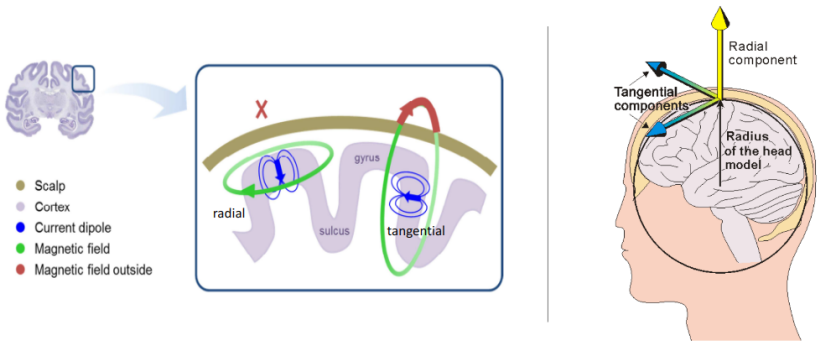

Figure 1.18: Left: Radial and tangential current dipoles and orientation of corresponding electric and magnetic field components. Taken from [Belaoucha 2017]. Right: Three orthogonal components of every current source. Taken from [Malmivuo *et al.* 1997].

of neocortical epilepsy. Lastly, MEG is reference-free, whereas scalp EEG relies on a reference that, when active, makes interpretation of the data troublesome.

1.5 Forward Modelling of EEG and MEG signals

The EEG/MEG forward problem aims to the determine the measured electric potentials (magnetic fields) at the sensor locations at the scalp, given the distribution of neuronal sources in the brain. The inverse problem, on the other hand, aims to localize and recover electrical activity of the brain from M/EEG measurements (See Figure 1.19). Since there are more cortical sources that generate electrical activity (i.e. unknowns) than sensors, the solution is non-unique and the problem ill-posed. Inverse problem will be discussed in details in Chapter 2. In this Chapter, we will try to explain basic concepts behind the forward problem. The forward problem answers to the question of what would be the electric/magnetic fields outside the head, given the current distribution inside the head, as well as geometry of the brain, skull, and scalp and their conductive properties [Sarvas 1987, Hamalainen & Sarvas 1989, Mosher *et al.* 1999]. A great review on forward modelling can be found in [Maksymenko 2019].

1.5.1 Quasi-static approximation of Maxwell's equations

Maxwell's equations are the fundamental pillars in the world of electromagnetics and also one of the most important equations in science in general. They provide a mathematical model for electric, optical, and radio technologies, electric motors, wireless communication, lenses, radars...and last but not the least, they play an essential role in computational neuroscience. They describe how electric and magnetic fields propagate and interact, and they relate the electromagnetic field to charge and current density. The electric field is denoted by $\boldsymbol{E}$, the magnetic field by $\boldsymbol{B}$, while ρ and $\boldsymbol{J}$ are the charge and current density, respectively.

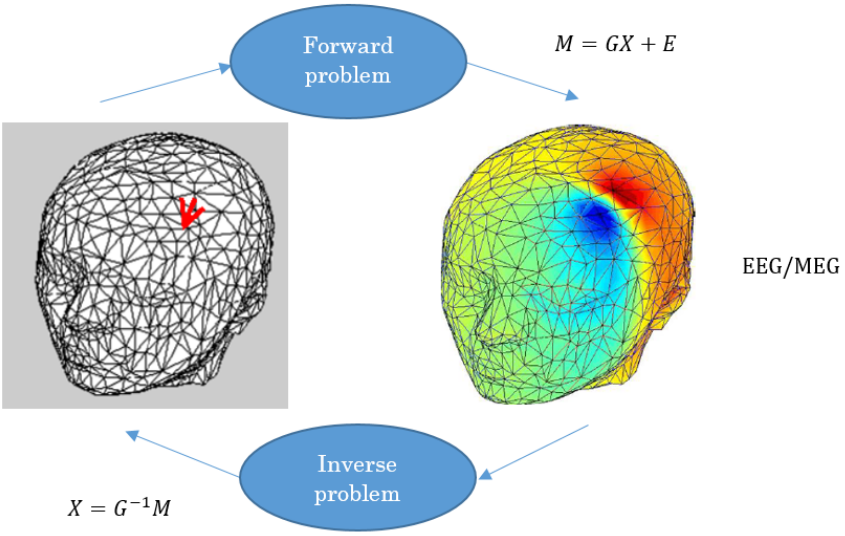

Figure 1.19: Forward and inverse problem. Image adapted from [Zeynep 2012].

These are the 4 partial differential equations:

$$\nabla \cdot \boldsymbol{E} = \frac{\rho}{\varepsilon_0} \tag{1.1}$$

$$\nabla \cdot \boldsymbol{B} = 0 \tag{1.2}$$

$$\nabla \times \boldsymbol{E} = -\frac{\partial \boldsymbol{B}}{\partial t} \tag{1.3}$$

$$\nabla \times \boldsymbol{B} = \mu_0(\boldsymbol{J} + \varepsilon_0 \frac{\partial \boldsymbol{E}}{\partial t}) \tag{1.4}$$

where ε_0 is the electric permitivity of the medium, μ_0 is the magnetic permeability, $\nabla\cdot$ is the divergence of a vector field and $\nabla\times$ is the curl of a vector field. Due to the low signal frequency measured with EEG/MEG sensors (typycally <1 kHz) and medium properties, the time derivatives in the Maxwell's equations can be omitted [Sarvas 1987]. This quasi-static approximation is used then to relate the brain activity, which is approximated by electric dipoles located on the cortical surface, to the electric potentials (in the case of EEG) or to the magnetic field (in the case of MEG). Due to this quasi-static approximation, we can see that the solution of the forward problem does not depend on ε_0.
The current density $\boldsymbol{J}$ produced by neuronal activity can be split into two components: the intracellular primary current $\boldsymbol{J}^p$ [Sarvas 1987] and the volume extracellular secondary current $\boldsymbol{J}^v = \sigma\boldsymbol{E}$:

$$\boldsymbol{J} = \boldsymbol{J}^p + \sigma\boldsymbol{E} = \boldsymbol{J}^p - \sigma\nabla V \tag{1.5}$$

where σ is the tissue conductivity.

1.5.2 The current dipole

In order to represent the electrical activity in the brain, the most used model is a "current dipole" (See Figure 1.15). It represents an oriented current source of located at a single position r_0 , with dipolar moment $\boldsymbol{q}$, and it is denoted by:

$$\boldsymbol{J}^p = \boldsymbol{q}\delta(\boldsymbol{r} - \boldsymbol{r_0}) \tag{1.6}$$

where $\delta(\cdot)$ is Dirac delta distribution.
Various neurophysiological and neuroimaging studies have shown that cortical activation is a distributed spatiotemporal dynamic process [Nunez *et al.* 2006, Fox & Raichle 2007, Jirsa *et al.* 2002]. In order to model the activity of the whole cortex, it is convenient to use distributed source models. They place the current sources at a large number of dipoles distributed on the cortex, whose orientation is fixed to be normal to the cortical mantle [Baillet *et al.* 2001, Dale & Sereno 1993]. The relationship between source amplitudes and M/EEG measurements can be expressed by the linear model

$$\boldsymbol{M} = \boldsymbol{G}\boldsymbol{J} + \boldsymbol{E} \tag{1.7}$$

where $\boldsymbol{M}$ is a matrix of measurements, $\boldsymbol{J}$ is the matrix of source amplitudes, $\boldsymbol{G}$ is the forward operator and $\boldsymbol{E}$ is additive noise in sensor space. Measurement matrix is given by $\boldsymbol{M} \in \mathbb{R}^{N\times T}$ for N sensors and T time samples. The unknown matrix of S source amplitudes is given by $\boldsymbol{J} \in \mathbb{R}^{S\times T}$. In distributed source models, the size of the source space is generally large ($S \approx 10^4$) and the number of sensors can vary depending on the modality. Typically, the number of electrodes in EEG is $N_{EEG} \approx 60 - 100$, while in MEG the number of gradiometers or magnetometers is $N_{MEG} \approx 300$. See Figure 1.19 for an illustration (where $\boldsymbol{J}$ is denoted as $\boldsymbol{X}$).
In this Chapter, we are interested in the lead field matrix $\boldsymbol{G}$. Computation of $\boldsymbol{G}$ requires modeling the geometry of the head and its electromagnetic properties [Hamalainen & Sarvas 1989, Mosher *et al.* 1999] such as conductivities of different tissues. More specifically, it requires having a conductor model for the head, a source space of dipole locations, and the sensor locations relative to those dipoles.

1.5.3 Head modelling

The human head is a bounded conductor. No electric current flows outside the head (except at the neck). The scalp and the brain have almost equal conductivities, while the conductivity of the skull is about 100 times smaller [Hamalainen & Sarvas 1989]. In order to correctly approximate the electric potential and magnetic field generated from the brain activity, conductivity should be included in the head model [Clerc & Papadopoulo 2008]. Let us mention the two most used types of head models: the **spherical head model** and the **realistic head model** (See Figure 1.20).

In the spherical model, a head is modelled set of nested concentric spheres with a piecewise constant conductivity i.e. each volume between consecutive spheres represents a head tissue with constant electrical conductivity σ. In this case, analytic solutions exist for both MEG and EEG [Mosher *et al.* 1999]. It can be shown that

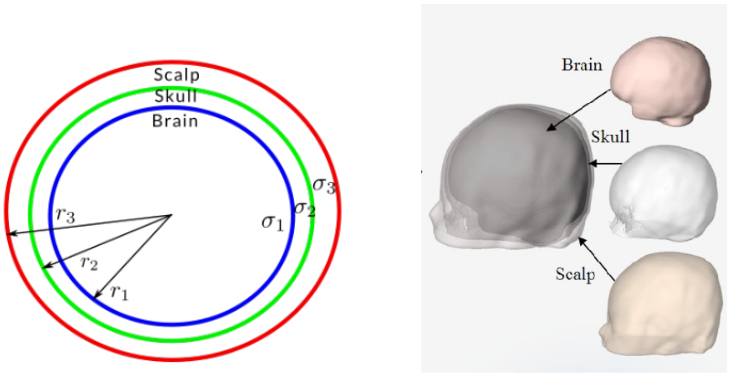

Figure 1.20: Left: Spherical model with 3 layers: the scalp, the skull and the brain. Taken from [Belaoucha 2017]. Right: realistic head model. Adapted from [Despotović *et al.* 2013].

with concentric spherical head models, the radial component of the magnetic field depends only on the primary current and it is independent of the conductivity profile i.e. different conductivities of the layers of the sphere [Sarvas 1987, Hamalainen & Sarvas 1989]. To compute the solution, only the center of the sphere and the location and orientation of the sensors are required, which is an advantage of MEG. For a realistic head model, tessellated surfaces separating regions of different conductivities such as skin, skull, and brain are needed. These compartments can be acquired by means of segmentation of magnetic resonance images of the head after which the relevant surfaces need to be tessellated. Although spherical models were a natural first step for head models, a realistic head model is needed to obtain more accurate results [Darvas *et al.* 2004]. In EEG studies, the head is usually divided into three homogeneous compartments: the scalp, the skull, and the brain. In MEG, on the other hand, 3 compartments are not imperative since the magnetic field is less dependent of the conductivity profile. A reasonably good solution can be obtained by using a single compartment, given the shape of the intracranial volume.
Another thing worth mentioning is the impact of volume conduction on source estimation, i.e. the transmission of electric or magnetic fields from an electric primary current source through biological tissues towards sensors. Single source projects its activity to many sensors outside the scalp (See Figure 1.21). This **superposition of source activity** is a fundamental challenge for source estimation.
Lastly, let us reflect again on some differences with EEG and MEG in this context. A radial source in a spherical head model will produce no magnetic field beyond the head. Since MEG is sensitive to tangential current sources, this means that it mainly captures the activity occurring on the walls of cortical fissures. Since $\sim 2/3$ of the cerebral cortex is located within fissures, this is the perk of MEG. Moreover, MEG is less sensitive to conductivities of different head tissues which is its another advantage over EEG. On the other hand, despite the fact the head is not an ideal sphere, MEG has a low sensitivity to radial sources, which makes it hard to detect deep sources in the brain (since any direction in the center of a sphere is radial). EEG on the other hand is sensitive to them.

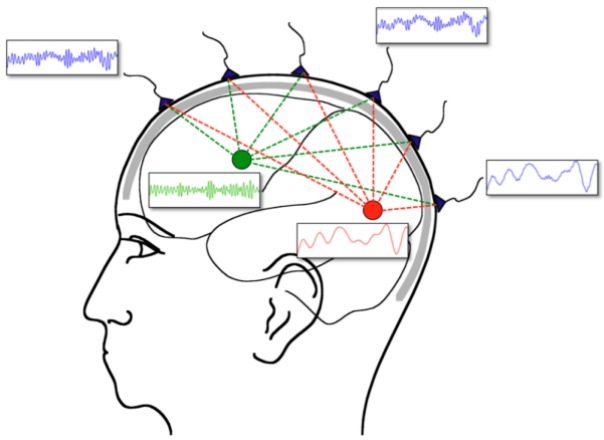

Figure 1.21: Superposition of source activity. Image taken from https://www.fieldtriptoolbox.org/assets/pdf/workshop/toolkit2019/.

1.5.4 Leadfield computation

The gain (lead field) matrix $\boldsymbol{G}$ is a linear relationship between source amplitudes and sensor data. It also called the M/EEG forward solution. For for each dipole of unit amplitude oriented perpendicularly to the cortical surface, the corresponding "forward field", i.e., the corresponding column of $\boldsymbol{G}$ estimates the electric potentials (magnetic fields) generated at the sensors [Grova *et al.* 2006]. For realistic head models the solution of the M/EEG forward problem does not exist in a closed form, so numerical methods are required to solve it. Computation of the lead field matrix can be done for example with a Boundary Element Method (BEM) [Ferguson *et al.* 1994, Kybic *et al.* 2005] or the Finite Flement Method (FEM) [Wolters *et al.* 2004]. As we already mentioned, this requires modeling the head geometry of the head together with its electromagnetic properties [Hamalainen & Sarvas 1989, Mosher *et al.* 1999] such as conductivities of different tissues. In the BEM model as a geometric head model, triangulations of the interfaces between different head compartments of piecewise-constant and isotropic conductivities are used. More details regarding the computation of the forward operator used in this thesis are explained in Chapter 3.

1.6 Diffusion Magnetic Resonance Imaging (dMRI)

Magnetic Resonance Imaging (MRI) is a noninvasive imaging technique that exploits the magnetization effects in atomic nuclei and generates images of different organs and tissues in the body. The main property of the atom nucleus used in MRI is the *spin*, which induces a magnetic field. The theory behind MRI is based on the quantum mechanical properties of spins that interact with an external magnetic field. MRI allows to differentiate between different tissue types. MRI scanners used

in clinical practice usually induce magnetic fields of 1.5 to 3 Tesla [T] of magnitude. In research the strength rises up to 7 T and the most powerful MRI machine up to date has the strength of 11.7 T [1]. The first MR images of a human brain were obtained in 1978. by two groups of researchers at EMI Laboratories led by Ian Robert Young and Hugh Clow. Denis Le Bihan [Le Bihan *et al.* 2001] obtained the first images and later patented diffusion MRI (dMRI).

Diffusion MRI is the only medical imaging modality that allows the access to the architecture of neural tissues and structural connectivity *in vivo* and noninvasively. The big success of dMRI is a result of its capability to accurately describe the geometry of the underlying microstructure and its integrity [Descoteaux 1999]. Diffusion MRI relies upon the assumption that water molecules do not diffuse freely in a constrained environment and it aims to quantify how the water molecules diffuse in the brain. The motion of the water molecules inside axons is hindered by its membrane when moving along any direction perpendicular to the axons' main axis. On the other hand, the water molecules can move freely parallel to the axons, so diffusion is restricted along the main axon axis. Consequently, characterizing diffusion can help to describe the underlying structure of the white matter.

Diffusion is a net displacement of molecules from a region of high to a region of low concentration. It is a result of a random walk of molecules, self-propelled by their thermal energy. Einstein showed that the movement of water molecules in a free medium due to thermal excitation follows random trajectories which is known as Brownian motion [Einstein 1905a]. Assuming a Gaussian diffusion, the probability that a water molecule will travel to a position $\boldsymbol{r} \in \mathbb{R}^3$ after a time delay τ is described by the **ensemble average propagator** (EAP) $P(r, \tau)$, whose probability density function is Gaussian:

$$P(\boldsymbol{r}, \tau) = \frac{1}{(4\pi D\tau)^{\frac{3}{2}}} e^{-\frac{||\boldsymbol{r}^2||}{4D\tau}} \tag{1.8}$$

where D is the diffusion coefficient and τ effective diffusion time. The diffusion coefficient is a measure of particle's mobility. In free diffusion, D is a constant scalar, independent of direction and is also reffered to as the apparent diffusion coefficient (ADC).

However, if the medium is *anisotropic*, D is spatially and directionally variable and can be generalized to the so-called **diffusion tensor** [Basser *et al.* 1994, O'Donnell & Westin 2011]. Diffusion tensor $\boldsymbol{D}$ can be viewed as the covariance matrix describing the Brownian motion of water molecules at every imaging voxel. Due to anisotropic morphology of the white matter, the EAP exhibits the same anisotropy. This phenomenon can be captured via dMRI, which in sensitive to the diffusivity along a certain direction. It was in 1965. that Stejskal and Tanner [Stejskal & Tanner 1965] invent the Pulse Gradient Spin Echo (PGSE) sequence to measure dif-

[1] https://www.cea.fr/english/Pages/News/Iseult-MRI-Magnet-Record.aspx

fusion in a specific direction – sequence for the acquisition of what was later called the dMRI signal. Diffusion-encoding gradients of the PGSE sequence induce signal attenuation when diffusion occurs along the diffusion-encoding gradients. We will not go into detailed explanation of design of such scheme since acquisition is not at the heart of this thesis. Rather, we will define some of the most important concepts in this field.
In 1985. Le Bihan and Breton [Le Bihan & Breton 1985] proposed the **b-value** (measured in s/mm^2) to quantify the extent to which diffusivity weights the signal, defined as

$$b = \gamma^2 G^2 \delta^2 \left(\Delta - \frac{\delta}{3} \right) \tag{1.9}$$

where γ is the gyromagnetic ratio and G is the gradient strength. The gradient strength allows to navigate not only in 3D image frequency space (aka the k-space) but also in 3D diffusion space (aka the q-space). Without going too much into details about each term in 1.9, the important thing is that, using PGSE, the diffusion-weighted signal attenuation $E(b)$ can be formulated in terms of b-value, given by the Stejskal-Tanner equation [Stejskal & Tanner 1965]:

$$E(b) = \frac{S(b)}{S_0} = e^{-bD} \tag{1.10}$$

where S_0 is the baseline T2-weighted image without any diffusion weighting. The diffusion attenuation is tuned by the b-value. The higher the b-value, the more water molecules are let to dephase or to be "sensitive" to their molecular displacement.
During acquisition, a series of 3D diffusion-weighted (DW) images are collected. Each DW image can be characterized by a 3D vector whose orientation corresponds to a DW orientation, while its magnitude corresponds to DW strength. The diffusion signal is weighted by the diffusivity along the gradient direction and this is why the technique is also called **diffusion-weighted imaging** (DWI). The diffusion signal depends on the gradient strength and orientation, leading to the most important points:

(1) The **more underlying diffusion** along the DW orientation, the larger the signal attenuation and therefore, **the lower the signal**. That is, the more the underlying structures are aligned to the measured diffusion direction, the more attenuated the measured signal is.
(2) The more diffusion weighting there is–**the higher the DW strength** (the b-value), **the bigger the diffusion contrast**.

For example, the fibers in corpus callosum (CC) are orientated in the left–right direction. In that gradient direction in the diffusion image, the signal is attenuated in the areas of CC (i.e. the image is very dark). DW images at higher b-values (using strong gradients) provide information on smaller details in the tissue geometry, but also have lower SNR.

1.6.1 Diffusion Tensor Imaging

In 1994.[2], Basser and colleagues proposed in a seminal paper [Basser *et al.* 1994] to measure the signal attenuation in different directions, and to model the diffusion coefficient D with a second order tensor. This gave rise to Diffusion Tensor Imaging (DTI). DTI represents the diffusion as a 3D ellipsoid, which can be coded in a symmetric positive definite matrix:

$$\boldsymbol{D} = \begin{pmatrix} D_{xx} & D_{xy} & D_{xz} \\ D_{xy} & D_{yy} & D_{yz} \\ D_{xz} & D_{yz} & D_{zz} \end{pmatrix}$$

The representation as an ellipsoid is in fact isoprobability surface of diffusion probability density function (See Figure 1.24 on top). Since $\boldsymbol{D}$ is symmetric, it has only 6 unknown coefficients to be estimated. Now, the scalar diffusion (Eq. 1.10) can be extended to the 3D anisotropic version with the diffusion tensor equation

$$S(\boldsymbol{g}, b) = S_0 e^{-b\boldsymbol{g}^T \boldsymbol{D}\boldsymbol{g}} \tag{1.11}$$

where $\boldsymbol{g}$ is the diffusion gradient vector and S_0 is the image acquired without diffusion gradients (b=0). Hence, DTI needs at least 6 diffusion-weighted images and 1 S_0 image to solve Eq. 1.11.

The eigenspace decomposition of the diffusion tensor opens the door for an algebraic framework to assess the geometry of the tensors [O'Donnell & Westin 2011]. Insights about the ellipsoid shape and direction allows the emmergence of scalar descriptors, which can be divided into two categories: *measures of tensors magnitudes* and *anisotropy measures*. They are rotationally and translationally invariant and measure parameters intrinsic to the tissue. The most known and the simplest measure describing the signal magnitude is the **mean diffusivity** (**MD**). The most famous anisotropy measure is the **fractional anisotropy** (**FA**) telling us how far we are from a sphere i.e. isotropic diffusion. It is a normalized measure in range $[0, 1]$ and for example, high FA values ($>$0.7) are obtained in voxels with highly organized fiber bundles (in a single direction), whereas low FA values ($<$0.15) reflect the voxels with isotropic diffusion [Descoteaux 1999]. Several other tissue measures (or maps) can be used to in addition to FA, to separate diffusivity along the principal direction of the tensor and orthogonal directions, such as parallel (axial) and perpendicular (radial) diffusivities. These are powerful properties that are exploited in dMRI applications as well as in clinical diagnosis. Indeed, ADC, FA, parallel diffusivity, and perpendicular diffusivity maps are the main part of several studies of neurological and pathological disorders (stroke, Alzheimer's disease, aging, brain tumors, multiple sclerosis...). Consequently, DTI still remains one of the most used techniques to model the diffusion signal in the clinical practise.

In research, however, it is no longer the case. This is due to its major limitation: it does not allow to correctly characterize the complex fiber configurations such as

[2]Which also happens to be the year in which the author of this thesis was born.

crossing, fanning, kissing and bending. In DTI, both the isotropic diffusion and the crossing of fibers end up getting modelled as spheres. This is a major pitfall since it was estimated [Jeurissen *et al.* 2014] that voxels contain crossing fibers comprise up to 90 % of all white matter voxels.
However, avoiding intersections between different fiber populations within all voxels would be impossible. Currently, the achievable resolution is just below 1 mm [Jones *et al.* 2013]. Even if we wanted to minimize the number of voxels in the brain containing fibers with multiple orientations, we would have to increase the resolution up to a point that each voxel contains only 1 fiber bundle. So, if coherent fiber bundles are $\sim 100\mu m$, we would need a voxel of $1\mu m$ in order not to have crossing fibers. Such a resolution is rather unrealistic, not only due to current hardware limitations and impractically longer scan times, but also because the resulting SNR would be so low that the data would be completely unreliable [Jones *et al.* 2013, Jeurissen *et al.* 2019]. Nevertheless, it is worth mentioning that there are invasive optical imaging techniques such as three dimensional Polarized Light Imaging (3D-PLI), which has the spatial resolution high enough to map the spatial organization of brain tissue at micrometer resolution [Axer *et al.* 2011]. This technique provides high-resolution 3D microscopic fiber orientation measurements recovered from unstained histological tissue sections. Complementing dMRI with 3D-PLI would allow to bridge the spatial scale information from micro to millimeter resolution. Recently, a fast analytical approach to define and reconstruct the fiber orientation distribution (FOD) from 3D-PLI data was proposed by [Alimi *et al.* 2020]. The authors analytically described FOD in a spherical harmonics basis and efficiently computed them via the spherical Fourier transform and by means of the Diracs, with a high angular resolution. This work enables closing the resolution gap with dMRI and it is a relevant step towards a higher goal to validate dMRI fiber orientation estimates and histology guided tractography via 3D-PLI. However, 3D-PLI is an invasive technique that can be applied only to postmortem tissues.

1.6.2 HARDI, voxel level modelling and spherical harmonics representation

The aim of voxel-level modelling is to extract quantitative and reproducible metrics about diffusion in the underlying tissue, from a series of DW images with different experimental settings. As mentioned already, DW images can be acquired across many angles with different b-values. Acquisitions using one b-value are called *single shell*, while *multi shell* acquisitions are done for several b-values (See Figure 1.22 for an illustration). Typically, multi-shell acquisition is performed with b-values of 1000, 2000 and 3000 s/mm^2. High Angular Resolution Diffusion Imaging (**HARDI**) techniques [Tuch 1999] rely on taking acquisitions across many angles, in order to reconstruct the true diffusion propagator. For an exceptional review on HARDI techniques see [Descoteaux 1999]. They were initially developed to address limitations of DTI such as the crossing fiber problem and to make tractography more robust. Numerous so-called "higher-order" fiber modeling methods have been pro-

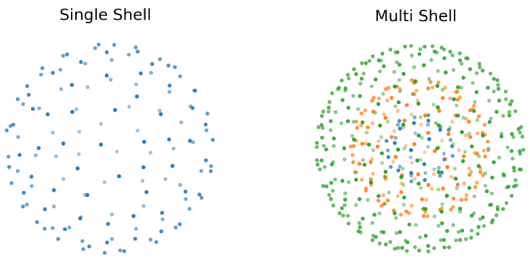

Figure 1.22: Single shell (left) vs. multi shell (right) sampling needed for HARDI. Image taken from [Frigo 2021].

posed, capable of estimating the orientations and relative contributions of multiple fiber populations within each voxel, without any explicit assumption regarding the number of underlying fiber populations [Jeurissen *et al.* 2014]. These methods often represent fiber orientations as a continuous function of the sphere, known as the **fiber orientation distribution function** (**fODF**) (see Figure 1.23). All models relating the raw dMRI images to the local fiber orientations rely on one fundamental assumption: when a number of axons is aligned along the same orientation, the diffusion of water molecules will be more hindered across this orientation than along it. When diffusion signal is acquired on a shell, it can be represented in spherical

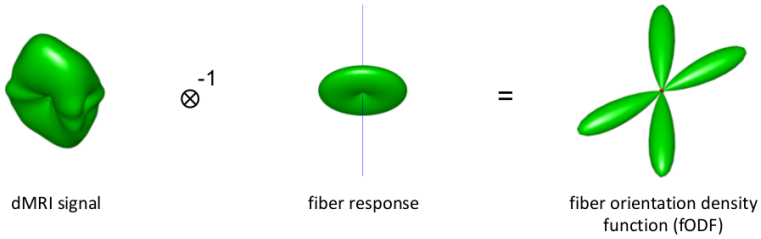

Figure 1.23: Illustration of Constrained Spherical Deconvolution. Image taken from https://www.mrtrix.org/.

coordinates as a function of the direction of the gradient. These functions can be expressed via **spherical-harmonics** (**SH**).[3] Symmetric functions on the sphere (like diffusion signal acquired on a shell) can be represented as a linear combination of symmetric SH basis function. We will not dive into the the math here since it is not needed for the rest of the thesis. Nonetheless, we will mention some main concepts and ideas. SHs can be used to represent the fODF within a voxel. Assume that WM fibres along one axis have a fixed and equal contribution to the dMRI signal, aka the *response function* or *kernel* (See Figure 1.23). Spherical convolution assumes that a distribution of fiber orientations convoluted with a single-fiber response function generates the measured diffusion signal. Given the dMRI signal and fiber response

[3] Spherical-harmonics are the S^2 equivalent of the Fourier basis in $\mathbb{R}^n$.

functions, we can obtain fODFs by a process process called *spherical deconvolution*. Response function(s) are a prerequisite for spherical deconvolution, which is/are used as the kernel(s) by the deconvolution algorithm.
The **Spherical Deconvolution** (**SD**) [Tournier *et al.* 2004] approach is one of the first techniques used to model multiple fiber populations in a voxel and for fiber-tracking. SD techniques assume that, in a given voxel, the acquired DW signal is measured on a single shell. Nonetheless, SC is an ill-conditioned inverse problem and it is susceptible to noise. This tends to introduce negative regions in the FOD (continuous representation of the fODF), which are actually artifacts, since they are physically impossible.
To adrdess these limitations, **Constrained Spherical Deconvolution** (**CSD**) was proposed [Tournier *et al.* 2007] in order to penalize physically implausible negative values. Therefore, CSD leads to more plausible estimates in crossing fibers in the full fiber ODF, but it has its limitations as well. CSD is used with single shell data, so it can only provide high quality fODF estimates in voxels containing WM only. In voxels containing other tissue types such as GM and CSF (cerebrospinal fluid), the WM response function may no longer be appropriate and spherical deconvolution produces unreliable, noisy fODF estimates.
This has led to the extension of the CSD approach for multi-shell data, in which a response function can be estimated for each brain tissue type using **Multi-Shell Multi-Tissue Constrained Spherical Deconvolution** (**MSMT-CSD**) algorithm [Jeurissen *et al.* 2014]. MSMT-CSD requires HARDI data (with multiple b-values), from which the fiber responses can be directly estimated. The number of tissue types that can be resolved is, however, limited by the number of b-values in the data (including b=0). For example, to resolve the 3 primary tissue types in the brain (WM, GM and CSF), the acquisition should contain at least 2 shells, along with the b=0 volumes (i.e. 3 unique b-values). Lastly, Figure 1.24 shows the comparison between voxel-level modelling using DTI and CSD. Approaches based on spherical deconvolution can resolve fiber crossings [Tournier *et al.* 2007] and result in sharper fiber orientations.

1.6.3 Diffusion MRI tractography

Once the fiber orientations are estimated either from diffusion tensors or fODFs, we can start exploiting the brain's long-range white matter connectivity. Following the local orientation of the fiber bundles estimated from dMRI data, we can obtain a representation of long-range white matter pathways in the brain. Yet, by using the fODF as a propagator, tracking can be performed even in white matter regions with complex fiber architecture. Fiber tractography assumes that each imaging voxel is characterized by one predominant fiber orientation and joins together these local orientations to infer global fiber trajectories (See Figures 1.25 and 1.26). The assessment of long-range connectivity on a macroscopic scale using dMRI tractography, through the reconstruction of white matter fiber tracts is the hallmark of dMRI. The output of tractography algorithms is a set of streamlines called a *tractogram*.

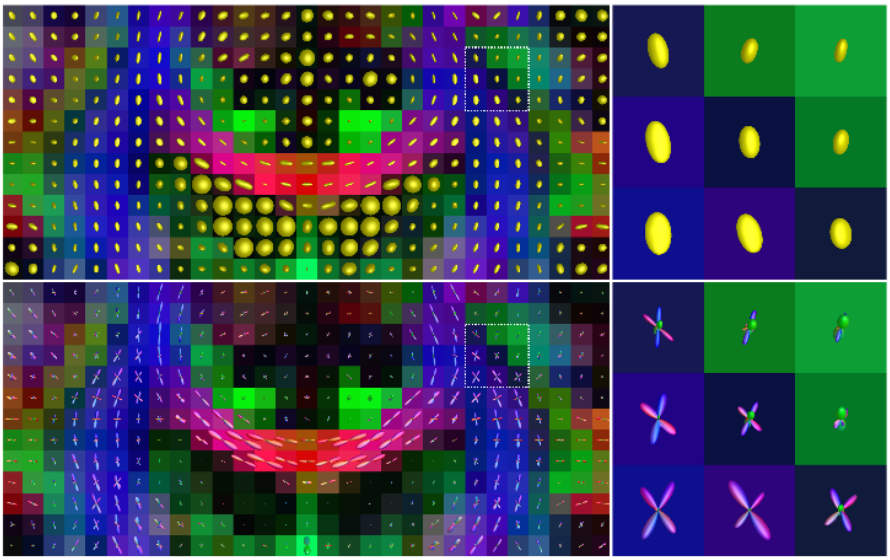

Figure 1.24: Voxel-level modelling. Top: DTI. Bottom: CSD. Image taken from https://www.mrtrix.org/.

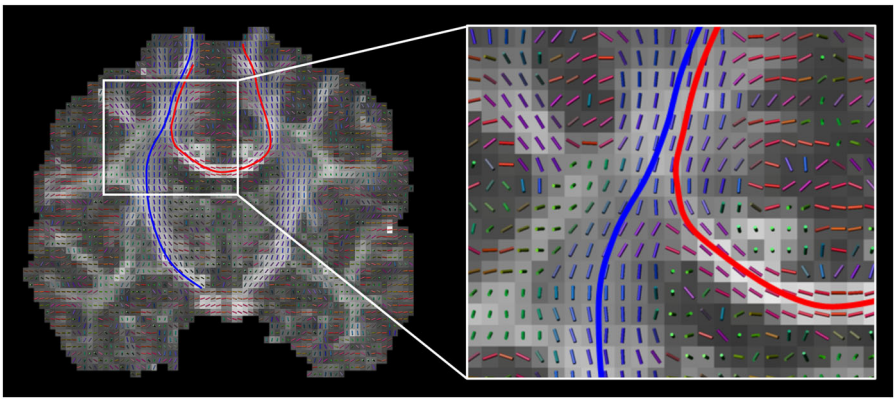

Figure 1.25: Vector field of local predominant fiber orientations and two of its streamlines. The red streamline is part of the corpus callosum, while the blue one is part of the corticospinal tract. Each streamline's tangent is parallel to the local vector field along its entire course. Image taken from [Jeurissen *et al.* 2019].

For a comprehensive review on fiber tractography, the interested reader is referred to [Jeurissen *et al.* 2019]. Numerous tractography algorithms have been developed in the past two decades years, but they all fall into two categories: *local* and *global* algorithms.

Local algorithms determine the streamline trajectory by propagating a line from a seed following the orientations estimated with some local model [Mori *et al.* 1999, Descoteaux *et al.* 2008, Tournier *et al.* 2012]. Global algorithms on the other hand do not perform tracking through local orientations, but in a global manner [Jbabdi *et al.* 2007]. They try to find the fiber configurations between pairs of regions that

best explains the diffusion signal i.e. they are solving a global problem aiming at fitting the measured raw dMRI data. We will consider only local tracking algorithms. In terms of neuroscience, a streamline represents a fiber population, i.e. a bundle of axons that follow the same course. In terms of mathematics, streamlines are parametrised curves obtained by integrating the field defined by the local directions, as a result of the chosen local model (tensor or an fODF) (See Figure 1.26).

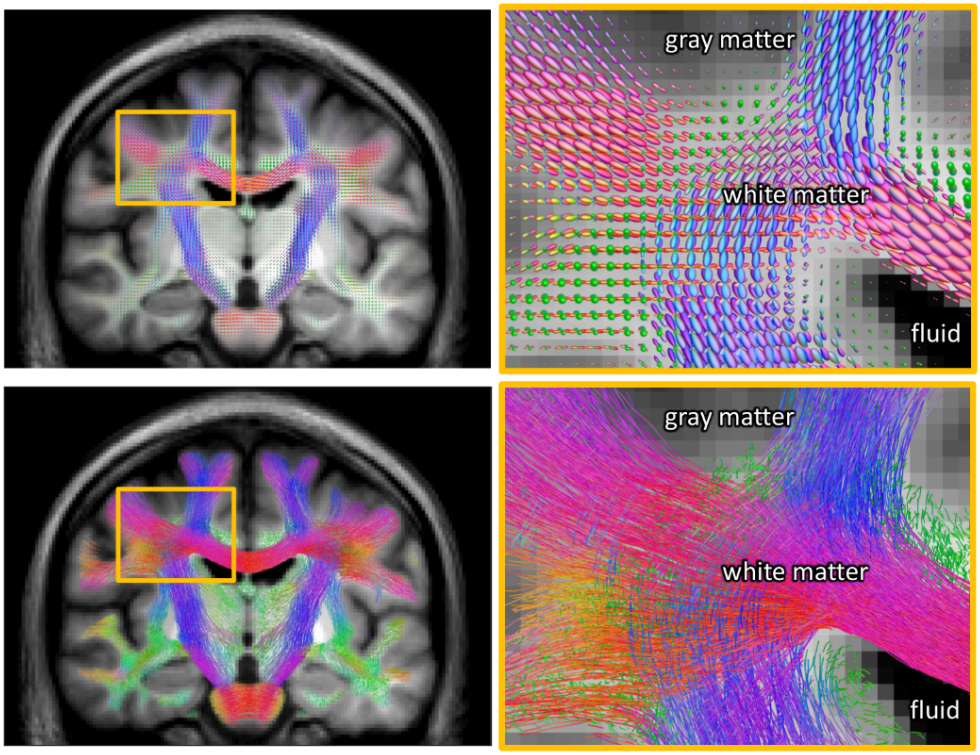

Figure 1.26: Top: white matter fibers as a function of orientation. Bottom: Fiber tractography i.e. "piecing together" local fiber orientation information to infer long-range fiber trajectories. Adapted from [Jeurissen *et al.* 2014] and [Jeurissen *et al.* 2019])

If the local directions are uniquely determined, the **tractography algorithm** will be called **deterministic**. On the other hand, if the local direction is sampled each time from a probability distribution like a normalised ODF or a diffusion tensor, the algorithm is called **probabilistic**. Deterministic tractography aims to estimate the most likely single path from a chosen starting point, assuming that the curve is always tangential/parallel to the principal direction of the fibers.
The main goals of tractography are to to describe the anatomy of the white matter fasciclesand to determine how two gray matter regions are connected [Maier-Hein *et al.* 2017]. Despite the great improvements obtained by researchers around the globe in the last decades, tractography remains an ill-posed problem and even advanced fiber-tracking approaches will still be subject to modeling errors [Jeurissen *et al.* 2014]. There are several reasons, such as (1) reliability of estimation of the

local geometry of the fiber orientations, (2) different integration schemes can yield different results, (3) seeds locations from which the streamlines are propagated are not fixed, (4) variability in track termination and track acceptance criteria etc. Improper termination also rises as a problem in areas that are, for example filled with fluid. To leverage this issue, anatomically constrained tractography (ACT) algorithms have been proposed to seed and terminate streamlines at the GM-WM interface [Smith *et al.* 2012]. Lastly, it is noteworthy to mention that tract lengths can be calculated after the streamline reconstruction. This is exploited later in the thesis since, given their lengths and the information transmission speed, we can estimate transmission delays for each connection.

1.7 Brain as a graph

The rise of network science has been a result of the growing recognition that many diverse complex systems ranging from metabolic networks, social interactions, electrical and telecommunication grids, transportation systems to the World Wide Web often share certain key organizational principles which can be quantitatively characterized by the same parameters. Despite the fundamental differences in the constituting elements of each of these various systems, many of them show surprisingly similar macroscopic behaviour, shaped by interactions among their constituent elements. Developments in the quantitative analysis of complex networks, based mostly on graph theoretical analysis, have gained significant attention in the past decades and paved their path to studies of brain network organization [Bullmore & Sporns 2009, Rubinov & Sporns 2010]. Graph theory provides a compelling mathematical framework for the analysis of large-scale brain network architecture and has the potential to help us identify organizational principles behind the architecture of the brain [Meunier *et al.* 2010, Fornito *et al.* 2013]. In this context, brain can be modelled as a graph of nodes which represent neural elements (e.g., neurons, brain regions), connected by edges which represent certain measure of physical (structural), functional or causal interaction between nodes. Methodological advances in networks science allow us to quantify topological properties of complex systems, such as modularity, hierarchy, centrality [Bullmore & Sporns 2009]. Still, defining the nodes of a macroscale connectome remains challenging due to the lack of agreement in the community on how best to define the constituent brain units [Craddock *et al.* 2013]. Anatomical modules correspond to groups of specialized functional areas, such as the visual and somatomotor regions, as previously determined by physiological recordings. The functional role, played by any component (e.g., cortical area, subarea, neuronal population, or neuron) of the brain, is defined largely by its connections [Friston 2002]. Similar to many real-world networks, application of graph theory approaches to the human brain has shown that it follows an efficient **'small-world'** functional architecture [Watts & Strogatz 1998], the individual network components (nodes) have greater local interconnections (edges) than expected for a random network, and smaller minimum path lengths between node

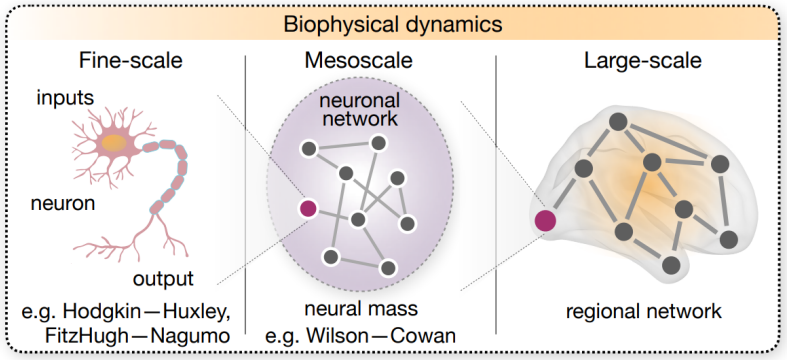

Figure 1.27: Left: biophysical models at microscale neuronal level capture functional features such as the propagation of the nerve impulse. Middle: mesoscale approaches like neural mass models such as the Wilson–Cowan model [Wilson & Cowan 1972] average over all neurons in a population to derive a mean firing rate. Right: macroscale dynamics of an entire brain, can be done with neural mass (or some other) models to represent brain regions and embed them into a structural connectivity derived from diffusion MRI. Image taken from [Lynn & Bassett 2019].

pairs than regular or lattice type networks. This configuration consists of densely intra-connected communities connected via hubs (nodes that have disproportionately high number of connections) which maximizes local and global network efficiency while minimizing wiring costs [Bullmore & Sporns 2009].

Two complementary organizational principles of the brain represent the hallmark of its complex neural dynamics: functional segregation and functional integration [Tononi *et al.* 1994, Friston *et al.* 1995, Friston 2002]. **Functional specialization** or **segregation** pertains to the brain's ability for specialized information processing to occur within locally clustered and densely interconnected neural populations. Cells within such neural populations that share common functional properties are grouped together. This property was exploited in functional parcellations where each parcel is said to be specialized to serve one cognitive function or to represent one essential aspect of the information processed by it [Glasser *et al.* 2016]. **Functional integration** refers to the coordinated activation and interaction of specialized brain regions distributed across different cortical areas. It represents the brain's ability to rapidly combine specialized information from distributed brain regions [Rubinov & Sporns 2010].

The functional significance of the "small-world" phenomenon of the human brain comes from the natural tendency of this architecture to promote functional segregation (high local clustering) and functional integration (short path lenghts) leading to global efficiency [Tononi *et al.* 1994, Sporns 2011].

Different quantities characterizing the architecture and the information flow of the brain functional network can be extracted, each informing on a particular aspect of the network (see [Rubinov & Sporns 2010] for a review). The degree to which the graph can be decomposed into local communities or clusters of nodes that are highly interconnected are quantified by the measures of segregation. Such network communities are often referred to as modules [Sporns 2011]. Measures of integration

estimate the ease with which brain regions communicate and are commonly based on the concept of a **path**. Paths are sequences of distinct nodes and links and in anatomical networks that represent potential routes of information flow between pairs of brain regions. Lengths of paths consequently estimate the potential for functional integration between brain regions, with shorter paths implying stronger potential for integration. It was shown that basic principles of neuroanatomical organization shape brain dynamics: demonstrated empirically from electrophysiological studies of animals and functional neuroimaging studies of human subjects [Friston 2002] and in computer simulations of cortical areas using a measure called neural complexity [Tononi *et al.* 1994]. Brain dynamics can be characterized by being simultaneously differentiated in local groups and integrated into a coherent behavior [Varela *et al.* 2001]. The connectivity structure of a neural system defines its internal dynamic states and its range of responses to external perturbations. The importance of the connectome derives from the principal role of the network of structural connectivity in shaping the rich and dynamical functional interactions of neural elements that underlie human cognition and behavior [Sporns 2011, Honey *et al.* 2007]. Yet, our comprehension of principles guiding dynamic integration across anatomically segregated functional regions remains limited [de Pasquale *et al.* 2012].

1.7.1 Brain connectivity

The connectome represents the complete set of neural elements and their interconnections that comprise the brain [Sporns *et al.* 2005]. Brain connectivity can be subdivided into three broad classes: **structural** (or neuroanatomical), **functional** and **effective** [Horwitz 2003, Bullmore & Sporns 2009, Rubinov & Sporns 2010, Bassett & Sporns 2017] (See Figure 1.28).

Structural connectivity (**SC**) refers to anatomical connections between different brain areas. On a macroscopic scale, these physical connections refer to white matter fiber pathways. Diffusion-weighted imaging (DWI) allows the assessment of structural connectivity through techniques such as diffusion tensor imaging (DTI) or fiber tractography. Tractography enables reconstruction of the white matter fiber pathways and yields an undirected (since tractography algorithms cannot distinguish between afferent and efferent fibers [Jbabdi & Johansen-Berg 2011]) and possibly weighted graph.

Functional connectivity (**FC**) refers to statistical dependencies between temporal signals of spatially distinct brain regions [Friston 1994]. It can be examined in sensor space (from time series of neurophysiological recordings) or in source space (after reconstruction of cortical activity). It can be undirected or directed.

- **Undirected FC** marks the presence of a relationship between brain regions but it does not reveal anything about the direction of influence between them. It is measured between regional activity time courses with different measures such as correlations, coherence and mutual information, resulting in undirected graphs [Bullmore & Sporns 2009]. Most often, FC is computed with correlation measures in time domain such as Pearson correlation coefficient,

partial correlation etc. Alternatives to aforementioned measures include mutual information or some coherence measures in frequency domain such as magnitude squared coherence and wavelet coherence.Edge weights in FC are typically scalar, continuous and symmetric and can be used to quantify both positive and negative covariations in regional activity [Fornito *et al.* 2013].

- **Directed FC** emerged since the information transfer from one region to another implies an order or directionality that is not captured by undirected FC. Measures of directed FC are asymmetric (conditional) statistical measures of temporal correlations. The ones used in fMRI studies can be grouped into those that depend upon conditional dependences, such as Patel's τ and Bayes nets, and lag based measures, such as Granger Causality (GC) [Granger 1969]. FC can also change dynamically over time, giving rise to the notion of *dynamic functional connectivity.*

Effective connectivity (**EC**) denotes causal influence that one neural system exerts over the other [Horwitz 2003] i.e. coupling among brain nodes. It represents dynamic directional interactions among brain areas and can be (1) data-driven (when estimated directly from the signals or (2) model-based combination of SC and FC (based on a model specifying the causal links). A comprehensive review of

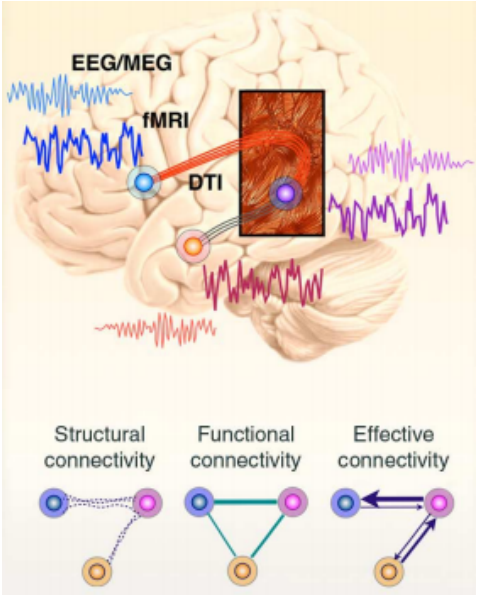

Figure 1.28: Illustration of structural, functional and effective connectivity. Image taken from [Park & Friston 2013].

the methods for assessment of functional and effective connectivity with M/EEG is given in [Sakkalis 2011]. EC is hidden behind neuronal states generating the measurements, it is directed, weighted, dynamic and context-specific. Most popular approaches to the assessment of EC are Dynamic Causal Modelling (DCM) [Friston *et al.* 2003] and Granger causality (GC) [Friston *et al.* 2013].

Dynamic Causal Modelling (**DCM**) assumes that the response of a dynamic system can be modeled by a network of discrete and interacting neuronal sources described in terms of *neural-mass*. Differential equations are used to express causal interactions among hidden state variables (e.g. specific aspects of neuronal population activity). They depict how the current state of one neuronal population causes dynamics (i.e., rate of change) in another via synaptic connections and how these interactions change under the influence of external perturbations (i.e., experimental manipulations) or endogenous brain activity [Stephan *et al.* 2010]. It allows representation of directed, weighted and heterogeneous (e.g. modulatory) edge types, though only for small networks and it is mostly used in fMRI studies [Fornito *et al.* 2013].
Granger causality (**GC**) is a data-driven technique based on the assumption that causes precede their effects in time. The main idea behind GC is that x "Granger causes" y if x contains information that can help to predict the future of y better than solely using information about the past of y (and in the past of other "conditioning" variables z). The most common implementation of GC is through linear vector autoregressive (VAR) modelling of time-series data, which enables testing of statistical significance and estimation of GC magnitudes.

Connectomics is not only vital for studying organizational principles in the healthy human brain but also in in disease. Psychiatric diseases like schizophrenia, depression, and autism have been associated with pathological alterations across the functional connectome. For this reason, connectomes may serve as intermediate phenotypes situated between the domains of genetics/molecules and expressions of individual (pathological) behavior [Fornito *et al.* 2013].
Another concept worth mentioning is *brain plasticity*. It refers to the brain's capacity to reorganize pathways and create new connections [Kolb & Whishaw 1998]. Changes in dendritic arborization play an important role in brain plasticity and behavior, especially in changing intrinsic circuitry of the cortex in processes such as learning. Two types can be distinguished:

- structural plasticity - brain's ability to actually change its physical structure, for example as a result of learning
- functional plasticity - brain's ability to move functions from a damaged to undamaged brain areas

Without it, learning and improving brain function would be challenging, as well as recovering from brain-based injuries and illnesses.

1.8 Conclusion

In this Chapter, we introduced the basic concepts needed to understand the rest of the thesis. Firstly, we gave an overview of the nervous system and neuroanatomy. Secondly, we talked about brain function in general and with a spotlight on functions

of brain areas involved in visuomotor tasks, since in this thesis we aim to recover brain activity during such task paradigms. Thirdly, we explained the origins of neural activity measured with EEG and MEG. We highlighted that the main primary currents that give rise to measurable M/EEG signals are the large cortical pyramidal neurons, oriented perpendicularly to the cortical surface. Moreover, we introduced, compared and contrasted EEG and MEG as functional imaging modalities that can measure brain activity on a fast, milisecond temporal resolution. Furthermore, we defined the forward problem in M/EEG, the theory and mathematical framework behind the M/EEG forward solution i.e. the leadfield matrix. On top of that, we described basic concepts in diffusion MRI: what is the information that DW signal captures, how fiber orientations can be represented and how tractography can be computed. The output of a tractography pipeline is a set of streamlines representing the white matter fiber bundles, which will be exploited in the remaining of the thesis. Lastly, we scratched the surface of a whole other, emerging field, *network neuroscience*. Although the functional properties of different brain areas are expressed locally, they are the outcome of an interactive network working as an integrated system. Regarding the brain as a graph (network) is one of the key aspects that lead to most contributions of this thesis.

Chapter 2

State of the art: M/EEG inverse problem

Contents

Overview

M/EEG provides information about the brain activity non-invasively, with a millisecond temporal resolution, allowing to track fast processes in the human brain on the millisecond scale [Hämäläinen *et al.* 1993, Niedermeyer & Lopes da Silva 1995]. Recall that these techniques are widely used in many clinical applications such as epilepsy, for localizing epileptogenic brain regions in surgical planning [Huppertz *et al.* 2001, Bénar *et al.* 2006], but also for improvement of understanding and treatment of neurological and neuropsychological disorders such as autism spectrum disorder, schizophrenia, depression, Parkinson's and Alzheimer's diseases,... The information about localization of active sources in the brain helps to diagnose pathological, physiological, mental and functional abnormalities [Baillet & Garnero 1997].
In this Chapter, we start by introducing the general formulation of M/EEG inverse problems and the reasons for its ill-posedness. Secondly, we present different approaches to solve the it, the main hypotheses behind them and mathematical frameworks used to obtain the source estimates. We describe the three main families of approaches (1) the dipole fitting approaches, (2) the scanning methods and

(3) distributed source models. We focus in more details on the last one, since our work falls into this category. Moreover, we present a taxonomy of the algorithms in the group of distributed inverse solvers according to the priors they deploy and we also elaborate the theoretical and practical aspects behind each prior.

2.1 M/EEG Inverse Problem - overview

Recall from Section 1.5 that the forward problem aims to compute electric potential (EEG) or magnetic field (MEG) outside the head, for a known configuration of the sources, provided that the geometry of the head and its electromagnetic properties are known [Kybic *et al.* 2005]. The inverse problem, on the other hand, aims to localize and recover the electrical activity of cortical sources from M/EEG measurements. This Chapter provides an overview of the state-of-the-art techniques used to estimate the neural activity from the measurements i.e. the different approaches to solve this problem. Numerous source reconstruction methods have been developed over the past few decades and their categorization is not trivial. They can be classified according to the hypotheses they rely upon, methodology, as well as mathematical frameworks adopted for their implementation. Some core methods are defined independently, while some are hybrid in nature. Nevertheless, three main families of approaches can be distinguished in the literature:

1. **Regularized least squares** (also called the **distributed source models** or **imaging approaches**).
2. **Dipole fitting approaches**.
3. **Scanning methods**.

We start by explaining the general formulation and why the problem is ill-posed. The last two approaches are explained rather briefly, while a more detailed explanation is given to the regularized least squares methods and different types of regularization from the literature, since our work falls into this category. For more detailed reviews on M/EEG inverse problem, the interested reader is referred to [Grova *et al.* 2006, Jatoi *et al.* 2014, Grech *et al.* 2008, Lei *et al.* 2015, Baillet *et al.* 2001, Pascual-Marqui 1999, Becker *et al.* 2015].
In distributed source models, a large number of dipoles is allocated to grid points over the entire brain surface or volume. Although in general the source space can be volumetric, we will follow the main stream of state-of-the-art and consider the surface-based source space, where each dipole has a fixed position on the cortical mesh, while their orientations are assumed to be normal to the cortical surface [Dale & Sereno 1993, Baillet *et al.* 2001]. When locations and orientations are fixed and only the dipoles' amplitudes need to be estimated, the inverse problem can be reduced to a linear one, with strong similarities to the problems encountered in image restoration and reconstruction. This is why these approaches are also called *the imaging approaches* [Baillet *et al.* 2001].
Recall from Section 1.5.2 that the relationship between source amplitudes and

M/EEG measurements is expressed by the linear model

$$\boldsymbol{M} = \boldsymbol{G}\boldsymbol{J} + \boldsymbol{E} \tag{2.1}$$

where $\boldsymbol{M}$ is a matrix of measurements, $\boldsymbol{J}$ is the matrix of source amplitudes, $\boldsymbol{G}$ is the forward operator and $\boldsymbol{E}$ is additive noise in sensor space. Measurement matrix is given by $\boldsymbol{M} \in \mathbb{R}^{N \times T}$ for N sensors and T time samples. The unknown matrix of S source amplitudes is given by $\boldsymbol{J} \in \mathbb{R}^{S \times T}$. In distributed source models, the size of the source space is generally large (typically $S \approx 10^4$) and the number of sensors can vary depending on the modality. Typically, the number of electrodes in EEG is $N_{EEG} \approx 60 - 100$, while in MEG the number of gradiometers or magnetometers is $N_{MEG} \approx 300$. Each row of $\boldsymbol{M}$ corresponds to the measurements of the n^{th} sensor, where $n = 0, ...N-1$ and $t = 0, ...T-1$. Each row of $\boldsymbol{J}$ corresponds to the current density amplitudes of the s^{th} source, where $s = 0, ...S-1$. The gain (lead field) matrix $\boldsymbol{G} \in \mathbb{R}^{N \times S}$ provides a linear relationship between source amplitudes and sensor data (a.k.a. the M/EEG forward solution) as explained in Section 1.5.4. The noise is in sensor space i.e. $\boldsymbol{E} \in \mathbb{R}^{N \times T}$. Figure 2.1 puts illustratively these concepts in a nutshell and Eq. (2.1) can be written in matrix form as

$$\boldsymbol{M} = \boldsymbol{G}\boldsymbol{J} + \boldsymbol{E} = \begin{bmatrix} m_{00} & \cdots & m_{0(T-1)} \\ \vdots & \ddots & \vdots \\ m_{(N-1)0} & \cdots & m_{(N-1)(T-1)} \end{bmatrix} = \begin{bmatrix} g_{00} & \cdots & g_{0(S-1)} \\ \vdots & \ddots & \vdots \\ g_{(N-1)0} & \cdots & g_{(N-1)(S-1)} \end{bmatrix} \begin{bmatrix} j_{00} & \cdots & j_{0(T-1)} \\ \vdots & \ddots & \vdots \\ j_{(S-1)0} & \cdots & j_{(S-1)(T-1)} \end{bmatrix} + \boldsymbol{E}$$

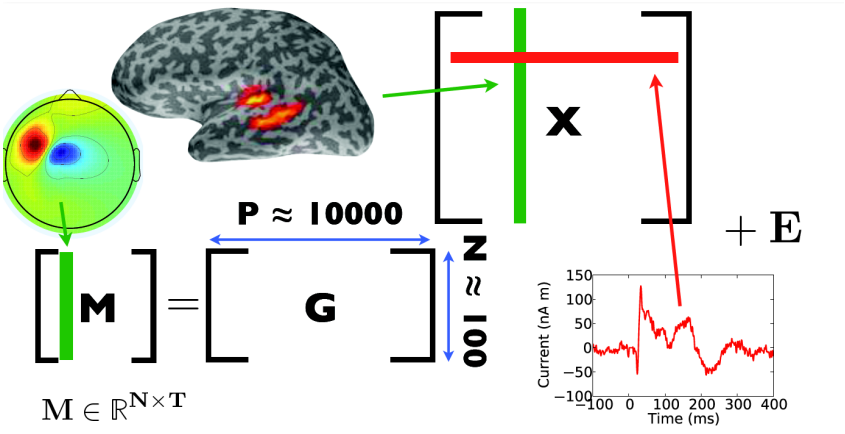

Figure 2.1: Small "N", large "P" problem (the correspondence to our notation: $\boldsymbol{P} \simeq \boldsymbol{S}$ and $\boldsymbol{X} \simeq \boldsymbol{J}$. Image taken from Alex Gramfort, Functional brain imaging with MEG and EEG (CoBCoM presentation))

2.2 Ill-posedness of the M/EEG inverse problem

Square matrix $\boldsymbol{A}$ of size $(m \times m)$ is *invertible* or *nonsingular* if there exists a matrix $\boldsymbol{A}^{-1}$ such that

$$\boldsymbol{A}\boldsymbol{A}^{-1} = \boldsymbol{A}^{-1}\boldsymbol{A} = \boldsymbol{I} \tag{2.2}$$

If $\boldsymbol{A}$ is singular (non-invertible), its determinant is zero and there exists some non-zero vector $\boldsymbol{x}$ for which $\boldsymbol{A}\boldsymbol{x} = \boldsymbol{0}$. Only square matrices of full rank are invertible [Strang 2011]. The rank of a matrix $\boldsymbol{A}$ is the dimension of the vector space spanned by its columns. This corresponds to the maximal number of linearly independent columns of $\boldsymbol{A}$. The rank r of a matrix of size $(m \times n)$ always satisfies that $\text{rank}(\boldsymbol{A}) \leq \min(m, n)$. For full rank matrices $r = m = n$. The nullspace of $\boldsymbol{A}$ is the set of all solutions $\boldsymbol{x}$ to $\boldsymbol{A}\boldsymbol{x} = \boldsymbol{0}$ i.e. $Null(A) = \{\boldsymbol{x} \in \mathbb{R}^n \mid \boldsymbol{A}\boldsymbol{x} = \boldsymbol{0}\}$. When the columns of $\boldsymbol{A}$ are independent, i.e. it has full column rank $(r = n)$ then $Null(\boldsymbol{A}) = \{\boldsymbol{0}\}$. Let us consider the following linear system

$$\boldsymbol{y} = \boldsymbol{A}\boldsymbol{x} \tag{2.3}$$

where $\boldsymbol{y}$ is the observed data, $\boldsymbol{A}$ is some linear operator and we are interested to find the solution to this system $\boldsymbol{x}$. If $\boldsymbol{A}$ is invertible, the solution is simply $\boldsymbol{x} = \boldsymbol{A}^{-1}\boldsymbol{y}$. The solution is unique if and only if the rank equals the number of variables, i.e. if the matrix $\boldsymbol{A}$ is square and full rank (invertible). However, problems appear[1] if $\boldsymbol{A}$ is not an invertible matrix. We could use a Moore-Penrose pseudoinverse denoted as $\boldsymbol{A}^+$ to estimate $\boldsymbol{x}$ as

$$\hat{\boldsymbol{x}} = \boldsymbol{A}^+\boldsymbol{y} = \boldsymbol{A}^+\boldsymbol{A}\boldsymbol{x}. \tag{2.4}$$

If $\boldsymbol{A}$ is a non-invertible matrix of size $(m \times n)$, this means we have one of the 2 following cases – depending on whether it has more rows or more columns:

1. If the matrix $\boldsymbol{A}$ is a so-called tall matrix (where $m \gg n$) with linearly independent columns, we can say that it has a full column rank $(r = n)$. In this case $Null(\boldsymbol{A}) = \{\boldsymbol{0}\}$, the matrix $\boldsymbol{A}^T\boldsymbol{A}$ is full rank and invertible and there exists a left pseudoinverse

$$\begin{aligned} \boldsymbol{A}^+_{left} &= (\boldsymbol{A}^T\boldsymbol{A})^{-1}\boldsymbol{A}^T \\ \boldsymbol{A}^+_{left}\boldsymbol{A} &= \boldsymbol{I}_{n\times n} \end{aligned} \tag{2.5}$$

   Here, the system (2.3) is an *overdetermined* system of equations with more constraints than unknowns and generally it has no exact solutions (except for degenerate cases). So by using $\hat{\boldsymbol{x}} = \boldsymbol{A}^+_{left}\boldsymbol{y}$, an approximate least squares solution can be found when no exact solution exists.

2. If the matrix $\boldsymbol{A}$ is a so-called wide matrix (where $n \gg m$) with linearly independent rows, it has full row rank $(r = m < n)$. In this case $Null(\boldsymbol{A}^T) = \{\boldsymbol{0}\}$,

[1] "Houston, we have a problem"– Jack Swigert, Apollo 13 mission

the matrix $\boldsymbol{A}\boldsymbol{A}^T$ is full rank and invertible and there exists a right pseudoinverse

$$\begin{aligned} \boldsymbol{A}^+_{right} &= \boldsymbol{A}^T(\boldsymbol{A}\boldsymbol{A}^T)^{-1} \\ \boldsymbol{A}\boldsymbol{A}^+_{right} &= \boldsymbol{I}_{m\times m} \end{aligned} \tag{2.6}$$

The dimension of the nullspace in this case is $n-m$, meaning there are $n-m$ free variables and (if $n > m$) the system (2.3) is *underdetermined*, with **infinitely many solutions to it**. So the least squares solution $\hat{\boldsymbol{x}} = \boldsymbol{A}^+_{right}\boldsymbol{y}$ is just one of the infinitely many, with specific properties.

The solutions to the system (2.3) using left and right pseudoinverse are also discussed in Section 2.3.1. The value $\kappa = \frac{\sigma_{max}(\boldsymbol{A})}{\sigma_{min}(\boldsymbol{A})}$ is called the condition number of a matrix [Strang 2011], where σ_{max} and σ_{min} are the biggest and the smallest singular values of $\boldsymbol{A}$, respectively. Matrix with a high condition number is called ill-conditioned, meaning that its inversion is numerically unstable. If at least two columns of $\boldsymbol{A}$ are perfectly correlated i.e. linearly dependent, the matrix $\boldsymbol{A}^T\boldsymbol{A}$ is singular ($\kappa(\boldsymbol{A}^T\boldsymbol{A}) = \infty$). Even if the correlation is not perfect but high enough, it will result in a high condition number. The higher the condition number, the greater the error in the calculation of the inversion.
In this context, we are interested in the properties of our linear operator, the lead field matrix $\boldsymbol{G}$, where each column corresponds to a lead field. Since $\boldsymbol{G}$ has many more columns than rows, this means that there are more unknown variables (brain sources), than the number of measurements (M/EEG sensors) at each time instant. This also implies that the solution of the inverse problem is not unique – different source configurations can produce the same M/EEG measurements. Since the solution is non-unique and also suffers from numerical instability (it is highly sensitive to small changes in the noisy data) the inverse problem said to be ill-posed [Sarvas 1987]. The mathematical definition of a well-posed problem was formulated by a French mathematician Jacques Hadamard, who stated that well-posed mathematical models of physical phenomena should have the following properties:

- A solution exists.
- The solution is unique.
- The solution's behavior changes continuously with the initial conditions.

Ill-posed problems are the ones that are not well-posed in the sense of Hadamard. Note that both overdetermined and underdetermined systems can be ill-conditioned. To conclude, at each time instant, M/EEG inverse problem is a regression with more variables than observations, also called a small "N" large "P" problem (see Figure 2.1). In this work, P is the number of sources S while N is the number of sensors, meaning that (2.1) is an underdetermined system with more unknowns ($S = 8196$) than equations ($N = 243$), with infinitely many solutions to it. The question is now: how can we solve it? The sections that follow provide some approaches to answer this question.

2.3 Regularized Least Squares Methods

In order to obtain a unique solution, prior constraints on the characteristics of source distributions need to be introduced. To recover electrical activity of the brain from M/EEG measurements, regularization methods aim to solve the following minimization problem

$$\hat{\boldsymbol{J}} = \arg\min_{\boldsymbol{J}} U(\boldsymbol{J}) = \arg\min_{\boldsymbol{J}} \{F(\boldsymbol{M}, \boldsymbol{J}) + \lambda P(\boldsymbol{J})\}\,. \tag{2.7}$$

The objective function $U(\boldsymbol{J})$ consists of 2 terms:

- A data fidelity term $F(\boldsymbol{M}, \boldsymbol{J})$ measuring the fit of the solution to the observed data. It is usually the squared l_2-norm of the residual i.e. $\|\boldsymbol{M} - \boldsymbol{G}\boldsymbol{J}\|_2^2$.
- A regularization (or penalty) term $P(\boldsymbol{J})$ which introduces *a priori* assumptions on source amplitudes and therefore penalizes potential solutions with undesired structures.

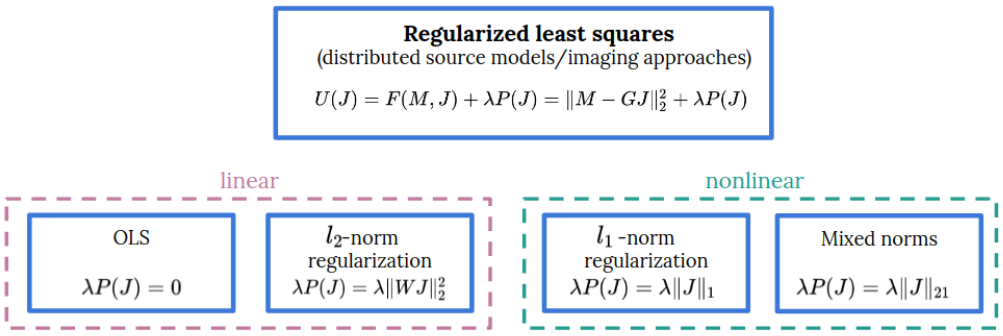

Figure 2.2: Diagram of the main most commonly used penalty terms in M/EEG community. Both linear and nonlinear constraints can be formulated as convex optimization problems. However, nonlinear constraints have no closed form solution to (2.7) and nonlinear optimization methods need to be used instead [Fuchs *et al.* 1999].

The regularization parameter $\lambda > 0$ controls the influence of the two terms on the minimizer i.e. it is a trade-off between the data fit and the regularity of the estimate. The bigger the λ, the more the solution is regularized. In signal and image processing, statistics and machine learning, a broad spectrum of such methods has been developed in order to solve problems such as signal and image denoising, deblurring, reconstruction, super-resolution, feature selection and many more. A diagram of some of the most popular regularization terms (choices of $P(\boldsymbol{J})$) used to encode different *a priori* hypotheses on signal $\boldsymbol{J}$ is shown in Figure 2.2. Table 2.1 is an overview of distributed inverse solvers according to the hypotheses (priors) they rely upon. In the sections that follow, each method is mentioned in a subsection dedicated to the primary hypothesis behind it. Clearly, many methods fall within more than one category, i.e. they have more than one hypothesis, so this table will inevitably provide some clarity.

Classification of distributed inverse solvers according to employed priors							
Method \ Prior	Min. energy	Depth weighting	Spatial smoothness	Temporal smoothness	Sparsity (spatial)	dMRI	dMRI & delays
MNE [Hämäläinen & Ilmoniemi 1994]	√						
[Lin *et al.* 2006]	√	√					
[Kohler *et al.* 2006]	√	√					
LORETA [Pascual-Marqui *et al.* 1994]			√				
[Philippe *et al.* 2013]	√		√			√	
[Belaoucha & Papadopoulo 2017]	√		√			√	
sLORETA [Pascual-Marqui *et al.* 2002]	√						
eLORETA [Pascual-Marqui *et al.* 2011]	√	√					
dSPM [Dale *et al.* 2000]	√						
FOCUSS [Gorodnitsky *et al.* 1995]					√		
MCE [Matsuura & Okabe 1995]					√		
MCE [Uutela *et al.* 1999]					√		
[Ou *et al.* 2009]				√	√		
MxNE [Gramfort *et al.* 2012]				√	√		
SISSY [Becker *et al.* 2017]				√	√		
gFOTV [Li *et al.* 2016]			√		√		
[Baillet & Garnero 1997]			√	√			
dMAP-EM [Lamus *et al.* 2012]			√	√			
[Schmitt *et al.* 2001]			√	√			
CGS [Hammond *et al.* 2013]			√			√	
[Fukushima *et al.* 2015]				√		√	√
iSDR [Belaoucha & Papadopoulo 2020]				√	√	√	√
CIMEM [Deslauriers-Gauthier *et al.* 2019]		√	√	√		√	√
[Deslauriers-Gauthier *et al.* 2020]		√	√	√		√	√

Table 2.1: Different distributed inverse solvers and prior(s) they employ. Note that this list is inexhaustible and other approaches could be added. We listed the most relevant ones for this thesis; some are mentioned in more details in the remaining of the manuscript.

2.3.1 l_2-norm regularization – linear inverse methods

In the linear distributed source approach, a large number of sources is allocated to discrete set of points (usually a grid) over the entire brain surface or volume. The amplitudes of thousands of sources with fixed locations and orientations are simultaneously estimated by solving a system of linear equations. Firstly, let us consider

the simplest case without any regularization. Ordinary Least Squares (OLS) is a method for estimating the unknown parameters in a linear regression model. It chooses the parameters of a linear function of a set of explanatory (independent) variables by minimizing the sum of the square differences between the observed dependent variables and those predicted by the linear function [Strang 2011]. When the linear operator has linearly independent columns, it is common to seek a solution $\hat{\boldsymbol{J}}$ minimizing the energy of the error (i.e. the sum of squared residuals), which can be written as the following optimization problem

$$\hat{\boldsymbol{J}} = \arg\min_{\boldsymbol{J}} \|\boldsymbol{M} - \boldsymbol{G}\boldsymbol{J}\|_2^2. \tag{2.8}$$

The smaller is the residual, the better the sources explain the data. It is convex in its argument $\boldsymbol{J}$, so if we want to minimize (2.8), we can first expand it as

$$\begin{aligned} U(\boldsymbol{J}) &= \|\boldsymbol{M} - \boldsymbol{G}\boldsymbol{J}\|_2^2 =< \boldsymbol{M} - \boldsymbol{G}\boldsymbol{J}, \boldsymbol{M} - \boldsymbol{G}\boldsymbol{J} > \\ &= (\boldsymbol{M} - \boldsymbol{G}\boldsymbol{J})^T(\boldsymbol{M} - \boldsymbol{G}\boldsymbol{J}) \\ &= \boldsymbol{M}^{\boldsymbol{T}}\boldsymbol{M} - 2\boldsymbol{J}^{\boldsymbol{T}}\boldsymbol{G}^{\boldsymbol{T}}\boldsymbol{M} + \boldsymbol{J}^{\boldsymbol{T}}\boldsymbol{G}^{\boldsymbol{T}}\boldsymbol{G}\boldsymbol{J}. \end{aligned}$$

The OLS solution can be obtained by setting the derivative of $U(\boldsymbol{J})$ w.r.t. $\boldsymbol{J}$ to zero

$$\begin{aligned} \nabla_{\boldsymbol{J}} U(\boldsymbol{J}) &= -2\boldsymbol{G}^T\boldsymbol{M} + 2\boldsymbol{G}^T\boldsymbol{G}\boldsymbol{J} = 0 \\ &= \boldsymbol{G}^T\boldsymbol{G}\boldsymbol{J} = \boldsymbol{G}^T\boldsymbol{M}. \end{aligned}$$

If $\boldsymbol{G}^T\boldsymbol{G}$ is invertible, we have a closed-form solution obtained with left pseudoinverse (2.5)

$$\hat{\boldsymbol{J}} = \left(\boldsymbol{G}^T\boldsymbol{G}\right)^{-1}\boldsymbol{G}^T\boldsymbol{M} \tag{2.9}$$

which is a solution that minimizes the error (2.8)

$$\begin{aligned} \hat{\boldsymbol{J}}_{OLS} &= \boldsymbol{G}^{+}_{left}\boldsymbol{M} = \boldsymbol{G}^{+}_{right}\boldsymbol{M} \\ \hat{\boldsymbol{J}}_{OLS} &= \left(\boldsymbol{G}^{\boldsymbol{T}}\boldsymbol{G}\right)^{-\boldsymbol{1}}\boldsymbol{G}^{\boldsymbol{T}}\boldsymbol{M} = \boldsymbol{G}^{\boldsymbol{T}}\left(\boldsymbol{G}\boldsymbol{G}^{\boldsymbol{T}}\right)^{-\boldsymbol{1}}\boldsymbol{M}. \end{aligned} \tag{2.10}$$

Let us now consider the following minimization problem which is commonly used to solve ill-posed problems, where we seek a solution $\hat{\boldsymbol{J}}$ with the minimum norm

$$\min_{\boldsymbol{J}} ||\boldsymbol{J}||_2^2 \quad \text{subject to } \boldsymbol{M} = \boldsymbol{G}\boldsymbol{J}. \tag{2.11}$$

Minimization with constraints can be solved using Lagrange multipliers. We can define the Lagrangian as

$$\mathcal{L}(\boldsymbol{J}, \boldsymbol{\mu}) = ||\boldsymbol{J}||_2^2 + \boldsymbol{\mu}^T(\boldsymbol{M} - \boldsymbol{G}\boldsymbol{J}) \tag{2.12}$$

where $\boldsymbol{\mu}$ is a Lagrangian multiplier. We can set the derivatives of the Lagrangian to zero

$$\nabla_{\boldsymbol{J}}\mathcal{L}(\boldsymbol{J}, \boldsymbol{\mu}) = 2\boldsymbol{J} - \boldsymbol{G}^T\boldsymbol{\mu} = 0 \tag{2.13}$$

$$\nabla_{\boldsymbol{\mu}}\mathcal{L}(\boldsymbol{J}, \boldsymbol{\mu}) = (\boldsymbol{M} - \boldsymbol{G}\boldsymbol{J})^T = 0. \tag{2.14}$$

By doing this, we obtain

$$\boldsymbol{J} = \frac{1}{2}\boldsymbol{G}^T\boldsymbol{\mu} \tag{2.15}$$

$$\boldsymbol{M} = \boldsymbol{G}\boldsymbol{J}. \tag{2.16}$$

Plugging (2.15) into (2.16) gives

$$\boldsymbol{G}\boldsymbol{G}^T\boldsymbol{\mu} = 2\boldsymbol{M} \tag{2.17}$$

Finally, if we assume that $\boldsymbol{G}\boldsymbol{G}^T$ is invertible then

$$\boldsymbol{\mu} = 2(\boldsymbol{G}\boldsymbol{G}^T)^{-1}\boldsymbol{M} \tag{2.18}$$

and by plugging (2.18) into (2.15), we get the closed-form solution

$$\hat{\boldsymbol{J}} = \boldsymbol{G}^T(\boldsymbol{G}\boldsymbol{G}^T)^{-1}\boldsymbol{M}. \tag{2.19}$$

Notice that this solution is obtained with the right pseudoinverse (2.6). Nevertheless, the constraint in (2.11) requiring that $\boldsymbol{M}$ should be exactly equal to $\boldsymbol{G}\boldsymbol{J}$ is true only with noiseless measurements. In reality, the measured signals always have some random noise in it, so such a constraint can be problematic (too strict). $\boldsymbol{G}$ is a so-called wide matrix (with more columns thank rows $S \gg N$), where each column corresponds to a lead field. If the lead fields are linearly independent (which should normally be the case when the measurements are made at different locations) the inner product matrix $\boldsymbol{G}\boldsymbol{G}^T$ (of size $N \times N$) should be non-singular. Nevertheless, in practice, the lead fields may be *nearly linearly dependent*. Thus, $\boldsymbol{G}\boldsymbol{G}^T$ can have some very small eigenvalues, that leads to large errors in the computation of $\boldsymbol{G}\boldsymbol{G}^T$ [Hämäläinen & Ilmoniemi 1994]. Recall that $\boldsymbol{G}$ is a so-called wide matrix (with more columns than rows $S \gg N$) and that the inverse problem is ill-posed, i.e. there are infinitely many solutions that can explain the observed measurements. However, in practise, neither $\boldsymbol{G}\boldsymbol{G}^T$ or $\boldsymbol{G}^T\boldsymbol{G}$ are invertible. This issue can be solved by adding regularization.

Tikhonov regularization [Tikhonov 1943] is the most commonly used regularization method of ill-posed problems, based on the l_2-norm. In order to give preference to a particular solution with desirable properties (e.g., minimum norm), a regularization term can be included in the minimization

$$\hat{\boldsymbol{J}} = \arg\min_{\boldsymbol{J}} \left\{ \|\boldsymbol{M} - \boldsymbol{G}\boldsymbol{J}\|_2^2 + \lambda\|\boldsymbol{W}\boldsymbol{J}\|_2^2 \right\} \tag{2.20}$$

for some suitably chosen matrix $\boldsymbol{W}$. It is also known as *ridge regression* in statistics or *minimum norm estimators* (MNE) [Hämäläinen & Ilmoniemi 1994, Wang *et al.* 1992] in the M/EEG community. These methods assume that the measurement noise is white Gaussian $\boldsymbol{E} \sim \mathcal{N}(0, C_E)$ with a known covariance matrix C_E. If, in practice, it is not the case, the data can be prewhitened based on an estimate of the noise covariance matrix [Engemann & Gramfort 2015]. The prewhitening

matrix can be computed as the inverse of the square root of the estimated noise covariance matrix, $C_E^{-\frac{1}{2}}$. To achieve prewhitening, the measurements and the leadfield matrices are multiplied from the left by the prewhitening matrix. Let us consider the general case without whithening, where the cost function can be written as:

$$\begin{aligned} U(\boldsymbol{J}) &= \|\boldsymbol{M} - \boldsymbol{G}\boldsymbol{J}\|_2^2 + \lambda\|\boldsymbol{W}\boldsymbol{J}\|_2^2 \\ &= (\boldsymbol{M} - \boldsymbol{G}\boldsymbol{J})^T(\boldsymbol{M} - \boldsymbol{G}\boldsymbol{J}) + \lambda(\boldsymbol{W}\boldsymbol{J})^T(\boldsymbol{W}\boldsymbol{J}) \\ &= \boldsymbol{M}^T\boldsymbol{M} - 2\boldsymbol{J}^T\boldsymbol{G}^T\boldsymbol{M} + \boldsymbol{J}^T\boldsymbol{G}^T\boldsymbol{G}\boldsymbol{J} + \lambda\boldsymbol{J}^T\boldsymbol{W}^T\boldsymbol{W}\boldsymbol{J}. \end{aligned}$$

Both data fidelity and regularization term are quadratic in $\boldsymbol{J}$, so the estimated sources can be derived by setting the derivative of $U(\boldsymbol{J})$ w.r.t $\boldsymbol{J}$ to zero

$$\begin{aligned} \nabla_{\boldsymbol{J}} U(\boldsymbol{J}) &= -2\boldsymbol{G}^T\boldsymbol{M} + 2\boldsymbol{G}^T\boldsymbol{G}\boldsymbol{J} + 2\lambda\boldsymbol{W}^T\boldsymbol{W}\boldsymbol{J} = 0 \\ &\Rightarrow (\boldsymbol{G}^T\boldsymbol{G} + \lambda\boldsymbol{W}^T\boldsymbol{W})\boldsymbol{J} = \boldsymbol{G}^T\boldsymbol{M} \end{aligned}$$

resulting in a closed-form solution

$$\hat{\boldsymbol{J}} = \left(\boldsymbol{G}^T\boldsymbol{G} + \lambda\boldsymbol{W}^T\boldsymbol{W}\right)^{-1}\boldsymbol{G}^T\boldsymbol{M}. \tag{2.21}$$

In minimum norm estimates (MNE) [Hämäläinen & Ilmoniemi 1994] this matrix is chosen as the identity matrix ($\boldsymbol{W} = \boldsymbol{I}$), giving preference to solutions with smaller norms. Then, MNE solution is then given by

$$\hat{\boldsymbol{J}} = \left(\boldsymbol{G}^T\boldsymbol{G} + \lambda\boldsymbol{I}\right)^{-1}\boldsymbol{G}^T\boldsymbol{M}. \tag{2.22}$$

Let us take a closer look of how adding regularization actually impacts the solution. We start start from the Singular Value Decomposition (SVD) of $\boldsymbol{G}$ in the form

$$\boldsymbol{G}_{m\times n} = \boldsymbol{U}_{m\times m}\boldsymbol{\Sigma}_{m\times n}\boldsymbol{V}^T_{n\times n} \tag{2.23}$$

$$\boldsymbol{U}\boldsymbol{\Sigma}\boldsymbol{V}^T = \underbrace{\begin{bmatrix}\mathbf{u}_1 & \dots & \mathbf{u}_r\end{bmatrix}}_{\text{Col}\,\boldsymbol{G}} \underbrace{\begin{bmatrix}\mathbf{u}_{r+1} & \dots & \mathbf{u}_m\end{bmatrix}}_{\text{Null}\,\boldsymbol{G}^T} \begin{bmatrix} \sigma_1 & 0 & \dots & 0 & 0 & \dots & 0 \\ 0 & \sigma_2 & \dots & 0 & 0 & \dots & 0 \\ \dots & & & & & & \\ 0 & 0 & \dots & \sigma_r & 0 & \dots & 0 \\ 0 & 0 & \dots & 0 & 0 & \dots & 0 \\ \dots & & & & & & \\ 0 & 0 & \dots & 0 & 0 & \dots & 0 \end{bmatrix} \begin{bmatrix} \mathbf{v}_1^T \\ \mathbf{v}_2^T \\ \dots \\ \mathbf{v}_r^T \\ \mathbf{v}_{r+1}^T \\ \dots \\ \mathbf{v}_n^T \end{bmatrix} \begin{matrix} \left.\vphantom{\begin{matrix}a\\a\\a\\a\end{matrix}}\right\} \text{Row}\,\boldsymbol{G} \\ \left.\vphantom{\begin{matrix}a\\a\\a\\a\end{matrix}}\right\} \text{Null}\,\boldsymbol{G} \end{matrix}$$

where

- $\boldsymbol{u}_i$ are the right singular vectors
- $\boldsymbol{v}_i$ are the left singular vectors
- $\sigma_1 \geq \sigma_2 \cdots \geq \sigma_r \geq 0$ are the non-zero singular values of $\boldsymbol{\Sigma}$.

Vectors $\boldsymbol{u}_i$ and $\boldsymbol{v}_i$ are orthonormal (i.e. $\boldsymbol{u}_i^T\boldsymbol{u}_j = \boldsymbol{v}_i^T\boldsymbol{v}_j = 1$ if $i = j$ and 0 otherwise) and the singular values σ_i are non-negative quantities that appear in non-decreasing order [Hansen 1999]. Since $\boldsymbol{U}$ and $\boldsymbol{V}$ are orthonormal matrices, this means that $\boldsymbol{U}\boldsymbol{U}^T = \boldsymbol{U}^T\boldsymbol{U} = \boldsymbol{I}$ and $\boldsymbol{V}\boldsymbol{V}^T = \boldsymbol{V}^T\boldsymbol{V} = \boldsymbol{I}$. Let us denote the matrix $\boldsymbol{G}^T\boldsymbol{G}$ (of size $(n \times n)$)[2] as $\boldsymbol{A}$

$$\begin{aligned}\boldsymbol{A} = \boldsymbol{G}^T\boldsymbol{G} &= \left(\boldsymbol{U}\boldsymbol{\Sigma}\boldsymbol{V}^T\right)^T\boldsymbol{U}\boldsymbol{\Sigma}\boldsymbol{V}^T = \boldsymbol{V}\boldsymbol{\Sigma}^T\boldsymbol{U}^T\boldsymbol{U}\boldsymbol{\Sigma}\boldsymbol{V}^T \\ &= \boldsymbol{V}\boldsymbol{\Sigma}^T\boldsymbol{\Sigma}\boldsymbol{V}^T = \boldsymbol{V}\boldsymbol{\Lambda}\boldsymbol{V}^T.\end{aligned}$$

Note that in general in the SVD, the number of non-zero singular values in $\boldsymbol{\Sigma}$ corresponds to the rank of the matrix r ($r \leq n$). In the equations that follow, we will consider that there are n singular values, even if $n - r$ of them are 0. That being said, the diagonal matrix $\boldsymbol{\Lambda}$ of singular values of $\boldsymbol{A}$ and its inverse are

$$\boldsymbol{\Lambda} = \boldsymbol{\Sigma}^T\boldsymbol{\Sigma} = \begin{bmatrix}\sigma_1^2 & \dots & 0 \\ \vdots & \ddots & \vdots \\ 0 & \dots & \sigma_n^2\end{bmatrix}, \boldsymbol{\Lambda}^{-1} = \begin{bmatrix}\frac{1}{\sigma_1^2} & \dots & 0 \\ \vdots & \ddots & \vdots \\ 0 & \dots & \frac{1}{\sigma_n^2}\end{bmatrix}$$

So the part that needs to be inverted in Eq. (2.22) is in fact

$$\left(\boldsymbol{G}^T\boldsymbol{G} + \lambda\boldsymbol{I}\right)^{-1} = \left(\boldsymbol{V}\boldsymbol{\Lambda}\boldsymbol{V}^T + \lambda\boldsymbol{I}\right)^{-1} = \boldsymbol{V}\begin{bmatrix}\frac{1}{\sigma_1^2+\lambda} & \dots & 0 \\ \vdots & \ddots & \vdots \\ 0 & \dots & \frac{1}{\sigma_n^2+\lambda}\end{bmatrix}\boldsymbol{V}^T$$

Using this formulation, we can write the Tikhonov solution as

$$\begin{aligned}\hat{\boldsymbol{J}}_\lambda &= \left(\boldsymbol{G}^T\boldsymbol{G} + \lambda\boldsymbol{I}\right)^{-1}\boldsymbol{G}^T\boldsymbol{M} \\ &= \left(\boldsymbol{V}\boldsymbol{\Lambda}\boldsymbol{V}^T + \lambda\boldsymbol{I}\right)^{-1}\boldsymbol{V}\boldsymbol{\Sigma}\boldsymbol{U}^T\boldsymbol{M} \\ &= \left(\boldsymbol{\Lambda} + \lambda\boldsymbol{I}\right)^{-1}\boldsymbol{V}\boldsymbol{\Sigma}\boldsymbol{U}^T\boldsymbol{M} \\ &= \sum_{i=1}^{n}\frac{\sigma_i}{\sigma_i^2+\lambda}\boldsymbol{v}_i\boldsymbol{u}_i^T\,\boldsymbol{M} \\ &= \sum_{i=1}^{n}\frac{\sigma_i^2}{\sigma_i^2+\lambda}\frac{\boldsymbol{u}_i^T\boldsymbol{M}}{\sigma_i}\boldsymbol{v}_i \\ &= \sum_{i=1}^{n} f_i\,\frac{\boldsymbol{u}_i^T\boldsymbol{M}}{\sigma_i}\boldsymbol{v}_i\end{aligned}$$

where $f_1, ..., f_n$ are called Tikhonov filter factors, which depend on σ_i and λ

$$f_i = \frac{\sigma_i^2}{\sigma_i^2+\lambda} \cong \begin{cases}1, & \sigma_i \gg \lambda \\ \sigma_i^2/\lambda, & \sigma_i \ll \lambda\end{cases} \tag{2.24}$$

[2] In this thesis, $m = 243$ and $n = 8196$.

The OLS solution can be obtained by setting $\lambda = 0$ in Eq. (2.22), then all filter factors are $f_i = 1$ [Hansen 1999]. It is clear that if the singular values σ_i are close to 0, the inversion will be highly unstable, leading to extremely large values in the inverted matrix. This is where the regularization plays its part. Filter factors filter out the contributions to $\hat{\boldsymbol{J}}_\lambda$ corresponding to small singular values (when $\sigma_i \ll \lambda$). On the other hand, they leave SVD components corresponding to the large singular values (when $\sigma_i \gg \lambda$) almost unaffected. So by adding a small positive value λ in the denominator, we prevent division by values close to 0 (when $\sigma_i \approx 0$) and the inversion becomes more stable. In our experiments we multiplied $\boldsymbol{G}$ by a factor of 10^4 to put its elements at the order of magnitude of ~ 1, to further avoid numerical instabilities in computations. This fundamentally does not change the nature of $\boldsymbol{G}$ (it still remains ill-posed), just leads to higher values of the regularization parameter. It can be shown by SVD of $\boldsymbol{G}$ that the same Tikhonov solution can be obtained with both types of the pseudoinverse (left or right):

$$\hat{\boldsymbol{J}}_\lambda = \underbrace{\left(\boldsymbol{G}^T\boldsymbol{G} + \lambda \boldsymbol{I}\right)^{-1}}_{(S \times S)} \boldsymbol{G}^T \boldsymbol{M} = \boldsymbol{G}^{\boldsymbol{T}} \underbrace{\left(\boldsymbol{G}\boldsymbol{G}^T + \lambda \boldsymbol{I}\right)^{-1}}_{(N \times N)} \boldsymbol{M} \tag{2.25}$$

So when $\boldsymbol{W} = \boldsymbol{I}$ it is computationally more efficient to use the formula which involves the right pseudoinverse, i.e. the inversion of matrix whose size is the squared number of sensors $(N \times N)$, compared to the left inverse where the matrix size is the squared number of sources $(S \times S)$. But, if we want to exploit the properties a specific type of penalty *on the sources*, it should be imposed with the matrix $\boldsymbol{W}$ of size $(S \times S)$. So bearing this in mind, the formulation (2.21) should be used instead.

There is a wide range of traditional linear inverse methods that can be found in the literature in the form (2.20). They differ by the choice/definition of the matrix $\boldsymbol{W}$, which incorporates a certain regularization property. Several different priors have been proposed for l_2-based solvers such as:

(1) $\boldsymbol{W}$ as the identity matrix, acting as a spatial prior which penalizes the Euclidean norm of the current sources, yielding a solution with the minimum norm i.e. the shortest current vector capable of explaining the measured data [Hämäläinen & Ilmoniemi 1994] (a.k.a MNE).
(2) $\boldsymbol{W}$ as a depth weighting matrix, which reduces the bias of MNE towards superficial sources [Lin *et al.* 2006, Kohler *et al.* 2006].
(3) $\boldsymbol{W}$ as a discrete spacial Laplacian operator which favours smoothness between neighboring sources – also known as Low Resolution brain Electromagnetic Tomography (LORETA) [Pascual-Marqui *et al.* 1994]
(4) $\boldsymbol{W}$ as a weighted block matrix which performs the role of a Laplacian regularization inside each cortical area, by constraining sources in a same area to have close values [Philippe *et al.* 2013, Belaoucha & Papadopoulo 2017].

All l_2-based inverse solvers lead to a linear solution that is obtained by simple matrix multiplications, making the estimation computationally efficient. Also, they

provides solid initial results in terms of resolution and current estimation. Nonetheless, they suffer from several limitations such as

(1) They tend to smear even focal activation, which often gives solutions with overestimated extents of the activated areas [Gramfort *et al.* 2012].
(2) They are sensitive to outliers (noise) since the square terms increases at the same time the error difference between the measurements and the outliers and between the measurements and the actual underlying data.
(3) They often fail to exploit specific knowledge about the brain such as, for example, the temporal dynamics of the underlying sources.

They also do not take into account the assumption that only a few brain regions are typically active during a cognitive task, which can be a disadvantage in reconstructing source activity in task-related experiments.
Several other methods also belong to the family of these linear inverse solvers. An extension of the LORETA approach has been proposed in the method called eLORETA (exact Low Resolution Electromagnetic Tomography) [Pascual-Marqui *et al.* 2011] as a particular form of weighted minimum norm solution, in order to give more importance to the deeper sources. It aims to seek an optimal depth weighting [Lin *et al.* 2006] resulting in minimized localization errors for noise-free data. Interestingly, minimum norm estimates can be converted into statistical parameter maps, which take into account the noise level, leading to noise-normalized estimates. One of them is dSPM (dynamic Statistical Parametric Mapping) algorithm [Dale *et al.* 2000], where measurement noise normalization was employed to establish the statistical significance of the current estimates. Another one is sLORETA [Pascual-Marqui *et al.* 2002], also relying upon the assumption of the standardization of the current density. It assumes that the current densities are all independent and with equal variances. In dSPM, the variance of the estimated current density is based on the assumption that the *only* source of variation is the measurement noise. On the other hand, sLORETA considers both the variance of the noise in the M/EEG measurements and the biological variance in the actual sources. The noteworthy difference of dSPM and sLORETA is that they transform the data into dimensionless statistical quantities, unlike other linear inverse estimation methods that provide in solutions in physical current units (Am).

2.3.2 Sparsity-inducing norms

In order to overcome the issue of l_2-based solvers which tend to smear the estimated cortical activity, *sparsity constraints* have been introduced on the number of active sources that generated the measured activity. For instance, visual or audio stimuli lead to characteristic stimulus-evoked responses in only certain functional areas of the brain. It has also been shown that during cognitive tasks, the spatial distribution of spectral power varies in a task-relevant manner [Chang *et al.* 2011, Buzsáki *et al.* 2012]. So for task- and stimulus-related experiments, it can be reasonable to assume that only a small fraction of sources contributes to the measured signals of

interest in a significant way. The signals of the other sources are thus expected to be zero. This concept of sparsity can be imposed on the source distribution using sparsity-inducing norms such as the l_p-norm with $p \geq 1$ or mixed norms.
The l_0 pseudo-norm[3] is popular in compressed sensing which aims to find the sparsest solution to an underdetermined system. l_0 pseudo-norm only counts the number of non-zero elements in a vector, promoting solutions with only a few coefficients. The problem (2.7) then becomes

$$\hat{\boldsymbol{J}} = \arg\min_{\boldsymbol{J}} \|\boldsymbol{M} - \boldsymbol{G}\boldsymbol{J}\|_2^2 + \lambda||\boldsymbol{J}||_0. \tag{2.26}$$

However, such penalty function leads to a non-convex optimization problem which is also NP-hard, hence costly in terms of computation. In the context of M/EEG inverse problems, Gorodnitsky and colleagues [Gorodnitsky *et al.* 1995] proposed to use Iterative Reweighted Least Squares (IRLS) with the FOCUSS algorithm (FOCal Underdetermined System Solution) that approximates the solution that would be obtained with an l_0 prior. By iteratively updating the minimum norm solution using a l_0 pseudo-norm, the source spatial distribution shrinks gradually, resulting in a sparse solution. Nonetheless, it involves heavy mathematical calculations and hence large computational time due to continuous iteration of a weight matrix. One avenue for translating this problem into a more tractable one is to use the l_1-norm, which is a convex approximation of the l_0 pseudo-norm [Davenport *et al.* 2012].

The approach based on the l_1-norm regularization (when $P(\boldsymbol{J}) = ||\boldsymbol{J}||_1$) is known as the Least absolute shrinkage and selection operator or **Lasso regression** [Tibshirani 1996] in statistics and machine learning communities and **minimum current estimates (MCE)** [Matsuura & Okabe 1995, Uutela *et al.* 1999] in the M/EEG community. The optimization problem then becomes

$$\hat{\boldsymbol{J}} = \arg\min_{\boldsymbol{J}} \|\boldsymbol{M} - \boldsymbol{G}\boldsymbol{J}\|_2^2 + \lambda||\boldsymbol{J}||_1. \tag{2.27}$$

This method penalizes the regression coefficients in the linear regression with the l_1 penalty, shrinking many of them to zero. In general, there is no closed-form expression for the optimal solution to this problem, analogous to Eq. (2.21) Minimizing (2.27) is still a convex problem, but the penalty term is non-smooth (not differentiable) at a finite number of points, so we cannot use methods such as simple gradient descent. Solving it is more of a computational challenge than solving the l_2 regularized least squares [Kim *et al.* 2007] and the approaches for solving it have been studied extensively. Numerous methods have been developed to find or approximate the solution to this problem. One of the most popular is the Least Angle Regression for Lasso (LARS) [Efron *et al.* 2004] algorithm that computes the entire solution path $\hat{\boldsymbol{J}}(\lambda)$ for all possible parameter values. It was shown that the solution to Eq. (2.27) is a piecewise linear path with respect to λ and LARS

[3] It is not a real norm because it does not satisfy the vector norm homogeneity property $||\alpha\boldsymbol{x}|| = |\alpha|||\boldsymbol{x}||$, $\forall$ scalar $\alpha \in \mathbb{R}$.

is able to "follow" and explicitly compute the entire path. Another group of algorithms are based on approximating the solution, such as proximal gradient descent (Iterative Shrinkage Thresholding Algorithm (ISTA) [Daubechies *et al.* 2004], the Fast Iterative Shrinkage Thresholding Algorithm (FISTA) [Beck & Teboulle 2009] and coordinate descent [Friedman *et al.* 2007]. On top of them, the generalized Split-Bergman algorithm [Goldstein & Osher 2009] can solve a very broad class of l_1 regularized problems. It reduces the l_1 regularized problem to a sequence of unconstrained optimization problems and Bregman updates, resulting in very fast convergence. Also, it can handle multiple l_2 and l_1 penalties at the same time.
Sparsity-based priors have been shown to be relevant for some clinical applications, such as in [Huppertz *et al.* 2001] where source localization was performed as part of presurgical evaluation of epilepsy patients with focal intracerebral epileptogenic lesions. Another advantage of the l_1 penalty is that it is somewhat indifferent to highly correlated variables. It will tend to pick a small subset of nonzero coefficient while putting most of them to zero, which makes it robust to outliers. Nevertheless, the two main drawbacks of including l_1 priors are that

(1) Differentiability of these functions is not always enssured.
(2) This type of penalty promotes spatial sparsity independently at each time instant, so the recovered source activations are non-continuous.

This limitation was later addressed allowing **structured sparsity**, firstly in the work of [Ou *et al.* 2009] whose $l_1 - l_2$ inverse solver integrates the l_1-norm regularizer in the spatial domain with l_2-norm regularizer in the temporal domain in order to avoid the unstable activation patterns and "spiky" reconstructed signals. This idea was used as a motivation in the method called mixed-norm estimates (MxNE) [Gramfort *et al.* 2012] where source estimates are promoted to be spatially focal but temporally smooth, by combining l_1 and l_2 norms in the l_{21}-norm defined as

$$||\boldsymbol{J}||_{21} = \sum_i \sqrt{\sum_j \boldsymbol{J}_i(j)^2} \tag{2.28}$$

where the row index i corresponds to the sources' spatial locations, while the column index j corresponds to time instants. l_{21}-norm is the sum of the l_2-norms of the lines (individual source time courses). Consequently, an estimation of $\boldsymbol{J}$ with the penalty (2.28) is sparse through the lines and smooth through columns, meaning that all coefficients of a line of $\boldsymbol{J}$ will be promoted to be either jointly nonzero, or all set to zero. This approach bypasses the drawback of irregular time series obtained with a simple l_1-norm. The authors later expanded the mixed-norm approach in order to also take into account the time-frequency decomposition of the signal [Gramfort *et al.* 2013].
A geometric interpretation of l_2-norm (ridge) regression and l_1-norm (Lasso) regression are depicted in Figure 2.3. Recall that the l_1-norm is the sum of all the coefficient's absolute values while the l_2-norm is the sum of the squares of the coefficients. Ridge regression is known to shrink the coeffcients of correlated independent

variables (predictors) towards each other. From a Bayesian point of view, the ridge penalty is ideal if there are many predictors, and all have non-zero coeffcients (drawn from a Gaussian distribution). The l_1 penalty is greatly impacted by larger coefficients, and there is no squaring of smaller coefficients, so smaller coefficients are more likely to drop out to zero. To conclude, while l_2 tends to shrink the coefficients to a small nonzero number, l_1 tends to cut off some unknown variables by turning their coefficients to zero.

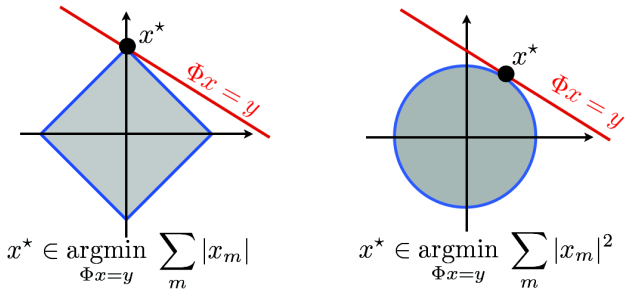

Figure 2.3: l_1 vs. l_2-norm regulariation. Note that in this image y is the observed data, Φ is the linear operator and x is the solution to be found. The optimal solution to (2.7) is the intersection of the norm constraint (the gray area) and the data fit. Taken from `https://speakerdeck.com/gpeyre/signal-processing-course-sparse-regularization-of-inverse-problems`.

One of the first studies on comparing the performance of l_2 and l_1 constraints in source reconstruction algorithms using simulated and epileptic spike data was done by [Fuchs *et al.* 1999]. Recently, a nice evaluation and comparison between some of the linear and nonlinear methods mentioned above was done by [Samuelsson *et al.* 2021]. The authors evaluated the spatial fidelity of M/EEG source estimates of MNE, dSPM, sLORETA, eLORETA and MxNE methods, from simulated patch activations over the whole neocortex superposed on measured resting-state data. The spatial fidelity was quantified in terms of localization error, spatial dispersion and the aggregate AUC metrics. Their results show that spatial fidelity of linear methods like MNE, dSPM, sLORETA and eLORETA was comparable, while the nonlinear MxNE method had much lower spatial dispersion, causing a lower sensitivity, but higher precision than the linear methods in most settings. They also reported that the spatial fidelity varies significantly with SNR, following a largely sigmoidal curve whose shape varies depending on which aspect of spatial fidelity that is being quantified and the source estimation method.

The last type of regularization in this family worth mentioning is the **Total Variation** (**TV**) regularization. It has been primarily used for image denoising since it preserves the edges in an image very well [Chambolle 2004, Rudin *et al.* 1992]. Mathematically, it is defined as the norm of the vector or image gradient, so the optimization problem (2.7) can be written as

$$\hat{\boldsymbol{J}} = \arg\min_{\boldsymbol{J}} \|\boldsymbol{M} - \boldsymbol{G}\boldsymbol{J}\|_2^2 + \lambda ||\nabla \boldsymbol{J}||_1. \tag{2.29}$$

Minimizing l_1-norm means favoring sparse solutions, so the TV regularization promotes recovery of piecewise constant signals, because their *derivatives* are sparse [Chambolle 2004]. Such priors have been widely used in the context of recovering brain activity in the fMRI community, for extracting information from brain images, both in regression and classification settings [Michel *et al.* 2011] as well as in deconvolution approaches [Karahanoğlu *et al.* 2013, Costantini *et al.* 2022]. fMRI time courses constitute the neural signal convolved with a Hemodynamic Responce Function (HRF). Deconvolution-based methods allow an approximation of the underlying neuronal activations given a model of the HRF.
In the context of M/EEG inverse problems, TV-based methods have been proposed to explore sparsity of the source spatial gradients (as discrete gradient on the surface mesh), mostly based on the assumption that the source activation should be constant in each subregion [Adde *et al.* 2005]. A graph Fractional-Order Total Variation (gFOTV) based method has been proposed in [Li *et al.* 2016], which also provides the freedom to choose the smoothness order by imposing sparsity of the spatial fractional derivatives, which, as claimed by the authors, allows to locate the source peaks more accurately. In [Becker *et al.* 2014, Becker *et al.* 2017] the authors exploited the structured sparsity, by combining l_1 and TV regularization to promote a small number of cortical regions, each of which has constant activity, while also taking into account the temporal structure of the data. The nice properties of TV norm lie in good edge preservation and limiting the overestimation of spatial extent of distributed sources. However, relying on the assumption that the underlying sources are spatially piecewise constant, i.e. that all sources have the same amplitudes in each subregion, the TV-based methods suffer from the so-called *staircase artifacts*. This leads to the loss of the gradual intensity change in the reconstructed sources and poorer localization of activity peaks.

2.3.3 Temporal smoothness priors

In a number of animal studies that used intracranial multiple microelectrode recordings, it has been shown that closely spaced neurons tend to get activated synchronously and simultaneously. This temporal coherence of neighbouring neurons was observed both during spontaneous brain activity and in the stimulated brain, in different areas of the visual, somatosensory and motor cortex, for different temporal frequencies [Engel *et al.* 1990, Eckhorn & Reitboeck 1990, Steinmetz *et al.* 2000, Silva *et al.* 1991]. Assumption of temporal independence of the underlying current sources neglects temporal structure observed in neural recordings [Buzsáki & Draguhn 2004, Cohen 2017]. Interconnected neuronal assemblies inevitably constrain the temporal evolution of neural activity detected by EEG and MEG. Consequently, the temporal dynamics has been addressed in several publications [Baillet & Garnero 1997, Ou *et al.* 2009, Gramfort *et al.* 2012, Lamus *et al.* 2012, Schmitt *et al.* 2001, Dinh *et al.* 2021] by incorporating **temporal smoothness constraints**.
For example, in [Baillet & Garnero 1997] temporal smoothness is enforced by encour-

aging small residuals in the least squares estimates of the current sources between consecutive time points. As already mention in Section 2.3.2, in [Ou *et al.* 2009] and in MxNE [Gramfort *et al.* 2012] spatially focal sources are promoted with smooth temporal estimates with a l_{21} mixed-norm.
In [Lamus *et al.* 2012] a model for cortical activity based on a nearest neighbor autoregression was used, which incorporates local spatiotemporal interactions between distributed sources in a manner consistent with neuroanatomy and neurophysiology. They proposed a dynamic Maximum a Posteriori Expectation-Maximization (dMAP-EM) source localization algorithm based on the Kalman Filter, the Fixed Interval Smoother, and the EM algorithms. The dMAP-EM algorithm was applied to simulated experiments and human experimental data and showed promising results. Although this method seems promising, it can be computationally demanding and could suffer from more practical issues like long time series to estimate the latent parameters reliably [Gramfort *et al.* 2013].
A deep learning approach has been exploited by [Dinh *et al.* 2021], with a special type of recurrent neural networks called Long Short-Term Memory (LSTM) cells, which showed great results when applied to data with a temporal structure, e.g., in natural language processing and grid-based Markov localization problems. The authors proposed to use LSTM cells whose input is a sequence of past source estimates and the output is a prediction of the following estimate. This prediction is then used as a spatial filter to correct the noise-normalized minimum norm estimates (MNE), i.e. the dSPM estimates. Since the correction of the estimates is found by using past activity (context), they named this method Contextual MNE (CMNE). In general, it can be used in conjunction with any source estimation method that has a temporal sequence and does not rely on strong and explicit *a priori* modeling assumptions. Using simulated epileptiform activity and recorded auditory steady state response (ASSR) data, the authors showed that their method showed a higher degree of spatial fidelity than the unfiltered estimates in their test cases. Finally, it is worth noting that the long-range white matter connectivity provided by dMRI was not considered in any of these methods.

2.3.4 Spatial smoothness priors

As explained in Section 2.3.3, from a physiological point of view, the solution of the M/EEG inverse problem should take into account that adjacent neurons are most likely to be activated simultaneously and synchronously. In the LORETA approach [Pascual-Marqui *et al.* 1994], similar activity is favoured between spatially adjacent vertices on the cortical mesh by choosing $\boldsymbol{W} = \boldsymbol{L}$ in (2.20), where $\boldsymbol{L}$ is the Laplacian matrix on the cortical surface. Each row of $\boldsymbol{L}$ acts as a finite difference operator by computing differences between the corresponding vertex and its direct (local) neighbors, thus providing the solution with the maximum spatial smoothness. It is worth noting that a relatively low spatial resolution comes as a consequence of the smoothness constraint, i.e. the solution produces a "blurred localized" image of a point source, preserving the location of maximal activity, but

with a certain degree of dispersion. Yet, at a macroscopic level, information transfer in the brain arises both from interactions between adjacent brain areas, referred to as "short-range" or local connections, and between distant brain areas connected via streamlines, referred to as "long-range" connections. Together, they form a complex distributed network [Proix *et al.* 2016].
In order to incorporate the long-range connectivity into the source reconstruction process, the LORETA approach was later extended in the CGS method [Hammond *et al.* 2013]. This was done by forming a hybrid local/nonlocal connectivity matrix with $\boldsymbol{A_{loc}}$ (spatial adjacency on the cortical surface) and $\boldsymbol{A_{tr}}$ (tractography-based connectivity matrix). As mentioned by [Hammond *et al.* 2013], short-range connections can also refer to the local radial connections that span through the gray matter (and cannot be represented with DWI) as well as short-range "U-fibers" that may connect gray matter regions through the white matter. $\boldsymbol{A_{loc}}$ and $\boldsymbol{A_{tr}}$ are used to form local $\boldsymbol{L_{loc}}$ and tractography-based $\boldsymbol{L_{tr}}$ graph Laplacians, respectively, resulting in the penalty term $P_{CGS}(\boldsymbol{J}) = \lambda_{loc}\boldsymbol{J^T L_{loc} J} + \lambda_{tr}\boldsymbol{J^T L_{tr} J}$. Therefore, the objective function minimized by CGS is defined by

$$U_{CGS}(\boldsymbol{J}) = \|\boldsymbol{M} - \boldsymbol{GJ}\|_2^2 + \lambda_{loc}\boldsymbol{J^T L_{loc} J} + \lambda_{tr}\boldsymbol{J^T L_{tr} J}. \tag{2.30}$$

Both the data fidelity and the prior penalty terms are quadratic in $\boldsymbol{J}$, so the problem has an analytic linear solution

$$\hat{\boldsymbol{J}}_{\boldsymbol{CGS}} = \left(\boldsymbol{G^T G} + \lambda_{loc}\boldsymbol{L_{loc}} + \lambda_{tr}\boldsymbol{L_{tr}}\right)^{-1}\boldsymbol{G^T M}. \tag{2.31}$$

This way CGS penalizes the weighted sum of squared differences in activity between anatomically connected cortical patches (both locally and non-locally) and promotes solutions with consistent activations across them. Since LORETA and CGS methods were the main inspiration for the approaches explored in this thesis, they are explained in more details in Section 4.5 with several illustrative examples.
In the context of spatial constraints, it is also worth mentioning that spatial fMRI priors have been included in several publications such as [Dale *et al.* 2000, Brookings *et al.* 2009, Daunizeau *et al.* 2005] which made the use of high spatial resolution of fMRI (since in M/EEG it is relatively low). However, the temporal resolution of BOLD signals in fMRI is at the order of seconds, while in M/EEG it is significantly higher, at the order of milliseconds, so combining these two modalities still remains challenging.

2.3.5 Anatomical priors from diffusion MRI

The use of anatomical priors coming from diffusion MRI has been addressed in several publications in the context of M/EEG source reconstruction. As we just mentioned in Section 2.3.4, the structural connectivity derived from white matter fiber tractography was exploited in CGS [Hammond *et al.* 2013] by promoting solutions with consistent activations across anatomically connected regions. However, the temporal dynamics of the data was not considered.

In [Belaoucha & Papadopoulo 2017] and [Philippe *et al.* 2013] diffusion data was used to parcellate the cortex into functional regions. This was used as a prior knowledge as a variant of the weighted minimum norm, where the elements of the weighting matrix depend on the structural homogeneity of the regions obtained from dMRI. The weighting matrix relates the dipoles' magnitudes of sources inside these functional regions, allowing their magnitudes to differ according to their structural homogeneity. This way sources in the same diffusion parcel are enforced to have close magnitude values.

In a context of modeling dynamic functional connectivity (FC) *networks* from non-stationary time-series, the authors in [Pascucci *et al.* 2020] proposed a variant of the classic Kalman filter called Self-Tuning Optimized Kalman filter (STOK) to model dynamic changes in large-scale functional networks during evoked brain activity. Later, they made an extension to this work and created a variant of this method called si-STOK (structurally-informed STOK) [Pascucci *et al.* 2021], where they proposed a linear adaptive filter for estimation of dynamic and directed functional connectivity using structural connectivity (SC) priors. STOK is an adaptive filter that derives time-varying Mutlivariate Autoregressive coefficients (tv-MAR) using least-squares regression of present on past signals. In si-STOK, SC priors are included in the filter as the prior variance on the expected zero functional connectivity (FC) between each pair of nodes (the larger the FC, the larger the influence from a sender to a target node). High SC values lead to large prior variance, enabling FC to deviate from zero (when supported by the sensor data). On the other hand, weak SC reduces the prior variance and shrinks FC towards zero. Their results showed that incorporating SC in dynamic FC promotes sparser and physiologically plausible functional network topologies, which helps to identify the most important network drivers and dynamics. Although this approach is interesting and closely related to our problem, it does not incorporate dMRI priors for source reconstruction but for estimation of FC networks.

Very few methods include **delays supported by dMRI** as a prior structural information in the the context of regularizing the dynamics of M/EEG. In [Fukushima *et al.* 2015] source intensities are modeled using a multivariate autoregressive (MAR) model whose elements are constrained by anatomical connections obtained from dMRI. Starting from MEG measurements, source magnitudes and their interactions (the posterior distribution of MAR coefficients) are jointly estimated using a variational Bayesian algorithm. Still, this method suffers from high computational complexity and requires tuning of multiple parameters. Similar source model was used in [Belaoucha & Papadopoulo 2020] where the authors reconstructed the brain activation and effective connectivity between the brain regions using an extension of the MxNE solver [Gramfort *et al.* 2012] called the iterative Source and Dynamic Reconstruction (iSDR). Lastly, in [Deslauriers-Gauthier *et al.* 2019, Deslauriers-Gauthier *et al.* 2020] and [Belaoucha *et al.* 2015] the authors rely upon a probabilistic technique called maximum entropy on the mean (MEM), which is explained in more details in Section 2.4.

2.4 MEM Approaches

Another family of nonlinear approaches are based on entropy. A probabilistic technique called maximum entropy on the mean (MEM) was exploited by the authors in [Amblard *et al.* 2004, Deslauriers-Gauthier *et al.* 2019, Deslauriers-Gauthier *et al.* 2020, Belaoucha *et al.* 2015]. MEM framework starts with the available data and aims to infer a probabilistic law which maximizes the missing information. Prior information regarding the current source distribution is introduced by the definition of a reference distribution (a predefined probabilistic law). By modifying this reference law in a way that only the available information is taken into account [Amblard *et al.* 2004] a MEM solution is obtained, i.e. the probability law closest to the reference law, whose average explains the measurements. This approach was further extended in a method called Connectivity Informed Maximum Entropy on the Mean (CIMEM) by [Deslauriers-Gauthier *et al.* 2019] to not only reconstruct the source activity, but also to estimate the information flow in the white matter of the brain by using jointly dMRI and EEG. Briefly, possible interactions between brain regions at different times are captured by a subject specific Bayesian network. This network encodes the macroscopic connections between cortical regions detected using dMRI tractography derived white matter bundles and their associated delays, which is further used to constrain the EEG inverse problem and estimate which white matter connections are used to transfer information between cortical regions. That is to say, this method allows the estimation of the directed dynamical functional connectivity between different regions using M/EEG measurements, whose delays are supported by dMRI. The output of the algorithm is a subset of white matter connections whose delays and cortical endpoints can explain the given measurements, so the ones which are active at a certain time can be identified. It was further enriched in [Deslauriers-Gauthier *et al.* 2020] by using fMRI as a prior information to automatically prune structural connections and increase the likelihood of certain regions being active, which avoids the manual selection of task-associated regions of interest. Using sensory–motor evoked MEG data, the authors demonstrated that this approach allows to identify both (1) brain regions known to be involved during this task paradigm and (2) white matter fiber bundles used for information transfer during the given task and the information flow along them. Nevertheless, MEM approaches can be highly sensitive to the initialization of the reference distribution representing the prior knowledge of the current distribution [Grova *et al.* 2006] and they also suffer from high computational complexity.

2.5 Dipole Fitting Approaches

Dipole fitting approaches assume that the measured M/EEG signals are generated by one or a small number of focal sources [Mosher *et al.* 1992], whose locations, orientations, and magnitudes are estimated. Each source is modelled by a dipole representing a small portion of the cortical surface of a few mm^2. The number of dipoles P has to be fixed a priori ($\text{P} \ll \text{N}$). For a dipole p_i with position $\boldsymbol{r}_i$ and

orientation $\boldsymbol{\Theta}_i$ in 3D space, its moment is given by $\boldsymbol{q}_i = q_i\boldsymbol{\Theta}_i$. Dipole's orientation $\boldsymbol{\Theta} = \boldsymbol{q}/||\boldsymbol{q}||$ is represented in spherical coordinates $\boldsymbol{\Theta} = \{\theta, \phi\}$ while its strength can be written as $x_i = ||\boldsymbol{q}_i||_2$. Let then $\boldsymbol{g}_i(\boldsymbol{r}_i, \boldsymbol{\Theta}_i)x_i$ be the forward field produced by the dipole p_i. Then for simultaneous activation of P dipoles, the measured M/EEG at time t can be written as

$$\boldsymbol{m}(t) = \sum_{i=1}^{P} \boldsymbol{g}_i(\boldsymbol{r}_i, \boldsymbol{\Theta}_i)x_i(t) + \boldsymbol{e}(t) \tag{2.32}$$

where $\boldsymbol{e}(t)$ is additive noise. Note that the leadifeld matrix $\boldsymbol{G}(\boldsymbol{r}, \boldsymbol{\Theta})$ is now a function of both the position and orientation. So we need to estimate dipoles' (1) intensities, (2) positions and (3) orientations that best describe the data, which corresponds to solving

$$\min_{\boldsymbol{r},\boldsymbol{\Theta},\boldsymbol{x}} \left\| \boldsymbol{M} - \sum_{i=1}^{P} \boldsymbol{g}_i(\boldsymbol{r}_i, \boldsymbol{\theta}_i)x_i \right\|_F^2 = \|\boldsymbol{M} - \boldsymbol{G}(\boldsymbol{r}, \boldsymbol{\Theta})\boldsymbol{X}\|_F^2 \tag{2.33}$$

where $\boldsymbol{X}$ is a time series matrix of dipole's amplitudes. The measure of the fit is in the least-squares (LS) sense – the square of the Frobenius norm, so we can denote the solution to this problem as $\hat{\boldsymbol{J}}_{LS}$. A way to minimize this would be either with a nonlinear algorithm which may fall into a local minimum or with a brute force grid search algorithm over all parameters $(\{\boldsymbol{r}_i, \boldsymbol{\Theta}_i\}, x_i)$ which has a better chance of finding the global minimum. Yet, if we assume that $P \ll N$ and that $\boldsymbol{G}$ has a full column rank then its left pseudoinverse exists. So for a selected dipole $\{\boldsymbol{r}_i, \boldsymbol{\Theta}_i\}$, the matrix $\boldsymbol{X}$ that will minimize $\boldsymbol{J}_{LS}$ is

$$\boldsymbol{X} = \boldsymbol{G}^{+}\boldsymbol{M} = (\boldsymbol{G}^T\boldsymbol{G})^{-1}\boldsymbol{G}^T\boldsymbol{M}. \tag{2.34}$$

We can then solve (2.33) by minimizing the following cost function and reduce computational burden [Baillet *et al.* 2001]

$$\begin{aligned} \boldsymbol{J}_{LS}(\{\boldsymbol{r}_i, \boldsymbol{\Theta}_i\}) &= \arg\min_{\boldsymbol{r}_i,\boldsymbol{\Theta}_i} \|\boldsymbol{M} - \boldsymbol{G}\boldsymbol{X}\|_F^2 = \left\|\boldsymbol{M} - \boldsymbol{G}(\boldsymbol{G}^{+}\boldsymbol{M})\right\|_F^2 \\ &= \left\|(\boldsymbol{I} - \boldsymbol{G}\boldsymbol{G}^{+})\boldsymbol{M}\right\|_F^2 = \left\|\boldsymbol{P}_{\boldsymbol{G}}^{\perp}\boldsymbol{M}\right\|_F^2 \end{aligned}$$

where $\boldsymbol{P}_{\boldsymbol{G}}^{\perp}$ is the orthogonal projection matrix onto the left null space of $\boldsymbol{G}$. This problem can be solved for a limited set of nonlinear parameters $\{\boldsymbol{r}_i, \boldsymbol{\Theta}_i\}$ with a nonlinear iterative minimization procedure such as Nelder-Meade downhill simplex search. The dipole magnitudes can then be linearly estimated from (2.34). If the dipoles locations are not fixed (i.e. the dipoles are allowed to move), the method is called the *moving dipole*, if they can only rotate it is referred to as the *rotating dipole* and when the dipoles' positions and orientations are fixed, it is called the *fixed dipole*. Three big limitations of this approach are that

(1) The number of dipoles must be fixed a priori.
(2) The optimization problem is nonlinear and non-convex.

(3) Interpretation of dipole results relies on the assumption that only a few dipoles are the active sources in the brain.

Nonlinear minimization procedures for multiple dipoles can fail to reach a global minimum and can get "stuck" in a local minima, thus providing relatively poor solutions, giving rise to a practical limit to how many dipoles can be estimated.

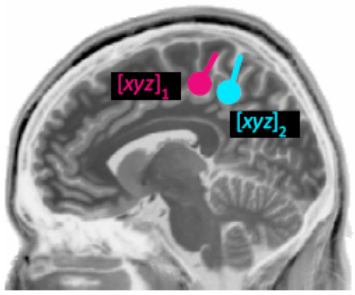

Figure 2.4: Example of dipole fitting (taken from [Cohen 2017])

.

Dipole fitting approaches make sense if only a small number of sources is assumed to be active. So regarding limitation (3), this could be a valid assumption for experiments that, for example, involve stimulation of primary sensory or motor cortices without concurrent cognitive or decision-making processes [Cohen 2014]. Nevertheless, in reality, brain activity is a widespread process and a large number of groups of neurons can contribute to the generation of M/EEG signals. During many cognitive and perceptual processes bigger brain networks get activated and they can dynamically change over time and over frequency. Therefore, it is important to realize that if a dipole is fit to a very small part of the signal (one time point from the grand-averaged ERP over many subjects), that dipole will provide insights into a correspondingly small aspect of brain dynamics. A single dipole can indeed sometimes account for over 80 % or 90% of the topographical variance. Nonetheless, in case of single-trials for example, it might be difficult to find a single dipole that can account for such a large portion of the variance.

2.6 Scanning Methods

Scanning methods were initially developed in other fields of signal processing such as sonar and radar applications, as well as seismic exploration [Van Veen & Buckley 1988]. They suppose that active sources are at predefined positions, i.e. in a region of interest. The orientations of the dipoles are either assumed to be known or left unconstrained. These methods scan through the regions of interest and try to decide among the possible dipole locations, where it is most suitable to place the sources, in order to best describe the M/EEG data.

Beamforming

The main hypothesis behind beamforming is that the sources are uncorrelated and that the activity of each source in the distributed source model is estimated independently of the other ones. An optimal spatial filter which maps the sensor data to the current source amplitude at the given grid point in the brain is computed. This is generally done by scanning through a set of predefined presumed source locations, by computing separately for each location a set of weights, a so-called *spatial filter*, and applying these weights to the measured sensor data to obtain the beamformer output for each location. Essentially, a beamformer monitors signals from a dipole at chosen location, while blocking contributions from all other brain locations [Van Veen *et al.* 1997, Baillet *et al.* 2001, Westner *et al.* 2022]. The most famous approach in this category is Linearly Constrained Minimum Variance (LCMV) beamformer [Van Veen *et al.* 1997], which computes a filter that minimizes the variance of sources. Its crucial assumption is that all activity contributing to the measured signal is captured in the data covariance matrix, so it heavily depends on it. The wanted spatial filter in LCMV is the one that best projects on a source of interest, e.g. on a column of the lead field matrix $\boldsymbol{G}$, while at the same time minimizing its projection on the data covariance matrix, that contains contributions from the source of interest, other to-be-suppressed brain sources and noise [Hauk & Stenroos 2014]. The difficulty of assessing beamformers in the same framework with distributed inverse solver is that they are sensitive to forward modeling errors [Steinsträter *et al.* 2010] and usually deploy a volumetric source space rather than a surface-based one which is most often used in distributed estimates. The interested reader can find a great review on beamformers in [Westner *et al.* 2022].

MUSIC

An alternative to spatial filtering is based on the separation of the data space into two mutually orthogonal subspaces: the signal space and the noise space, using SVD. The most famous approach within this category is MUltiple SIgnal Classification (MUSIC) [Mosher *et al.* 1992], developed as a special case of the original MUSIC method [Schmidt 1986]. The solution (multiple dipole locations) is found by scanning potential locations using a simple one dipole model. The authors provide solutions for three cases: i) unconstrained dipoles, ii) dipoles with a fixed location and iii) dipoles with a fixed location and orientation. Briefly, the MUSIC algorithm scans a single dipole model through the brain volume or cortical surface and computes projections onto the signal space. By using SVD of the data, the locations and orientations of p unsynchronised cortical sources are found, by projecting each candidate dipole onto the noise subspace and finding which ones gives the lowest error. For more details see [Mosher *et al.* 1992].

Convenience of MUSIC and beamformers over distributed source models is that each source can be found by scanning through the possible set of locations and orientations, finding each source in turn, instead of estimating simultaneously for all sources [Baillet *et al.* 2001, Mosher *et al.* 1992]. A distinct advantage of MUSIC over beamformers is the relaxation of the requirement of orthogonality between dis-

tinct sources. MUSIC has a weaker assumption that different sources have linearly independent time series. In noiseless data, partially correlated sources will still result in a cost function equal to zero at true dipole locations, making it more robust to time-correlated sources. In the presence of noise, however, MUSIC will fail when two sources are strongly correlated [Baillet *et al.* 2001]. This problem was later addressed by adjusting the concept of single dipole models to allow sets of sources in a variant called Recursively APplied MUSIC (RAP MUSIC) [Mosher & Leahy 1998]. As the name implies, it applies MUSIC successively after removing the contribution of the previously identified dipole.

2.7 Conclusion

In this Chapter, different approaches to solve the M/EEG inverse problem have been presented, with the main hypotheses behind them and mathematical frameworks used to obtain the source estimates. Let us firstly briefly recall the 3 main families of approaches. The dipole fitting approaches assume the measurements are obtained from a small number of focal sources whose locations and amplitudes are estimated by nonlinear optimization algorithms. The scanning approaches scan through the source space aiming to chose the sources which best explain the M/EEG data. The distributed source models do not fix *a priori* the number of sources but allocate a large number of dipoles to the cortical mesh and aim to estimate their amplitudes simultaneously. In these approaches, the number of sensors is smaller than the number of sources, so priors constraints on the source distributions need to be set in order to obtain a unique solution. Secondly, a taxonomy of the algorithms in this group of approaches has been presented according to the priors they deploy and each prior has been carefully elaborated. Most attention has been dedicated to distributed source models since the approaches in this thesis belong to them.

Chapter 3

Data preprocessing and simulation

Contents

Overview

Integrating structural and functional neuroimaging data can allow us to get a more detailed picture of brain structure and dynamics. However, the actual process of its integration is often a hefty and a time-consuming task. This is mostly due to the various coordinate systems and units the data are acquired and expressed. Nevertheless, it is an essential step that requires meticulous quality control at each stage since, if done erroneously, invalidates any further analysis.
In this Chapter, we first show our multimodal preprocessing pipeling used for integration of structural MRI, diffusion MRI and MEG data into a same framework. Several preprocessing steps such as the extraction of the cortical surfaces, their parcellation and source space creation are elaborated. Secondly, we describe the head conduction model and the computation of the lead field matrix. Thirdly, we specify

the processing of MEG data, dMRI data (notably dMRI tractography) used in the thesis. Further, we clarify and illustrate the 5 different coordinate systems in which the used data were acquired and expressed, along with the transforms that bring the data from one system to another. We also outline the 3 spatial scales for brain's surface representation, their mapping to the underlying streamlines and explain the computation of the structural connectivity matrix and the delay matrix. Lastly, we define the simulation of source-level brain activity that was used as a synthetic dataset to validate the reconstruction approaches presented in Chapter 4 and 5.

3.1 Multimodal Preprocessing Pipeline

In this thesis we use the publicly available data from the Human Connectome Project (HCP) consortium [Van Essen *et al.* 2013, Larson-Prior *et al.* 2013]. The structural MRI, diffusion MRI and MEG data were taken for 10 subjects (ages 22–35 years, 6 females, 4 males). Several steps comprise the preprocessing pipeline, such as the extraction of the cortical surfaces and their parcellation, head modelling and lead field computation, diffusion MRI tractography and preprocessing of MEG signals. These steps are outlined in the following sections and the diagram of the whole preprocessing pipeline is shown in Figure 3.1.

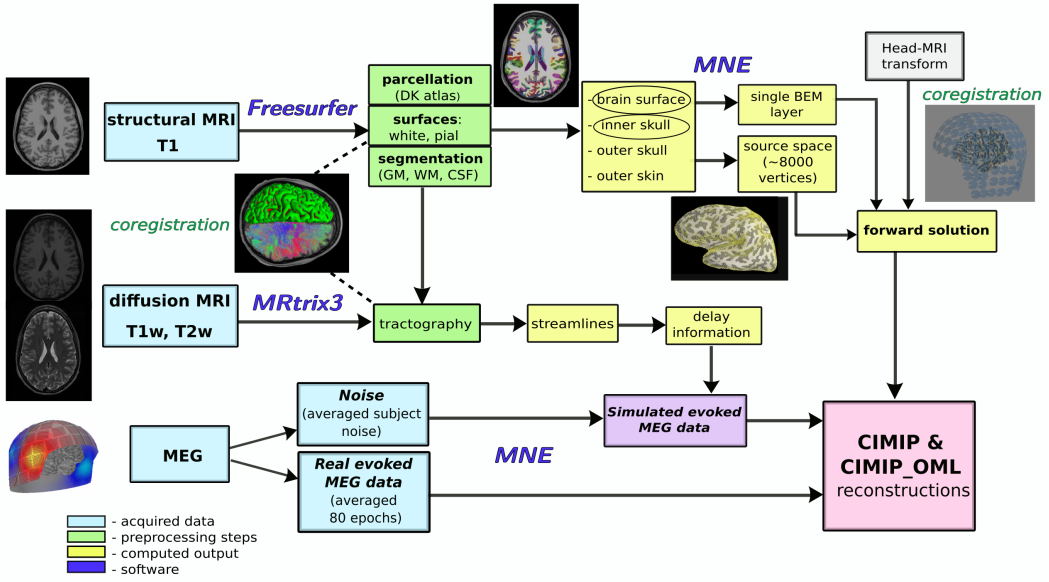

Figure 3.1: Preprocessing pipeline diagram: integration of structural MRI, dMRI and MEG data.

Firstly, we start with structural MRI images, which were used to:

- Segment the brain into gray matter (GM), white matter (WM) and cerebrospinal fluid (CSF).
- Extract cortical surfaces.
- Parcellate the brain into neuroanatomical regions of interest.
- To segment the head compartment(s) needed for computation of the lead field operator with the BEM method. For MEG only the the shape of the intracranial volume (a.k.a "inner skull") is needed.

Secondly, diffusion MRI images were used to perform diffusion tractography which generates a set of streamlines that represent white matter fiber bundles. Given streamlines' lengths and the information transmission speed, transmission delays can be estimated for each connection. These delays were used both for simulation and reconstruction of source-level brain activity.
Thirdly, MEG data was used in two ways:

- Sensor-level physiological MEG noise was added as realistic noise to the synthetic MEG dataset.
- Real evoked MEG data for a sensory-motor task was used to test our reconstruction method and compare it to state-of-the-art approaches.

All images in the following sections are of subject 105923 from the HCP dataset, unless stated differently.

3.2 Cortical Surface Extraction and Parcellation

Cortical surfaces were extracted from the subject's anatomical T1 MR images from the Human Connectome Project[1] [Van Essen *et al.* 2013] dataset using Freesurfer[2] software [Fischl 2012]. The images acquired on an MRI scanner are 3D volumes and these images are extracted into smooth, continuous, 2D surfaces, such as white matter, gray matter, pial surface and others. The intersections of pial and white surfaces with the brain volume are shown in Figure 3.2 in pink and green, respectively. The distance between the white and the pial surface can give us the thickness at each location of cortex [Fischl & Dale 2000]. The high resolution meshes representing the cortical surfaces provided by FreeSurfer comprise of around 300,000 vertices for both hemispheres. Generally, we only need a subset of these vertices to create a source space, which is represented by a tessellated white matter cortical surface. To decimate the high resolution surface meshes, we can obtain a uniform sampling by subsampling in the spherical space. To do this, we can use for example a recursively subdivided icosahedron or octahedron. We used the latter, which resulted in a source space represented by a grid of 8196 candidate source (dipole) locations, with an average distance of 5 mm between adjacent sources. The source

[1] https://www.humanconnectome.org
[2] https://surfer.nmr.mgh.harvard.edu/

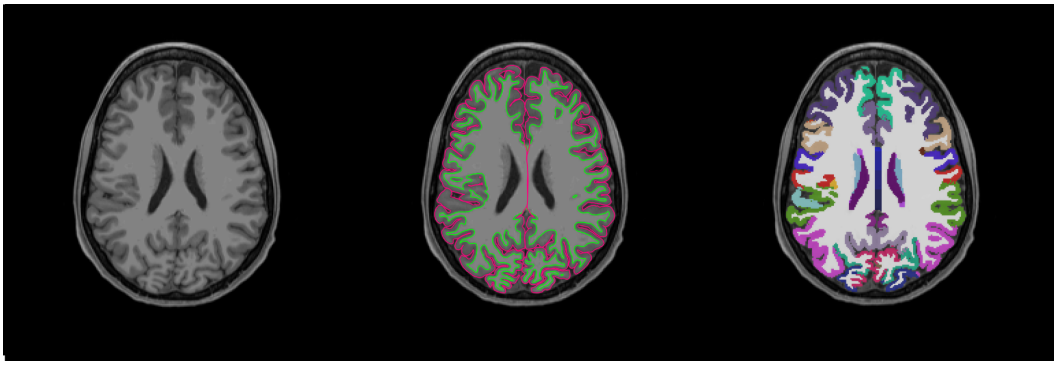

Figure 3.2: Axial view of T1 image (left), overlaid with pial and white surface (in pink and green, respectively) (middle) and Desikan-Killiany atlas (right).

space was created using MNE-Python [Gramfort *et al.* 2014] software package and it is illustrated in Figure 3.3 on the left. The dipole orientations were fixed to be normal to the cortical surface [Dale & Sereno 1993, Baillet *et al.* 2001]. The white matter cortical surface was parcellated into 68 neuroanatomical regions of interest according to Desikan-Killiany atlas [Desikan *et al.* 2006] using Freesurfer. This anatomical parcellation overlaid on the T1 image is shown in Figure 3.2 on the right. In Figure 3.3 on the right, we can see the lateral view of this parcellation on the left hemisphere, overlaid on the white matter surface obtained by the FreeSurfer.
This parcellation (representation of the brain's surface in the "region space") was used in 2 ways

- In the simulation of cortical activity, in which a subnetwork of active regions is chosen.
- In the reconstruction of cortical activity with a proposed reconstruction method called $CIMIP\_OML$ (which will be described in Chapter 5 in Section 5.2), for both simulated and real MEG data, since this method requires a set of *a priori* identified active regions.

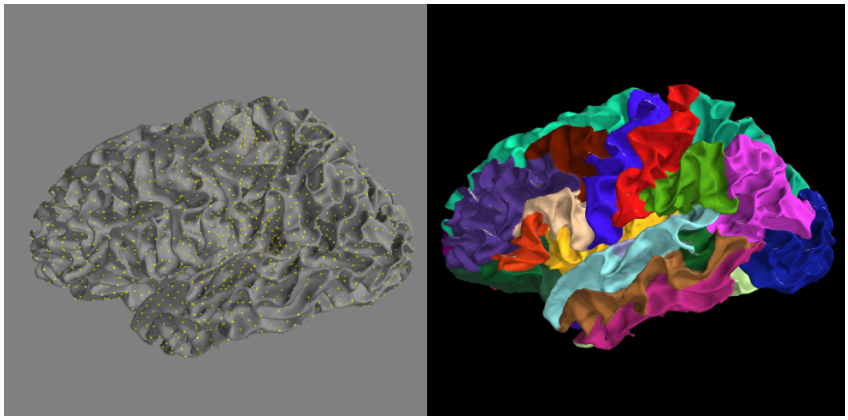

Figure 3.3: The source space (left) and Desikan-Killiany atlas on the white matter surface a.k.a the "region space" (right).

3.2.1 Head modelling and lead field computation

Computation of the lead field matrix, e.g. with a Boundary Element Method (BEM) [Ferguson *et al.* 1994, Kybic *et al.* 2005], requires modeling the geometry of the head and its electromagnetic properties [Hamalainen & Sarvas 1989, Mosher *et al.* 1999] such as conductivities of different tissues. More specifically, it requires having a conductor model for the head, a source space of dipole locations, and the sensor locations relative to those dipoles. For a realistic head model, computation of M/EEG forward solution with the BEM method requires having tessellated surfaces separating regions of different conductivities such intracranial space (brain), the skull, and the scalp. These compartments can be acquired by means of segmentation of magnetic resonance images of the head, after which the relevant surfaces need to be tessellated. The scalp and the brain have almost equal conductivities, while the conductivity of the skull is about ∼100 times smaller [Hamalainen & Sarvas 1989]. For MEG this is not an issue since the magnetic field is less dependent of the conductivity profile and a reasonably good solution can be obtained by using a single-compartment BEM, given the shape of the intracranial volume. As a quality control step, we needed to verify that the input surfaces are complete and topologically correct, i.e. that the surfaces do not intersect and that they are correctly ordered (outer skull surface inside the scalp and inner skull surface inside the outer skull), as shown in Figure 3.4, along with the white matter surface. To compute

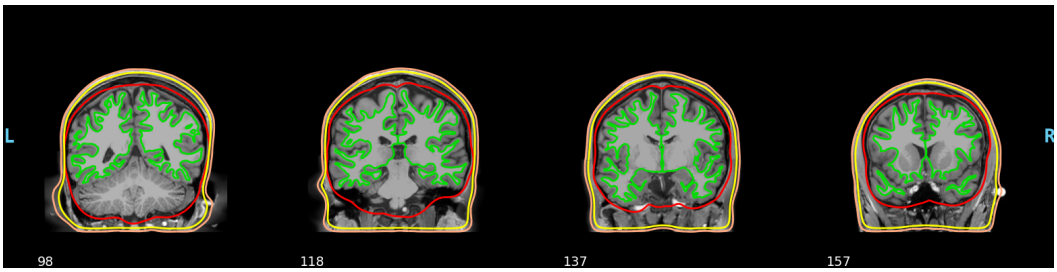

Figure 3.4: BEM countours overlaid on T1 image, representing the the scalp (orange), outer skull (yellow), inner skull (red). White matter surface is shown in green.

the MEG forward solution, we employed a subject-specific single-compartment head conductor model, bounded by the inner skull surface obtained using Freesurfer watershed algorithm [Ségonne *et al.* 2004], with electrical conductivity of the brain set to 0.3 S/m. Finally, after the co-registration of MEG sensor locations to the underlying source space, the lead field matrix was numerically computed with the BEM method using the MNE-Python [Gramfort *et al.* 2014] for $N = 243$ magnetometers at $S = 8196$ dipolar sources.

3.3 dMRI data

Let us first mention some specifications regarding the acquisition. Diffusion-weighted magnetic resonance images (DWI) provided by the HCP were acquired on a clinical

Siemens 3T Skyra MRI system and preprocessed with the minimal preprocessing pipeline for the Human Connectome Project [Glasser *et al.* 2013]. For a detailed description of the preprocessing pipeline applied to this dataset, the interested reader can refer to the original paper of [Glasser *et al.* 2013]. Acquisition was performed for 90 uniformly distributed gradient directions on three shells with b values of 1000, 2000 and 3000 s/mm^2 (TE = 89.5 ms, TR = 5.52 s), plus 18 b = 0 s/mm^2 volumes, giving 288 volumes in total per subject. Each volume consists of $145 \times 174 \times 145$ voxels with $1.25 \times 1.25 \times 1.25$ mm^3 resolution.
Whole-brain probabilistic tractography was implemented using the MRtrix3[3] software [Tournier *et al.* 2019]. Firstly, a five-tissue-type segmentation image [Smith *et al.* 2012] was generated using the segmentation volume, with the Freesurfer pipeline implemented in Mrtrix3. With this segmentation image, a mask suitable for seeding streamlines from the GM-WM interface was created. Afterwards, using diffusion weighted and the five-tissue-type image, a fiber response function was estimated for the WM, GM, and CSF using using Multi-Shell Multi-Tissue Constrained Spherical Deconvolution (MSMT-CSD) algorithm [Jeurissen *et al.* 2014]. Lastly, the obtained fODFs were used for probabilistic anatomically constrained tractography (ACT) with backtracking, with the iFOD2 algorithm [Smith *et al.* 2012]. Seeding from the gray matter - white matter interface, 1 million streamlines were generated for every subject. The minimal and maximal fiber length were set to 10 and 300 mm, respectively. This minimal value criterion was chosen to avoid tracking the so-called "local association fibres" i.e. the short tracks that pass through superficial white matter [Schmahmann *et al.* 2009, Smith *et al.* 2012]. For computational purposes, a subset of 200,000 streamlines was used in the rest of this work. An example of the resulting tractogram is shown in Figure 3.5 on the left, while on the right we chose to show a subset of the streamlines connecting the two lateral occipital regions.

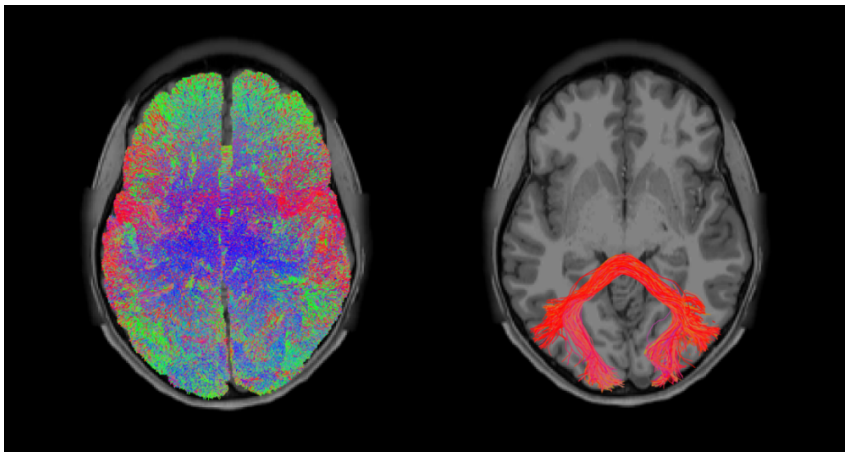

Figure 3.5: Left: the whole tractogram, right: subset of streamlines connecting the two lateral occipital regions.

[3] http://www.mrtrix.org

3.4 MEG task data

The MEG data were made available by the HCP [Larson-Prior *et al.* 2013], recorded using a whole head MAGNES 3600 (4D Neuroimaging, San Diego, CA) magnetometer system in a magnetically shielded room at Saint Louis University. The system comprises of 248 magnetometer channels and 23 reference sensors to capture environmental signals. The data were recorded with a sampling frequency of 2034.5 Hz. Digitization of the participants' head shape and of the locations of the fiducial coils was done with a Polhemus 3SpaceFasttrak system. The MEG data were accessed using MNE-HCP library[4] and further processed using MNE-Python software.

3.4.0.1 Evoked task MEG data

The task MEG dataset involves three experimental paradigms: a sensory-motor task, a working memory task and a language processing task. We focused on the sensory-motor task in which the subjects were asked to perform one of the 4 limb movements: right hand (RH), left hand (LH), right foot (RF) or left foot (LF), after having been presented with a visual stimulus. This is illustrated in Figure 3.6. It was performed in two 14 *min* sessions, with a small break between them. Each session consisted of 42 blocks; 32 of them were partitioned into 16 hand movements blocks (8 right and 8 left) and 16 foot movements blocks (8 right and 8 left). The remaining 10 blocks were interleaved resting/fixation blocks [Larson-Prior *et al.* 2013]. Each task block started with a 3 s visual cue that indicates to the subject to either tap their left/right index and thumb fingers or to squeeze their left/right toes. The next 12 s in the block consisted of 10 sequential movements (trials), each initiated with a 150 ms pacing stimuli (a small arrow in the center of the screen), followed by a 1050 ms black screen for task execution. Therefore, for each of the 4 movements, there were 8 blocks with 10 trials, giving a total of 80 repetitions (epochs) per task. The evoked data were preprocessed by the HCP "eravg" pipeline, where the trials were segmented to time windows of –1.2 to 1.2 s before and after the visual cue onset [5]. The purpose of this pipeline is to compute average of the event related fields/potentials (ERFs/ERPs), i.e. to make evoked data and to calculate condition differences (contrasts) at the channel level. Averaging brain activity across trials is a powerful way to increase signal-to-noise ratio (SNR) in M/EEG data. It includes removal of bad channels, bad segments and independent components from the task data. Briefly, prior to baseline correction, the ERFs were bandpass filtered between 0.5 and 60 Hz. Environmental noise was subtracted away by using reference sensors at the periphery of the head. Independent component analysis (ICA) was used to remove components not related to brain activity (cardiac and ocular artifacts, i.e. heart beats and eye blinks). Bad trials and bad segments were removed with a combination of automated methods as well as annotations by a human observer.

[4] https://github.com/mne-tools/mne-hcp

[5] https://www.humanconnectome.org/study/hcp-young-adult/document/500-subjects-data-release

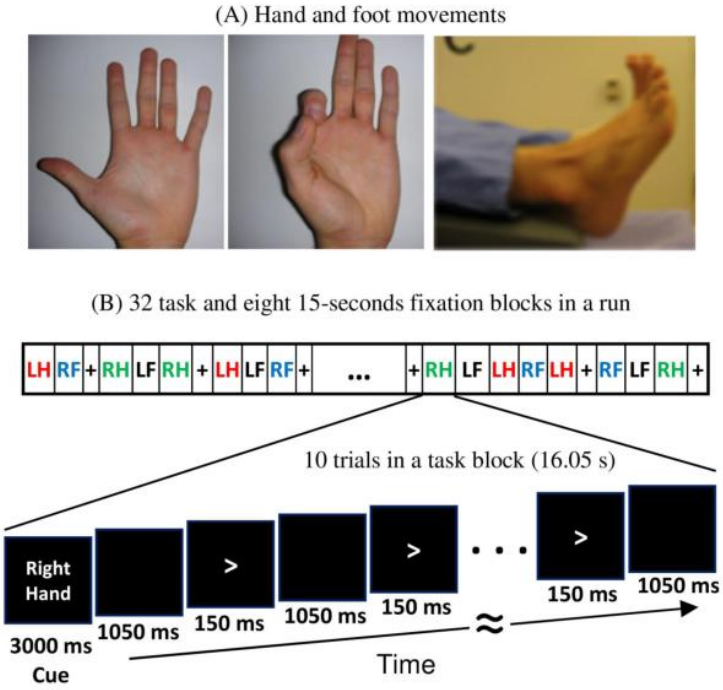

Figure 3.6: The motor task paradigm. (A) Performed with both right (RH/RF) and left (LH/LF) limbs. (B) Every block starts with a 3 s cue telling the subject which limb to move in that trial. Adapted from [Larson-Prior *et al.* 2013].

After the removal of bad channels, evoked data from 243 sensors (magnetometers) were kept. For further details on the HCP pipelines, the interested reader is referred to [Larson-Prior *et al.* 2013] and the HCP S1200 reference manual.

On top of that, we performed a few additional preprocessing steps. We further resampled the evoked data to 500 Hz to match the sampling frequency of our simulated data. Also, we restricted the time window of each trial by extracting 400 ms of data following the visual cue, since ERF oscillations are expected to die away within 500 ms [Robinson *et al.* 2006]. The averaged evoked responses after the visual cue, for the 4 movements are shown in Figure 3.7. This data will be used to evaluate reconstruction methods proposed in Chapter 4 and Chapter 5.

3.4.0.2 Epoched physiological noise extraction

Sensor-level physiological MEG noise was used to add realistic noise to the simulated datasets (simulation of source-level brain activity is explained in Section 3.7). Since the raw (patient) noise data provided by the HCP was unprocessed, the following preprocessing pipeline was performed. Firstly, only the MEG channels that appear in the evoked task data were kept. Secondly, signals were bandpass filtered between 1 and 100 Hz, after which a notch filter was applied at 60 Hz to attenuate power line noise artefacts. In order to corrupt the noiseless measurements with realistic

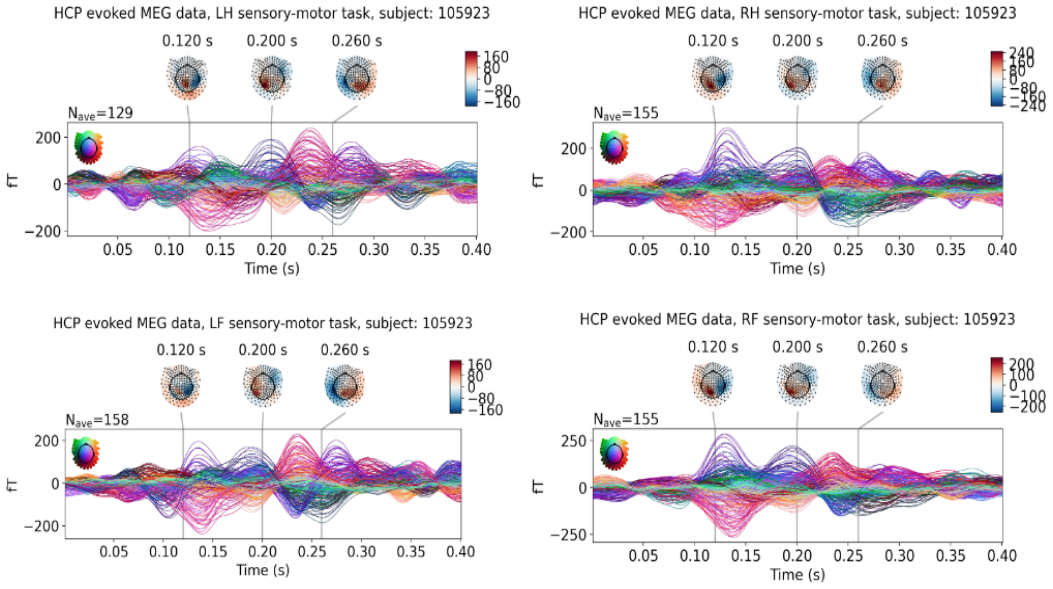

Figure 3.7: Averaged evoked responses to the visual cue prior to the 4 limb movements, with the corresponding topographic maps.

noise that would resemble the one that appears in evoked potentials, we first needed to epoch the raw data and then average the epochs. HCP evoked data contains 80 epochs, so we randomly chose 80 independent sections (epochs) of 100 ms of noise data, filtered as just described, and then averaged them across epochs. The time window of 100 ms was chosen to match the time window of simulated data. Finally, the signal ("evoked noise") was downsampled from 2034.5 Hz to 500 Hz in order to match the sampling frequency of the simulated data.
The noise was further rescaled to obtain the noise-corrupted measurements for 2 different SNR levels, 3 and 10, which is explained in more details in Section 3.7.3.

3.5 Coordinate Systems and co-registration

One of the challenges when dealing with medical signals and images that come from different modalities is the difference between the coordinate systems in which the data are acquired and expressed. Each coordinate system has a specific purpose and represents their data in different ways. The three main and most commonly used coordinate systems in medical imaging are called the the scanner native (or "world"), anatomical and the image (or "voxel") coordinate system [SlicerWiki 2021]. They are illustrated in Figure 3.8 with their corresponding axes. Although these are the main ones, the total number of coordinate systems needed for the purpose of this work was five and they are described below.

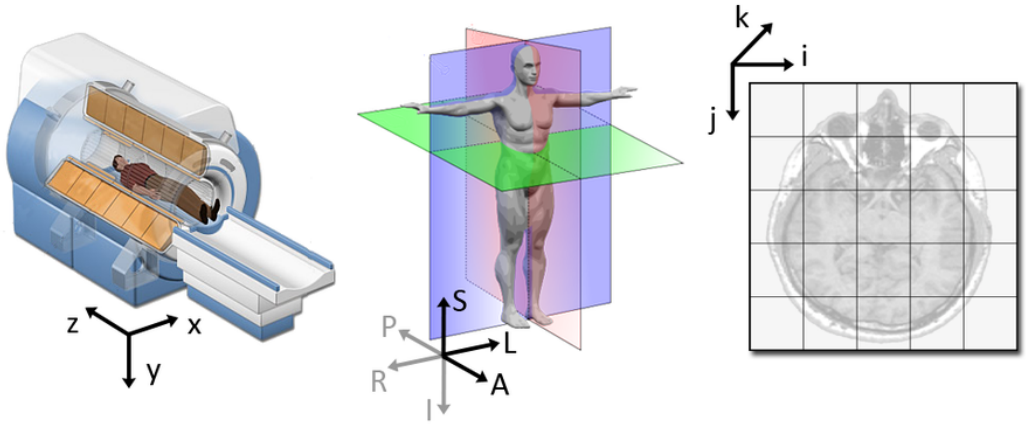

Figure 3.8: World (left) anatomical (middle) and the image coordinate system (right). Adapted from *https://www.slicer.org/*.

3.5.1 MRI voxel coordinates – the image coordinate system

MRI images are 3D or 4D arrays (voxel arrays) of image data. In digital photographs, a pixel is a 2D unit of the image with a single value. A voxel is a pixel with volume, i.e. a 3D unit of the image with a single value, and its size defines the spatial resolution of the image. Medical scanners create regular, rectangular arrays of points (cells) which start at the upper left corner. Each scanner has its own coordinate system called the **IJK coordinate system**, the **image coordinate system** or the **"voxel space"**. There are three orthogonal axes, (i, j, k) (hence the name) that originate from the voxel $(0, 0, 0)$ in the upper left corner: the i axis (index) increases from left to right, the index j from top to bottom and the index k increases into the screen, to another slice. This is illustrated in Figure 3.8 on the right, with a 2D grayscale image that represents a slice of the 3D image with a certain thickness. Every pixel in this 2D slice grayscale image also represents a voxel. Each voxel has an intensity value, usually a 32-bit unsigned integer, although it can also be a floating point value. The values of the voxel array can, as for any array, be selected by indexing. However, the voxel coordinates tell us nothing about where the data came from in terms of position in the scanner. A voxel at a given index triplet (i, j, k) does not tell us whether this voxel position is on the left or right of the brain, or came from the left or right of the scanner [NiBabel 2021], but it does correspond to some real-world physical location (x, y, z) in space.

3.5.2 Scanner native RAS coordinate frame

To get its physical location, we would have to choose what coordinate frame to use. Instead, every scanner defines a more practical, **native coordinate system** that it uses during acquisition, usually related to the physical orientation of the scanner itself and/or the subject within it. For our 3D spatial world, this space is defined by an ordered set of 3 independent axes. Firstly, we can define a set of 3 orthogo-

nal "scanner XYZ" axes with the origin at the magnet isocenter and axes units in millimeters. However, "scanner XYZ" will not tell us about the subject's left and right, but only the scanner's left and right. Therefore, it would be more useful to know the position in terms of the subject's left and right.
To address this problem, most reference spaces use subject-centered scanner coordinate systems. In these systems, the axes are still the same as the scanner axes, but their ordering and direction comes from the position of the subject [NiBabel 2021]. The most common subject-centered scanner coordinate system in neuroimaging is called **"scanner native RAS coordinates"**. The term "RAS" (Right, Anterior, Superior) means that the axes are (in terms of the subject): left to Right; posterior to Anterior; and inferior to Superior, respectively. During acquisition, the relationship between the voxel indices (i, j, k) and the physical location (x, y, z) in the scanner's native RAS coordinate frame is saved in the image's *affine transformation* (see Figure 3.9). The 3D anatomical and 4D diffusion images are saved in the NIfTI (Neuroimaging Informatics Technology Initiative) file format. These files have the extension .nii (or .nii.gz if gzip-compressed), like for example T1.nii, dwi.nii and they can be accessed with different softwares such as MRTrix3, Freesurfer or in Python for example with the NiBabel software package[6]. The affine transform is stored in the header of the NIFTI file and NiBabel can be used to access it. One thing to bear in mind is that NiBabel uses millimeter units, unlike MNE-Python which uses SI units (meters). The affine takes an arbitrary voxel space coordinate (i, j, k) and transforms it to the scanner's native physical space (x, y, z) (in mm), as shown if Figure 3.9. This 3D affine transformation is a sequence of transformations that can consist of a shear, a reflection, a rotation, a scaling, and a translation. It consists of a linear transformation A followed by a translation $\vec{t}$, defined as:

$$\begin{pmatrix} x \\ y \\ z \end{pmatrix} = \begin{pmatrix} a_{11} & a_{12} & a_{13} \\ a_{21} & a_{22} & a_{23} \\ a_{31} & a_{32} & a_{33} \end{pmatrix} \begin{pmatrix} i \\ j \\ k \end{pmatrix} + \begin{pmatrix} t_1 \\ t_2 \\ t_3 \end{pmatrix}$$

The linear transformation matrix A carries the information about space directions and axis scaling, while the translation vector $\vec{t}$ contains information about the geometric position of the first voxel. Conversely, if we have a point (x, y, z) in scanner-native RAS space and we want the corresponding voxel number, we can get it using the inverse of the affine transform.

3.5.3 Freesurfer RAS coordinate frame

NiBabel uses scanner native RAS (x, y, z) coordinates, defined by the original MRI data, i.e. it is subject-centered, and the origin is in a scanner-dependent location. On the other hand, FreeSurfer uses a slightly different coordinate frame: **"MRI Surface RAS"** where MRI images and surface vertex positions are defined. Figure 3.9 depicts 3 coordinate systems: voxel space, NiBabel's scanner native RAS

[6] https://nipy.org/nibabel/

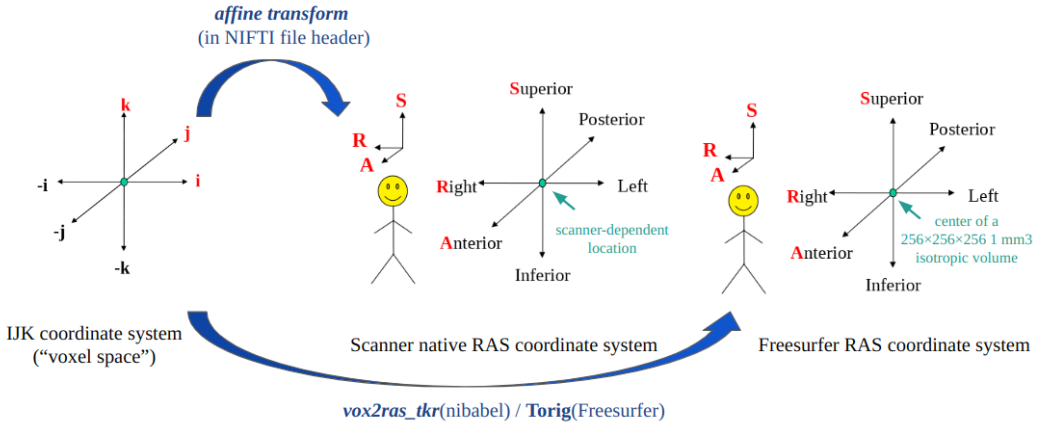

Figure 3.9: Image coordinate system, scanner native c.s. and Freesurfer RAS c.s. with corresponding transforms between them.

and Freesurfer RAS. The origin of the MRI surface RAS coordinate space is at the center of a 256×256×256 1 mm^3 isotropic volume, i.e. its origin is the voxel with volume (IJK) index (128, 128, 128) (in RAS coordinates (0,0,0) mm). One voxel has dimensions 1×1×1 in Freesurfer RAS space and the axes are oriented along the axes of this volume. It is worth mentioning that the RAS coordinate space is *not* centered

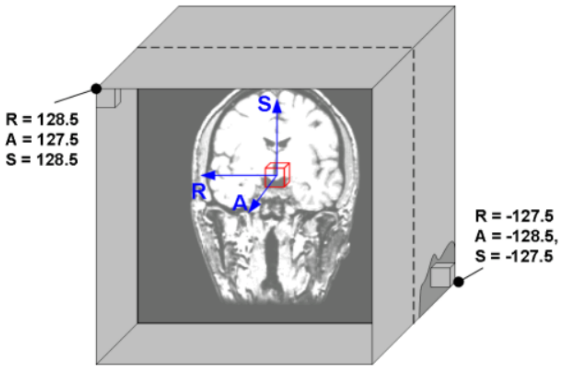

Figure 3.10: Freesurfer's MRI Surface RAS coordinates. Adapted from [Wideman 2003].

in the overall MRI volume i.e. this center may not correspond to the anatomical center of the subject's head [Wideman 2003]. In MNE-Python, it is called the "MRI coordinate frame". The transformation from voxels to the FreeSurfer MRI surface RAS coordinate frame is known in the FreeSurfer documentation as *Torig*, and in NiBabel as *vox2ras_ tkr*.[7] This transformation sets the center of voxel coordinate frame in the middle of the conformed volume i.e. to Freesurfer RAS coordinates (see Figure 3.9). Since MNE-Python uses FreeSurfer extensively for surface computations (e.g., inner/outer skull meshes, white matter surface), the BEM surfaces

[7] https://mne.tools/dev/overview/implementation.html#coordinate-systems

and the source space locations (in the .fif files) are expressed Freeurfer surface RAS coordinate system (not the NiBabel scanner native RAS). The source space vertices are the vertices on the white matter surface mesh.
Diffusion streamlines can be loaded with NiBabel, in NiBabel's scanner native RAS coordinate system. When Freesurfer surface mesh vertices are loaded with NiBabel, the file contains metadata which indicates the shift from NiBabel's scanner RAS to Freesurfer RAS coordinate system. This alignment between the streamline endpoints and the sources in the source space was visually verified, as illustrated in Figure 3.11, with axes in mm. In Figure 3.12, we can see the intersection of 3

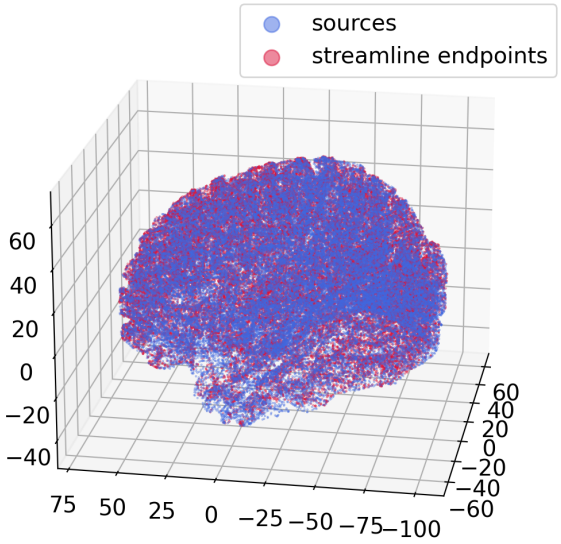

Figure 3.11: Alignment of source space dipoles with streamline endpoints

anatomical planes: saggital, coronal and axial and the view for each of them for one slice. When it comes to M/EEG source imaging, apart from the "MRI Surface RAS coordinate system" we just defined, there are two more coordinate frames that should be aligned: the "MEG device coordinate frame" and the "head coordinate frame". They can be aligned with two 3D transformation matrices which specify how to rotate and translate points from one coordinate system to their equivalent locations in another one.

3.5.4 The head coordinate frame

The head coordinate frame is defined with the help of anatomical reference points called fiducial landmarks, on the subject's head: the nasion (NAS), and left and right preauricular points (LPA and RPA). This coordinate frame is shown in Figure 3.13 on the left, with fiducial points NAS (green), LPA (red) and RPA (blue). The origin is at the intersection between a line connecting the LPA and RPA and the line orthogonal to LPA-RPA that passes through the naison. It is in RAS orientation, meaning that

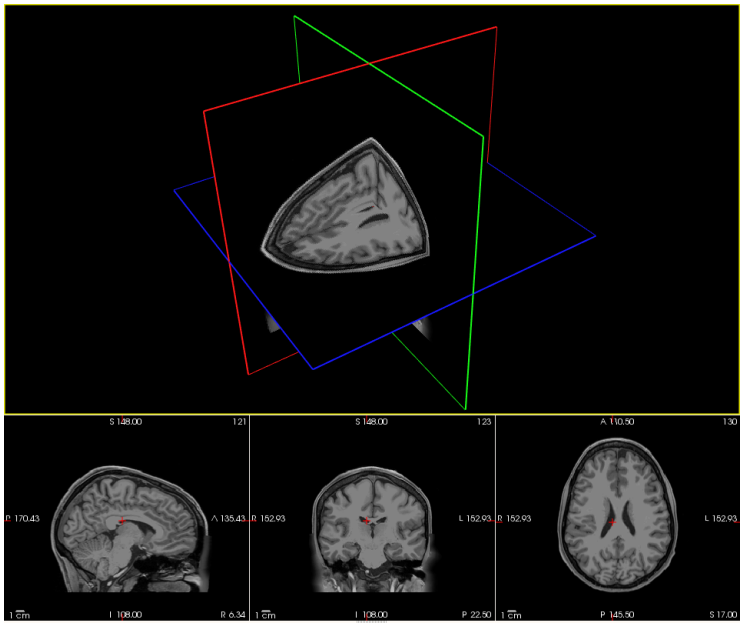

Figure 3.12: Up: intersection of anatomical planes. Down (from left to right): saggital, coronal and axial view of slice with volume index (127,127,128), corresponding to the spatial position (0.0, 0.0, 0.0) mm in Freesurfer surface RAS (which is (0.00, -17.50, 20.0) mm in NiBabel's scanner RAS). Recall that Freesurfer surface mesh file contains metadata which indicates this shift between Freesurfer RAS and NiBabel's scanner RAS.

- the X-axis goes toward the RPA
- the Y-axis goes toward the NAS
- the Z-axis is orthogonal to X and Y, pointing upward to the head vertex.

Head digitization data acquired in the beginning of a MEG acquisition are expressed in these coordinates. In MNE-Python, this is the "Neuromag" head coordinate frame. The required 3D coordinates for defining this coordinate frame (NAS, LPA, RPA) are measured at a stage separate from the MEG data recording. There are numerous devices that can perform such measurements, usually called "digitizers". As mentioned before, in the case of HCP data, head digitization was done with a Polhemus 3SpaceFasttrak system.

3.5.5 The MEG device coordinate frame

This coordinate frame is related to the MEG device and it is defined by the MEG manufacturer. The coordinate system of HCP MEG data is BTi/4D Neuroimaging, expressed in meters [Oostenveld 2021]. It is illustrated in Figure 3.13 on the right. The origin is exactly between LPA and RPA while the principal axes go through fiducials as:

- the X-axis goes towards NAS
- the Y-axis goes towards LPA, orthogonal to X
- the Z-axis orthogonal to X and Y, going upwards.

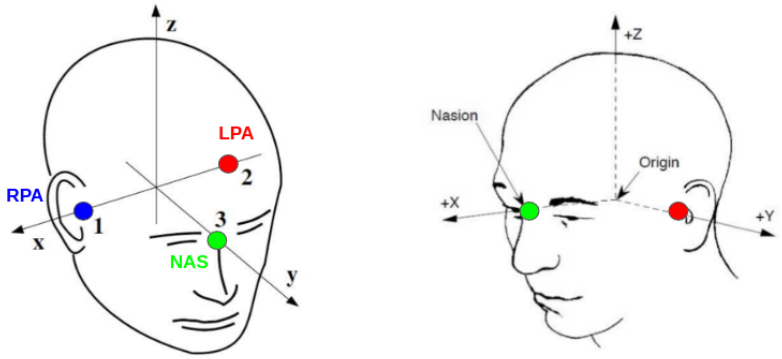

Figure 3.13: Left: The "Head" coordinate frame in MNE with fiducial points. Right: The BTi/4D coordinate system. Adapted from *https://www.fieldtriptoolbox.org/*

Finally, the co-registration of the MEG sensors with the BEM surfaces (skin and inner skull) and the source space (with fiducial points) is shown in Figure 3.14 in the "head" coordinate frame.

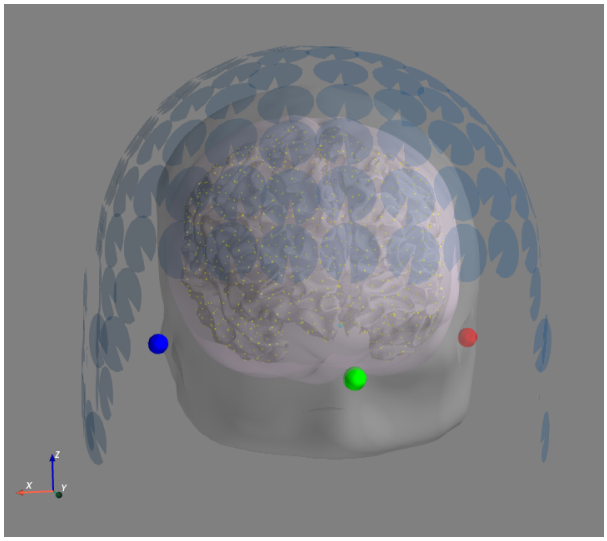

Figure 3.14: Alignment of MEG sensors with BEM surfaces and the source space.

3.6 Structural Connectivity Mapping

Starting from cortical surface extraction, parcellation and lead field computation, to simulating and recovering the brain activity, we had to integrate 3 spatial scales of the brain's surface representation (ordered from finest to coarsest):

- vertices of the high resolution mesh (cardinality: $V \sim 300,000$)
- sources (cardinality: $S = 8196$)
- regions (cardinality: $R = 68$)

To start, we needed to make correspondences between them, as well as to map them with the underlying streamlines. Representation in the form of vertices is created by the FreeSurfer upon generation of cortical surfaces, as explained in Section 3.2. Such representation is too fine for reconstruction of cortical activity [Baillet *et al.* 2001]. Hence, a source space is created with 8196 dipoles (sources), each representing a 5mm×5 mm patch of the cortical surface (a.k.a the "low resolution mesh").
The mapping between high and low resolution meshes is contained as an attribute in MNE-Python's source space file. For each vertex of the high resolution mesh and therefore each source, the corresponding label from Desikan-Killiany atlas is known given the atlas [Desikan *et al.* 2006] and it can be loaded in MNE-Python. The average number of vertices in a source is 36, while the average number of sources in a region is 112. Therefore, now we have the surface points on 3 spatial scales (vertices, soruces, regions) and correspondences between them.
Next step is to map the cortical surface (at source and region scale) to the underlying streamlines. Due to the large size of the connectivity matrices in the source space ($S \times S$), all illustrations are shown in region space (of size ($R \times R$)) for visual clarity. To represent the long-range structural connectivity, we start by making a *streamline count matrix in the source space*, by mapping the streamline endpoints to sources (see Figure 3.11). We did this by performing a radial search from each streamline endpoint to locate the nearest source on the white matter surface, with the maximum acceptable distance (radius) of 10 mm. If no source was found within this radius, the streamline endpoint was not assigned to any source and that streamline was discarded. We were interested in the *presence* or *absence* of a structural connection, so we binarized this matrix by assigning a value of 1 to all sources linked with 1 or more streamlines. This binarized matrix is our **structural connectivity matrix in the source space**.
Next, we wanted to map the regions to streamlines. Given the mapping from sources to streamlines and the Desikan label we know for of each source, we built a *streamline count matrix in the region space* by counting the number of streamlines appearing between each region pair (See Figure 3.15 on the left). However, the spatial scale is now much coarser. Therefore, we set a threshold of 10 % of the average number of streamlines to consider a pair of regions connected. This yields a **structural connectivity matrix in the region space** (See Figure 3.15 on the right). This threshold is chosen to be similar to the literature [Mårtensson *et al.* 2018] and in our work its value corresponds to ∼10 streamlines, depending on the subject. Quantifying the connectivity strength will be discussed in more details in Chapter 4. Although it was out of the scope of this thesis, it would be interesting and useful to address in future work.
For every streamline f connecting a pair of cortical sources, assuming a constant information transmission speed across the brain, we can calculate the transmission delay between them as

$$\Delta_f = \frac{l_f}{v} \tag{3.1}$$

where l_f is the streamline length in meters, v is the information transmission speed

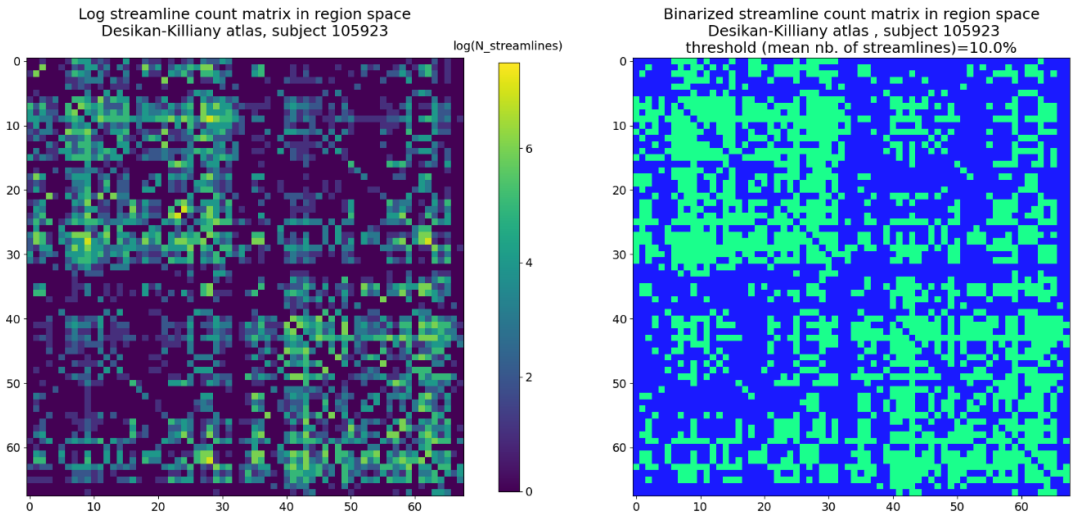

Figure 3.15: Structural connectivity matrices in region space, subject 105923. Left: streamline count matrix on log scale for better visualization. Right: binarized streamline count matrix. Larger number of nonzero values exist between the regions in the ipsilateral hemisphere compared to the contralateral.

in m/s. The unit of this delay is in seconds, so for a signal sampling frequency F_s, the delay in time samples can be obtained as $F_s \cdot \Delta_f$. Tract lengths can be calculated after the streamline reconstruction using diffusion tractography, as the sum of the Eucledian distances between consecutive streamline points. The histogram of their lengths is shown in Figure 3.16.

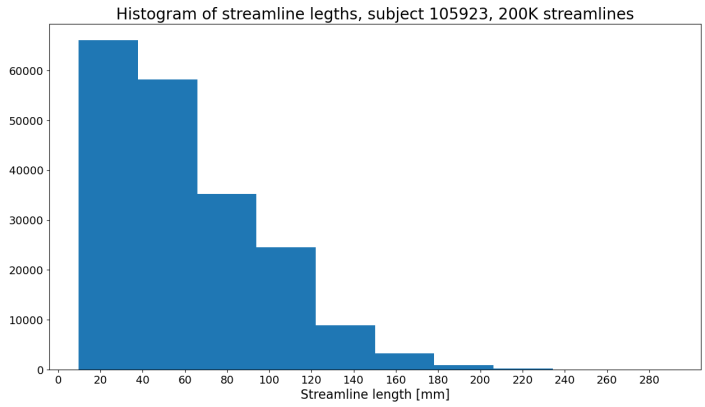

Figure 3.16: Histogram of streamline lengths, subject 105923.

Axon conduction velocity, on the other hand, is affected by the axon diameter and myelin thickness [Innocenti *et al.* 2014, Horowitz *et al.* 2015, Drakesmith *et al.* 2019]. Diffusion microstructure techniques can give us an estimate of axonal density and axon diameter. It was recently demonstrated by [Drakesmith *et al.* 2019] through

simulated diffusion and relaxometry MRI data that the proportionality between fiber diameter and conduction velocity is $6.67ms^{-1}/\mu m$. In accordance to these findings, as well as previous works of [Fukushima *et al.* 2015] and [Deslauriers-Gauthier *et al.* 2019], information transmission speed is assumed to be constant across brain and equal to 6 m/s.

Given the length of each streamline and their mapping to the sources, we can construct a *length connectivity matrix in the source space*. With the length connectivity matrix and the information transmission velocity, we can construct a symmetric **delay matrix** $\boldsymbol{\mathcal{D}} \in \mathbb{R}^{S\times S}$ containing the information about delays between source pairs, with entries

$$\delta_{ij} = \delta_{ji} = \begin{cases} \frac{1}{NF_{ij}} \sum_{k=1}^{NF_{ij}} \Delta_{f_k}, & \text{if source } i \text{ and } j \text{ share } NF_{ij} \text{ streamlines} \\ 0, & \text{otherwise.} \end{cases} \tag{3.2}$$

Distribution of delays naturally follows the distribution of streamline lengths, so for the lengths ranging from 10 to 290 mm, the delays span from 1.61 ms to 49.81 ms. The average delay found across 10 subjects is 9.32 ms. These values comply with other studies, such as [Caminiti *et al.* 2013] where the authors estimated the delays non-invasively also from diffusion tractography and found that the mean conduction delay at axons in the corpus callosum midline was 6-7 ms for humans. Recent findings exist from intrasurgical studies [Filipiak *et al.* 2021] where transmission delays measures were based on propagation of Cortico-Cortical Evoked Potentials (CCEPs), induced with intrasurgical direct electrical stimulation and recorded with Electrocorticography (ECoG) electrodes during craniotomy. They showed that, in most of the cases, CCEPs emerged 20–40 ms after the stimulation onset and propagated 10–60 mm away from the stimulation sites. Other examples exist mostly in histological animal studies such as [Innocenti *et al.* 2014, Battaglia-Mayer *et al.* 2015], in which the expected delay from parietal cortex (PE) to cingulate region (Brodmann area 24) is at the order of 3.5 ms in macaque monkeys.

Initially, delay matrix in region space was used for simulation of source-level brain activity, where the delay between a pair of regions is taken as the *average* delay between connected sources that comprise them. However, we noticed a non-negligible variability in inter-source delays connecting a region pair, so assigning a single time lag with such averaging could lead to information loss. As a consequence, the delay matrix in source space was used the remaining of this work. For the sake of visualization, we show an example of a region-based delay matrix in Figure 3.17. Note that the colorbar indicates the maximal (averaged) inter-region delay of 15 time samples i.e. 30 ms (for $F_s = 500$ Hz), while the maximal inter-source delay found is 49.81 ms.

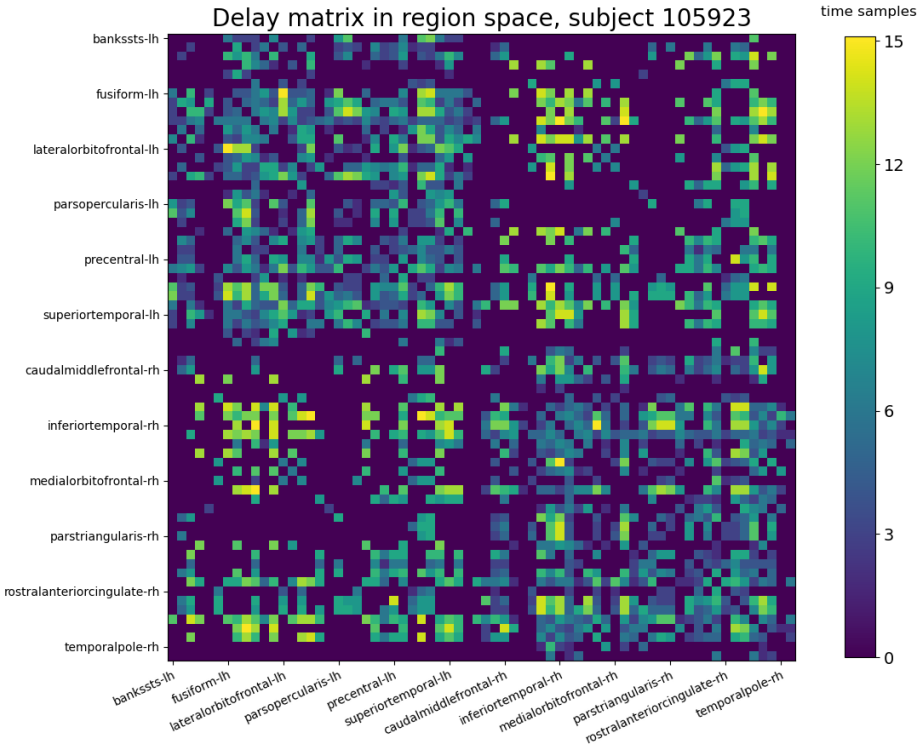

Figure 3.17: Delay matrix in region space, for subject 105923. The names of every 6^{th} region are shown for visual clarity instead of all 68.

3.7 Simulation of Cortical Activity

Since the ground truth of source-level brain activity is unknown, simulations are needed in order to validate the accuracy of the proposed reconstruction methods. Numerous neurophysiological and neuroimaging studies have shown that cortical activation is a distributed spatiotemporal dynamic process [Nunez *et al.* 2006, Fox & Raichle 2007, Jirsa *et al.* 2002]. When it comes to specific tasks, it has been shown that during their execution, the spatial distribution of spectral power varies in a task-relevant manner [Chang *et al.* 2011, Buzsáki *et al.* 2012]. The focus of our work has been to investigate the patterns of brain activity during a specific task, like the sensory-motor task provided by the HCP.

3.7.1 Related work

Several platforms for brain activity simulations exist in the literature, such as Brainstorm [Tadel *et al.* 2011], BESA Simulator[8], The Virtual Brain (TVB) [Sanz Leon *et al.* 2013]. The only simulator allowing to incorporate the long-range anatomical connectivity is TVB, a framework for the simulation of dynamics of large-scale brain

[8]https://www.besa.de/

networks at a mesoscopic scale, with biologically realistic connectivity. It allows generation of time courses of various forms of neural activity, such as Local Field Potentials (LFP) and firing rate, as well as brain imaging data such as M/EEG and BOLD activations observed in fMRI. The main interest in TVB lies in using mesoscopic laws governing the behaviour of neural populations and unveiling the laws driving the processes on a macroscopic brain network scale. At its core, it deploys neural field modelling (or network of neural masses) where each node represents a neural population model. Neural mass models are lumped representations of the dynamics of a set of similar neurons via common variable (e.g. mean firing rate and mean postsynaptic potential). They can be described by non-linear dynamic systems via differential equations and TVB deploys some of the mesoscopic models from the literature such as Wilson-Cowan model [Wilson & Cowan 1972], Wong-Wang model [Wong & Wang 2006] etc. Neural field equations describe the spatiotemporal evolution of coarse grained variables such as synaptic voltage or firing rate activity in neuronal populations. Intrinsic and extrinsic coupling parameters within and between neuronal populations can be defined, as well as local connectivity kernels representing short-range intra-cortical connections. Despite their sophistication, this leads to complex models that are not easily tractable due to their non-linearity and dependency on a large number of parameters. For this reason, we opted to simulate the brain activity with a more simple and tractable model as described below.

3.7.2 MAR model of cortical activity

In order to model the cortical activity which would account for anatomical connections in both space and time, the use of multivariate autoregressive (MAR) models has been proposed in several publications in the context of the inverse problem, as a way to constrain the sources' dynamics. In [Lamus *et al.* 2012] the neuronal currents at a given point in time and space are a function of past neuronal currents within a small local neighborhood along the cortical surface. The authors in [Fukushima *et al.* 2015] and [Belaoucha & Papadopoulo 2020] constrained the elements of the MAR model by anatomical connections obtained from dMRI.
We define the activity of S sources to be a function of both its local and long-range connections as the following MAR model:

$$\boldsymbol{j}_t = \sum_{i=1}^{p} \boldsymbol{C}_i \boldsymbol{j}_{t-i} + \boldsymbol{\nu}_t \tag{3.3}$$

where $\boldsymbol{j}_t \in \mathbb{R}^S$ is the amplitude of all sources at time t, p is the order of the MAR model, $\boldsymbol{C}_i \in \mathbb{R}^{S \times S}$ are the coefficient matrices and $\boldsymbol{\nu}_t \in \mathbb{R}^S$ is the input term. The order of the MAR model p is chosen to be equal to the maximum delay found in the streamlines, measured in number of time samples

$$p = \max(\Delta_f) \tag{3.4}$$

where $f = 1, ...N_f$ with N_f number of streamlines. As a reminder, the information transmission speed is assumed to be constant across brain and equal to 6 m/s, which

would correspond to an average axon diameter of 1 μm. Sampling frequency of 500 Hz yields time samples of 2 ms. To produce a realistic source activity time course [Robinson *et al.* 2006, Brookings *et al.* 2009] which would resemble a somatosensory evoked response potential (ERP), the waveform of the initial input activity is chosen to be a damped sinusoid in the form

$$\boldsymbol{\nu}(t) = ae^{-\beta(t-\varphi)^2} sin(2\pi ft) \tag{3.5}$$

for $t > 0$, and $\nu(t) = 0$ for $t < 0$ (See Figure 3.18 at the bottom for an illustration). The amplitude a is set to be 10 nA-m, consistent with empirical observations and invasive studies [Baillet *et al.* 2001], which is a net current expected to be yielded by a 5mm x 5mm patch (given the thickness of the cortex of 4 mm). The positive constant $\beta = \frac{1}{2\sigma^2}$ is the rate of decay, where σ is the standard deviation of the Gaussian, φ is the Gaussian latency and f is the sine wave oscillating frequency. Frequency content of ERPs is $\approx 2-40Hz$ and consists of oscillations which die away within $500ms$ [Brookings *et al.* 2009]. This waveform type is also consistent with the with previous works in the field [Baillet & Garnero 1997, Fukushima *et al.* 2015, Belaoucha & Papadopoulo 2017]. The following parameter values were taken: $\sigma = 6$, $\varphi = 20ms$, $f = 20Hz$.

MAR coefficient matrices represent the source interactions across brain areas. Each coefficient matrix $\boldsymbol{C}_i \in \mathbb{R}^{S\times S}$ corresponds to a delay of i, where $i = 1, ...p$, and defines the contribution of *all* sources at time $t - i$ to *all* sources at time t, i.e. it relates sources' current values to its past ones. Normally, these matrices are unknown and need to be estimated from the data. Here, on the other hand, they are constructed according to delays found in the streamlines, so the positions of nonzero coefficients are set according to the prior anatomical knowledge. Since a single time lag is assigned to each pair of anatomically connected sources, most entries of $\boldsymbol{C}_i$ matrices are zero. Any MAR i.e. VAR(p) process can be written as a first order model, in the VAR(1) form. If $\boldsymbol{j}_t$ is a VAR(p) process as in (3.3), a corresponding $Sp-$dimensional VAR(1) can be written as:

$$\tilde{\boldsymbol{J}}_t = \tilde{\boldsymbol{C}}\tilde{\boldsymbol{J}}_{t-1} + \widetilde{\boldsymbol{\mathcal{V}}}_t. \tag{3.6}$$

In other words, $\tilde{\boldsymbol{J}}_t = (\boldsymbol{j}_t, \boldsymbol{j}_{t-1}, ..., \boldsymbol{j}_{t-p+1})^T \in \mathbb{R}^{Sp}$ is a dynamic source model of all current sources over the whole brain. The input term is denoted as $\widetilde{\boldsymbol{\mathcal{V}}}_t = (\boldsymbol{\nu}_t, \mathbf{0}, \mathbf{0}, ..., \mathbf{0})^T \in \mathbb{R}^{Sp}$. The additional noise term could be added as $\tilde{\boldsymbol{\omega}}_t = (\boldsymbol{\omega}_t, \mathbf{0}, \mathbf{0}, ..., \mathbf{0})^T \in \mathbb{R}^{Sp}$ However, we decided to exclude the noise in source space since we corrupted the measurements with realistic subject noise in sensor space, as explained in Section 3.4.0.2. Creating noiseless source time courses and adding noise in the sensor space also complied with the simulations from the literature [Baillet & Garnero 1997, Grova *et al.* 2006, Lamus *et al.* 2012]. Augmented coefficient matrix (also called the companion matrix) $\tilde{\boldsymbol{C}} \in \mathbb{R}^{Sp\times Sp}$ is given by

$$\tilde{\boldsymbol{C}} = \begin{bmatrix} \boldsymbol{C}_1 & \dots & \boldsymbol{C}_{p-1} & \boldsymbol{C}_p \\ \boldsymbol{I}_S & \dots & \boldsymbol{0} & \boldsymbol{0} \\ \boldsymbol{0} & \dots & \boldsymbol{0} & \boldsymbol{0} \\ \vdots & \dots & \vdots & \vdots \\ \boldsymbol{0} & \dots & \boldsymbol{I}_S & \boldsymbol{0} \end{bmatrix}$$

Using the Z-transform, the reverse characteristic matrix of a MAR model [Lütkepohl 2005] can be written as:

$$C(z) = I - \sum_{i=1}^{p} C_i z^i \tag{3.7}$$

MAR process $\tilde{\boldsymbol{J}}_t$ is stable if the following stability condition is met:

$$\det(\boldsymbol{I}_S - \boldsymbol{C}_1 z - ... - \boldsymbol{C}_p z) \neq 0 \quad \text{for } |z| \leq 1 \tag{3.8}$$

$$\det(\boldsymbol{I}_{Sp} - \tilde{\boldsymbol{C}} z) \neq 0 \quad \text{for } |z| \leq 1 \tag{3.9}$$

meaning that the absolute values of all eigenvalues λ_k have to satisfy

$$|\lambda_k| \leq 1 \tag{3.10}$$

i.e. that they lie within the unit circle [Lütkepohl 2005, Zivot & Wang 2006], implying that damping time is positive and bounded. Conversely, when $|\lambda_k| > 1$, the process is unstable and signal magnitudes grow exponentially, while when $|\lambda_k| = 1$ it results in an oscillating behaviour. Nonzero elements in all coefficient matrices are set as hyperparameter α, which represent the "strength" of the source interactions. This value is chosen manually ($\alpha = 1$) so, in theory, we would have to test the stability of $\tilde{\boldsymbol{J}}_t$ by checking if the maximal eigenvalue $|\lambda_{max}|$ of $\tilde{\boldsymbol{C}}$ satisfies 3.10. However, in practise, the size of $\tilde{\boldsymbol{C}}$ is very large ($Sp \times Sp$, where $S = 8196$ and p can go up to 24), making this check computationally demanding. Rather, we constructed a stable MAR process, which excludes recurrent activity (resulting in asymmetric C_i matrices) and in addition, in the implementation we re-initialized the companion matrix for activity propagation between each region pair. Overall, when the activity is spread from one region to another, the amplitudes remain the same. Initially, the simulations were preformed with a delay threshold of $\Delta_{max} = 7$ due to memory limitations (the size of the companion matrix was too big). Therefore, only the streamlines whose length would yield a delay of 7 time samples (14 ms) were considered. This limitation was later leveraged and *all* delays were included, by changing the implementation to be able to handle sparse matrices, by using a module of SciPy, *scipy.sparse*[9].

[9] https://docs.scipy.org/doc/scipy/reference/sparse.html

3.7.3 Propagation of activity as a graph path

The brain can be modelled as a directed graph where its nodes are the current sources (or regions) and edges long-range connections between them. As mentioned in the beginning of this section, we wanted to simulate task-related brain activity. Following the assumption that only a few regions are typically significantly activated during a specific cognitive task, the brain activity is simulated for 5 chosen subnetworks as a graph path with different lengths, where the number of active regions (visited graph nodes) varied from 2 to 5. Such graphs are also called Directed Acyclic Graphs in graph theory. The activity is propagated between sources that share a long-range connection, with an appropriate delay. We start by constructing a dataset called *multiple focal sources* in which only the sources in the active region that have a long-range connection in the next active region were assigned the input activity $\nu(t)$. Since each of S sources in the source space represents a small portion of the cortical surface, it is reasonable that the neighboring sources will have similar intensities. Therefore, the activity of multiple focal sources was also spread to its adjacent neighbours, and we denote this data set as **multiple spread sources** (**MSS**) which will be used for reconstruction of brain activity. For each active source, the waveform resembling a somatosensory ERP was propagated to one of the sources it is connected to via streamlines in the following region, with an appropriate delay. Let us denote the region that is the driver of activity as the "origin node" (n_{origin}) and the region to which its activity is transmitted as the "target node" (n_{target}). The term "origin" in this context is related to the graph terminology, to designate a directed edge that goes out of the origin node and terminates in the target node. Since this propagation is directed, for every edge ("jump") $n_{origin} \rightarrow n_{target}$, nonzero elements in C_i matrices will appear in positions (n_{target}, n_{origin}).

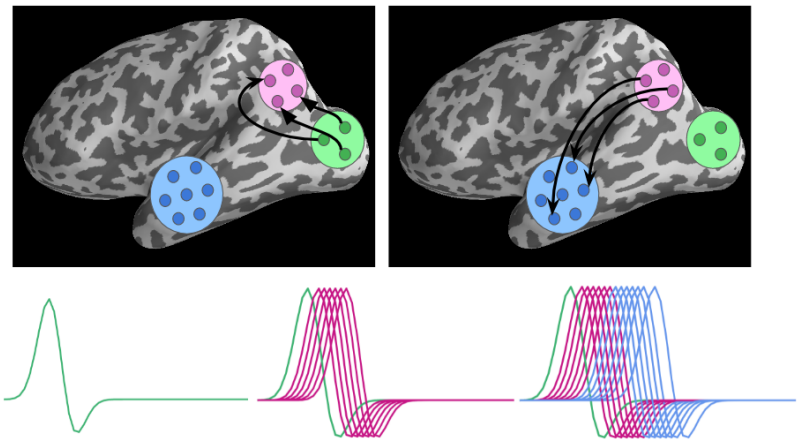

Figure 3.18: Illustration of simulated activity propagation, subnetwork 1 (MSS_01). Note that the number of pairs of connected indicated with black arrows is smaller than what we see in the signals below, just for visual clarity. Also note that different arrow lengths illustrate different streamline lengths, resulting in *multiple delays* that can appear between a region pair.

As an example, imagine having 6 nodes $[n_0, ...n_5]$ and the path length (number of jumps) of 2. For the following walk $n_0 \rightarrow n_5 \rightarrow n_2$, nonzero elements would appear at positions $(n_5, n_0), (n_2, n_5)$. Note that, even though a subset of active regions is chosen, each region edge actually comprises of *all* inter-source edges between the connected region pair, resulting in multiple delays. To make this more clearly, in Figure 3.18 we illustrate this activity propagation for 1 subnetwork with 3 active regions. This activity is also illustrated in Figure 3.20 on the top left, along with simulated source time courses of another subnetwork, on the top right. In the first subnetwork (MSS_01), the activity was propagated starting from the lateral occipital lobule in the left hemisphere, spreading to the inferior parietal lobule and finally to the middle temporal gyrus, in the ipsilateral hemisphere. This activity propagation for 3 time instants is illustrated on the brain in Figure 3.19. As a reminder, the

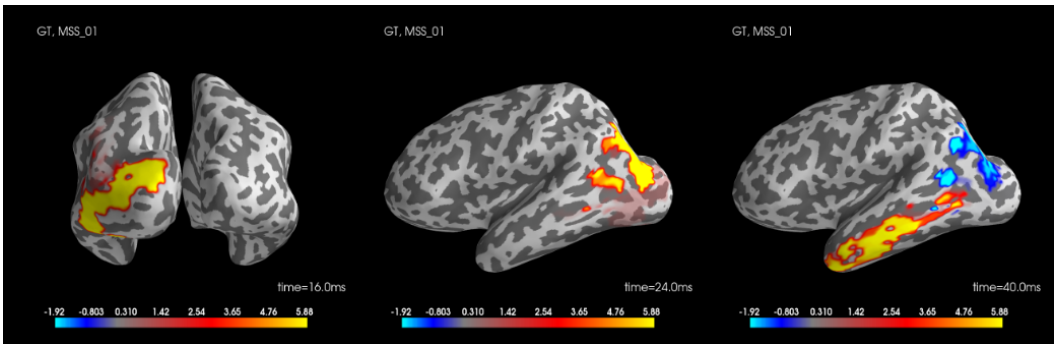

Figure 3.19: Simulated source-level brain activity for MSS_01, for 3 time instants. "GT" refers to the "Ground Truth".

relationship between source amplitudes and M/EEG measurements is expressed by the linear model $\boldsymbol{M} = \boldsymbol{GJ} + \boldsymbol{E}$, where $\boldsymbol{M} \in \mathbb{R}^{N \times T}$ is a matrix of measurements, for N sensors and T time samples, $\boldsymbol{J}$ is the matrix of source amplitudes, $\boldsymbol{G}$ is the forward operator and $\boldsymbol{E} \in \mathbb{R}^{N \times T}$ is the unscaled noise in sensor space. The physiological noise was preprocessed and epoched from the raw (patient) noise MEG data as explained in Section 3.4.0.2. This preprocessed noise was then rescaled to obtain the noise-corrupted measurements for 2 different SNR levels, 3 and 10. The measurements corrupted with noise for the chosen SNR level X become

$$\boldsymbol{M}_{SNR_X} = \boldsymbol{GJ} + \boldsymbol{E}_{SNR_X}, \text{ where } X \in \{3, 10\}. \tag{3.11}$$

The SNR is defined as the variance of the signal divided by the variance of the noise, so SNR_X can be computed as

$$SNR_X = \frac{Var(\boldsymbol{GJ})}{Var(\boldsymbol{E}_{SNR_X})}. \tag{3.12}$$

To obtain the noise for the chosen SNR level, we can rescale the noise as

$$\boldsymbol{E}_{SNR_X} = \beta_{SNR_X} \boldsymbol{E} \tag{3.13}$$

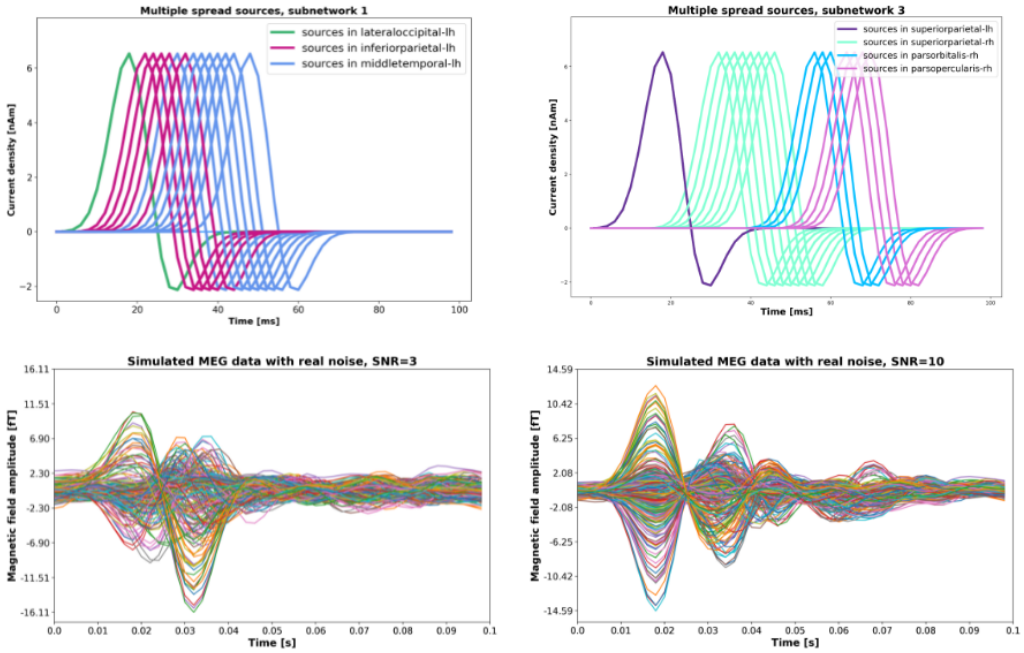

Figure 3.20: Top: simulated source time courses for 2 different subnetworks. Bottom: their corresponding MEG measurements with realistic noise. Left: MSS_01; right: MSS_02. As an example, in MSS_01, we see that all sources in left lateral occipital region get active simultaneously. Then, when their activity is spread to the next active region (left inferior parietal), a phase differences between the sources in that region appear, resulting from different inter-source delays between that region pair.

with some scaling coefficient β that depends on the SNR. We can compute the value of this coefficient as following

$$
\begin{aligned}
Var(\boldsymbol{E}_{SNR_X}) &= \frac{Var(\boldsymbol{GJ})}{SNR_X} \\
Var(\boldsymbol{E}_{SNR_X}) &= Var(\beta_{SNR_X}\boldsymbol{E}) = \beta^2_{SNR_X} Var(\boldsymbol{E}) \\
\Rightarrow \beta_{SNR_X} &= \sqrt{\frac{Var(\boldsymbol{E}_{SNR_X})}{Var(\boldsymbol{E})}} = \sqrt{\frac{Var(\boldsymbol{GJ})}{SNR_X Var(\boldsymbol{E})}}.
\end{aligned}
$$

Therefore, for each simulation we had two measurement matrices, namely $\boldsymbol{M}_{SNR_3}$ and $\boldsymbol{M}_{SNR_{10}}$, shown in Figure 3.20 on the bottom. On the top, we show the simulated source time courses. Note that the amplitude of MEG data is in femto Teslas [fT]. We will note the simulated activity as the "ground truth" (GT) and the methods for its reconstruction are described in the sections that follows. Simulations were implemented in MNE-Python and the author of this manuscript was one of the contributors to the simulation module of this package[10].

[10] https://mne.tools/stable/index.html

3.8 Conclusion

In this Chapter, we presented the multimodal preprocessing pipeling used to integrate structural MRI, diffusion MRI and MEG data into the same framework. Firstly, in Section 3.1, we explained in more details the extraction of the cortical surface meshes, the source space and the brain parcellation into different regions with the Desikan-Killiany atlas. Secondly, in Section 3.2 we described the realistic head conduction model and how the lead field matrix (i.e. the MEG forward solution) was computed. Thirdly, in Sections 3.3 and 3.4 we mentioned how diffusion MRI data and MEG data were processed and how they were used for the remaining of the thesis. In addition, in Section 3.5 we depicted the 5 different coordinate systems in which the used data were were acquired and expressed and the different transforms that bring the data from one system to another. Further, in Section 3.6 we described the 3 spatial scales used to represent the brain's surface, how they were mapped to the underlying streamlines representing white matter fiber bundles and how the structural connectivity matrix and the delay matrix were computed. Lastly, in Section 3.7, we described the simulation of source-level brain activity that was used as a synthetic dataset to validate the reconstruction approaches that will be presented in Chapter 4 and 5.

Chapter 4

Connectivity-informed M/EEG inverse problem

Contents

Overview

Human brains process information incredibly quickly. Yet, the transfer of information between the brain regions is carried out through white matter fibers whose physical properties introduce communication **delays**. These delays are on a millisecond scale, and the only non-invasive functional brain imaging modalities that have the temporal resolution sufficient to track them are MEG and EEG.
In this Chapter, we first highlight the importance of including the delays in the M/EEG inverse problem. Then we mention some of the current methods used for the choice of regularization parameters. Moreover, we describe the evaluation error metrics used for evaluation of different reconstruction methods. Basic concepts in graph theory are described, as well as the role of the Laplacian operator as a smoothness constraint in inverse problems. We propose Connectivity-Informed M/EEG

Inverse Problem (CIMIP) to solve the M/EEG inverse problem, where prior transmission delays supported by dMRI are included to enforce temporal smoothness. In addition, we show 3 different variations of the CIMIP regularization matrix and the assumptions behind them. Furthermore, we show results for simulated and real data and compare with 3 different state-of-the-art approaches. Lastly, we highlight the limitations and open questions regarding the proposed approach. Part of the work from this Chapter was presented at international conferences GRAIL 2020. [Kojčić *et al.* 2020] and ISBI 2021. [Kojčić *et al.* 2021].

4.1 Including delays into the M/EEG inverse problem

Long-range anatomical connections obtained with dMRI tractography can give us an insight on interaction delays of the macroscopic brain network; their estimation was explained in Section 3.6. With regard to regularizing the dynamics of M/EEG, transmission delays are almost always neglected (except, as discussed in Section 2.3.5, in the works of [Fukushima *et al.* 2015, Belaoucha & Papadopoulo 2020, Belaoucha *et al.* 2015, Deslauriers-Gauthier *et al.* 2019, Deslauriers-Gauthier *et al.* 2020]). Recall that action potentials represent the most basic form of neuronal communication [Hodgkin & Huxley 1952]. They propagate with a finite velocity, leading to the unavoidable fact that transmission cannot be instantaneous.

The timing of communication between different brain regions has an impact on different functions [Battaglia-Mayer *et al.* 2015]. Estimation of parieto-frontal transmission delays using light and electron microscopy has been done in monkeys [Innocenti *et al.* 2014] to characterize the axon diameter, speed, and the length of parietal axons terminating in different frontal areas. Another study of parieto-frontal interactions, namely on the communication timing between parietal and frontal areas (also in monkeys) is offered by [Battaglia-Mayer *et al.* 2015]. They provide new insights on the sensorimotor cortical delays associated to different functions, such as eye–hand coordination and online control of hand movement. Fewer studies are done on humans due to the necessity of an invasive procedure. As we mentioned in Chapter 3, intrasurgical studies [Filipiak *et al.* 2021] measured transmission delays based on propagation of Cortico-Cortical Evoked Potentials (CCEP), induced with intrasurgical direct electrical stimulation and recorded with ECoG electrodes in vivo during craniotomy. In most of the cases, CCEPs emerged 20–40 ms after the stimulation onset, which again highlights the importance of accounting for transmission delays.

The limit of propagation speed of action potentials in the brain connectome has been exploited by [Le Bihan 2020], where the author sheds light on the fact that "simultaniety" across the brain nodes is only relative. He brings up a new concept–uniting the space and time in the brain through a combined "spacetime", by drawing a parallel with the spacetime of the Universe we live in. Concepts from theories of special and general relativity are applied in a framework that melds brain's spatial organisation with time, giving a 4-dimensional (4D) *spacetime*, shaped by the ac-

tivity of brain nodes. Since Special Relativity theory [Einstein 1905b] has put and end to the concept of *absolute time*, [Le Bihan 2020] argues that there is also no absolute time in our brain. The 4D spacetime complies with relativistic principles and presents a functional curvature generated by brain activity, similarly as gravitational masses give our 4D Universe spacetime its curvature. The author proposes a coherent physical and biological system at global level, aiming to merge gray matter activity and white matter transmission into a unique framework to describe how neural activity flows within the brain. Although this framework is rather outside the scope of this thesis, it emphasizes the importance of *transmission delays* and how they should not be omitted from functional and effective connectivity studies, brain function modeling and other related studies.

4.2 Selection of Regularization Parameters

When it comes to recovering electrical activity of the brain from M/EEG data, let us recall briefly the regularized least squares methods we described in Section 2.3. We mentioned that if a matrix has some singular values close to 0, the inversion becomes highly unstable and that a remedy to this issue is to add regularization. We mentioned that the regularization parameter $\lambda \in \mathbb{R}^+$ represents the relative contribution between the data fitting term and the penalty term in Eq. (2.7), i.e. it is a trade-off between the two. Its choice plays an important role since it can greatly influence the source reconstruction accuracy. There exist several approaches to estimate it, such as (1) the L-curve method [Hansen 1992, Hansen & O'Leary 1993, Hansen 1999], (2) Generalized Cross Validation (GCV) [Golub *et al.* 1979], (3) Composite REsidual and Smoothing Operator (CRESO) [Franzone *et al.* 1985], (4) the discrepancy principle [Morozov 2012]. The L-curve and GCV remain the most popular ones and will be discussed below. A brief reminder that the solution obtained with l_2-norm regularization is in the form

$$\hat{\boldsymbol{J}} = \arg\min_{\boldsymbol{J}} \left\{ \|\boldsymbol{M} - \boldsymbol{G}\boldsymbol{J}\|_2^2 + \lambda \|\boldsymbol{W}\boldsymbol{J}\|_2^2 \right\}. \tag{4.1}$$

The residual norm $||\boldsymbol{M} - \boldsymbol{G}\boldsymbol{J}||_2$ is the data fit, telling us how well a given $\boldsymbol{J}$ explains the data, while $||\boldsymbol{W}\boldsymbol{J}||_2$ represents the "size" of the of the regularized solution. Recall that the filter factors (Eq. (2.24)) filter out the contributions to $\hat{\boldsymbol{J}}_\lambda$ corresponding to small singular values (when $\sigma_i \ll \lambda$) while they leave SVD components corresponding to the large singular values (when $\sigma_i \gg \lambda$) almost unaffected. So we have seek a trade-off when faced with the following compromise:

1. If too much regularization (damping) is imposed, the obtained solution will not fit the given data $\boldsymbol{M}$ properly and the residual $||\boldsymbol{M} - \boldsymbol{G}\boldsymbol{J}||_2$ will be large. In this case, we have the so-called *underfitting* (see Figure 4.1 on the left).

2. If too little regularization is imposed, then the fit will be good, but the solution will be dominated by by the contributions from data errors (i.e. the noise will

be fitted as well) leading to the norm $||\boldsymbol{WJ}||_2$ being too large. In this case we have the so-called *overfitting* (see Figure 4.1 on the right).

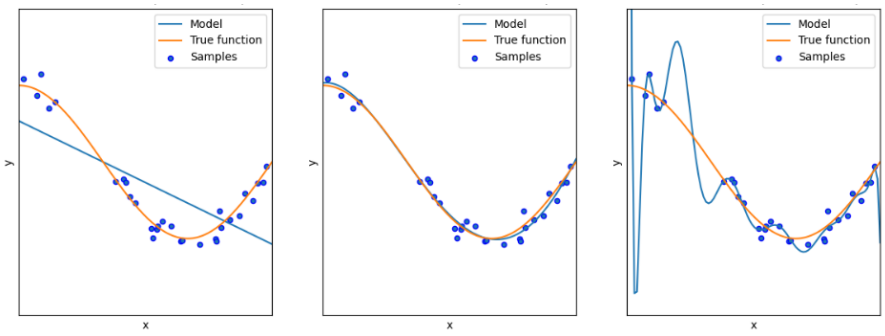

Figure 4.1: An example of possible three different choices of λ, leading to underfitting (left) , a good recovery (middle), and overfitting (right). Taken from https://scikit-learn.org/stable/auto_examples/model_selection/plot_underfitting_overfitting.html

Let us illustrate this on our data. We show the simplest case, when $\boldsymbol{W} = \boldsymbol{I}$ (MNE solution), perform the reconstructions for different values of the regularization parameter, and see how the MNE solutions behaves (See Figure 4.2). It is clear that the bigger the λ, the bigger the residual, and the smaller the solution norm. Our

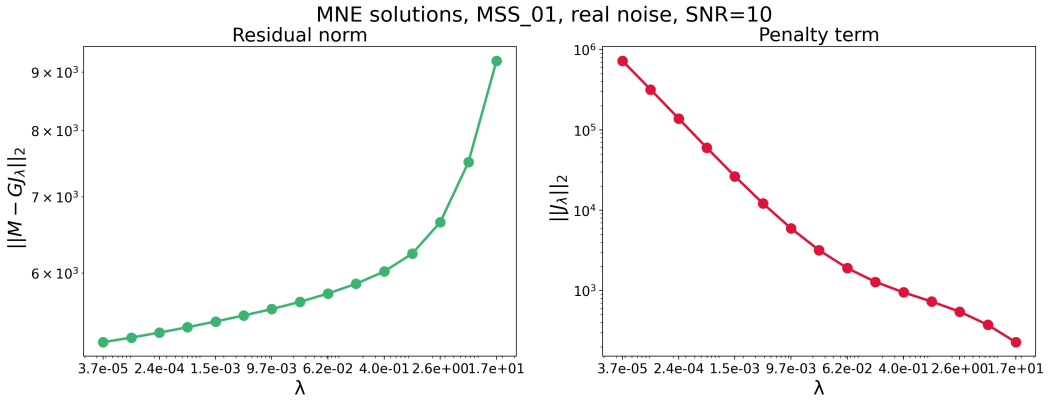

Figure 4.2: Residual and solution norm for MNE reconstructions obtained for different values of λ. These graphs are for simulated data, for the first subnetwork (MSS_01) with additive noise, SNR=10.

choice for the range of values of λ was guided by the range of singular values of $\boldsymbol{G}$. We chose 15 logarithmically spaced values in range $\lambda = [\sigma_{min}(\boldsymbol{G}), ...\sigma_{max}(\boldsymbol{G})]$.

4.2.1 The L-curve

The L-curve has been proposed by Hansen and O'Leary back in the 90's [Hansen 1992, Hansen & O'Leary 1993, Hansen 1999] and since then it has been the most used method for selecting the regularization parameter in a broad spectrum of inverse

problems. It is a log-log plot of the norm of a regularized solution against the norm of the corresponding residual norm, i.e. a curve

$$\left(\frac{\hat{\rho}}{2}, \frac{\hat{\eta}}{2}\right) = (\log ||\boldsymbol{M} - \boldsymbol{G}\boldsymbol{J}_\lambda||_2,\ \log ||\boldsymbol{W}\boldsymbol{J}_\lambda||_2) \tag{4.2}$$

parametrized by the regularization parameter λ, where $\hat{\rho}$ and $\hat{\eta}$ are the following

$$\hat{\rho} = \log \rho, \quad \hat{\eta} = \log \eta$$
$$\rho = ||\boldsymbol{M} - \boldsymbol{G}\boldsymbol{J}_\lambda||_2^2, \quad \eta = ||\boldsymbol{W}\boldsymbol{J}_\lambda||_2^2.$$

The optimal regularization parameter λ^* is the one that corresponds to the corner

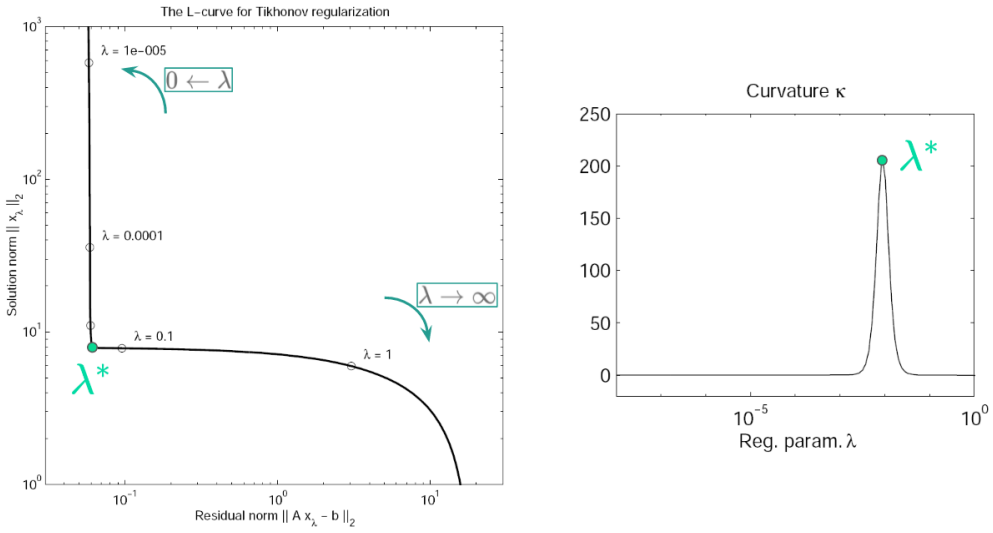

Figure 4.3: Left: A typical L-curve. The optimal λ^* (in green) chosen as the corner of the curve (point of maximal curvature). Right: Associated curvature function $\kappa(\lambda)$. Adapted from [Hansen 1999].

of the curve (if there is a clear corner in ideal case). The rationale behind this is that the corner separates the flat and vertical parts of the curve where the solution is dominated by regularization errors and perturbation errors, respectively [Hansen 1999]. Finding the corner point (optimal λ^*) is a geometrical problem that can be solved numerically. There are several strategies for this choice, such as (1) the closest point to the origin (0,0) of the Cartesian axes (in terms of Euclidean distance), (2) the point of the maximal curvature [Hansen & O'Leary 1993] (3) the triangle method [Castellanos *et al.* 2002],...
We chose the most popular strategy, which is λ^* as the point of the maximal curvature

$$\lambda^* = \arg\max_\lambda \kappa(\lambda) \tag{4.3}$$

where the curvature $\kappa(\lambda)$ is defined as:

$$\kappa(\lambda) = \frac{\hat{\rho}'\hat{\eta}'' - \hat{\rho}''\hat{\eta}'}{((\hat{\rho}')^2 + (\hat{\eta}')^2)^{3/2}} \tag{4.4}$$

where $\hat{\rho} = \log \rho$ and $\hat{\eta} = \log \eta$. For differentiation of $\kappa(\lambda)$, the interested reader is refered to the original paper of [Hansen & O'Leary 1993]. We opted to follow the "recipe" of the original papers of Hansen and colleagues where the curvature is computed using the log of the values and plotted the norms on a log-log scale (see Figure 4.4). For each reconstruction method (which will be discussed in the following sections), for simulated data, we computed $\kappa(\lambda)$ across 5 simulated MSS subnetworks and took λ^* as the one that appears most among those 5, for both SNR values (3 and 10). For real MEG data, we computed λ^* for each subject, for each of the 4 movement types, and took the value that appears most since the variability across subnetworks or across movements was minor. Nevertheless, there are a few

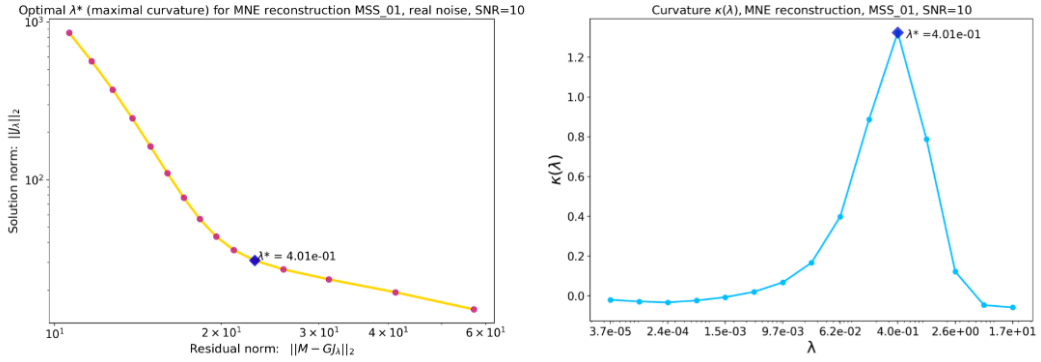

Figure 4.4: Example of L-curve (left) and the curvature $\kappa(\lambda)$ (right) obtained for MNE reconstruction of MSS_01 for SNR=10

interesting points to mention. This choice was not trivial, mainly due to numerous options which yielded different results. We mentioned that L-curve should be a log-log plot. Justification about this can be found in [Hansen & O'Leary 1993] where the authors claim that, by their experiments, it was advantageous to consider the L-curve on a log-log scale. Firstly because singular values usually span several orders of magnitude so L-curve should be more easily seen on a log-log scale. Secondly, they claim that the log-log scale should emphasize the "flat" parts of the L-curve where the variation in either ρ or η is small compared to the variation in the other variable; that these parts of the L-curve are often "squeezed" close to the axes in a lin-lin scale and that the log-log scale should emphasize the corner.

Interestingly, in our case it turned out to be the opposite. L-curve on a lin-lin scale showed a more prominent corner than on the log-log scale (see Figure 4.5). Regarding taking the log of the values for curvature computation, notice the range of $||\boldsymbol{M} - \boldsymbol{G}\boldsymbol{J}_\lambda||_2$ and $||\boldsymbol{W}\boldsymbol{J}_\lambda||_2$ in Figure 4.5 in the middle: the residual norm is a few orders of magnitude (OOM) bigger than the solution norm. So by considering this, it is reasonable to take the log in order to bring the two norms on the same OOM, otherwise one norm will always dominate. Another thing to point out is the potential benefits of normalization. In [Hammond *et al.* 2013] the authors normalized both residual and the solution norm prior to curvature computation. So if we normalize each quantity by its maximal value as $\rho_n = \frac{\rho}{\rho_{max}}$ and $\eta_n = \frac{\eta}{\eta_{max}}$, a different

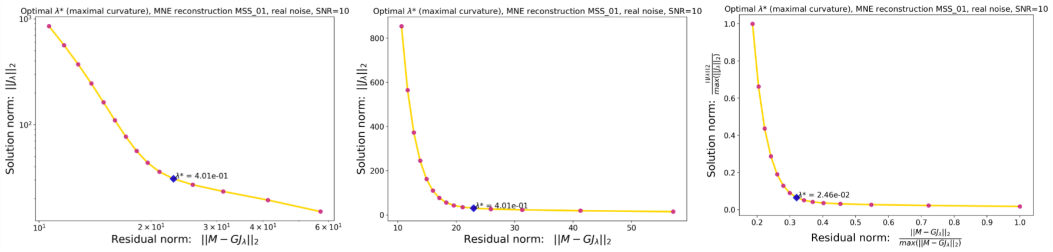

Figure 4.5: Comparison of 3 different L-curves (and therefore different λ^* values) obtained with the same data. Left: L-curve as a log-log plot of $\left(\frac{\hat{\rho}}{2}, \frac{\hat{\eta}}{2}\right)$ (this was the choice used in the remainder of this thesis). Middle: L-curve as a plot (ρ, η) on a lin-lin scale. Right: L-curve on a lin-lin scale with ρ and η normalized to the range $[0, 1]$ i.e. $\left(\frac{\rho}{\rho_{max}}, \frac{\eta}{\eta_{max}}\right)$

value of λ^* is obtained (see Figure 4.5 on the right). Such normalization seems to be most suitable for a choice of λ^* as the closest point to (0,0). Another interesting thing to point out (which is rarely discussed in the literature) is the range of values of the regularization parameter. We mentioned that we chose 15 logarithmically spaced values in range $\lambda = [\sigma_{min}(\boldsymbol{G}), ...\sigma_{max}(\boldsymbol{G})]$. Out of curiosity, we wanted to

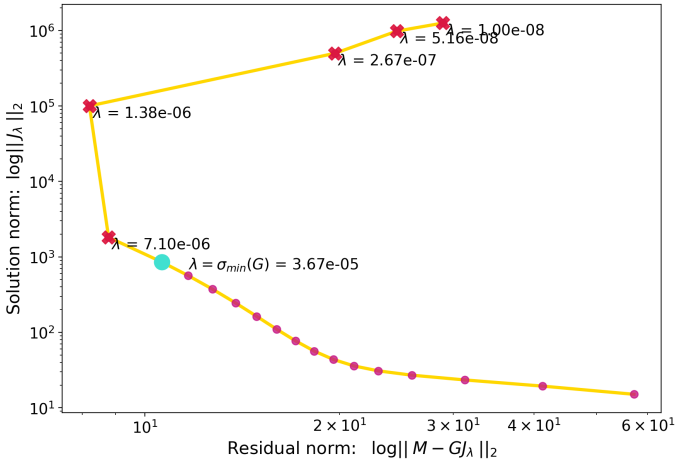

Figure 4.6: Example of an L-curve for an unsuitable choice of the range of λ values (MNE reconstruction of MSS_01, SNR=10).

see how the residual and solution norm behave for $\lambda < \sigma_{min}(\boldsymbol{G})$. In Figure 4.6, we chose 15 values in range $\lambda = [10^{-8}, ...\sigma_{max}(\boldsymbol{G})]$. Interestingly the L-curve lost the "L" shape when λ became too small and the residual norm $\|\boldsymbol{M} - \boldsymbol{GJ}\|$ became unstable- it started to increase again. This is due to the fact the inversion of $\boldsymbol{G}^T\boldsymbol{G}$ in Eq.(2.22) becomes unstable when λ is too small (recall that it is in the denominator of Tikhonov filter factors (Eq.(2.24)).

Multidimensional extension of the L-curve

What happens when we have multiple regularization parameters like in the CGS [Hammond *et al.* 2013] reconstruction method? In that case, a multidimensional extension

to the L-curve method is required to optimize all the parameters simultaneously. One possible approach is the L-hypersurface, introduced by [Belge *et al.* 2002]. Similarly to the 1D case where the corner of the L-curve is chosen as the point of maximal curvature, the generalized corner of the L-hypersurface is defined as the point with maximum Gaussian curvature.
Another approach, as proposed by [Hammond *et al.* 2013] is to use a modified L-curve procedure that alternates between keeping one regularization constant fixed, while maximizing the curvature in terms of the other ("active") one. As a reminder, the optimal regularization parameters for the CGS method, namely λ_{loc} and λ_{tr} in Eq. (2.30) describe the relative contribution of local and tractography-based components of the graph, as well as the overall contribution of the CGS penalty. We followed the modified L-curve approach since that one was used in their paper and we would like to thank the authors for providing us their MATLAB implementation of the code used for its computation. For more details, the interested reader is referred to the original paper of [Hammond *et al.* 2013].

4.2.2 GCV

Generalized Cross-Validation is, as the name suggests, based on the principle of cross-validation; the regularized inverse problem is solved omitting at each realization one point of the observed data [Golub *et al.* 1979]. In other words, it seeks a regularization parameter λ^* that best predicts the missing information from a sensor i using the measurement from the remaining sensors. For the minimization problem such as Eq. (2.20) when $\boldsymbol{W} = \boldsymbol{I}$, the estimate λ^* is the minimizer of the function $V(\lambda)$ defined as

$$V(\lambda) = \frac{\|(\boldsymbol{I} - \boldsymbol{A}(\lambda))\boldsymbol{M}\|_2^2}{trace(\boldsymbol{I} - \boldsymbol{A}(\lambda))^2}$$
$$\lambda^* = \arg\max_{\lambda} V(\lambda)$$

where the so-called influence matrix is given by

$$\boldsymbol{A}(\lambda) = \boldsymbol{G}(\boldsymbol{G}^T\boldsymbol{G} + \lambda^2\boldsymbol{I})^{-1}\boldsymbol{G}^T$$

It relies on the assumption that the measurements are affected by independent and identically distributed (i.i.d.) noise across sensors. An example of optimal λ^* obtained with GCV is shown in Figure 4.7. The purpose of this illustration is to demonstrate that different values of λ^* can be obtained depending on the criterion of choice (e.g. L-curve vs. GCV). The shape of the GCV function complies with the literature [Golub *et al.* 1979, Hansen & O'Leary 1993]. However, we do not use use the GCV results for 3 reasons (1) the noise we add is realistic and not i.i.d. (2) one of our formulations of the objective function we seek to minimize does not have a closed-form solution and thus there is no closed-form for the GCV function and (3) to better compare our methods to the CGS method [Hammond *et al.* 2013], who used a modified L-curve procedure. Hence, we kept the L-curve strategy.

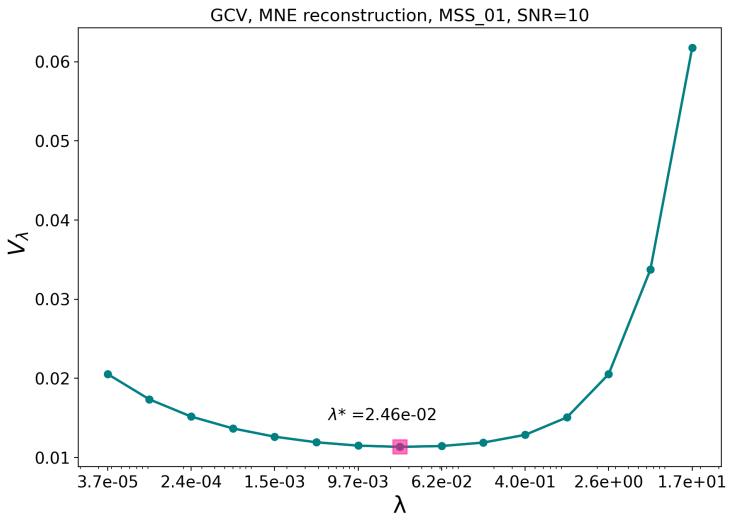

Figure 4.7: GCV example

4.3 Evaluation Error Metrics

Quantifying the performance of distributed source methods is not trivial and still lacks a well-established consensus [Im *et al.* 2003, Grova *et al.* 2006, Hauk *et al.* 2019, Samuelsson *et al.* 2021]. For this reason, we employ several validation metrics from the literature [Grech *et al.* 2008, Grova *et al.* 2006, Samuelsson *et al.* 2021, Lin *et al.* 2006, Lamus *et al.* 2012, Darvas *et al.* 2004] to evaluate the results of the reconstructed brain activity from simulated MEG measurements. As a reminder, every source represents the spatial location of a time series, which can be written into a matrix where, to each source (row) at multiple time points (columns) a value can be assigned. This value is the strength of the signal at a given point in space and time. The column vector $\boldsymbol{j}_{:,t} = (j_{0,t}, j_{2,t}, ..., j_{S-1,t})^T \in \mathbb{R}^S$ is a vector of all source amplitudes at time t (with $t = 0, ...T-1$), while the row vector $\boldsymbol{j}_{s,:} = (j_{s,0}, j_{s,2}, ..., j_{s,T-1}) \in \mathbb{R}^T$ is a time series of s^{th} source (with $s = 0, ...S-1$). Therefore, the matrix of time series of S source amplitudes for T time instants is given by $\boldsymbol{J} \in \mathbb{R}^{S \times T}$. We denote the simulated source time courses as the ground truth, with the subscript GT, while we refer to the reconstructed ones with the subscript REC (see Figure 4.8 for an illustration). To verify the localization error, we use two standard metrics (1) peak-to-peak localization error and (2) center of mass (aka center of gravity) localization error. For both of these metrics, we can exclude weak insignificant dipole estimates by setting a threshold τ on the absolute value of dipoles' amplitudes, when compared to the maximal one. In order to avoid the question of choice of another threshold, we show the errors for different values of τ, ranging from 10% to 70% of the maximal amplitude, within the given source time courses. We denote with $\{\boldsymbol{J}_\tau\}$ the set of all sources i whose signal amplitude exceeds a certain threshold

$$|\boldsymbol{j}_i| \geq \tau * |\boldsymbol{J}|_{max}. \tag{4.5}$$

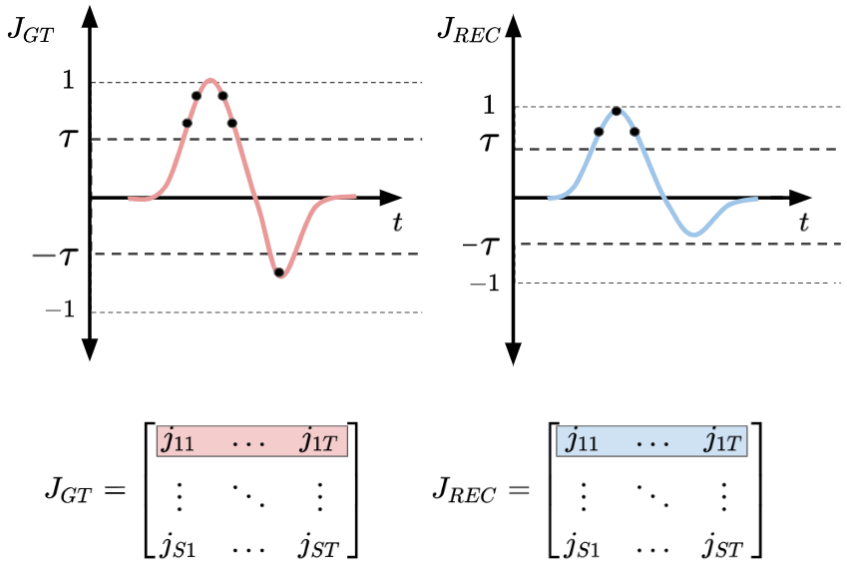

Figure 4.8: Toy example of amplitude thresholding. Notice that $|\boldsymbol{j}_i| \geq \tau * |\boldsymbol{J}|_{max}$ i.e. $|\boldsymbol{J}|_{max}$ is the maximal value for a given $\boldsymbol{J}$, i.e. can be different for simulated (GT) and reconstructed (REC) data. The amplitudes of recovered source estimates depend on the regularization parameter and may not be recovered at the same order of magnitude as the GT, while the locations and the waveform may still be accurate. This type of thresholding leverages this issue.

See Figure 4.8 for an illustration. The set of all time points in which Eq.(4.5) holds is denoted with $\{T_\tau\}$, while the set of time points where it holds *both* in the ground truth(simulated noiseless source time courses) and reconstructed data is defined as $\{T_\tau^{PT}\} = \{T_\tau^{GT}\} \cap \{T_\tau^{REC}\}$. "PT" stands for "Peak Times". We also evaluated the detection accuracy based on receiver operating characteristic (ROC) [Metz 1986] curves, similarly as the authors in [Grova *et al.* 2006], [Lamus *et al.* 2012] and [Darvas *et al.* 2004]. The evaluation criteria is based on the area under the ROC curve (AuC) which was estimated empirically and it is explained in more details below. All evaluations were done for 2 different SNR levels, 3 and 10.

4.3.1 Peak-to-peak localization error

For each time instant $t \in \{T_\tau\}$, the source index with the peak amplitude is found as

$$p^* = \arg\max_j \left(|\boldsymbol{j}_{:,t}|\right) \tag{4.6}$$

while its position vector in 3D surface RAS coordinates is denoted as $\vec{r}(p^*)$. Peak-to-peak (PtP) localization error at time time instant t is defined as the Eucledian distance between the location of the peak in the simulated (GT) and the reconstructed (REC) sources

$$d(\vec{r}(p^*, t)) = |\vec{r}_{GT}(p^*, t) - \vec{r}_{REC}(p^*, t)|. \tag{4.7}$$

The errors are then averaged across these time instants as

$$\overline{d}_{PtP} = \frac{1}{|T_\tau^{PT}|} \sum_{t \in \{T_\tau^{PT}\}} d(\vec{r}(p^*, t)). \tag{4.8}$$

This metric would be the most suitable in simulations where the activity is rather focalized in a small brain area. In the context of M/EEG source reconstruction, this indicator is not sufficient to fully quantify the quality of the recovery of brain activity. Firstly, due to the fact that all l_2- based inverse solvers suffer from smearing of activation, which often gives solutions with overestimated extents of the activated areas [Gramfort *et al.* 2012]. Secondly, due to the spatial spread of the activity in the simulations. Yet, it is a reasonable choice as a first step in the evaluation, to identify how close the locations of the largest magnitudes in simulated and recovered activity are. In the ground truth, multiple sources on the cortex can be simultaneously active with the same amplitude. We took this into account in the implementation of this metric, by taking a centroid if multiple peaks with the same magnitudes are found. Clearly, when comparing different reconstruction methods, method A has better localization than method B if $d_A \leq d_B$.

4.3.2 Center of gravity localization error

An extension of the peak-to-peak error is a metric where the source locations are weighted by the their amplitudes, called the center of gravity (CoG) (or center of mass) localization error. The position vector of the center of mass in 3D surface RAS coordinates is defined as

$$\vec{r}(c^*) = \frac{\sum\limits_i |\boldsymbol{j}_i| \vec{r}_i}{\sum\limits_i |\boldsymbol{j}_i|}, \; i \in \{\boldsymbol{J}_\tau\}. \tag{4.9}$$

with c^* being its source index. For each such location in the ground truth and the reconstruction, center of mass localization error can be computed for each time instant t as

$$d(\vec{r}(c^*, t)) = |\vec{r}_{GT}(c^*, t) - \vec{r}_{REC}(c^*, t)|. \tag{4.10}$$

The center of mass activity may not be at exact position of an existing vertex on the surface mesh, so in those cases, the closest existing vertex is taken. The average center of gravity error in the time window is then computed as

$$\overline{d}_{CoG} = \frac{1}{|T_\tau^{PT}|} \sum_{t \in \{T_\tau^{PT}\}} d(\vec{r}(c^*, t)) \tag{4.11}$$

4.3.3 ROC curve

The ROC curve was developed during World War II to quantify the performance of target detection systems using radars and sonars. It is still widely used in machine learning classification tasks for performance assessment of binary classifiers.

In medical imaging, it first appeared in the 1980s [Metz 1986] to evaluate the efficiency of radiologists' image-based diagnoses with the actual state of the patient (sick/healthy). The ROC curve is created by plotting the true positive rate (TPR) against the false positive rate (FPR) as a function of a threshold [Swets 1988]. It depicts the trade-off between the TPR (also called the *sensitivity*, *recall* or the *probability of detection*) and the FPR (also called the *fall-out rate* or the *probability of false alarm*). The values above the decision threshold indicate that the condition is "positive", which, for example, in a diagnostic system can mean that a patient has a disease. A convenient way to represent the true positives (TP), true negatives (TN), false positives (FP) and false negatives (FN) is with a confusion matrix, as shown in Table 4.1. In this context, we are interested in how many sources are above ("positive") or below ("negative") a certain amplitude threshold in the ground truth and the reconstruction. The maximal current magnitude in the simulated data was 6 nAm. In the reconstructions, however, the amplitudes of recovered sources depend on the regularization parameter and may not be on this order of magnitude, while the locations and the waveform may still be correct. For this reason, we firstly normalize both the simulated and reconstructed source time courses to the range $[0, 1]$ as

$$\bar{\boldsymbol{J}}_{GT} = \frac{\boldsymbol{J}_{GT}}{max(|\boldsymbol{J}_{GT}|)} \text{ and } \bar{\boldsymbol{J}}_{REC} = \frac{\boldsymbol{J}_{REC}}{max(|\boldsymbol{J}_{REC}|)}. \tag{4.12}$$

For an amplitude threshold τ in the interval $[0.1, 0.7]$ (with a step of 0.1), we consider a source i at time t to be active if its magnitude satisfies $|\bar{j}_{i,t}| \geq \tau$. The TPR is given

Table 4.1: Confusion matrix

	$\lvert\bar{\boldsymbol{J}}_{REC}\rvert \geq \tau$	$\lvert\bar{\boldsymbol{J}}_{REC}\rvert < \tau$
$\lvert\bar{\boldsymbol{J}}_{GT}\rvert \geq \tau$	True Positive TP(τ)	False Negative FN(τ)
$\lvert\bar{\boldsymbol{J}}_{GT}\rvert < \tau$	False Positive FP (τ)	True Negative TN(τ)

by the number of recovered true positives over the number of active sources generated during the simulations, as a function of τ. A recovered source was considered a false positive or a "ghost" source if it appeared in the reconstruction but it was not active in the simulated scenario. The FPR is the probability of appearance of ghost sources. In our simulations, the active sources were not active during the whole time window. In those time instants, the "True Negative" refers to the absence of simulated activity. TNR quantifies how well true negatives are identified. We can estimate TPR, FPR and TNR as follows

$$TPR(\tau) = \frac{TP(\tau)}{TP(\tau) + FN(\tau)} \tag{4.13}$$

$$FPR(\tau) = \frac{FP(\tau)}{FP(\tau) + TN(\tau)} = 1 - TNR(\tau) \tag{4.14}$$

$$TNR(\tau) = \frac{TN(\tau)}{TN(\tau) + FP(\tau)} \tag{4.15}$$

Detection accuracy of each reconstruction method can be assessed by computing the area under its ROC curve (AuC) (see an example in Figure 4.9). AuC values can be in the range [0,1]. A model whose predictions are 100% wrong has an AUC of 0.0, while the one whose predictions are 100% correct has an AUC of 1.0. In practice, a reconstruction method showing an AUC index bigger than 0.8 is generally considered as sufficiently accurate, meaning it gives 80% of correct detections. In clasiffication tasks in machine learning, AuC represents the degree or measure of separability, i.e. it is a measure of classifier's ability to distinguish between classes. Here, AuC values refer to how correctly can a reconstruction identify a presence and absence of source activity.

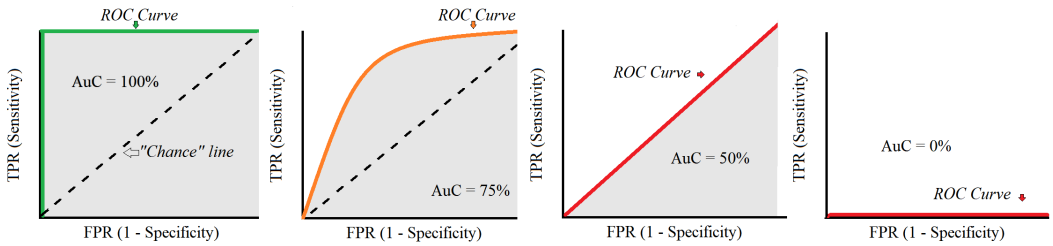

Figure 4.9: Example of ROC curves. Source: `https://www.datasciencecentral.com/profiles/blogs/roc-curve-explained-in-one-picture`

4.4 Some concepts in graph theory

Graph theory provides a compelling mathematical framework for analysis of large-scale brain network structure and dynamics. In this context, brain can be modelled as a graph of nodes which represent certain neural elements (e.g., current sources/brain regions), connected by edges representing some measure of physical, functional or causal interaction between them [Meunier *et al.* 2010, Sporns 2011, Fornito *et al.* 2013]. The physical connections can be **local** (e.g. between neighbouring vertices on the cortical mesh) or **non-local** (e.g. long-range white matter fibers). Functional connections can, for example, pertain to a temporal dependence between physically connected sources. Causal relations refer to the influence that activity in one neural population has over the activity in another one. Although in general brain connectivity can be structural, functional and effective, as mentioned in Section 1.7.1, we will focus only on the structural connections. In graph terminology, the terms "node" and "vertex" are used interchangeably. In order not to create a confusion with the vertices of the high resolution mesh from Chapter 3, a "vertex" v_i in this context represents a source from the source space.

A graph $G = (V, E)$, is made up of a set of nodes or vertices $V = \{v_1, ...v_S\}$ ($|V| = S$) and a set of edges $E = \{e_1, ...e_K\}$ ($|E| = K$) that connect the vertices. In *undirected* graphs, E is a set of two-element subsets of V (i.e. $\{u, v\}$ with $u, v \in V$ and $u \neq v$. In *directed* graphs, E is a set of ordered pairs of distinct nodes (i.e. pairs (u, v) with $u \neq v$). We will consider *simple graphs*, in which there is at most one edge

from a node u to a node v. Let us first consider the brain as an *undirected* graph and define some important concepts in graph theory [Biggs *et al.* 1986, Bollobás & Bollobas 1998]. The adjacency (connectivity) matrix $\boldsymbol{A}$ indicates whether a pair of vertices is adjacent or not in the graph, defined with entries

$$a_{i,j} = \begin{cases} 1, & \text{if nodes } v_i \ \& \ v_j \text{ are connected by an edge} \\ 0, & \text{otherwise.} \end{cases} \tag{4.16}$$

Given the adjacency matrix $\boldsymbol{A}$, we can construct the diagonal degree matrix $\boldsymbol{D}$, with elements

$$d_{i,i} = \sum_j a_{i,j} \tag{4.17}$$

which contains information about number the of edges attached to each vertex. The standard Laplacian matrix $\boldsymbol{L} = \boldsymbol{D} - \boldsymbol{A}$ of a graph can be defined as

$$l_{i,j} = \begin{cases} deg(v_i), & \text{if } i = j \\ -1, & \text{if } i \neq j \text{ and } v_i \text{ is connected to } v_j \\ 0, & \text{otherwise.} \end{cases} \tag{4.18}$$

For a graph with S nodes, the matrices $\boldsymbol{A}$, $\boldsymbol{D}$ and $\boldsymbol{L}$ are of size $S \times S$.

Let us consider briefly a **directed** graph, and introduce the *incidence matrix* which is an important object that will be used and discussed later. Each edge is associated with two vertices, called its source (or origin) and target vertices, i.e. the edge connects its origin to its target. While the term "source" is often encountered in graph theory, we will refer to a source of an edge as the *origin*, to avoid any ambiguity. Given an edge $e = (v_i, v_j)$, we can say that $origin(e) = v_i$ is the origin of e and $target(e) = v_j$ is the target of e. Given a *directed* graph $G = (V, E)$ with $V = \{v_1, ...v_S\}$ and $E = \{e_1, ...e_K\}$. The incidence matrix $\boldsymbol{B}$ (of size $S \times K$) can be defined as:

$$b_{i,k} \begin{cases} -1, & \text{if origin}(e_k) = v_i \\ +1 & \text{if target}(e_k) = v_i \\ 0, & otherwise \end{cases} \tag{4.19}$$

where $i = 1, ...S$ and $k = 1, ...K$. The Laplacian can be made from the incidence matrix as $\boldsymbol{L} = \boldsymbol{B}\boldsymbol{B}^T$. See Figure 4.10 for a toy example of a directed graph with its corresponding incidence and Laplacian matrices. A *walk* or a *chain* is a sequence of vertices and edges of a graph, both of which can be repeated. A *trail* is a walk with no repeated edges. A *path* of l vertices is a trail in which neither vertices nor edges are repeated, i.e. it is a sequence of l distinct vertices, such that consecutive vertices are adjacent. The graph G is connected if for any 2 distinct node $u, v \in V$ there is a path from u to v.

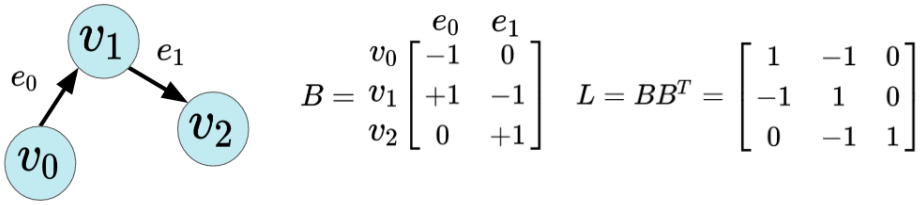

Figure 4.10: Toy example of a directed graph with its incidence and Laplacian matrix.

4.5 Laplacian as a smoothness constraint

Laplacian matrix measures to what extent the value of a graph at one vertex differs from its values at connected vertices. It is symmetric positive semidefinite (meaning that $\boldsymbol{x}^T\boldsymbol{L}\boldsymbol{x} \geq 0, \forall \boldsymbol{x}$) and it has real and nonnegative eigenvalues. Furthermore, 0 is always an eigenvalue of L since the vector $(1, 1, ..., 1)^T$ is a corresponding eigenvector. An interesting fact is that the multiplicity of the eigenvalue 0 is equal to the number of connected components of the graph G [Chung & Graham 1997], a property often exploited in graph spectral clustering.
In the LORETA approach [Pascual-Marqui *et al.* 1994], similar activity is favoured between spatially adjacent vertices on the cortical mesh by choosing $\boldsymbol{W} = \boldsymbol{L}$ in Eq.((2.20)), where $\boldsymbol{L}_{loc}$ is the Laplacian matrix on the cortical surface ("LOC" in the subscript refers to local or short-range connections). Therefore, the LORETA solution is given by

$$\hat{\boldsymbol{J}} = \left(\boldsymbol{G}^T\boldsymbol{G} + \lambda \boldsymbol{L}_{loc}^T\boldsymbol{L}_{loc}\right)^{-1}\boldsymbol{G}^T\boldsymbol{M}. \tag{4.20}$$

The physiological assumption behind it is that neighboring points on the cortical grid are more likely to be synchronized (i.e. of similar orientation and strength). Let us make a small toy example of an undirected graph containing only local edges to illustrate this (Figure 4.11). Each row of $\boldsymbol{L}$ acts as a finite difference operator by

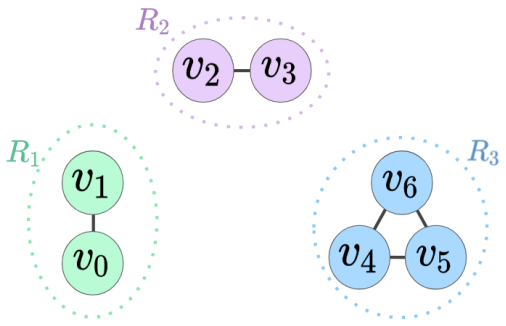

Figure 4.11: Toy example of a graph with only local edges. The vertices belong to three different regions, R_1, R_2 and R_3. Although this may look like a graph with three connected components, it is worth noting that we omitted to show edges between sources in different regions only for illustration purposes. This toy example, in fact, should represent a small part of the cortical surface mesh, which is a connected graph.

computing differences between each vertex and its direct (local) neighbors, thus providing the solution with the maximum spatial smoothness. For such a graph where edges exist only between spatially adjacent sources, we will denote its adjacency, degree and Laplacian matrices as $\boldsymbol{A}_{loc}$, $\boldsymbol{D}_{loc}$ and $\boldsymbol{L}_{loc}$, respectively, all of size $S \times S$. For a graph shown in Figure 4.11, these matrices are illustrated in Figure 4.12.

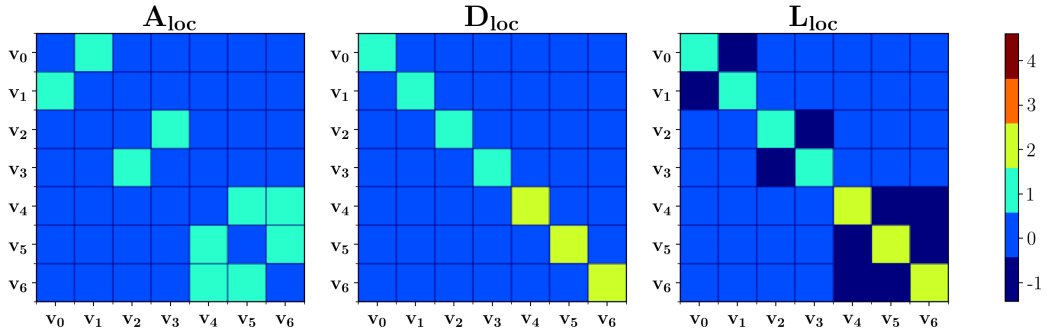

Figure 4.12: Toy example of $\boldsymbol{A}_{loc}$, $\boldsymbol{D}_{loc}$ and $\boldsymbol{L}_{loc}$. Notice that nodes with more connections are weighted more.

Since LORETA does not account for long-range connectivity, it was later extended in the Cortical Graph Smoothing (CGS) method [Hammond *et al.* 2013] by forming a hybrid local/nonlocal connectivity graph with $\boldsymbol{A_{loc}}$ (spatial adjacency on the cortical surface) and $\boldsymbol{A_{tr}}$ (tractography-based connectivity matrix). They are used to form local $\boldsymbol{L_{loc}}$ and tractography-based $\boldsymbol{L_{tr}}$ graph Laplacians, resulting in the penalty term $P_{CGS}(\boldsymbol{J}) = \lambda_{loc}\boldsymbol{J^T L_{loc} J} + \lambda_{tr}\boldsymbol{J^T L_{tr} J}$. The analytic solution, linear in $\boldsymbol{M}$ is given by

$$\hat{\boldsymbol{J}}_{CGS} = (\boldsymbol{G^T G} + \lambda_{loc}\boldsymbol{L}_{loc} + \lambda_{tr}\boldsymbol{L}_{tr})^{-1}\boldsymbol{G^T M}.$$

This way CGS penalizes the weighted sum of squared differences in activity between anatomically connected cortical patches and promotes solutions with consistent activations across them. Diffusion tractography is not able to distinguish afferent and efferent connections [Jbabdi & Johansen-Berg 2011], so the matrix $\boldsymbol{A}_{tr}$ is symmetric. The example of a tractography-based graph is shown in Figure 4.13, and its corresponding degree, adjacency and Laplacian matrix in Figure 4.14.
Remark: A graph is *disconnected* if at least 2 vertices are not connected by a path. If a graph G is disconnected, then every maximal connected subgraph of G is called a *connected component* of the graph G. Because of the high resolution of the source space ($S = 8196$), some sources turned out to be isolated (i.e., not connected to any other source). This results in a disconnected tractography-based graph, where the matrix $\boldsymbol{A}_{tr}$ is singular (and therefore $\boldsymbol{L}_{tr}$ as well). $\boldsymbol{L}_{loc}$ on the other hand is always well-conditioned since the surface mesh is a connected graph. The penalty on disconnected sources will be discussed in the section that follows.

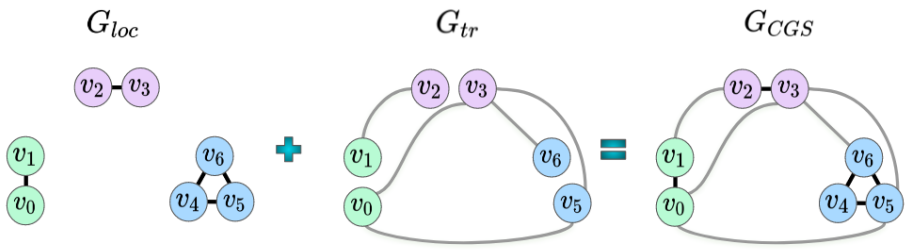

Figure 4.13: Toy example of a graph used in CGS, comprising of a graph with local edges G_{loc}(black) and long-range edges G_{tr} (grey).

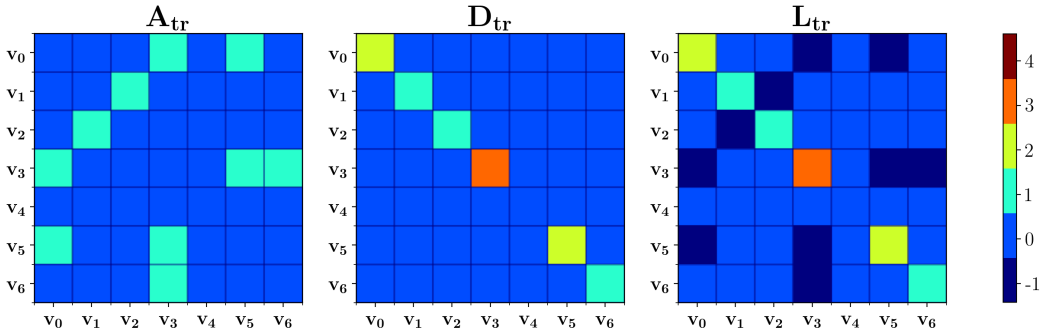

Figure 4.14: Toy example of $\boldsymbol{A}_{tr}$, $\boldsymbol{D}_{tr}$, and $\boldsymbol{L}_{tr}$ matrices for a tractography-based graph.

4.6 Connectivty-Informed MEG Inverse Problem (CIMIP)

Even though previous approaches exploited the information about structural connectivity between different cortical areas, transmission delays were not taken into account. Our goal was to keep the constraint of imposing spatial smoothness along the cortical surface, across all time instants, but also to enforce temporal smoothness across anatomically connected sources, with delays consistent with the information given by diffusion MRI. To make this idea more clearly, let us illustrate a toy example of a graph used in CIMIP in Figure 4.15. This graph evolves with time, with the following connections (which are added in time gradually to the graph, according to their delay):

- local (adjacent), no delay: $\{(v_0, v_1), (v_2, v_3), (v_4, v_5), (v_4, v_6), (v_5, v_6)\}$
- long-range, $\Delta = 1 : \{(v_1, v_2), (v_3, v_6)\}$
- long-range, $\Delta = 2 : \{(v_0, v_3), (v_0, v_5), (v_3, v_5)\}$

As a reminder, regularized inverse methods are in the form

$$\hat{\boldsymbol{J}} = \arg\min_{\boldsymbol{J}} U(\boldsymbol{J}) = \arg\min_{\boldsymbol{J}} \{F(\boldsymbol{M}, \boldsymbol{J}) + \lambda P(\boldsymbol{J})\} \tag{4.21}$$

We mentioned that some of the existing $P(\boldsymbol{J})$ in the literature are LORETA and CGS, that is:

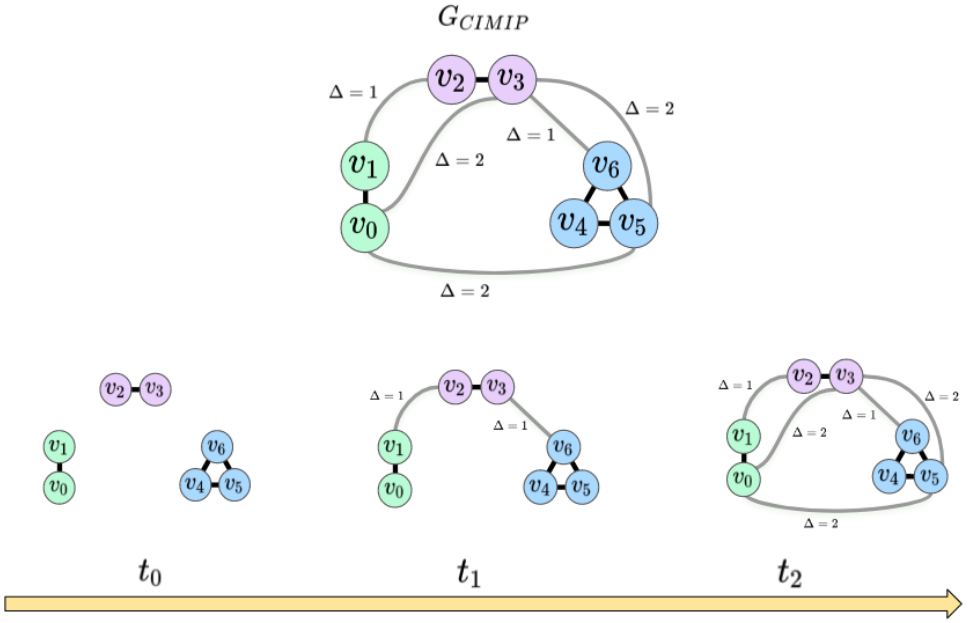

Figure 4.15: Toy example of a CIMIP graph in time. Smoothness between adjacent nodes is imposed at each time instant, while at t_1, it will also be imposed between nodes connected with streamlines whose lengths would yield delay of 1 time sample. The same stands for t_2 and so on.

1. $P_{LORETA}(\boldsymbol{J}) = \|\boldsymbol{L_{loc}J}\|_2^2$
2. $P_{CGS}(\boldsymbol{J}) = \lambda_{loc}\boldsymbol{J^T L_{loc} J} + \lambda_{tr}\boldsymbol{J^T L_{tr} J}$

We developed our method in a similar mathematical framework. In order to enforce temporal smoothness between the time courses of connected sources, incorporating a modified version of the Laplacian operator into the regularization process was a convenient technique to achieve this. Starting from MEG measurements, we can consider all time samples in a single very large problem written as

$$\boldsymbol{m} = \tilde{\boldsymbol{G}}\boldsymbol{j} + \boldsymbol{\varepsilon} \tag{4.22}$$

where $\boldsymbol{j} \in \mathbb{R}^{ST}$ and $\boldsymbol{m} \in \mathbb{R}^{NT}$ are vectors of concatenated source intensities and measurements i.e.

$$\boldsymbol{J} = \begin{bmatrix} | & & | \\ \boldsymbol{j}(t_0) & \dots & \boldsymbol{j}(t_{T-1}) \\ | & & | \end{bmatrix} \xrightarrow{\text{vec}} \boldsymbol{j} = \begin{bmatrix} \boldsymbol{j}(t_0) \\ \vdots \\ \boldsymbol{j}(t_{T-1}) \end{bmatrix} \tag{4.23}$$

$$\boldsymbol{M} = \begin{bmatrix} | & & | \\ \boldsymbol{m}(t_0) & \dots & \boldsymbol{m}(t_{T-1}) \\ | & & | \end{bmatrix} \xrightarrow{\text{vec}} \boldsymbol{m} = \begin{bmatrix} \boldsymbol{m}(t_0) \\ \vdots \\ \boldsymbol{m}(t_{T-1}) \end{bmatrix} \tag{4.24}$$

The column vector $\boldsymbol{j}(t) = (j_1(t), j_2(t), ..., j_S(t))^T \in \mathbb{R}^S$ is a vector of all source amplitudes at time t. The column vector $\boldsymbol{m}(t) = (m_1(t), m_2(t), ..., m_N(t))^T \in \mathbb{R}^N$

is a linear combination of all source amplitudes $\boldsymbol{j}(t)$ at time t. The forward operator is now block diagonal:

$$\tilde{\boldsymbol{G}} = diag(\boldsymbol{G}, ...\boldsymbol{G}) = \begin{bmatrix} \boldsymbol{G}_{N\times S} & & \\ & \boldsymbol{G}_{N\times S} & \\ & & \boldsymbol{G}_{N\times S} \end{bmatrix} \in \mathbb{R}^{NT\times ST} \tag{4.25}$$

and $\boldsymbol{\varepsilon} \in \mathbb{R}^{NT}$ is concatenated additive realistic subject noise in sensor space for a chosen SNR level (see Eq.(3.13)). As a reminder, there are S sources, N sensors and T time samples ($t = 0, ...T-1$). Whenever we denote a matrix with a $\sim$ above the letter that denotes it, it means that its size is $(NT \times ST)$. To recover electrical activity of the brain from M/EEG measurements, we minimize the objective function in the form

$$U_{\text{CIMIP}}(\boldsymbol{j}) = \|\boldsymbol{m} - \tilde{\boldsymbol{G}}\boldsymbol{j}\|_2^2 + \lambda P(\boldsymbol{j}) \tag{4.26}$$

where different choices of the penalty term $P(\boldsymbol{j})$ and the variant of the Laplacian matrix $\tilde{\boldsymbol{L}}$ were tested (See Table 4.2).

Laplacian type	$P(\boldsymbol{j})$	
	$A: \lambda\|\tilde{\boldsymbol{L}}\boldsymbol{j}\|_2^2$	$B: \lambda(\boldsymbol{j}^{\boldsymbol{T}}\tilde{\boldsymbol{L}}\boldsymbol{j})^2$
1. $\tilde{\boldsymbol{L}}_1 = (1-\beta)\tilde{\boldsymbol{L}}_{loc} + \beta\tilde{\boldsymbol{L}}_{tr}$	♠ (CIMIP1)	/
2. $\tilde{\boldsymbol{L}}_2 = \tilde{\boldsymbol{I}} - \tilde{\boldsymbol{A}} = \tilde{\boldsymbol{I}} - (\tilde{\boldsymbol{A}}_{loc} + \tilde{\boldsymbol{A}}_{tr})$	/	♠* (CIMIP2)
3. $\tilde{\boldsymbol{L}}_3 = \tilde{\boldsymbol{L}}_{loc} + (\tilde{\boldsymbol{I}} - \tilde{\boldsymbol{A}}_{tr})$	♠ (CIMIP3)	/

Table 4.2: Variants of CIMIP penalty. Cases presented in the thesis are designated with ♠. * Presented at GRAIL 2020. and ISBI 2021. [Kojčić *et al.* 2020, Kojčić *et al.* 2021]

Before we start explaining the reasoning behind different penalties and variants of the Laplacian matrix, let us start with the general idea. Firstly, we can build a binary time-dependent connectivity matrix as

$$\tilde{\boldsymbol{A}} = \tilde{\boldsymbol{A}}_{loc} + \tilde{\boldsymbol{A}}_{tr}. \tag{4.27}$$

Short-range connections are encapsulated in

$$\tilde{\boldsymbol{A}}_{loc} = diag(\boldsymbol{A}_{loc}, ...\boldsymbol{A}_{loc}) \in \mathbb{R}^{ST\times ST} \tag{4.28}$$

meaning that temporal smoothness along the cortical surface is imposed across all time instants. In order to include connections for different delays, we build a tractography-based graph $\tilde{\boldsymbol{A}}_{tr} \in \mathbb{R}^{ST\times ST}$ with elements

$$a_{i,j}^{tr} = \begin{cases} 1, & \text{if nodes } v_i \ \& \ v_j \text{ are connected with a delay of } \Delta \\ 0, & \text{otherwise.} \end{cases} \tag{4.29}$$

where nonzero elements designate the presence of a long-range connection *for a specific delay*, which was not considered in CGS. A toy example of $\tilde{\boldsymbol{A}}$ for 3 time instants is illustrated in Figure 4.16. This is a symmetric block matrix where each block corresponds to a specific delay. Note that $\boldsymbol{A}_{tr} \in \mathbb{R}^{S \times S}$ only indicates a *presence* of a long-range connection, while in CIMIP it will be split into multiple blocks of $\tilde{\boldsymbol{A}}$, where each block would correspond to a specific delay. See Figure 4.16 where it is split into 2 blocks, namely $\boldsymbol{A}_1$ and $\boldsymbol{A}_2$, which encompass all streamlines that would yield the days of 1 and 2 time samples, respectively.

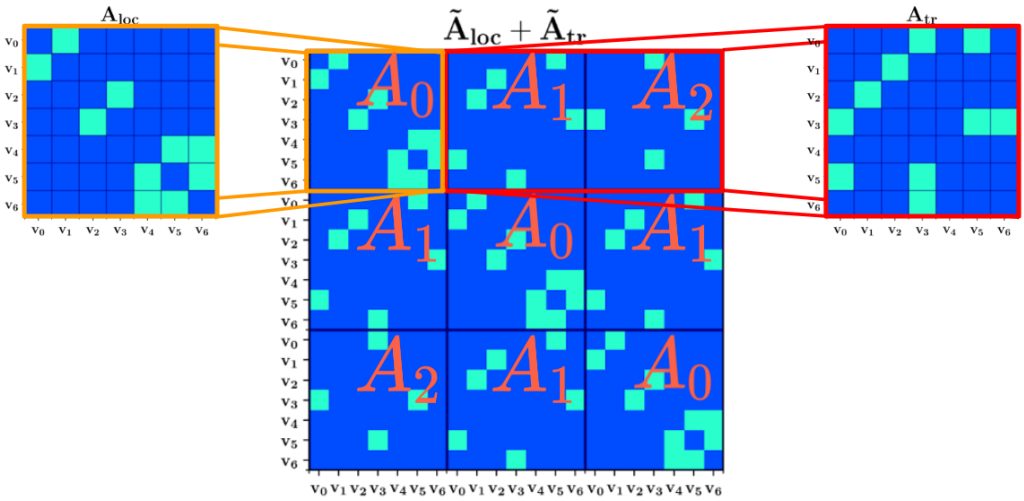

Figure 4.16: Toy example of a time-dependent connectivty matrix $\tilde{\boldsymbol{A}}$. In this schematic example we can see that $\boldsymbol{A_{loc}} = \boldsymbol{A_0}$ and $\boldsymbol{A_{tr}} = \boldsymbol{A_1} + \boldsymbol{A_2}$.

$\tilde{\boldsymbol{A}}_{loc}$ and $\tilde{\boldsymbol{A}}_{tr}$ refer to the local and tractography-based connectivity matrices which we use to form different variants of graph Laplacians ($\tilde{\boldsymbol{L}}$). The regularization matrix $\tilde{\boldsymbol{L}}$ can be one of the following:

- $\tilde{\boldsymbol{L}}_s = \tilde{\boldsymbol{D}} - \tilde{\boldsymbol{A}} = \tilde{\boldsymbol{L}}_{loc} + \tilde{\boldsymbol{L}}_{tr}$
- $\tilde{\boldsymbol{L}}_n = \tilde{\boldsymbol{I}} - \tilde{\boldsymbol{A}}_n = \tilde{\boldsymbol{I}} - \tilde{\boldsymbol{D}}^{-1/2}\tilde{\boldsymbol{A}}\tilde{\boldsymbol{D}}^{1/2}$
- $\tilde{\boldsymbol{L}}_1 = \tilde{\boldsymbol{L}}_{balanced} = (1-\beta)\tilde{\boldsymbol{L}}_{loc} + \beta\tilde{\boldsymbol{L}}_{tr}$
- $\tilde{\boldsymbol{L}}_2 = \tilde{\boldsymbol{L}}^* = \tilde{\boldsymbol{I}} - \tilde{\boldsymbol{A}} = \tilde{\boldsymbol{I}} - (\tilde{\boldsymbol{A}}_{loc} + \tilde{\boldsymbol{A}}_{tr})$
- $\tilde{\boldsymbol{L}}_2 = \tilde{\boldsymbol{L}}_{loc} + (\tilde{\boldsymbol{I}} - \tilde{\boldsymbol{A}}_{tr})$

Notation: Standard and normalized Laplacians are denoted as $\tilde{\boldsymbol{L}}_s$ and $\tilde{\boldsymbol{L}}_n$, respectively; $\tilde{\boldsymbol{L}}_1$ will be referred to as the 'balanced' Laplacian ($\tilde{\boldsymbol{L}}_{balanced}$) since the parameter $\beta \in [0, 1]$ balances the contribution of the two terms, the local and tractography-based Laplacians.
All variants of $\tilde{\boldsymbol{L}}$ are symmetric block matrices. Most of them have the same off-diagonal elements (except for $\tilde{\boldsymbol{L}}_n$), the main difference is their diagonal. $\tilde{\boldsymbol{L}}_n$ is rather mentioned as an example of another option that *can* be used. In our experiments, it did not show any particular advantages over the other Laplacians, so it was excluded from the results section. As a reminder from Section 3.6, for every streamline

f connecting a pair of cortical sources, the transmission delay between them is calculated as $\Delta_f = \frac{l_f}{v} F_s$ (Eq.(3.1)), where l_f is the streamline length in meters and v is the information transmission speed in m/s. The illustrations of $\tilde{\boldsymbol{A}}$, $\tilde{\boldsymbol{L}}_s$ and $\tilde{\boldsymbol{L}}^*$ for 3 time instants are shown in Figure 4.17. Let us take a closer look at the

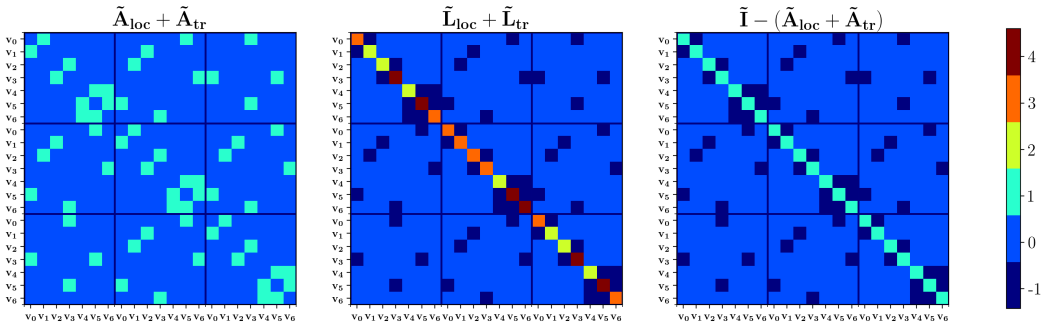

Figure 4.17: Toy example of $\tilde{\boldsymbol{A}}$, $\tilde{\boldsymbol{L}}_s$, and $\tilde{\boldsymbol{L}}^*$ matrices.

Laplacian matrix and the penalty it imposes in this context (see Figures 4.18 and 4.19). Let us discuss the different penalties and Laplacian types from Table 4.2

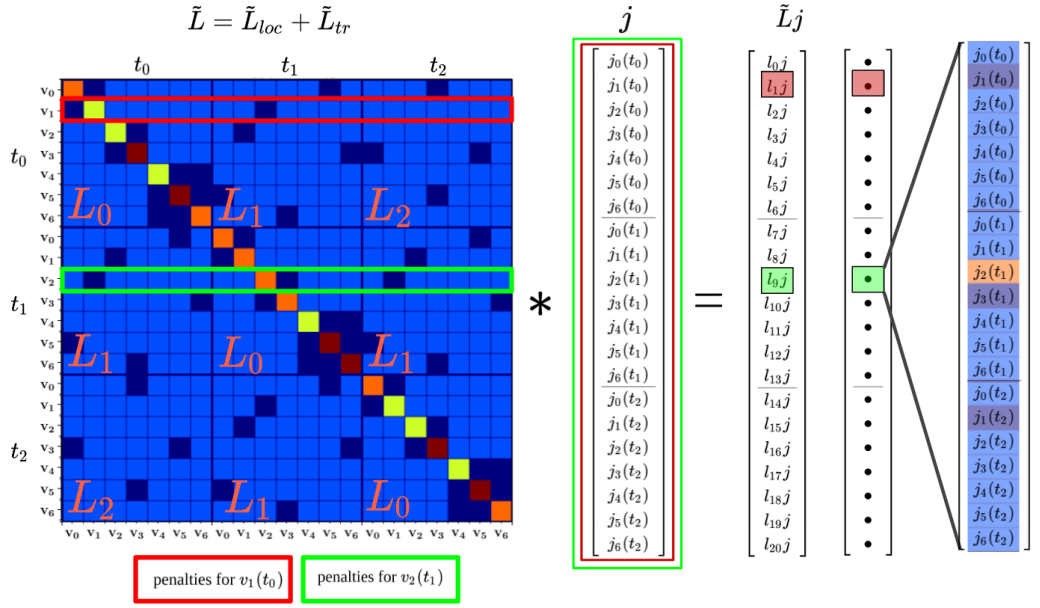

Figure 4.18: Example of $\tilde{\boldsymbol{L}}$ with penalties it imposes of different nodes at different time instants.

and the hypotheses behind them. Firstly, in the standard Laplacian ($\boldsymbol{L} = \boldsymbol{D} - \boldsymbol{A}$, here $\tilde{\boldsymbol{L}}_s$) the sum of each row is equal to 0. This means that the preferred solutions would be the ones where *all* connections of a given node have the same amplitude. Consequently, highly connected nodes would have higher values on the diagonal and would be more heavily penalized. We were interested to see the impact of the 2 components in the regularization term: the local and the tractography-based one, by using the classic l_2^2-norm term (see A1 case from Table 4.2).

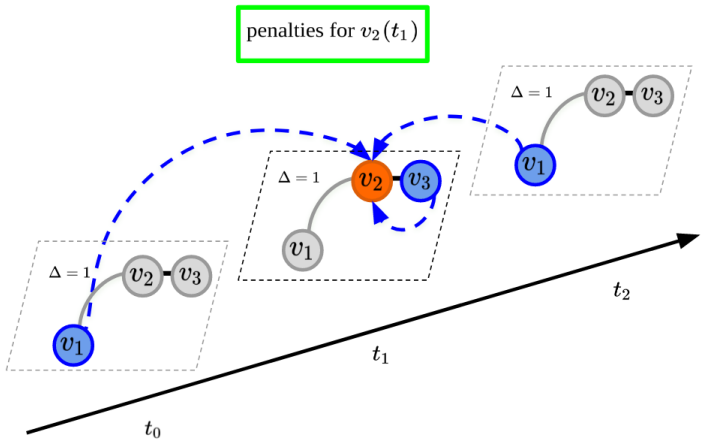

Figure 4.19: Illustration of impact of activity of other nodes at different time instants to activity of $v2(t_1)$. The colors correspond to the vector in Figure 4.18 on the right. Note that other nodes exist but only the ones that influence the activity of $v_2(t_1)$ are shown for visual clarity. One important thing to note here is that Laplacians in undirected graphs results in a penalty where the activity of a node at any time t is penalized with the activity of all connected nodes from both *past* and *future* time instants. E.g. we see that v_2 is connected to v_1 with $\Delta_{v_1,v_2} = 1$ and that v_1 influences v_2 both 1 time sample before and after.

The parameter $\beta \in [0, 1]$ balances the contribution of the two graphs. By setting $\beta = 0$, LORETA solution is obtained.
Secondly, let us consider the case B2. The reason behind using $\tilde{\boldsymbol{L}}^* = \tilde{\boldsymbol{I}} - \tilde{\boldsymbol{A}}$ was in order to favour solutions where the activity of a source is equal to the *sum* of activities of its connections. This was done under the assumption that each node's activity (in terms of energy) is distributed, for example:

- to only one connection (i.e. the signal passes through 1 edge in the graph)
- distributed to several connections (the signal passed through multiple edges), where the amplitude each target node receives is inversely proportional to the number of connections

Now, among all solutions that would yield a zero cost, the optimal one *should* be the one that best matches the data. As we mentioned earlier, $\tilde{\boldsymbol{L}}^*$ is a singular matrix. The penalty term $\lambda \boldsymbol{j}^{\boldsymbol{T}} \tilde{\boldsymbol{L}} \boldsymbol{j}$ is quadratic in $\boldsymbol{j}$, but the matrix $\tilde{\boldsymbol{L}}$ is not positive semidefinite, meaning that $\lambda \boldsymbol{j}^{\boldsymbol{T}} \tilde{\boldsymbol{L}} \boldsymbol{j} < 0$ for some $\boldsymbol{j}$. In order to ensure that the value of the penalty term at optimum is equal to 0, it was made quadratic, i.e. $\lambda(\boldsymbol{j}^{\boldsymbol{T}} \tilde{\boldsymbol{L}} \boldsymbol{j})^2 \geq 0$. We will discuss this later in the results section.
Thirdly, the case C3 is rather similar as the ones described above. In this case, similar assumptions regarding the distribution of energy as in $\tilde{\boldsymbol{L}}^*$ exist, the difference is that now this refers only to long-range connections (while the adjacent nodes are expected to have the same or very similar activity as the main node). Another reason for using $(\tilde{\boldsymbol{I}} - \tilde{\boldsymbol{A}}_{tr})$ instead of $(\tilde{\boldsymbol{D}}_{tr} - \tilde{\boldsymbol{A}}_{tr})$ was the fact that some sources have a very high degree (hundreds of long-range connections (> 400), while the average degree is 34 (for subject 105923)), which lead to stronger penalizations of activity

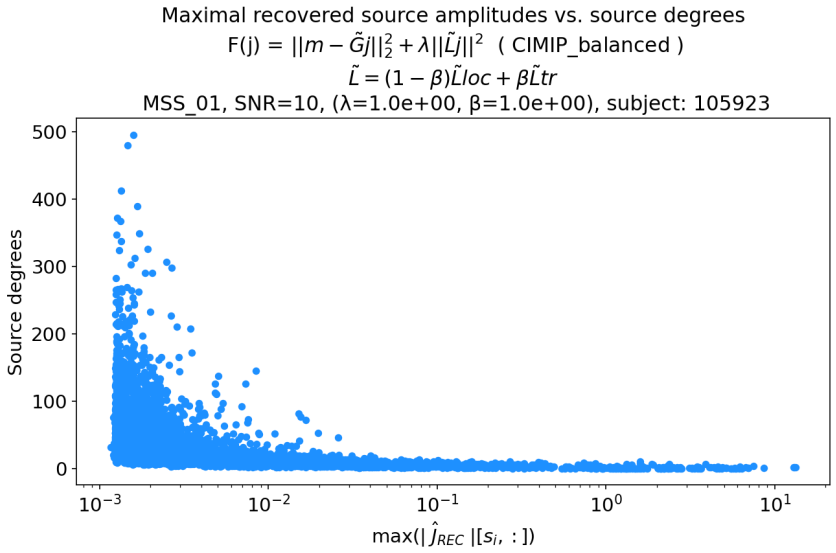

Figure 4.20: Maximal absolute values of recovered source amplitudes vs. source degrees. Here, only long-range connections were considered, i.e. in the Laplacian variant $\tilde{\boldsymbol{L}}_1 = \tilde{\boldsymbol{L}}_{balanced} = (1-\beta)\tilde{\boldsymbol{L}}_{loc} + \beta\tilde{\boldsymbol{L}}_{tr}$, we show for $\beta = 1$, meaning there was no impact of local connectivity. Source degree refers to the number of long-range connections. For clarity, s_i refers to the time course of i^{th} source, while REC in $\hat{J}_{REC}$ stands for "reconstruction". We can see that highly-connected sources were penalized more and had a low reconstructed amplitude. Conversely, disconnected sources had no penalty and some of their amplitudes were a lot higher.

of highly connected sources (see Figure 4.20). Regarding the implementation, the functional $U_{CIMIP}(\boldsymbol{j})$ (for all aforementioned types of $P(\boldsymbol{j})$) was minimized using Conjugate Gradient (CG) method, implementated by *scipy.optimize.minimize* routine in Python. The implementation of CG method in *scipy* deploys a nonlinear conjugate gradient algorithm by Polak and Ribiere [Polak & Ribiere 1969, Nocedal & Wright 2006], a variant of the Fletcher-Reeves method [Fletcher & Reeves 1964].

4.7 Results on Simulated Data

Results of the reconstruction of brain activity from simulated MEG measurements were compared to the **MNE** [Hämäläinen & Ilmoniemi 1994], **LORETA** [Pascual-Marqui *et al.* 1994] and **CGS** [Hammond *et al.* 2013] methods for 5 simulated subnetworks, for 2 SNR values (3 and 10). Firstly, let us show again the simulation (ground truth, GT) for the first and the fifth subnetwork (MSS_01 and MSS_05, respectively). In Figure 4.21 in the top row, we can see MSS_01 activity propagation for 3 time instants, starting from the left lateral occipital region, spreading to the left inferior parietal region and lastly to the left middle temporal region. As a brief reminder, the regions are chosen based on the Desikan-Killany atlas [Desikan *et al.* 2006]. When it comes to MSS_05, we simulated the consecutive activation of 3 brain areas in the right hemisphere: postcentral, precentral and caudal anterior cingulate regions (see the top row in Figure 4.23).

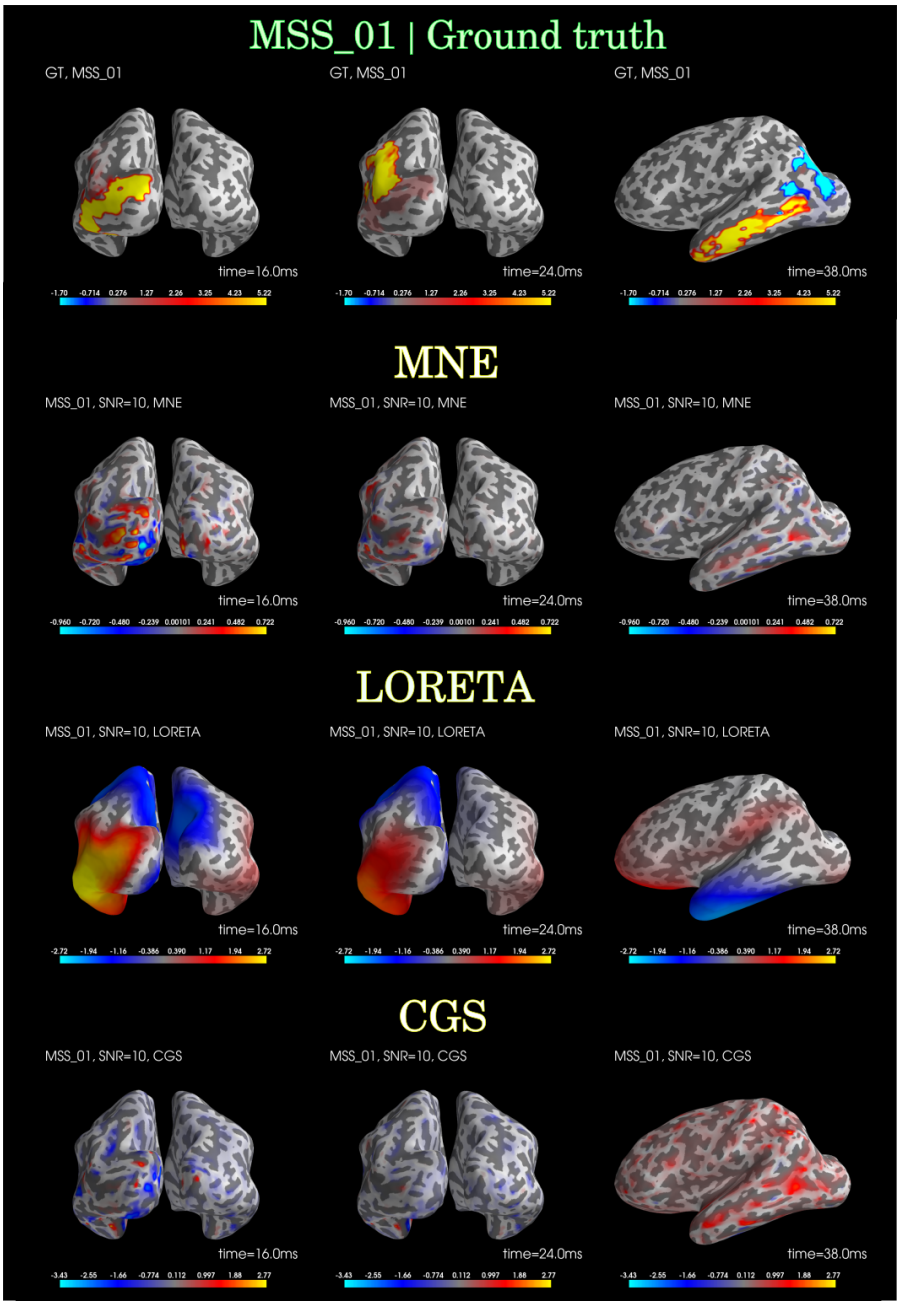

Figure 4.21: Top row: Simulated subnetwork MSS_01. 3 brain areas in the left hemisphere were activated consecutively: lateral occipital, inferior parietal and middle temporal regions. Other rows: Reconstruction of MSS_01 with MNE, LORETA and CGS for 3 time instants (16, 24 and 38 ms), SNR=10.

The activity was chosen to propagate between sources (nodes) that share a long-range connection, with appropriate delays. Moreover, the activity of each node was spread to its adjacent neighbours. Figures 4.21 and 4.23 show the reconstruction

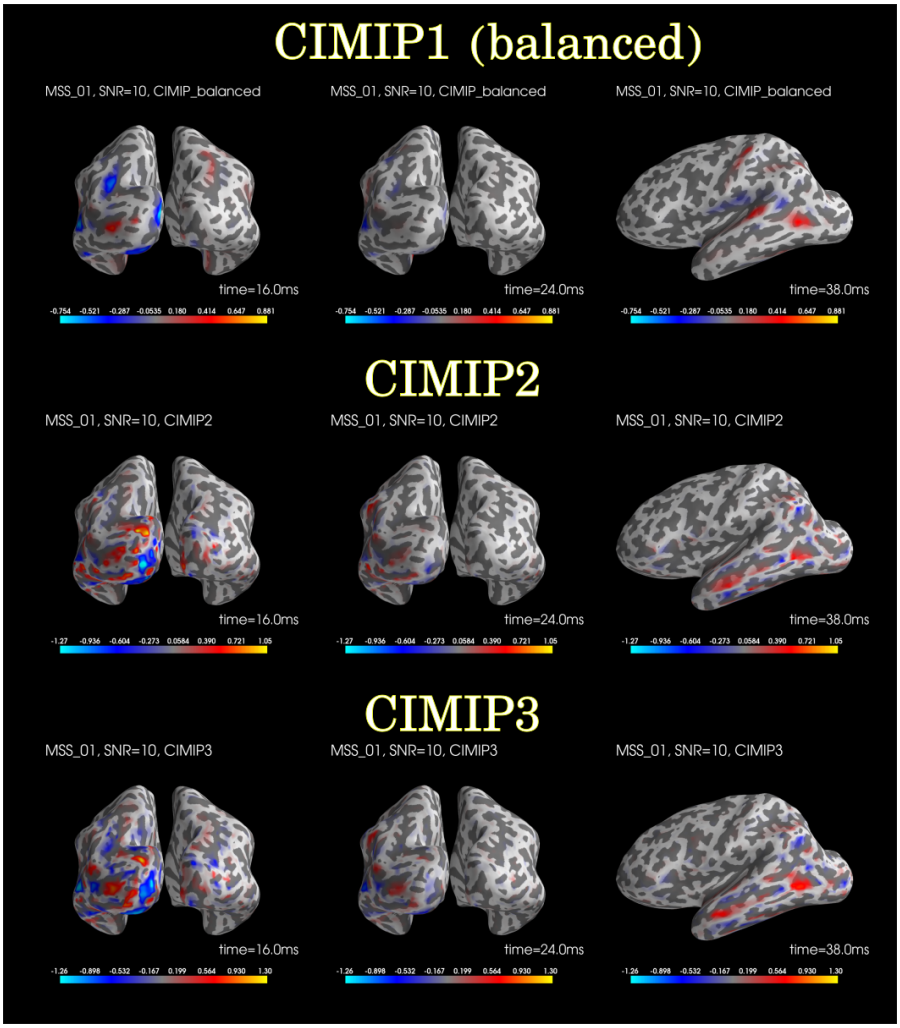

Figure 4.22: Reconstruction of MSS_01 with 3 variants of CIMIP for 3 time instants (16, 24 and 38 ms), SNR=10.

of the first and the fifth subnetwork with MNE, LORETA and CGS for 3 time instants.

MNE gives the solution with the minimum norm i.e. the shortest current vector capable of explaining the measured data. It has prominent activity peaks, which are localized fairly well, but it fails to recover the correct spatial spread. LORETA, on the other hand, leads to over-smoothed solutions since it favours similar activity across adjacent vertices. CGS results we obtained are different than the ones obtained by the authors [Hammond *et al.* 2013] where they found their approach to give improved localization accuracy relative to MNE, and equivalent localization accuracy to LORETA. This could be due to several reasons. First, the dataset is not the same and the acquisition protocol differs as well (e.g. they had single-shell data while we had multi-shell). Second, the softwares we deployed for many steps in the preprocessing pipeline are not the same (such as for MRI tissue segmentation,

leadfield computation and dMRI tractography). Major differences between our tractography pipelines are that (1) they used DTI while we used CSD for the estimation of local orientations of fiber bundles, (2) our tracking algorithms are not the same. For more details see [Hammond *et al.* 2013]. Overall, all these points combined can have an important impact on the results. However, it is worth noting that more accurate CGS reconstructions are possible.

The "optimal" regularization parameters for the CGS method (λ_{loc} and λ_{tr}) were chosen based on the modified L-curve approach, as described in the original paper and obtained with the original implementation in MATLAB, provided by the authors (see Figures 4.21 and 4.23 at the bottom). In Figures 4.25 and 4.26, we show that rather different solutions can be obtained for another set of pairs λ_{loc} and λ_{tr}. We performed CGS reconstruction across 64 pairs in range $[10^{-7}, 1]$ with increments of 10^{-1}. We manually chose the values for the reconstruction shown in Figure 4.25 on the bottom, as results that gave lower localization errors, especially when compared to the ones obtained with automatically chosen parameters. This gave rise to the idea that CGS could perform more accurately if the optimal values were chosen in another way. This illustration was done for qualitative purposes, to highlight the importance of the choice of regularization parameters, which is often disregarded in the literature of M/EEG inverse problems. However, their choice can significantly alter the results and the methods for their choice should be considered carefully.

Figures 4.22 and 4.24 show the reconstruction of MSS_01 and MSS_05 with 3 CIMIP variants, for 3 time instants. Firstly, we can see that CIMIP2 and CIMIP3 result in recoveries rather similar to MNE. This is probably due to the fact that in both cases, we subtracted the identity matrix from the time-dependent long-range connectivity matrix, instead of the degree matrix as in the standard Laplacian (see Table 4.2). Therefore, the regularization matrix corresponding to delays in long-range connectivity had the same diagonal elements as in MNE (identity), which had a larger impact in the reconstruction than the off-diagonal elements (long-range connections with specific delays).

Secondly, let us discuss in more details CIMIP1. We wanted to see the impact of adding tractography-based Laplacian using the CIMIP formulation and examine the relative contribution of local and long-range connectivity components. Let us consider the the penalty term in the form $\lambda||\tilde{\boldsymbol{L}}\boldsymbol{j}||_2^2$, where $\tilde{\boldsymbol{L}}_1 = (1-\beta)\tilde{\boldsymbol{L}}_{loc} + \beta\tilde{\boldsymbol{L}}_{tr}$. Clearly, we can obtain the LORETA solution for $\beta = 0$. By increasing the value of β, more contributions are given to long-range connections while the impact of local connectivity decreases. We can see this impact in Figure 4.29 where reconstructed source time courses are shown across different values of β. We can see that (1) fewer sources get active and (2) their amplitude start to decrease. Interestingly, when $\beta = 1$ (no impact of local connectivity) only a few sources get active with high amplitudes. The corresponding data fits are given in Figure 4.30. The chosen value $\lambda = 1.015$ was chosen to be the one obtained as the optimal value for LORETA

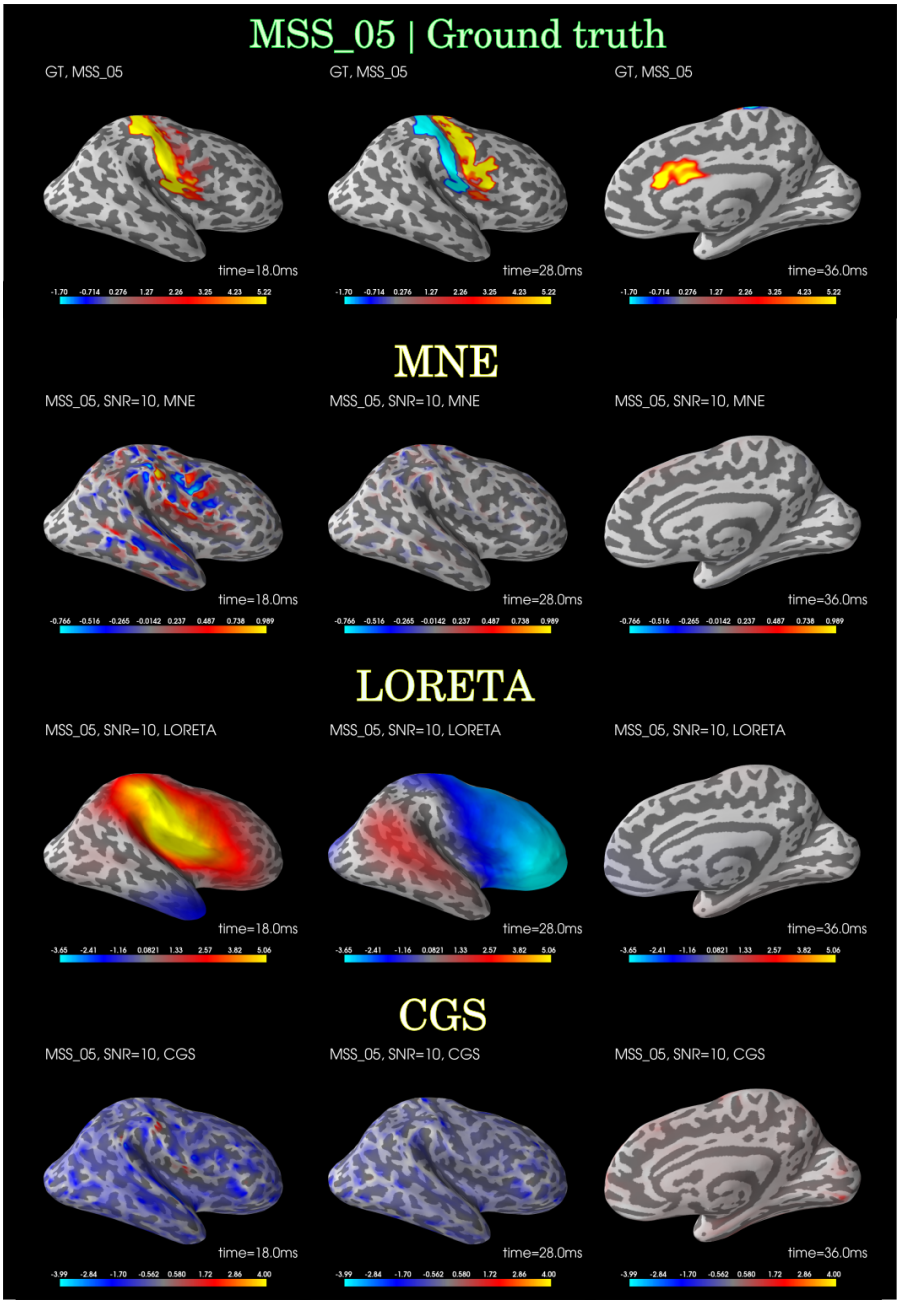

Figure 4.23: Top row: Simulated subnetwork MSS_05. 3 brain areas in the right hemisphere were activated consecutively: postcentral and precentral gyri and caudal anterior cingulate gyrus. Rows below: reconstruction of MSS_05 with MNE, LORETA and CGS for 3 time instants (18, 28 and 36 ms), SNR=10.

reconstructions, according to the aforementioned L-curve criteria. Note that if for different values of λ, the same range of values of β would yield different results.

Average PtP and CoG errors across different amplitude thresholds are shown in Figures 4.31 and 4.32 respectively. In the sense of these metrics, in our experiments,

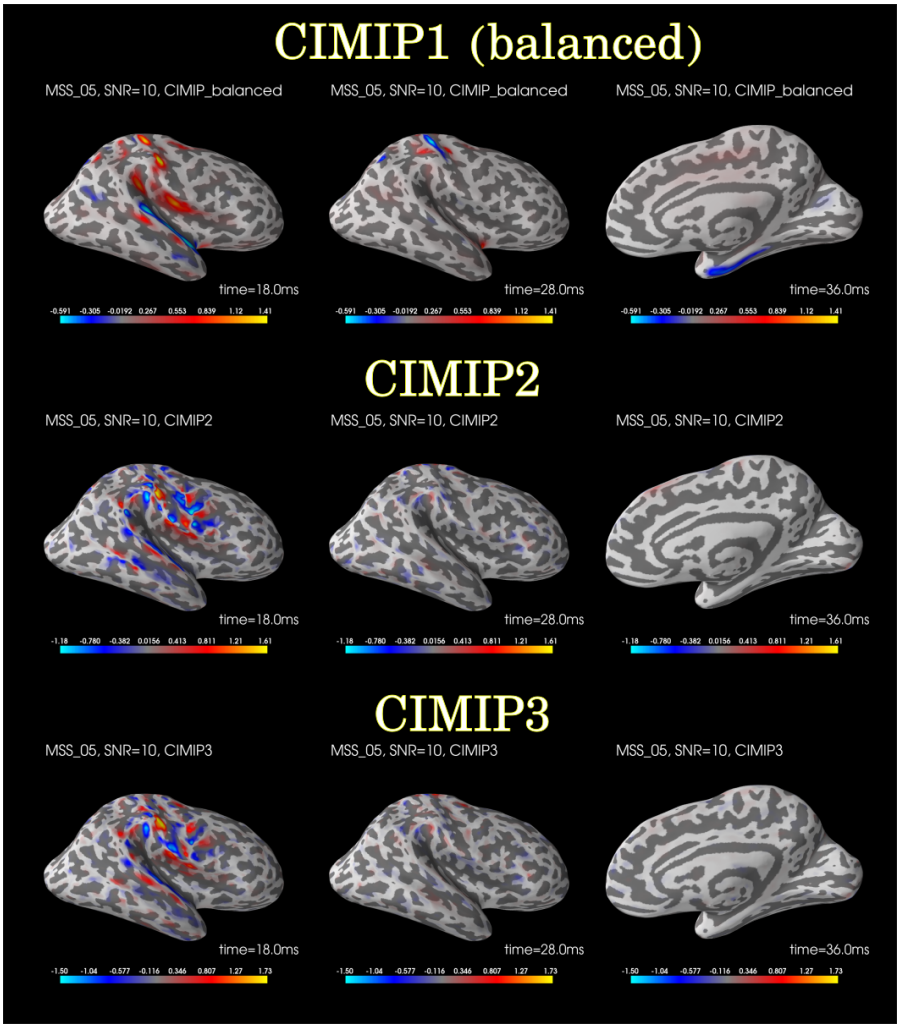

Figure 4.24: Reconstruction of MSS_05 with 3 variants of CIMIP for 3 time instants (18, 28 and 36 ms), SNR=10.

CGS had higher localization errors when compared to other methods. When it comes to PtP errors, MNE gives more accurate results for lower threshold values, while CIMIP3 outperforms it for larger ones ($\tau > 0.5$). This is probably due to the fact that CIMIP3 reconstructs more sources with low amplitudes than MNE (although this is not clearly reflected with the figures, since they show only 3 time instants). A possible reason why this happens is because the constraint in CIMIP3 (See Table 4.2) favours solutions with temporal smoothness across long-range anatomically connected sources (with corresponding delays). So for example, if an active source distributes its activity to many other sources it is connected to, and divides its amplitude across them, this would be a favourable scenario for this type of constraint. Recall that, if multiple peaks with the same amplitude are found, a centroid among them is taken. Consequently, for lower values of τ, peak locations would vary a lot more in CIMIP3 than in MNE.

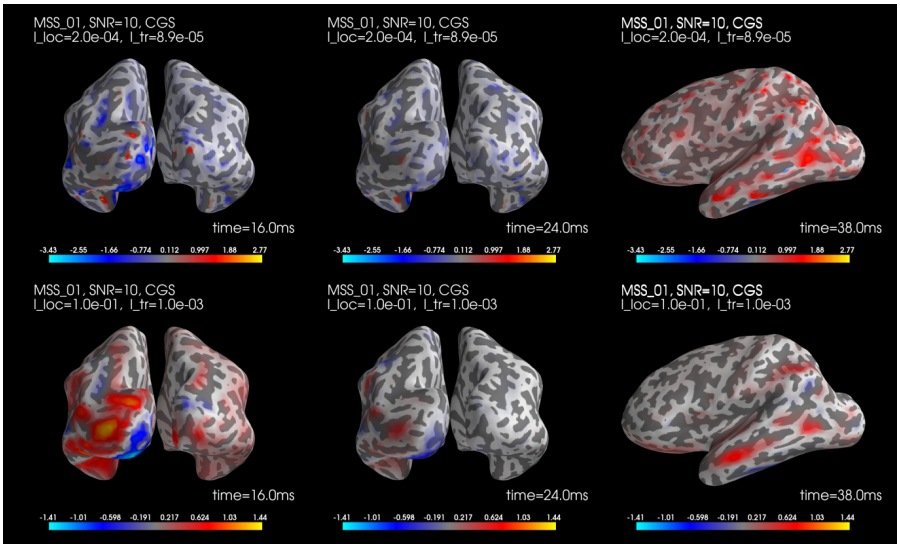

Figure 4.25: CGS reconstruction of MSS_01 for 3 time instants (16, 24 and 38 ms), SNR=10. Top: reconstruction using regularization parameters with the modified L-curve algorithm as described and implemented by [Hammond *et al.* 2013]. Bottom: reconstruction obtained using manually chosen values of λ_{loc} and λ_{tr} (denoted as l_loc and l_tr in the figure, respectively).

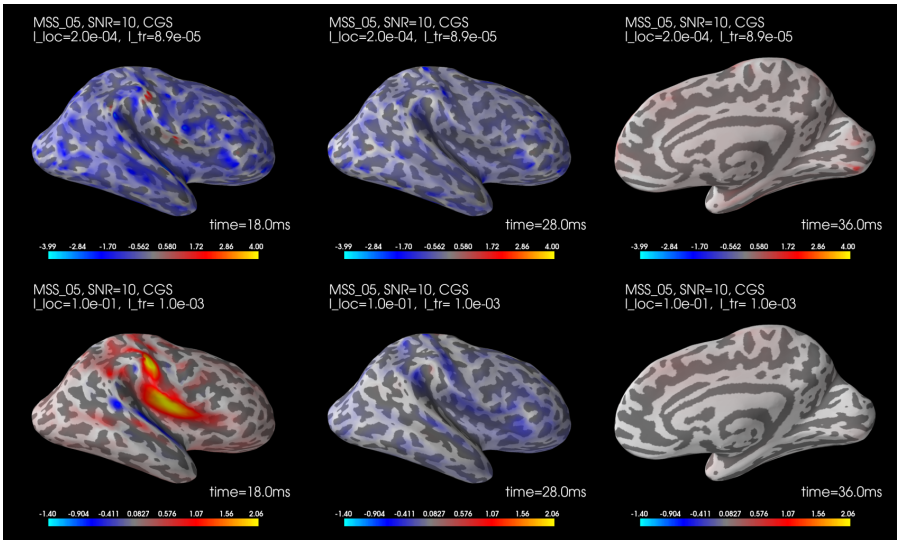

Figure 4.26: CGS reconstruction of MSS_05 for 3 time instants (18, 28 and 36 ms), SNR=10. Top: reconstruction using regularization parameters with the modified L-curve algorithm as described and implemented by [Hammond *et al.* 2013]. Bottom: reconstruction obtained using manually chosen values of λ_{loc} and λ_{tr} (denoted as l_loc and l_tr in the figure, respectively).

As an example, in [Lin *et al.* 2006] they use CoG error with the threshold set to 50% of the maximal amplitude. Regarding the CoG errors, MNE outperforms all methods consistently regardless of the threshold. A possible reason is the fact that in CoG error, *all* source locations are weighted by the their amplitudes (See Eq.(4.9)). So due to the fact that all methods tend to overestimate the spatial spread (including MNE but to a smaller extent), even with lower amplitudes (or

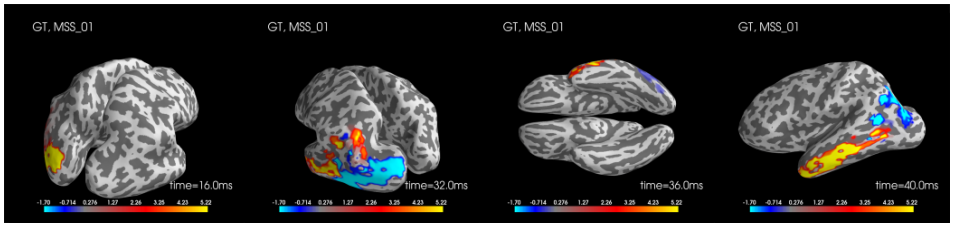

Figure 4.27: Another illustration of the ground truth of MSS_01, for different views, for 4 time instants (16, 32, 36, 40 ms).

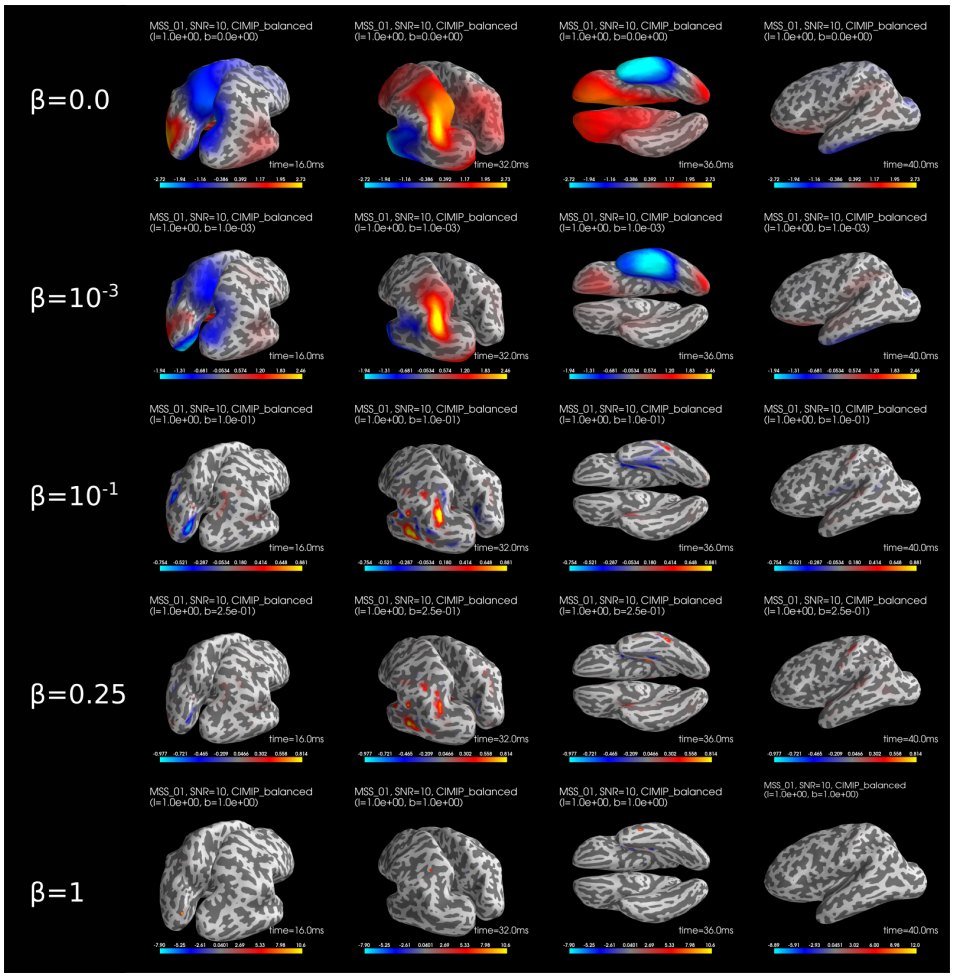

Figure 4.28: Reconstruction with CIMIP1 across different values of β for 4 time instants (16, 32, 36, 40 ms), SNR=10.

similar ones, in the case of LORETA), this leads to a localization bias in the center of gravity.

When looking at the ROC curve (Figure 4.33) LORETA has the highest AuC score. This is probably because LORETA overestimates the spatial extent of the recovered activity (with similar amplitudes), so it results in very few False Negatives (and therefore in high TPR). Also, the fact that the number of active sources (TP) is

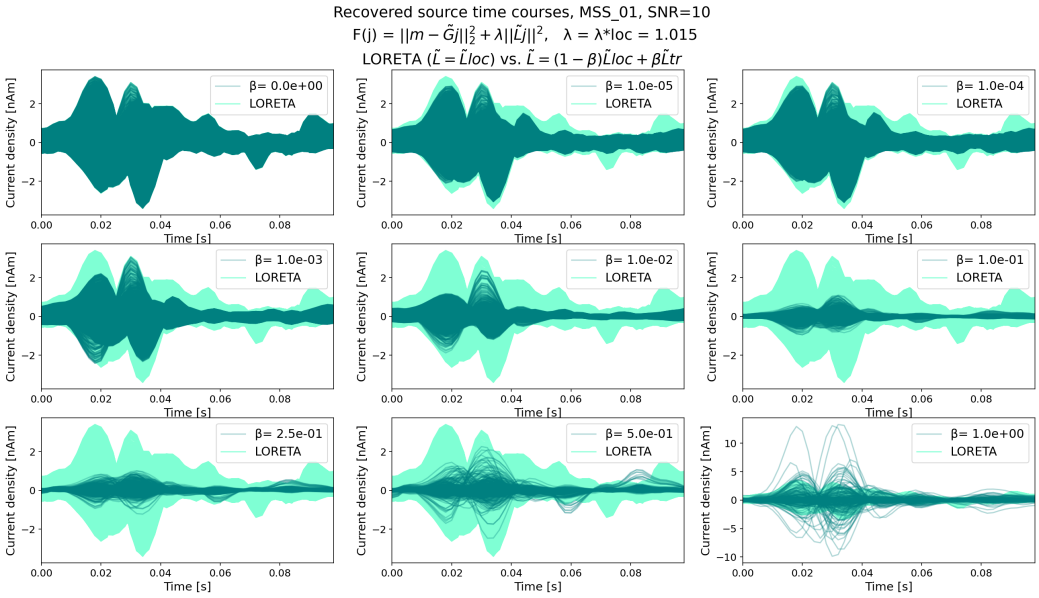

Figure 4.29: Recovered source time courses with CIMIP1, across different values of β.

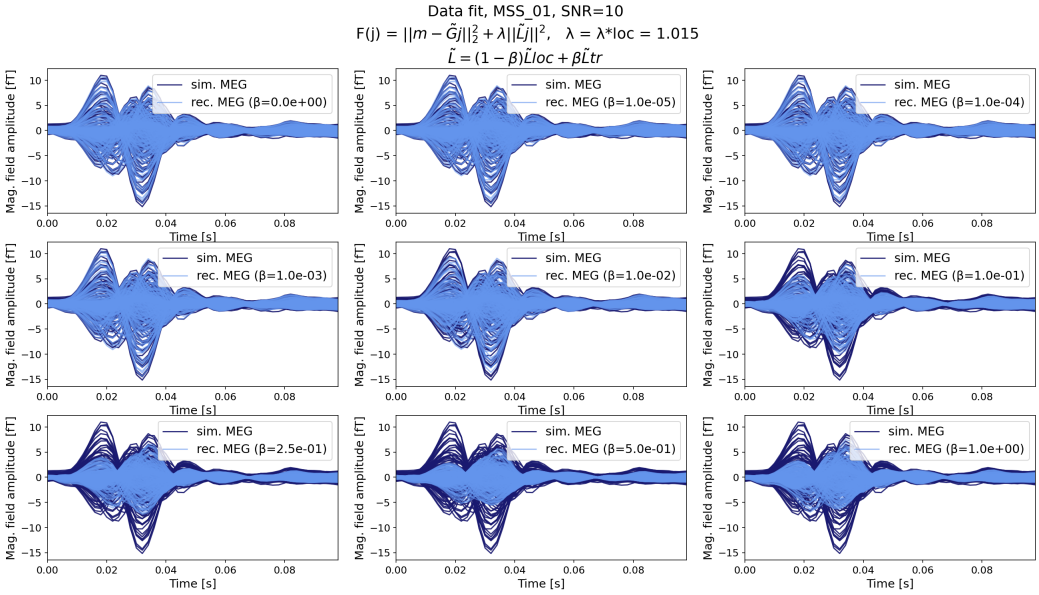

Figure 4.30: Data fit for different solutions obtained with CIMIP1, across different values of β.

much larger than the number of inactive sources (TN) may cause the TPR to be the dominating part in the ROC curve, and therefore in the AuC score.

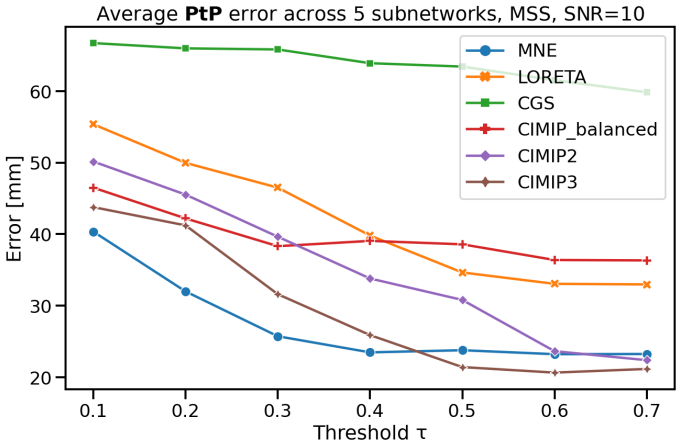

Figure 4.31: Average PtP errors across 5 subnetworks for SNR=10.

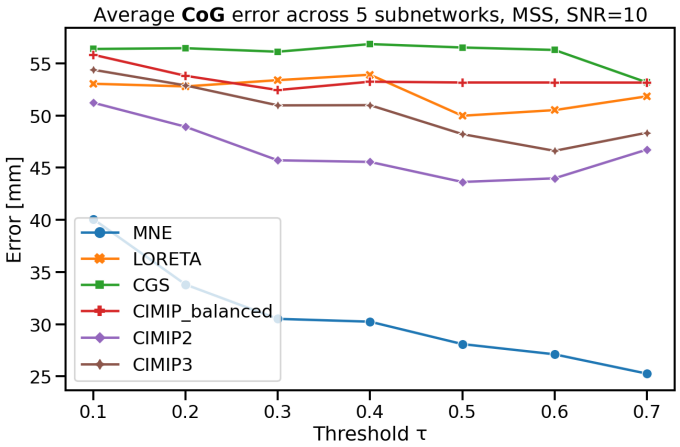

Figure 4.32: Average CoG errors across 5 subnetworks for SNR=10.

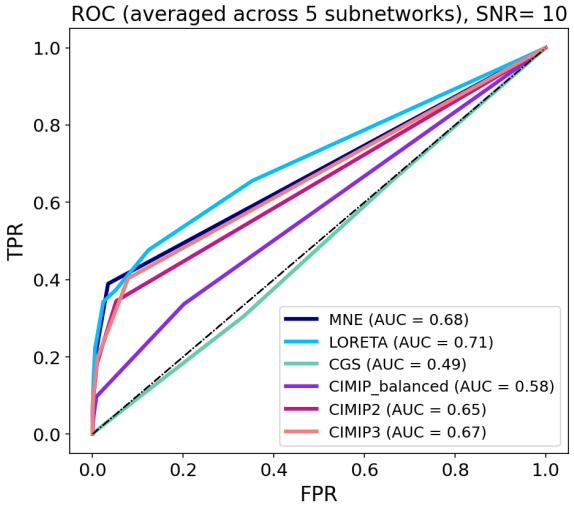

Figure 4.33: ROC curve for all reconstruction methods, for SNR=10. AUC values are the average values across 5 subnetworks.

4.8 Results on Real MEG Data

We tested our source reconstruction method on the real MEG data for a visuomotor task, in which the subjects were asked to move their right/left fingers or toes after seeing a visual stimulus. Details on the preprocessing of HCP data are described in Chapter 3, in Section 3.4. Quantification of the results on the real data is rather challenging since we do not know the ground truth, i.e. the source-level brain activity that actually happened in the brain during the experiment. For this reason, it is convenient to examine reconstruction methods for specific tasks, where the areas involved have been examined in former studies.

Recall from Section 1.2.3.2 that the areas in the brain in charge of visual processing are located in the occipital lobe, while the main motor areas are the primary motor cortex (M1), premotor area (PMA) and supplementary motor area (SMA). In HCP MEG data the presentation of visual stimuli is not dichotic, i.e. it is presented to both eyes, so the activation of in brain areas in charge of processing visual information is expected to be bilateral. On the other hand, the activation during motor planing and motor execution happens in the motor areas M1 and SMA ares have been shown to be mostly active (though not exclusively) contralateral to the hand movement [Martuzzi *et al.* 2006, Frässle *et al.* 2021] mostly associated to the motor potential (MP), while the spatial distribution of the premotion positivity (PMP) is more widespread and bilaterally symmetrical [Deecke *et al.* 1969].

MEG data for left and right foot movement is shown in Figures 4.34 and 4.36, respectively, at the top, along with MNE and LORETA reconstructions. CGS, CIMIP2 and CIMIP3 reconstructions are shown in Figures 4.35 (left foot) and 4.37 (right foot). Recall that CIMIP1 includes gradually adding tractography-based Laplacian as a constraint using the CIMIP formulation to the existing LORETA solution, with the aim to examine the relative contribution of local and long-range connectivity components. CIMIP1 reconstructions across different values of β (right foot) are shown in Figure 4.38.

Most methods recover the visual response, which is expected to appear $\sim$100ms after the visual stimulus, notably in the occipital lobe. However, none of the methods recover the motor response which is expected in the M1, PMA and SMA (corresponding to precentral, caudal middle frontal and partially superior frontal region in the Desikan atlas). It seems to appear in the LORETA reconstructions around 200 ms, though the activity is rather smeared and spread over other areas as well. Also, reconstructions across more subjects need to be done in order to draw final conclusions. This will be further elaborated in Chapter 5. One possible reason for the lack of the expected motor response is the fact that the stimulus onset is the visual cue. We mentioned in Section 3.4.0.1 that the subjects were asked to perform one of the 4 limb movements after seeing a visual cue. Recall that evoked data for each movement type are the averages across 80 epochs (80 repetitions of the same movement). This is a common technique for estimating stimulus-evoked activity, i.e. to obtain the average responses of the event related potentials. This averaging was done with HCP "eravg" pipeline, by segmenting the trials to time windows of

–1.2 to 1.2 s before and after the visual cue onset. We later extracted 400 ms of data following the visual cue.
The first evoked response in the brain that comes after the given trigger (visual cue) is the visual response. After epoching, this response remains prominent since it has a high amplitude and it appears first. The visual response should be followed by a motor response. However, the timing of the motor response has a higher variability across epochs than the visual one, and also has a lower amplitude. Therefore, it tends to get smeared during epoch averaging and consequently, does not appear very prominently after averaging, in the evoked data.
A possible way to leverage this issue would be to trigger the epochs at the peak of the visual response and then average them to make the evoked data. In this case, we would take the time sample of the peak of the visual response for each epoch and make that sample the "new" trigger. This way the peak of the motor response would most probably be less smeared and thus more prominent. Since the new trigger would be the peak of the visual response in each epoch, it doesn't necessarily have to be the same time sample, i.e. an inter-epoch variability of this time point would arise. Another option would be to take the average time sample where the visual peaks appear across epochs and than take that sample as a trigger for all epochs. This could be addressed in the future studies.

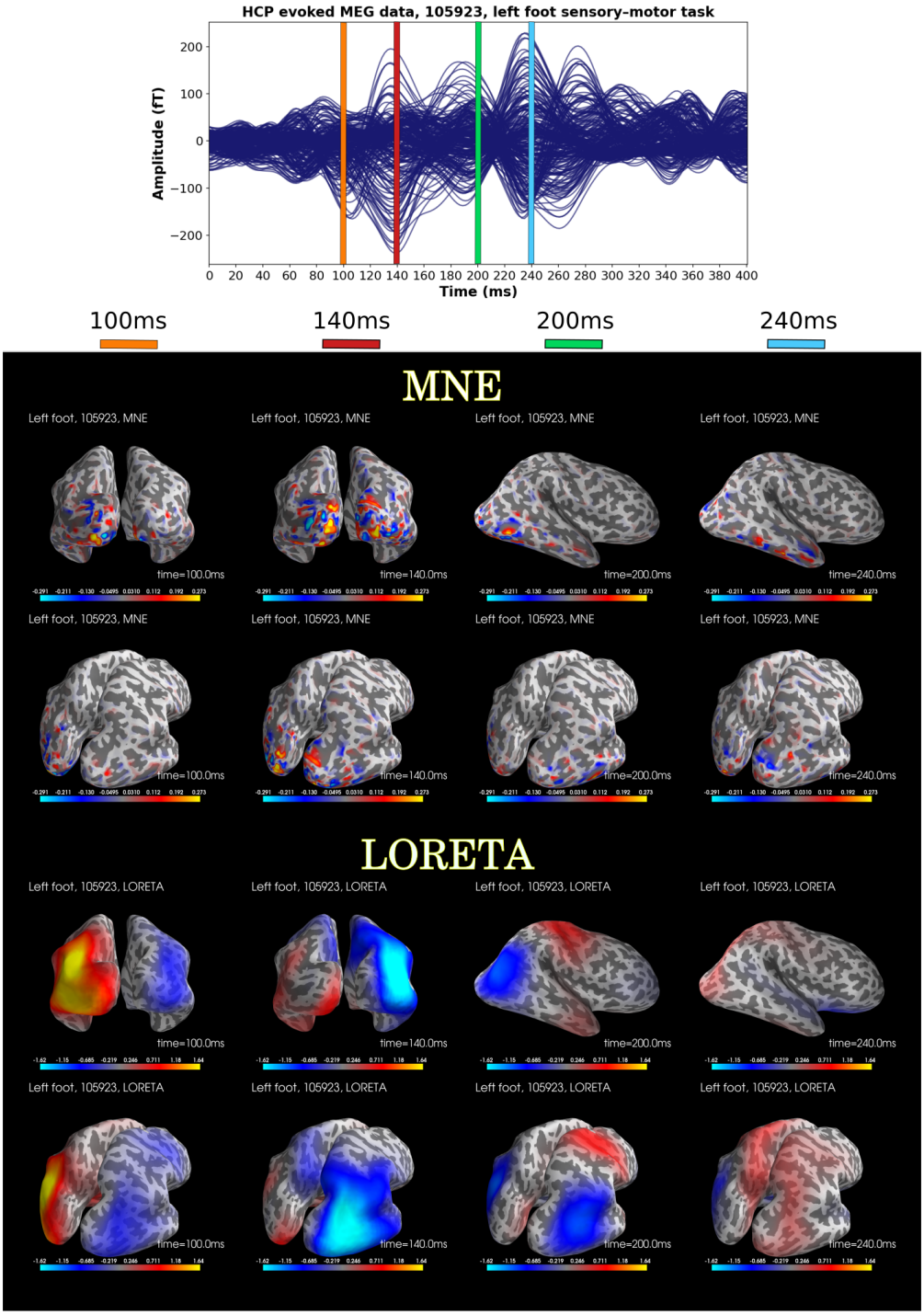

Figure 4.34: HCP left foot visuomotor task. Top: real evoked MEG data. Rest: MNE and LORETA reconstructions (subject 105923).

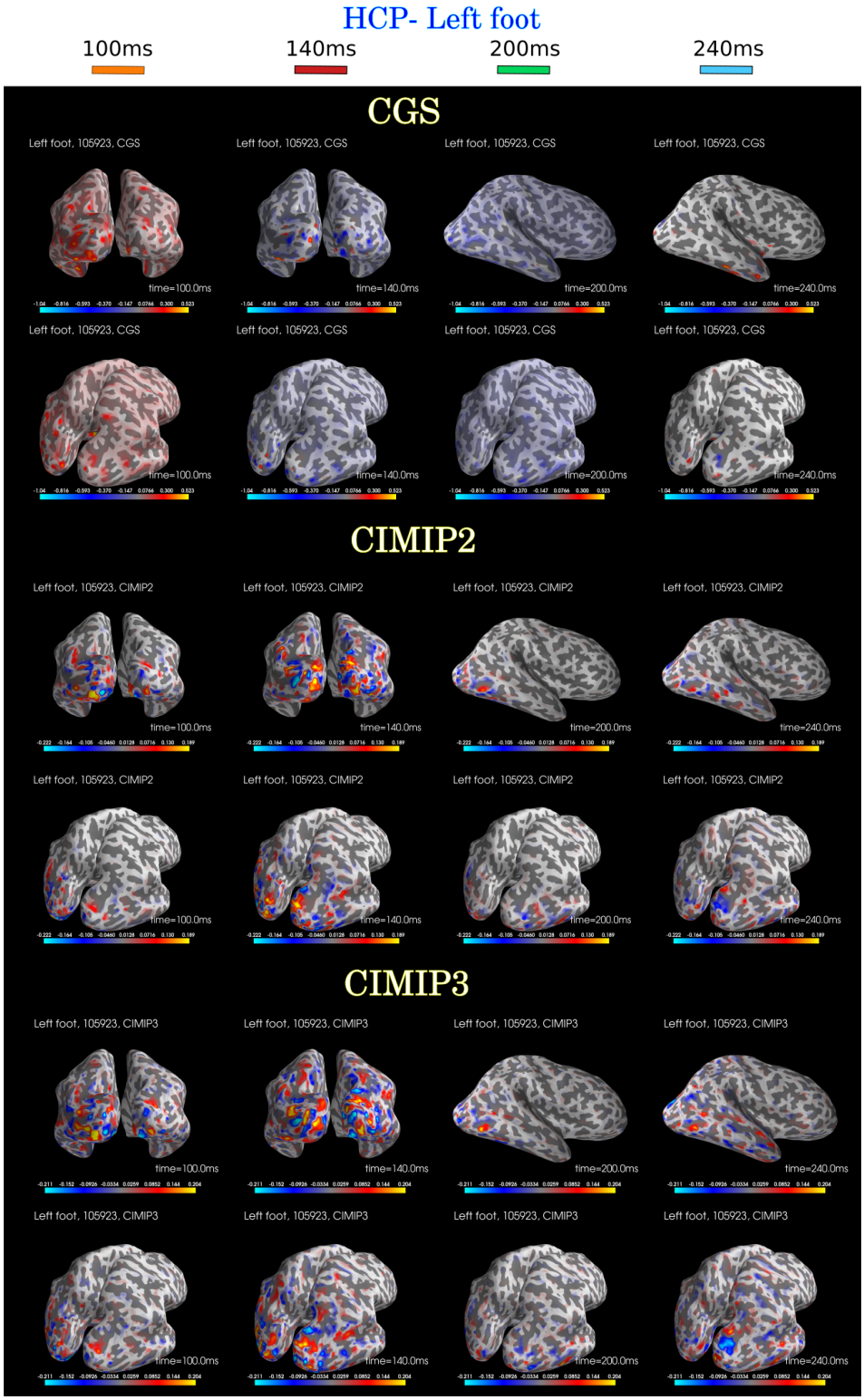

Figure 4.35: HCP left foot visuomotor task. CGS, CIMIP2 and CIMIP3 reconstructions (subject 105923).

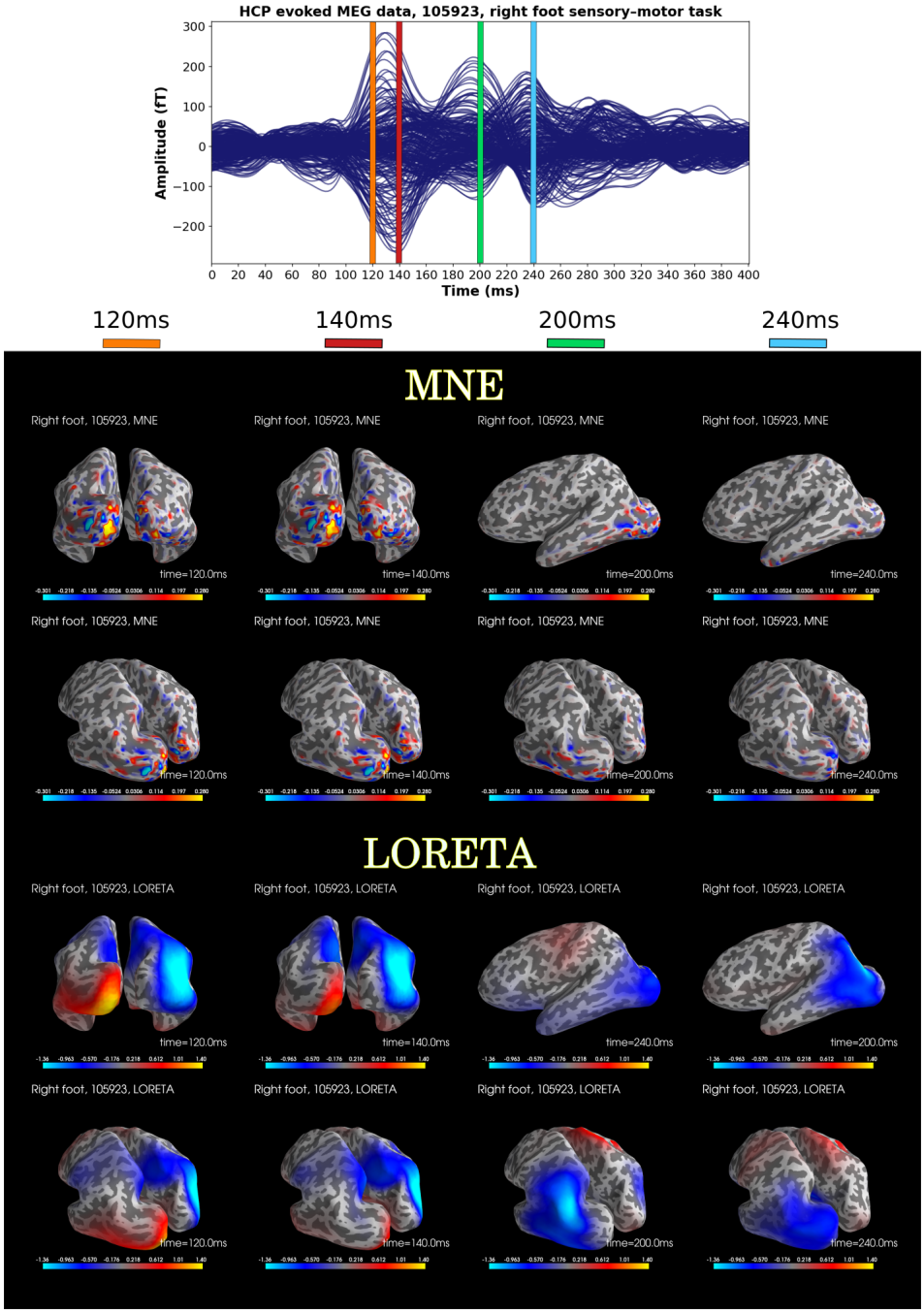

Figure 4.36: HCP right foot visuomotor task. Top: real evoked MEG data. Rest: MNE and LORETA reconstructions (subject 105923).

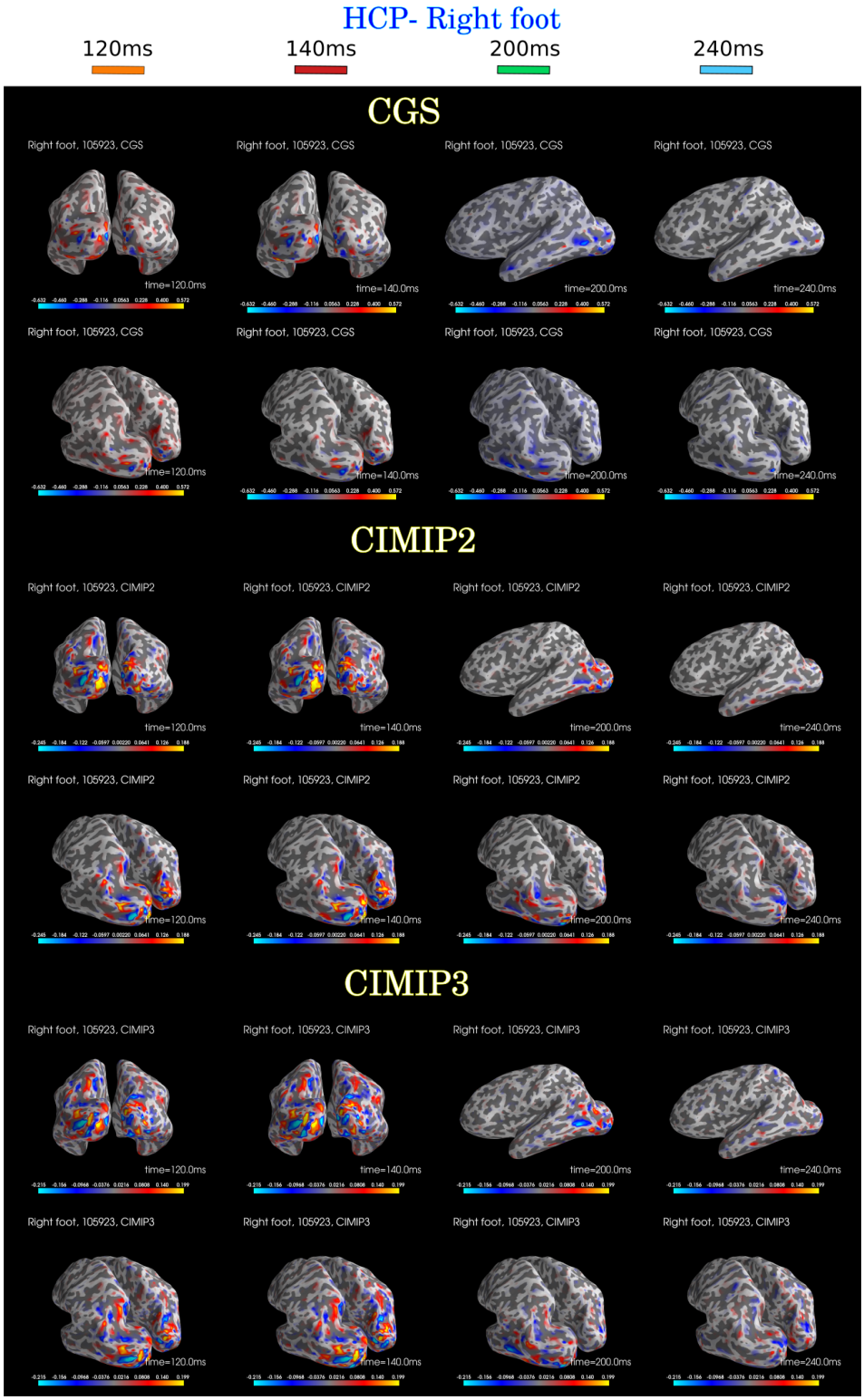

Figure 4.37: HCP right foot visuomotor task. CGS, CIMIP2 and CIMIP3 reconstructions (subject 105923).

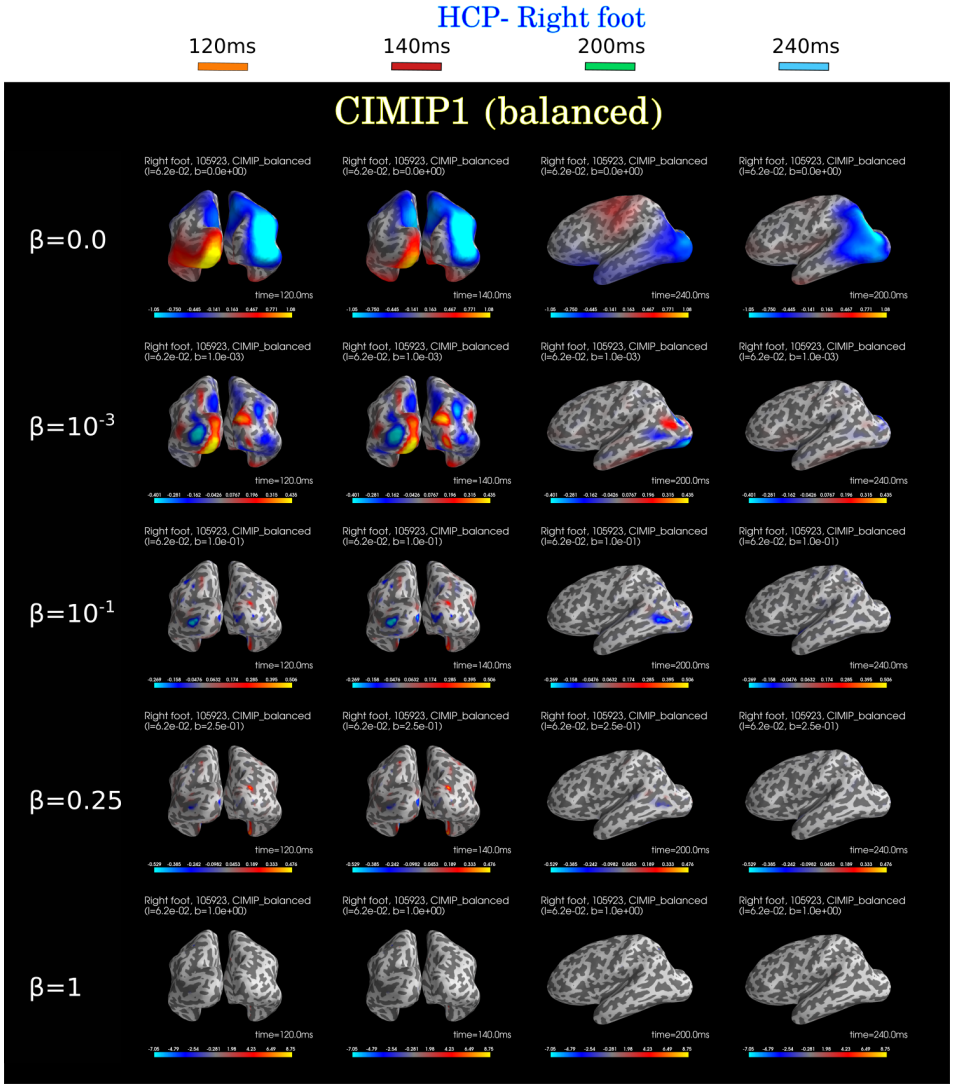

Figure 4.38: HCP right foot visuomotor task. CIMIP1 reconstructions across different values of parameter β (subject 105923). LORETA solution is obtained for $\beta = 0$. Similarly as in synthetic data, when $\beta = 1$ there is no impact of local connectivity, only long-range connections comprise the penalty. Although it seems there is no recovered activity for $\beta = 1$, a few (disconnected) sources do get activated with very high amplitudes (however they are not clearly visible at these specific views and time instants).

4.9 Limitations

There are a few limitations of the CIMIP approach. Although the formulation as in Eq.((4.26)) allows us to treat a data window of arbitrary size as a single problem, the computational time required for the inversion increases linearly with the number of time samples. Another limitation is that all sources that share long-range connections with the corresponding delay are treated with equal probability of activity. As already mentioned, information is transferred between different cortical sources through white matter fibers. Although neural activity has been widely studied the microslace level, at the level of individual neurons and axons [Buzsáki & Draguhn 2004, Buzsáki *et al.* 2012], macroscale brain activity still has many open questions.
Macroscale M/EEG and electrophysiological studies showed that neuronal processes at different frequency ranges can have different functional associations, such as sleep rhythms, memory processes, processes related to sensation, executive functions (like working memory), visual and other task processing [Becker & Hervais-Adelman 2020, Buzsáki & Draguhn 2004]. Regarding the nature of information transfer between brain regions, there are a few open questions:

1. **What is the number of streamlines used for information transfer?**
   Currently, there is no invasive or non-invasive technique to infer how many structural connections are used for information transfer in the human brain. Even if we know that neural signals were transmitted from e.g. region A to region B, there are multiple sources that connect them (many-to-many connections).
2. **How the number of streamlines influence the amplitude of neural activity?**
   It is well known that action potentials (APs) need to have minimal amplitude in order to be transmitted. Up to our knowledge, on the macroscale level, it still unclear if signal attenuation happens during information transfer and how it is related to the number of connections used for it. That is, if a node distributes its activity to many other nodes, does the amplitude in all of them remain the same or it is divided across them. If divided, what are the properties of such a distribution and what does it depend on? Intrasurgical ECoG studies [Filipiak *et al.* 2021] measured transmission delays measures based on propagation of Cortico-Cortical Evoked Potentials, induced with intrasurgical direct electrical stimulation, and showed empirically a positive correlation between streamline lengths and counts with the delays and a negative correlation with amplitudes of N1 peaks (i.e. the amplitudes decrease with streamline length). Nevertheless, the number of streamlines cannot be assessed with this technique.
3. **What is the impact of connectivity strength?**
   Recall from Section 3.6 that we constructed the long-range connectivity matrix by binarizing a streamline count matrix. Such connectivity matrix only represents the presence or absence of a long-range connection and does not assess any notion of structural connection strength. The strength of the biological

connectivity within the brain spans over several order of magnitudes [Bassett & Bullmore 2017], so a low number of streamlines in the streamline count matrix does not necessarily correspond to a false negative connection. Also, it is worth noting that dMRI-based tractography is not quantitative per-se, so it should be complemented in order to associate to each streamline the corresponding connectivity strength. Tractography filtering techniques have been developed as post-processing techniques on an existing tractogram, with a goal to assign to each streamline a quantitative marker of the connectivity strength. A notable example is SIFT2 (Spherical-deconvolution Informed Filtering of Tractograms) [Smith *et al.* 2012] which associates weighting factors to each streamline, that can be interpreted as the mean cross sectional area along the streamline. However, it is questionable how this would impact the velocity and how it could tell us which connections were actually used for the information transfer. In addition, these methods come with limitations as well. It has recently been shown that tractography filtering techniques change the topology of brain networks, and therefore alter network metrics both in the pathological and the healthy cases [Frigo *et al.* 2020].

Let us discuss the limitations of the used regularization. There are a a few limitations of the Laplacian operator, such that it is:

(i) **Isotropic across space**
All connections are treated equally (with an equal probability of activity). Imagine a source in region A (s_A) is connected to multiple sources in regions B and C. If a signal transmission happened between s_A and one or more sources in region B, all long-range connections between s_A and sources in both regions B and C will still be favoured in an equal manner. One potential way to overcome this issue would be to introduce a sparsity constraint on the number of active sources or to "mask" the source space and consider only a subset of sources.

(ii) **Isotropic across delays**
Smooth solutions are favoured between connected sources for a specific delay along the whole time window, even though connection(s) might have been active only during a certain time slot.

(iii) **Agnostic to directionality**
See again the toy example in Figure 4.17. Each block L_k of the Laplacian is symmetric, $L_k[n_{target}, n_{source}] = L_k[n_{source}, n_{target}], (k = 0, ...T - 1)$. On the other hand, the activity was simulated in a *directed* way, where the nonzero elements are at positions $[n_{target}, n_{source}]$. This leads to a significant discrepancy between the simulated data and the operator used to reconstruct it.

Therefore, the Laplacian operates on the whole graph, favours smooth solutions across all connections, for all delays, regardless of the direction of each connection. Another limitation is the identity on the diagonal on CIMIP2 and CIMIP3, which yields solutions that looks very similar to MNE and smoothness across all specific

delays is not promoted enough. Last but not the least, another issue is that the penalty of all CIMIP variants at ground truth is greater than zero ($\mathrm{P}(\boldsymbol{j}_{GT}) > 0$)), so the value of the cost function is also greater than zero. This is not surprising due to the fact that there is a discrepancy between the simulated data and the operator used to reconstruct it. In the simulations, only a subset of directed connections were used, while the Laplacian in the reconstruction was made from the whole undirected tractogram. The question is now– what is the optimal solution? The solutions obtained are only optimal in the sense of the constraint. This issue will be addressed and discussed in more details in Chapter 5.

4.10 Conclusion

In this Chapter, we first discussed the importance of including the delays in the M/EEG inverse problem. We mentioned some of the existing techniques used for the choice of regularization parameters and explained in more details the L-curve since it is the one used in this thesis. Moreover, we described the evaluation error metrics used to quantify the performance of different reconstruction methods. Basic concepts in graph theory were described, as well as the role of the Laplacian as a smoothness constraint in inverse problems. We introduced the second contribution of this thesis, Connectivity-Informed M/EEG Inverse Problem (CIMIP), to solve the M/EEG inverse problem, where prior transmission delays supported by dMRI are included to enforce temporal smoothness across anatomically connected sources. We have shown different 3 different variations of the CIMIP regularization matrix and the hypotheses behind them. Furthermore, we showed results for both simulated and real data and compared them with 3 different state-of-the-art reconstruction methods. We also highlighted the limitations and open questions regarding the proposed approach. Lastly, since the impact of adding delays supported by long-range connectivity is not completely clear and its potential not fully exploited, an extension of the CIMIP approach is introduced in Chapter 5.

Chapter 5

Optimal Masked Laplacian

Contents

Overview

The aim of this Chapter is to present a method that addresses and partly resolves the limitations of the CIMIP approach presented in Chapter 4. Most of the pitfalls related to CIMIP were related to the nature of the Laplacian operator. Recall that the Laplacian operates on the whole graph, favours smooth solutions across all connections, for all delays, regardless of the direction of each connection. Therefore, in this Chapter, we aim at addressing the impacts of the following aspects:

(1) **Restraining the source space to a few regions**
We mentioned that the Laplacian is isotropic across space. So what happens if we restrain the source space, i.e. set *a priori* assumptions on the active subnetwork of regions? We will use the term *network of interest* (NoI) to refer to a set of predefined active regions. The networks of interest in the synthetic data are chosen manually. In the real MEG data, they can either be set based on the previous literature findings for the task at interest (here, visuomotor) or inferred from another modality, such as fMRI.

(2) **Directionality**
Diffusion tractography does not provide information about the directionality of the streamlines and therefore, the direction of information transfer. We will examine the role of considering the underlying structural graph as directed, instead of undirected as assumed in Chapter 4.

(3) **Transmission speed**
A white matter tract can be comprised of axons of different lengths, diameters and with different myelination properties. Myelin content plays the key role for the propagation speed of action potentials. To state it simply, the thicker the axon the quicker the signals propagate [Innocenti *et al.* 2014]. In the current framework, we attributed a single speed to all streamlines. We will investigate the impact of considering different transmission velocities and their influence on cortical activity reconstructions.

In this Chapter we first make a recap on the brain ares shown to be active during visuomotor tasks and the networks they belong to needed to integrate the processing of visual information, motor planning and execution. We introduce our last contribution, CIMIP_OML which is an algorithm that (1) searches for an optimal network motif, i.e. an optimal pattern of interaction between different regions and (2) reconstructs the source activity given the found motif. We kept the idea to include transmission delays supported by dMRI to enforce temporal smoothness between time courses or structurally while also addressing the issues of the Laplacian operator. Moreover, we show the found optimal motifs and the source estimates obtained with them, for both simulated and real data. We compare our reconstruction results with 3 different state-of-the-art methods and the CIMIP approach proposed in Chapter 4. Finally, we mention some limitations of CIMIP_OML and highlight some future perspectives.

5.1 Background

Let us make a quick recap of the main brain areas involved with visuomotor tasks. Recall from Sections 1.2.3.1 and 1.2.3.2 that the main motor areas responsible for motor planing and motor execution are the primary motor cortex (M1), premotor area (PMA) and supplementary motor area (SMA) which have different roles in movement. SMA and M1 ares have been shown to be mostly active (though not exclusively) contralateral to the hand movement [Martuzzi *et al.* 2006, Frässle *et al.* 2021] mostly associated to the motor potential (MP), while the spatial distribution of the premotion positivity (PMP) is more widespread and bilaterally symmetrical [Deecke *et al.* 1969]. In the Desikan-Killiany atlans, PMA, SMA and M1 correspond to a large extent to the precentral and the caudal middle frontal regions (See Figure 5.16). When in comes to visual processing, the areas in the brain in charge (V1-V5) are located in the occipital lobe.
Recall from Section 1.7.1 that the structural connectivity in the brain widely determines the types of mental processes and cognitive functions that can be supported, such as memory, learning, vision, motion and many more [Lynn & Bassett 2019]. Although the functional properties of different brain areas are expressed locally, they are the outcome of an interactive network working as an integrated system [Bullmore & Sporns 2009]. In this thesis, our focus was on visuomotor networks and the interactions among different brain regions needed to integrate the processing

of visual information, as well as motor planning and execution. Recent findings suggest that the premotor cortex along with the primary motor cortex, the primary sensory cortex, and the prefrontal cortex are organized in a neuronal network responsible for complex control of movements and sensorimotor integration [Lavrov *et al.* 2021]. Further, the authors in [Ionta 2021] present a summarizing review of the available neuropsychological evidence on the development of visual competences, with a focus on the associated visuomotor integration (See Figure 1.11 illustrating the main cortical areas involved in visual perception and visuomotor coordination). Functional integration is essential since it mediates the union of specialized brain areas [Friston 2002]. It happens through information transfer in the white matter whose physical properties introduce communication delays. The fibers in the corpus callosum play an important role in the interhemispheric interactions both in visuo-visuo and visuo-motor interhemispheric interactions [Kust Küst 2003, Martuzzi *et al.* 2006].

5.2 CIMIP_OML

Firstly, let us make a brief reminder on notation: sources are denoted with s_i, s_j, with indices $i, j = 0, ...S-1$, where S is the total number of sources in the source space ($S = 8196$); time instants are denoted with $t = 0, ...T-1$. Secondly, let us mention that different concepts in this Chapter are described on two spatial scales: the *region scale* (coarser) and the *source scale* (finer). The algorithm for the CIMIP_OML method and most illustrations are depicted on the region scale, since it allows for a simpler explanation of interactions among different brain regions. Nevertheless, in the actual implementation of the algorithm, all computations are done at the source level. Thirdly, let us clarify again some terms to avoid potential confusion. In M/EEG inverse problems a "source" represents an electrical dipole, a small portion of the cortical surface. In graph theory, an edge of a directed graph $e(s_i, s_j)$ connects its "source" s_i to its target s_j. Recall that, to avoid any ambiguity, we refer to a source of an edge as the *origin* of that edge. For example, in the case of a region edge, $origin(E_{12}) = R_1$ means an edge is leaving from region R_1, and it terminates in R_2, i.e. $target(E_{12}) = R_2$. With this in mind, let us denote edges between source pairs with e_k where $k = 0, ...K-1$ (i.e. white matter streamlines). Edges between different regions are denoted with E_{yu}, with indices $y, u = 0, ...R-1$, where R is the number of regions (here, with the Desikan-Killiany atlas $R = 68$). Both source edges and region edges are directed (see Figure 5.1 on the right). It is important to emphasize that each region edge comprises of all directed source edges between these regions (i.e. all directed fiber bundles going from origin region to target region). So, a region edge from R_y to R_u is denoted by $E_{yu} = \{e_k(s_i, s_j) \mid origin(e_k) = s_i \in R_y \text{ and } target(e_k) = s_j \in R_u\}$. Note that diffusion tractography is agnostic to directionality, so we have to consider each fiber bundle as 2 source edges, with opposite directions.

Let us assume we know *a priori* which are the brain regions responsible for some

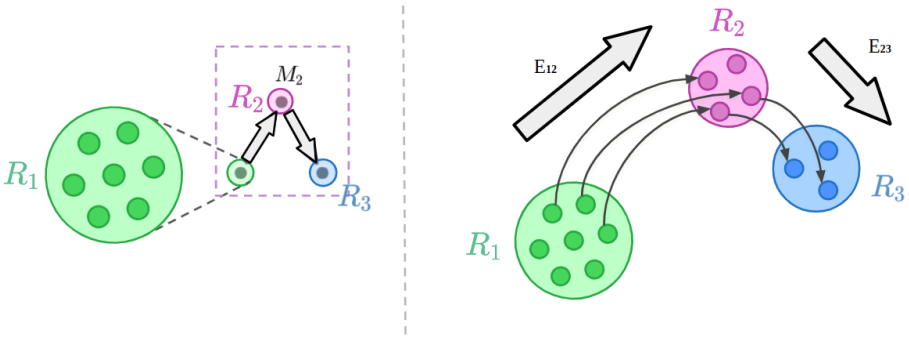

Figure 5.1: Illustration to disambiguate source edges and region edges. Each region edge (big arrows with black contours) comprises of multiple source edges – all directed fiber bundles going from the origin region to the target region (thin grey arrows). This is also an example of a network motif.

particular (e.g. visuoimotor) task. Yet, we do not know what is the pattern of activation, i.e. how is the information transferred between them. As already mentioned, we will use the term **network of interest** (NoI) to refer to the set of predefined active regions. In order to describe the interactions among nodes in a directed graph,

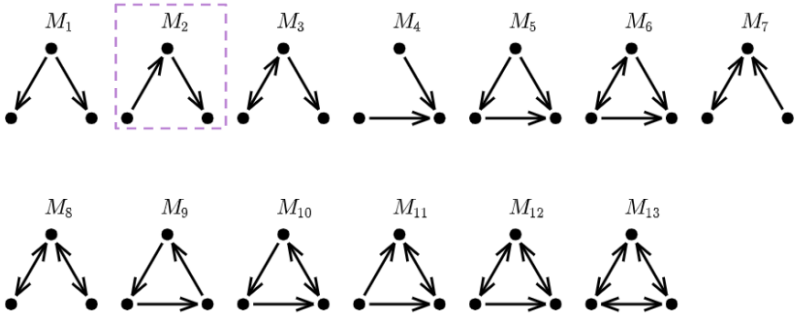

Figure 5.2: Network motifs: all 13 possible directed subgraphs of size 3, with all nodes connected. Adapted from [Xie *et al.* 2021]. Motif M_2 is highlighted as an example since it is also shown in Figure 5.1

we need the concept of **network motifs**. Motifs are patterns of interconnections (or subgraphs) occurring in complex networks significantly more often than those in randomized networks, as first introduced into the field of Systems Biology by Milo and colleagues [Milo *et al.* 2002]. We are interested in the possible interaction patterns among a small given number of brain regions. All motifs i.e. all possible ways to connect 3 nodes with directed edges (without leaving any node disconnected) are shown in Figure 5.2.

Recall from Chapter 4 that before solving the inverse problem with the CIMIP method, we considered all time samples in a single very large problem written as

$$\boldsymbol{m} = \tilde{\boldsymbol{G}}\boldsymbol{j} + \boldsymbol{\varepsilon} \tag{5.1}$$

where $\boldsymbol{j} \in \mathbb{R}^{ST}$ and $\boldsymbol{m} \in \mathbb{R}^{NT}$ are vectors of concatenated source intensities and measurements, respectively, while the forward operator is block diagonal $\tilde{\boldsymbol{G}} = diag(\boldsymbol{G}, ...\boldsymbol{G}) \in \mathbb{R}^{NT \times ST}$.
In CIMIP_OML, we restrict the source space to a *network of interest* (NoI) and impose structurtal connectivity priors on the sources within the predefined NoI. To recover the source-level brain activity, we minimize the following cost function

$$U_{\text{CIMIP\_OML}}(\boldsymbol{j}) = \|\boldsymbol{m} - \tilde{\boldsymbol{G}}\boldsymbol{j}\|_2^2 + \lambda\|\tilde{\boldsymbol{L}}_{OML}\boldsymbol{j}\|_2^2. \tag{5.2}$$

We denote with the regularization matrix $\tilde{\boldsymbol{L}}_{OML} \in \mathbb{R}^{ST \times ST}$ as "Optimal Masked Laplacian", which can be defined as

$$\bar{\boldsymbol{L}}_{OML} = \bar{\boldsymbol{L}}_{loc} + \bar{\boldsymbol{L}}_{tr} + \bar{\boldsymbol{I}} \tag{5.3}$$

$\bar{\boldsymbol{L}}_{OML}$ comprises of

- $\bar{\boldsymbol{L}}_{loc} \in \mathbb{R}^{ST \times ST}$ – masked local Laplacian imposing smoothness between adjacent sources in the network of interest across all time instants. It is a block diagonal matrix with replicates of masked local Laplacians $\boldsymbol{L}_{loc}^* \in \mathbb{R}^{S \times S}$ on its diagonal

  $$\bar{\boldsymbol{L}}_{loc} = diag(\boldsymbol{L}_{loc}^*, ...\boldsymbol{L}_{loc}^*) \in \mathbb{R}^{ST \times ST} \tag{5.4}$$

  $\bar{\boldsymbol{L}}_{loc}$ can be defined as

  $$\bar{\boldsymbol{L}}_{loc} := \begin{cases} \bar{l}_{ti,ti} = +1, & \text{if } i \text{ belongs to the NoI} \\ \bar{l}_{ti,tj} = \bar{l}_{tj,ti} = -1, & \text{if } i \neq j \text{ and } s_i \text{ and } s_j \text{ are spatially adjacent, and they belong to the NoI} \\ 0, & \text{otherwise.} \end{cases} \tag{5.5}$$

  Therefore, $\bar{\boldsymbol{L}}_{loc}$ is symmetric, block-diagonal and singular since it contains zeros on the diagonal at positions of inactive sources.

- $\bar{\boldsymbol{L}}_{tr} \in \mathbb{R}^{ST \times ST}$ – masked tractography-based Laplacian. It is made from the masked incidence matrix as $\bar{\boldsymbol{L}}_{tr} = \bar{\boldsymbol{B}}\bar{\boldsymbol{B}}^T$.
  $\bar{\boldsymbol{B}} \in \mathbb{R}^{ST \times E}$ is the masked incidence matrix of edges between sources in active regions connected via white matter streamlines, with elements

  $$\bar{\boldsymbol{B}} := \begin{cases} \bar{b}_{St+i,k} = -1, & \text{if source}(e_k) = s_i \\ \bar{b}_{S(t+d)+j,k} = +1, & \text{if target}(e_k) = s_j \text{ with a delay of } d \\ 0, & \text{otherwise.} \end{cases} \tag{5.6}$$

  Here, E refers to the number of source edges.
  So the elements of $\bar{\boldsymbol{L}}_{tr}$ are the following

  $$\bar{\boldsymbol{L}}_{tr} := \begin{cases} \bar{l}_{x,y} = \bar{l}_{y,x} = +1, & \text{if } x = y \\ \bar{l}_{x,y} = \bar{l}_{y,x} = -1, & \text{if there is a directed edge from } s_i \text{ to } s_j \text{ with a delay of } d. \\ 0, & \text{otherwise.} \end{cases} \tag{5.7}$$

where $x = St + s_i$ and $y = S(t + d) + s_j$, and s_i and s_j belong to NoI.

- $\bar{\boldsymbol{I}} \in \mathbb{R}^{ST \times ST}$ is a complementary, binary diagonal matrix, added to make $\bar{\boldsymbol{L}}_{OML}$ positive semidefinite. It is defined as

$$\bar{\boldsymbol{I}} := \begin{cases} \bar{i}_{ti,ti} = +1, & \text{if source } s_i \text{ is disconnected in the network of interest i.e. has neither local or long range connection in it } (\bar{l}_{ti,ti} = 0,\ \forall t). \\ 0, & \text{otherwise.} \end{cases} \tag{5.8}$$

  This corresponds to setting a minimum norm prior to disconnected sources. Also, it prevents the pitfalls of having a regularization matrix that is not positive semidefinite ($\exists \boldsymbol{j}$ where $\lambda \boldsymbol{j}^T \bar{\boldsymbol{L}} \boldsymbol{j} < 0$), which leads to issues in optimization.

Note that, even if the structural connectivity penalty is imposed on sources in the network of interest, all other "disconnected" sources still have a minimum norm penalty and their activity could also be reconstructed. By "disconnected sources" in this context we mean with no connections in the network of interest (they can still be connected to sources in other brain regions outside of NoI).

But how do we know what is the "optimal mask" i.e. the pattern of region activation that generated the given measurements and how do we find it?
We propose an algorithm that (1) searches for the optimal network motif i.e. optimal activation pattern and (2) reconstructs the source activity, given the found motif (see Alg. 1). Upon initialization, an initial set is made ($p_{set} = p_{set-init}$) of pairs (p) of connected active regions (i.e. connected source pairs between region pairs). At each step, all possible edges remaining in p_{set} are tested for addition in the network. For N_R active regions, the number of directed region edges (N_{ED}) is the number of initial pairs (permutation without repetition)

$$N_{ED} = P(N_R, 2) = \frac{N_R!}{(N_R - 2)!} = N_R(N_R - 1). \tag{5.9}$$

If all regions are interconnected, we would need to do *at most* $\frac{N_{ED}(N_{ED}+1)}{2}$ reconstructions (the sum of first N_{ED} numbers). *At most* means that it would be the case if the optimal motif is a complete digraph i.e. a directed graph where each pair of distinct regions is connected by two unique edges (one in each direction).

As an example, consider $N_R = 3$ active regions, all interconnected. To activate 1 directed region edge, there are $P(3, 2) = 6$ possible permutation pairs: $p_{set-init} = [(R_1, R_2), (R_2, R_1), (R_1, R_3), (R_3, R_1), (R_2, R_3), (R_3, R_2)]$. So we would need to do at most $\frac{6 \cdot 7}{2} = 21$ reconstructions in total. Notice the that the upper limit of the total number of reconstructions increases polynomially with the number of regions due to the combinatorial nature. For example, for 6 and 8 regions, the maximal number of reconstructions would be 465 and 1596, respectively.

After the initialization, we perform **STEP 1** in Alg. 1 i.e. reconstruct the sources for the current permutation set. For each pair p, we first construct a hybrid masked Laplacian mask using Eq. 5.3 and reconstruct the source activity using Eq. 5.2. Then we look at the cost of each permutation. The permutation with the lowest cost value is assumed to be the optimal one ($p^* = \arg\min_p F(\hat{\boldsymbol{j}}_{\boldsymbol{p}}^*)$). The output of **STEP 1** are the optimal permutation p^*, the optimal source reconstruction $\hat{\boldsymbol{j}}_{\boldsymbol{p}}^*$ and its cost $F(\hat{\boldsymbol{j}}_{\boldsymbol{p}}^*)$.
After that, we proceed to **STEP 2**. We iteratively add new possible directed region edges that have not appeared before [1] and see how the cost behaves (perform **STEP 1**). If the cost decreases, we keep the new region edge (i.e. update the optimal motif) and go back to **STEP 2**, otherwise we discard it. At the end we end up with the optimal permutation p^* i.e. optimal network motif M^*, the optimal source reconstruction obtained with it $\hat{\boldsymbol{j}}_{p^*}$ and the minimal cost $F(\hat{\boldsymbol{j}}_{p^*})$. In the text and figures, the notation p^* and M^* are used interchangeably.
We demonstrate the impact of directionality on the penalty in Figure 5.3. It is a toy example illustrating what the toy mask looks like if the underlying structural graph is considered to be undirected or directed. If the mask is made with undirected connections, the activity of a node will be penalized by both the *past* and *future* activity of a connected node. On the contrary, if the mask is made with directed connections, the penalty will depend on whether the node was the origin or the target of an edge. The edge target is penalized by the past activity of the edge origin i.e. if one node A transmitted its activity to node B, then the activity in node B will only depend on the past activity of A.
A similar framework has been proposed in the context of Graph Signal Processing, for learning graph topologies (graph Laplacians) from signal observations, under the assumption that the signals are smooth on the learned graph [Dong *et al.* 2016]. They have developed a method for learning graphs that enforces the smoothness property of the graph signals, under a Gaussian prior distribution imposed on the latent variables in a generalized factor analysis model. They try to infer jointly the graph Laplacian (assumed to be unknown) and the estimates of graph signals, which are assumed to be close to their observations. The major difference here is that (1) their observations do not have a any forward operator that projects the signal values of the underlying graph onto their observations (whereas here, $\boldsymbol{M} = \boldsymbol{GJ}$) so their problem does not have to be ill-posed and (2) they assume the underlying graph to be unknown while we seek for an optimal way to mask a known graph.

[1] Consider for example $N_R = 3$ active regions, all interconnected. To activate 1 region edge, there are 6 possible cases: $p_{set-init} = [(1,2),(2,1),(1,3),(3,1),(2,3),(3,2)]$. Let us say the edge $(1,2)$ is optimal after the inital run of STEP1. Then there would be 5 possible ways to add a new edge (5 new network motifs) i.e. $p_{set-new} = [((1,2),(2,1)),((1,2),(1,3)),((1,2),(3,1)),((1,2),(2,3)),((1,2),(3,2))]$

Algorithm 1: Source reconstruction with optimal motif search

Input: MEG data $\boldsymbol{m}$
Forward operator $\boldsymbol{G}$
Active regions (network of interest)
Source delay matrix

Output: Optimal order of region activation p^*
Optimal source reconstructions $\hat{\boldsymbol{j}}_{p^*}$
Associated cost $F(\hat{\boldsymbol{j}}_{p^*})$

Initialization: Make initial permutation set ($p_{set} = p_{set-init}$) of pairs (p) of connected active regions (i.e. connected source pairs between region pairs with corresponding delays). For N_R active regions, there are $P(N_R, 2) = \frac{N_R!}{(N_R-2)!}$ initial pairs.

STEP 1: **Reconstruct the sources for the current region permutation set**

for *each pair* $p \in p_{set}$ **do**
  Construct masked Laplacian $\tilde{\boldsymbol{L}}_{\boldsymbol{tr}}(p)$
  $\tilde{\boldsymbol{L}}_p = \tilde{\boldsymbol{L}}_{\boldsymbol{tr}}(p) + \tilde{\boldsymbol{L}}_{\boldsymbol{loc}}(p) + \tilde{\boldsymbol{I}}(p)$
  $\hat{\boldsymbol{j}}_p = \arg\min_{\boldsymbol{j}} F(\boldsymbol{j}) = \arg\min_{\boldsymbol{j}} \|\boldsymbol{m} - \tilde{\boldsymbol{G}}\boldsymbol{j}\|_2^2 + \lambda\|\tilde{\boldsymbol{L}}_p j\|_2^2.$
end
$F_{p_{set}} = \{F(\hat{\boldsymbol{j}}_p) \mid p \in p_{set}\}$
$p^* = \arg\min_p F_{p_{set}} \leftarrow$ optimal permutation
$\hat{\boldsymbol{j}}_{p^*} \leftarrow$ optimal reconstruction
$F(\hat{\boldsymbol{j}}_{\boldsymbol{p^*}}) \leftarrow$ lowest cost
return $p^*, \hat{\boldsymbol{j}}_{p*}, F(\hat{\boldsymbol{j}}_{p^*})$

STEP 2: **Add new (directed) region edges (i.e. update network motif)**

if $\exists$ *a region edge which can be added to the current motif* **then**
  $p_{set} = p_{set-new} \leftarrow$ update permutation set with new edges
  Go back to ***STEP 1***
  $\rightarrow p^*_{new}, \hat{\boldsymbol{j}}^{new}_{p*}, F(\hat{\boldsymbol{j}}^{new}_{p^*})$
  if $F(\hat{\boldsymbol{j}}^{new}_{\boldsymbol{p^*}}) < F(\hat{\boldsymbol{j}}_{p^*})$ **then**
    Update:
    $p^* \leftarrow p^*_{new}$
    $\hat{\boldsymbol{j}}_{p*} \leftarrow \hat{\boldsymbol{j}}^{new}_{p^*}$
    $F(\hat{\boldsymbol{j}}_{p*}) \leftarrow F(\hat{\boldsymbol{j}}^{new}_{p*})$
    Go back to ***STEP 2***
  else
    break
else
  break
return $p^*, \hat{\boldsymbol{j}}_{p^*}, F(\hat{\boldsymbol{j}}_{p^*})$

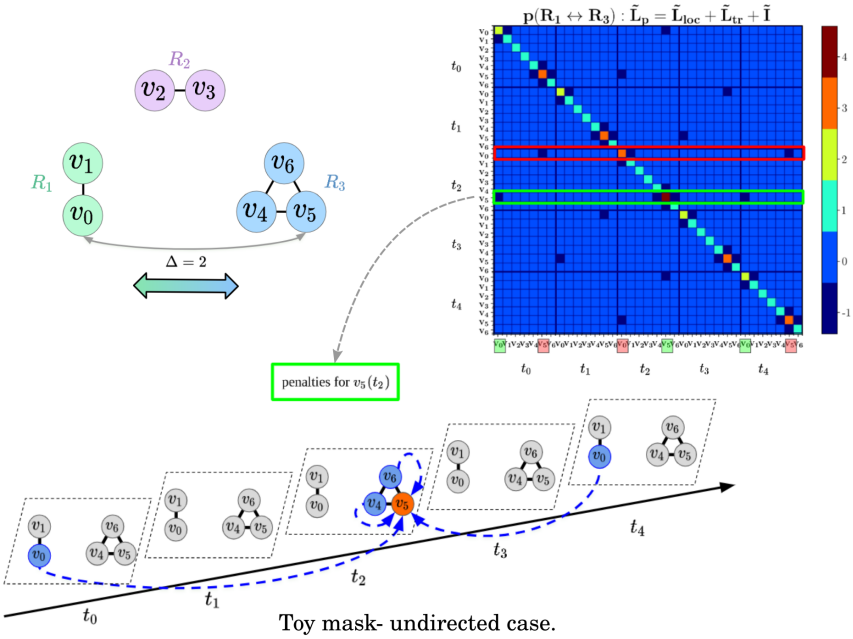

Toy mask- undirected case.

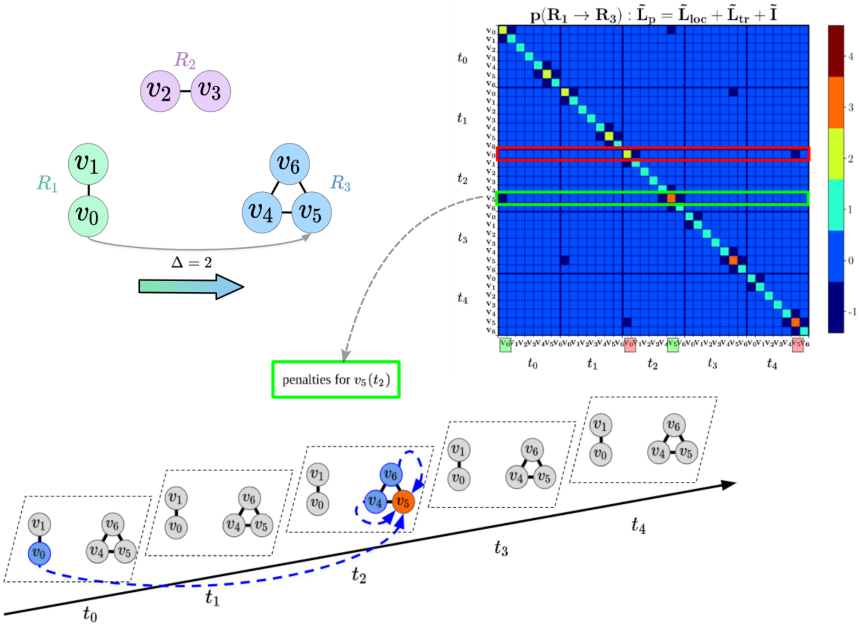

Toy mask- directed case.

Figure 5.3: Toy mask for the case of an undirected graph (top) and directed graph (bottom). Top: the mask is made with undirected connections ($R_1 \leftrightarrow R_3$). Notice that the activity of node v_5 at time t_2 ($v_5(t_2)$) is penalized by $v_0(t_0)$ and $v_0(t_4)$ (by both the *past* and *future* activity of a connected node (the green rectangle in $\tilde{\boldsymbol{L}}_p$). Bottom: the mask is made with a directed connection ($R_1 \rightarrow R_3$) Consider an edge e_k where $origin(e_k) = v_0$ and $target(e_k) = v_5$. In this case $v_5(t_2)$ is penalized only by $v_0(t_0)$, i.e. the current edge target is penalized by the past activity of the current edge origin (the green rectangle in $\tilde{\boldsymbol{L}}_p$). Notice also that, in both cases, the adjacent nodes impact the penalty at each time instant.

5.3 Methodology

Details on the simulation of synthetic data and preprocessing of HCP data are described in Chapter 3. In this Chapter we first compare the reconstruction of brain activity obtained CIMIP_OML from simulated MEG measurements to MNE [Hämäläinen & Ilmoniemi 1994], LORETA [Pascual-Marqui *et al.* 1994] and CGS [Hammond *et al.* 2013] methods for 5 simulated subnetworks, for 2 SNR values (3 and 10). Secondly, we evaluated the proposed approach on the real the sensory-motor task real MEG data, in which the subjects were asked to perform one of the 4 limb movements after the indication by the a visual cue.
Optimal regularization parameter was chosen empirically based on the results obtained in Chapter 4. The value for CIMIP_OML was set to $\lambda = 1$ for simulated data and $\lambda = 0.5$ for real MEG data.
Regarding the quantification the performance on the synthetic data, the evaluation error metrics are the same as described in Chapter 4:

- peak-to-peak (PtP) localization error
- center-of-gravity (CoG) localization error
- area under the ROC curve (AuC).

On the other hand, we mentioned the difficulties regarding the assessment of the results on the real data, due to the lack of access to the ground truth. Therefore, although the the results we show are rather qualitative, they offer a promising insight into the nature of information transfer in the brain.
Regarding the implementation, the objective function $U_{\text{CIMIP\_OML}}$ (Eq. 5.2) was minimized using Conjugate Gradient (CG) method, implemented by *scipy.optimize.minimize* routine in Python. The Algorithm 1 was implemented in Python.

5.4 Results on Simulated Data

Recall that the activity was simulated for 5 different subnetworks as a directed path, i.e. as a sequence of regions in which directed edges point from each region in the sequence to its successor in the sequence, with no repeated edges. Such graphs are called Directed Acyclic Graphs (DAG) in graph theory. CIMIP_OML algorithm is not constrained only to DAGs: it searches for a network motif, meaning that it can reconstruct edges in both directions. Firstly, let us illustrate what the structural connectivity of a network of interest looks like (see Figure 5.4). In the simulation, the used tracts were 1-to-1 connections. In the reconstruction, all streamlines between the regions in NoI were used (1-to-many connections). This was done firstly because we wanted to keep the same amplitudes in the simulation when the activity was spread from one source to another. Secondly, this was also a test of robustness of the reconstruction, due to the fact that tractograms are not perfectly reproducible even for the same subject, using the same MR machine and tractography algorithm [Maier-Hein *et al.* 2017], notably in probabilistic tractography.

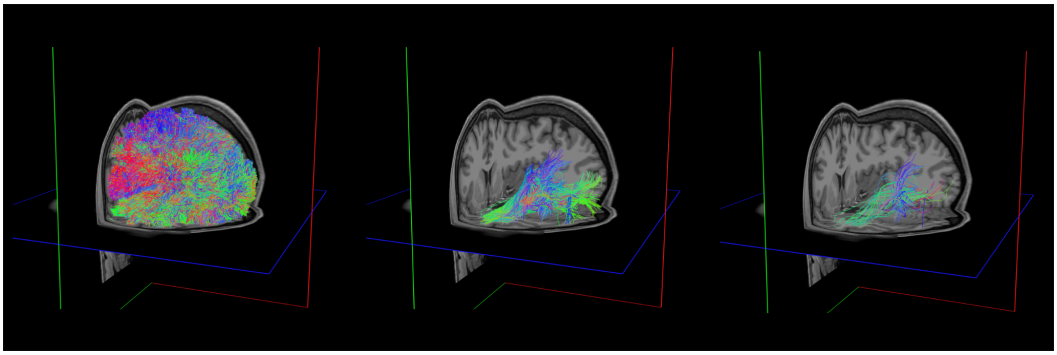

Figure 5.4: Left: the whole tractogram. Middle and Right: subset of streamlines between simulated active regions in subnetwork MSS_01 (lateraloccipital, inferiorparietal and middletemporal, all in left hemisphere). Right: tracts used in the simulation (1-to-1 connections). Middle: tracts used in the reconstruction- all streamlines between these 3 regions ((1-to-many connections)).

Let us compare the simulated and reconstructed motifs. Figures 5.5 and 5.6 show the simulated and reconstructed network motifs for SNR 10 and 3, respectively. The node numbers correspond to Desikan-Killiany atlas region indices (IDs), whose corresponding names can be found in the Table 5.1. We can see that all reconstructed

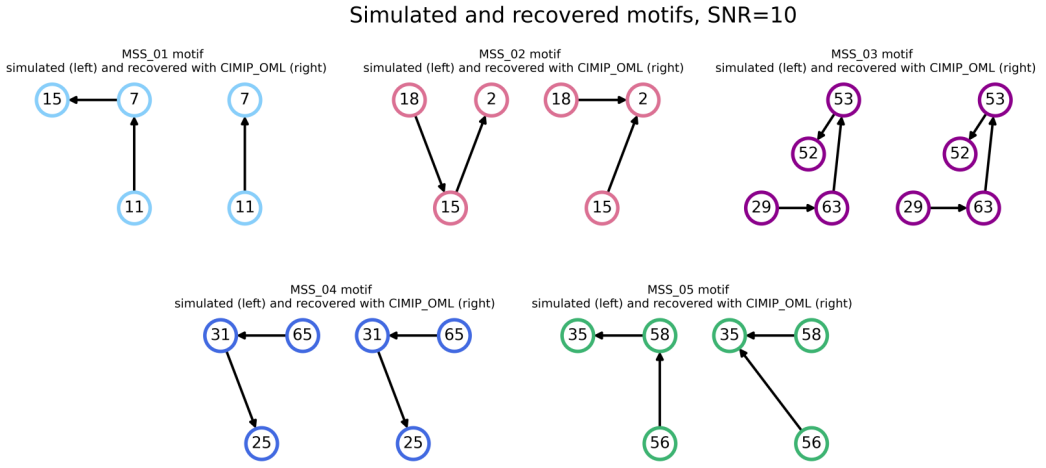

Figure 5.5: Simulated and recovered network motifs with CIMIP_OML for SNR=10.

region edges are directed; no bidirectional edges appear, making the method robust for detection of DAGs, if the underlying network is indeed a DAG. Moreover, the exact simulated motif is reconstructed in 2/5 cases for $SNR = 10$, while in only 1 case for $SNR = 3$. From the Figures 5.5 and 5.6 we can see that 2 types of errors emerge: (1) that either 1 edge is missing, or (2) that a directed edge appears between a pair of nodes that are connected indirectly (for example via 2 egdes) in the simulation. Let us discuss the second case. The algorithm found the intermediate region in the information transfer to be redundant, if a structural connection exists

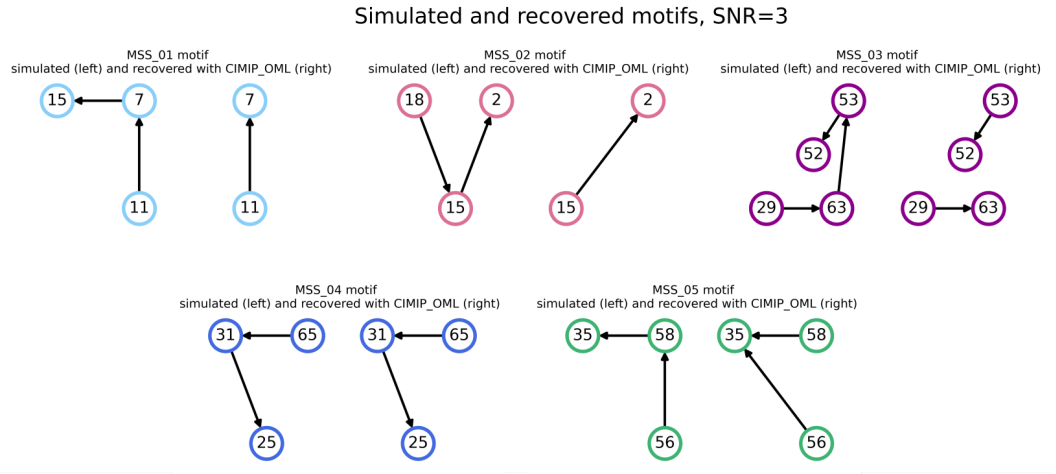

Figure 5.6: Simulated and recovered network motifs with CIMIP_OML for SNR=3.

Table 5.1: Desikan-Killiany region names and IDs used in simulation

Region name	**Region ID**	**Region name**	**Region ID**
lateraloccipital-lh	ID = 11	parsopercularis-lh	ID = 18
inferiorparietal-lh	ID = 7	middletemporal-lh	ID = 15
middletemporal-lh	ID = 15	caudalmiddlefrontal-lh	ID = 2
superiorparietal-lh	ID = 29	supramarginal-rh	ID = 65
superiorparietal-rh	ID = 63	supramarginal-lh	ID = 31
parsorbitalis-rh	ID = 53	precuneus-lh	ID = 25
parsopercularis-rh	ID = 52		
postcentral-rh	ID = 56		
precentral-rh	ID = 58		
caudalanteriorcingulate-rh	ID = 35		

between the originating region of activity and the final target. (e.g. like region 15 in MSS_02 and region 58 in MSS_05 in Figure 5.5) For example, consider the case of MSS_05 (see Figures 5.5 and 5.6). The simulated motif is: $(e(56,58), e(58,35))$ (postcentral right $\rightarrow$ precentral right $\rightarrow$ caudal anterior cingulate right) while the recovered motif is $(e(56,35), e(58,35))$ meaning that a directed edge between regions 56 and 35 emerged in the reconstruction, while in simulation the signal was relayed through the intermediate node 58. The data fit is also a part of the cost (Eq. 5.2). So from the point of view of the data fit, such a reconstruction can be completely valid i.e. the reconstruction obtained with the recovered motif fits well the measured data. A possible reason why, is that the simulated delays between the region from which the activity originated (56) and the final target region (35) are a *sum* of delays

appearing in all directed edges between them ($e(56, 58)$, $e(58, 35)$). On the other hand, the reconstructed edge is $e(56, 35)$, can comprise of longer streamlines, that yields very similar delays as the sum of delays induced by $e(56, 58)$ and $e(58, 35)$. The average delays ($\bar{\Delta}$) are the following: $\bar{\Delta}(e(56, 58)) + \bar{\Delta}(e(58, 35)) = 16.19$ ms while $\bar{\Delta}(e(56, 35)) = 17.5$ ms, which is indeed extremely similar. This is a very interesting observation highlighting the difficulty to identify the exact bundles used in the information transfer.

Moreover, let us see how this activity looks like on the brain. Figures 5.7 - 5.11 show the ground truth with the reconstructed activity for all 5 subnetworks, obtained with CIMIP_OML, for 3 or 4 time instants. Note the correspondence between these figures and the motifs in Figures 5.5 and 5.6. If the correct motif is found, the spatial pattern is recovered correctly. Notice the slightly higher spatial spread in the reconstructed activity and the increased intraregional homogeneity. This is a result of (1) the fact that the local Laplacian was used in the regularization, which favours smooth solutions between adjacent sources and (2) that *all* structural connections in the NoI are used, as opposed to a smaller subset used in the simulation.

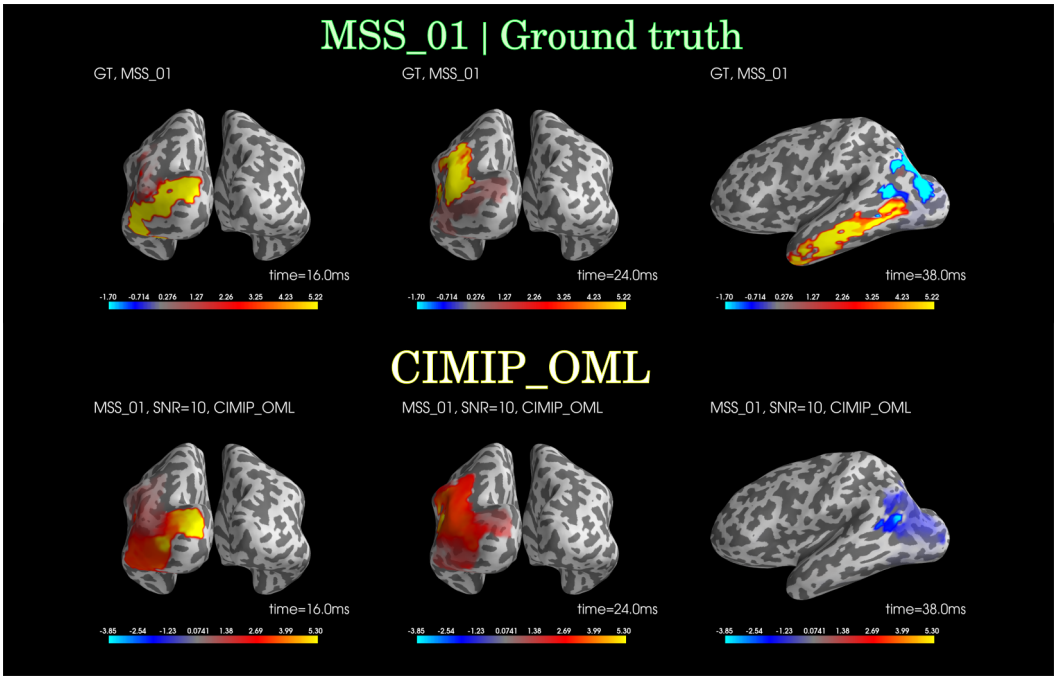

Figure 5.7: Top row: MSS_01, Ground Truth activity. Bottom row: its reconstruction of with CIMIP_OML, SNR=10.

In addition, we show average Peak-to-peak (PtP) and Center-of-gravity (CoG) errors across 5 subnetworks, across different amplitude thresholds τ in Figures 5.12 and 5.13 respectively. When it comes to PtP errors, CIMIP_OML has lower errors only for lower amplitude thresholds. Nevertheless, as we mentioned already, this metric would be more suitable if in simulations the activity was rather focalized in a small brain area since it does not encompass the activity spatial spread.

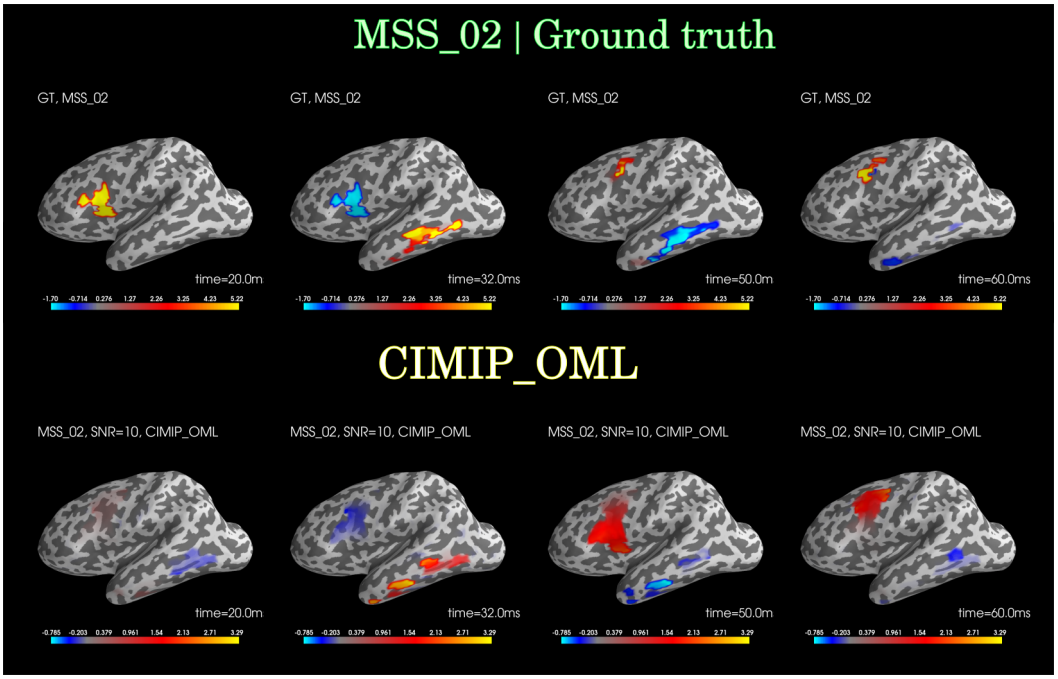

Figure 5.8: Top row: MSS_02, Ground Truth activity. Bottom row: its reconstruction of with CIMIP_OML, SNR=10.

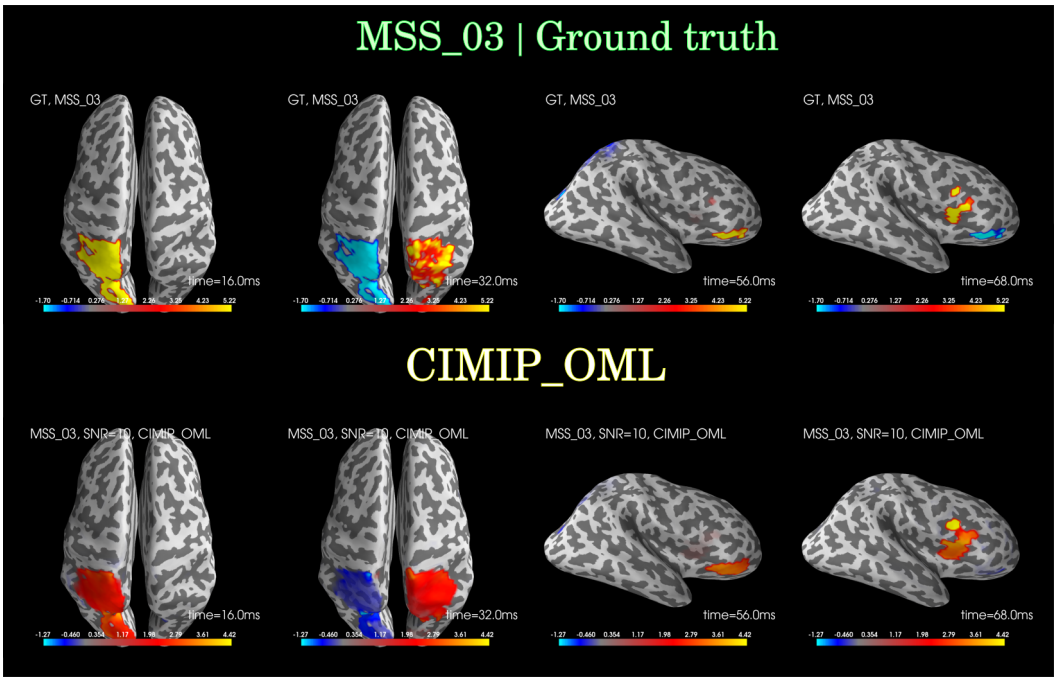

Figure 5.9: Top row: MSS_03, Ground Truth activity. Bottom row: its reconstruction of with CIMIP_OML, SNR=10.

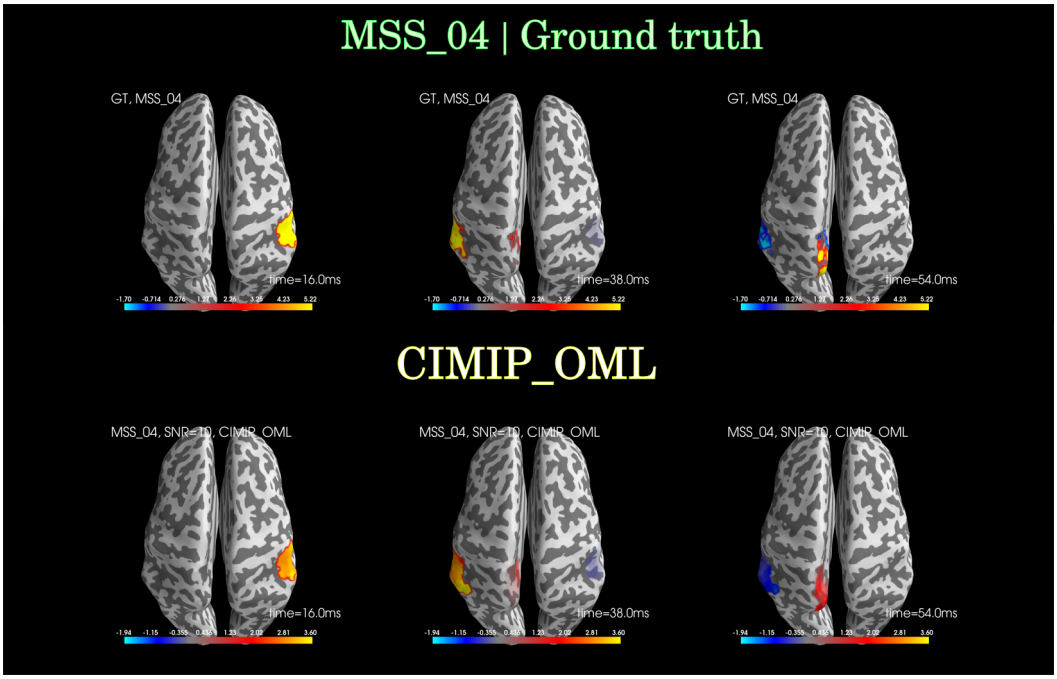

Figure 5.10: Top row: MSS_04, Ground Truth activity. Bottom row: its reconstruction of with CIMIP_OML, SNR=10.

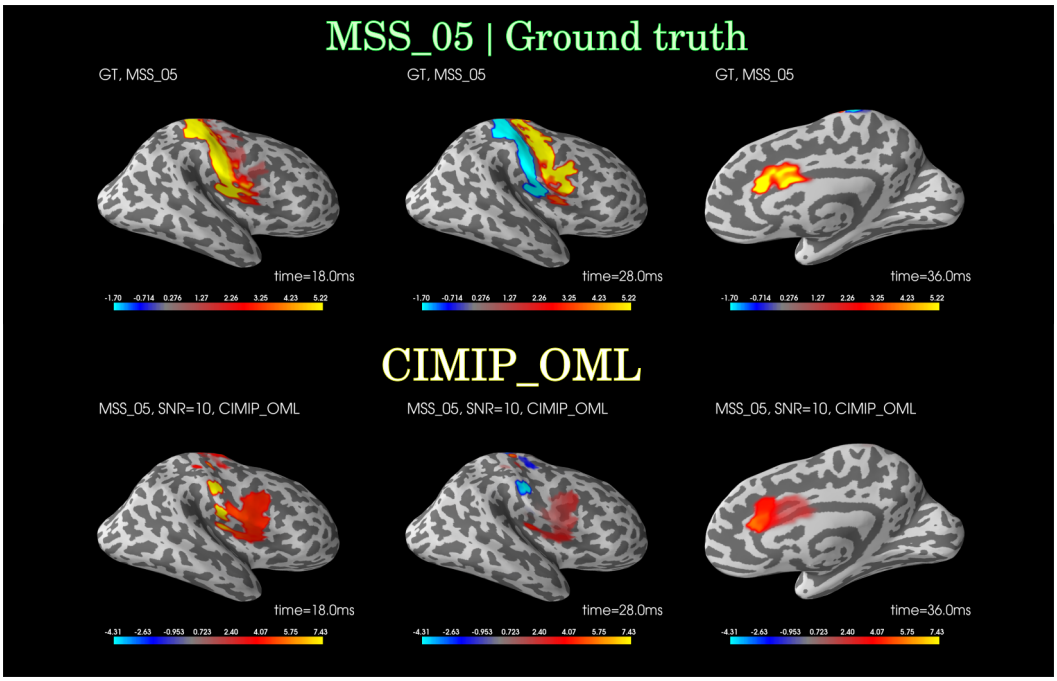

Figure 5.11: Top row: MSS_05, Ground Truth activity. Bottom row: its reconstruction of with CIMIP_OML, SNR=10.

Regarding the CoG error, which is a more suitable metric in this case, CIMIP_OML consistently and substantially outperforms all other reconstruction metods, across all amplitude thresholds. The ROC curves are shown in the Figure 5.14, where we see that CIMIP_OML had the highest AuC score of 0.79.

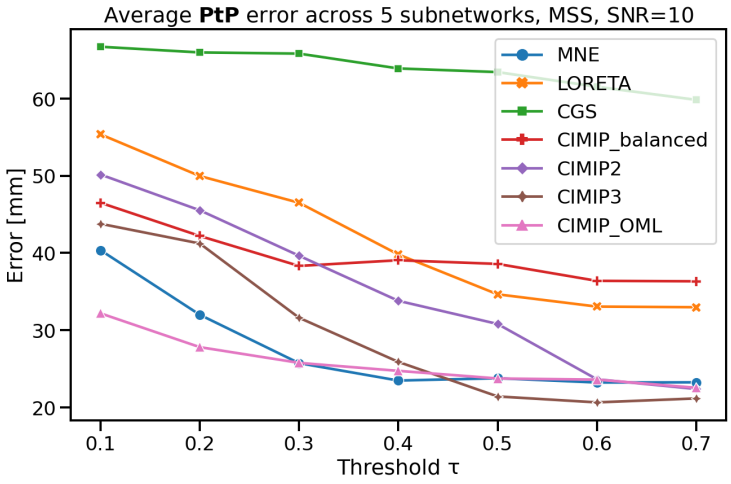

Figure 5.12: Average PtP errors for all reconstruction methods, across 5 subnetworks, SNR=10.

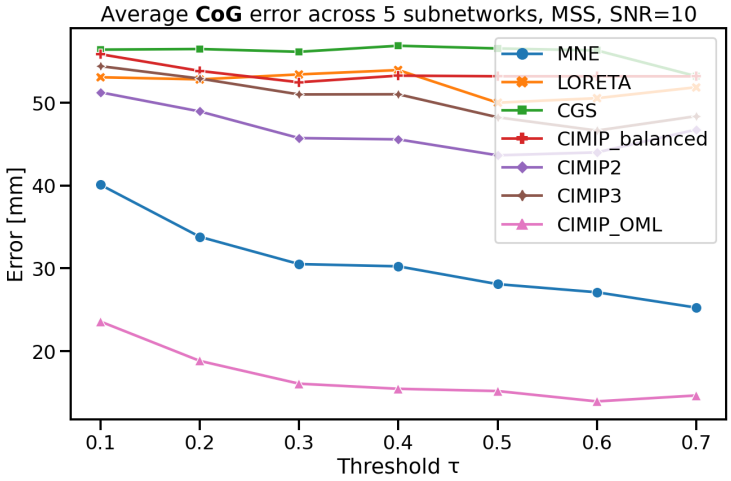

Figure 5.13: Average CoG errors for all reconstruction methods, across 5 subnetworks, SNR=10.

5.4.1 The ideal mask and the impact of transmission speed

We were interested in some questions that arised during the development of CIMIP_OML, such as

1. What happens if we know the exact connections used in the information transfer i.e. if we have an "ideal mask"?
2. What happens if our estimated delays are wrong?

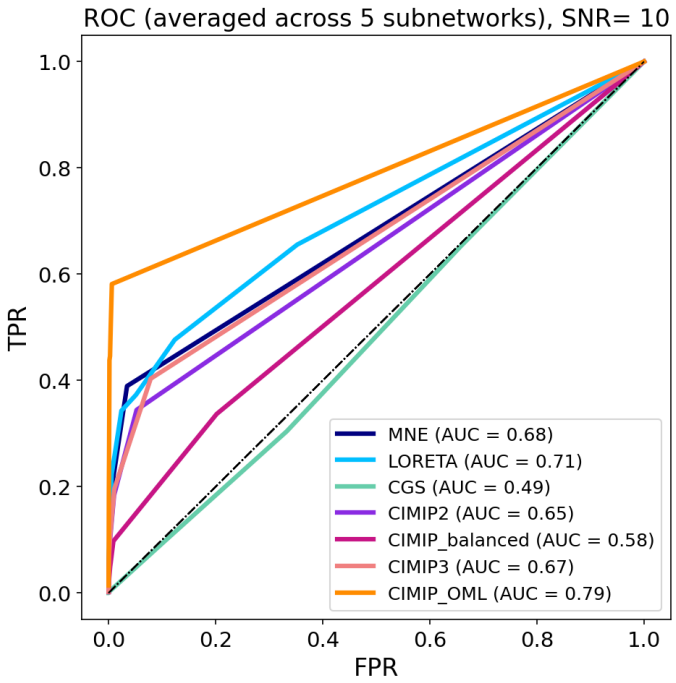

Figure 5.14: ROC curve for all reconstruction methods, for SNR=10. AUC values are the average values across 5 subnetworks.

The "ideal mask"

In the case of "ideal mask", the Laplacian in Eq. 5.3 was masked with identical connections as in simulation, in the correct direction, and during the activity time window, i.e. only at time instants when the sources were active in simulation. This was done purely as a proof of concept. As expected, it results in the perfect reconstruction. Note that this is essentially the CIMIP approach with a given ideal mask (we did not perform motif search here). Since these results look identical as simulated, it is redundant to show them visually. However, first, we cannot expect to know the *exact* connections that were used in the information transfer. This is why in other CIMIP_OML reconstructions, *all* connections between region pairs (existing in a given tractogram) were used. Secondly, we cannot know the exact activity time window. Thus, in all other CIMIP_OML experiments, we masked the Laplacian during the whole time window ($t = [0, ...T-1]$). This was the initial implementation. However, some artefacts appeared at the beginning and the end of time window because the number of occurrences of each edge with a delay of d is in fact $T - d$ and not T. So each edge would *not* appear for every time sample. For example, if there was an edge with a delay of $d = 2$ with an origin node at t_{-2} and a target node at t_0, an edge *is* supposed to appear in the incidence matrix $\bar{\boldsymbol{B}}$ (Eq. 5.6), resulting in a non-zero element in $\bar{\boldsymbol{L}}_{tr}$. Without extending the time window, this was not the case; such an edge would not appear in $\bar{\boldsymbol{B}}$ and therefore not in $\bar{\boldsymbol{L}}_{tr}$. Consequently, there were no penalties for such sources at the very beginning and the end of the time window. In order to correct this issue and take

into account the past and future activity that is beyond the data time window, the time window used for contruction of the incidence matrix $\bar{\boldsymbol{B}}$ was extended to the range $t = [-d_{max}, ...0, ...T, ...T + d_{max}]$, i.e. with the maximal delay appearing in the subset of tracts. This way the past and future samples are also considered. This value slightly differs in simulated subnetworks in the synhtetic data, as well as across subject in real HCP data.

The impact of transmission speed

Given streamlines' lengths and the information conduction speed, transmission delays can be estimated for each connection. We mentioned in Chapter 3 that axon transmission speed is affected by the axon diameter and myelin thickness [Innocenti *et al.* 2014, Horowitz *et al.* 2015, Drakesmith *et al.* 2019] and that diffusion microstructure techniques can give us an estimate of axonal density and axon diameter. As recently shown by [Drakesmith *et al.* 2019], the proportionality between fiber diameter and transmission velocity is $6.67ms^{-1}/\mu m$. Following these findings, as well as previous works of [Fukushima *et al.* 2015] and [Deslauriers-Gauthier *et al.* 2019], in this thesis the information transmission speed is assumed to be constant across brain and equal to 6 m/s. This would correspond to an average axon diameter of 1 μm. While this is the average, we know that the human brain comprises of axons that are both thinner and thicker. The thicker the axon, the higher the transmission speed and *vice versa*. So what if the estimated delays are imprecise?

We assumed the correct network motif is known, and performed CIMIP_OML reconstructions for 5 subnetworks across transmission velocities in range $v = 3 - 12m/s$. Note that in this case, we used the exact connections as in simulations, and reconstructed from noiseless measurements, because we were interested purely in the impact of speed, while aiming to reduce the impact of other factors (such as noise, for example) on the errors. The results are shown in Figure 5.15 in terms of PtP and CoG errors. We can observe that the errors do not increase excessively for most of the tested velocities. Interestingly, CoG errors seems to increase more rapidly if the estimated velocity is underestimated. This suggests that, if estimation errors have to be made, it is safer (in terms of this error) to have overestimated than underestimated delays. Yet, we acknowledge that the assumption of a constant information transmission speed across the brain is a strong hypothesis. Nonetheless, we want to emphasize this assumption is not inherent to our approach since we could include perhaps a distribution of delays, which would lead only to a change of values in the delay matrix.

5.5 Results on Real MEG Data

As a reminder, the real MEG data consists of a visuomotor task in which the subjects were asked to move their right/left fingers or toes. For this task paradigm, we set a prior network of interest- 6 regions expected to be active during a visuomotor task

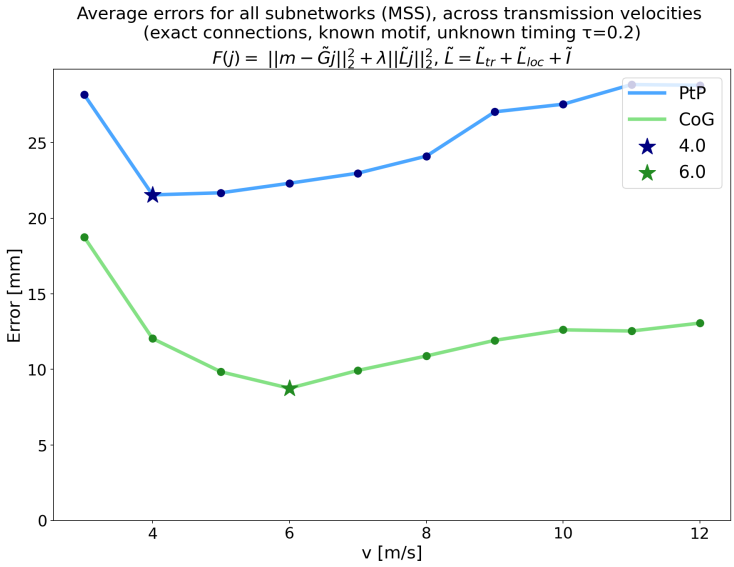

Figure 5.15: Average PtP and CoG errors for CIMIP_OML reconstructions across different transmission speeds v. The correct motif is assumed and the exact connections were used as in simulation. The amplitude threshold is set to $\tau = 0.2$.

based on previous findings of [Martuzzi *et al.* 2006, Abe & Hanakawa 2009, Yeo *et al.* 2011, Napadow *et al.* 2013, Ionta 2021, Frässle *et al.* 2021, Lavrov *et al.* 2021] as explained in Section 1.2.3.2 and try to recover the pattern of activity between those regions. These findings allowed us to set priors on the regions comprising the NoI, as a proxy for the unknown ground truth cortical activity in order to evaluate the quality of the recovered source activity. In the Desikan-Killiany atlas, this prior

Table 5.2: Desikan-Killiany region names and IDs

Region name	**Region ID**
lateraloccipital-lh	ID = 11
lateraloccipital-rh	ID = 45
precentral-lh	ID = 24
precentral-rh	ID = 58
caudalmiddlefrontal-lh	ID = 2
caudalmiddlefrontal-rh	ID = 36

network comprises of the following 6 regions: lateral occipital region, precentral and caudal middle frontal gury, in both hemispheres, as the areas most expected to be involved in a visuomotor task. Their full names are as shown with their IDs in Table 5.2. Figure 5.16 visually illustrates these prior regions on the cortex.
We chose 6 regions due to computational limitations caused by the combinatorial nature of CIMIP_OML approach. For example, for $R = 6$ regions (if they are

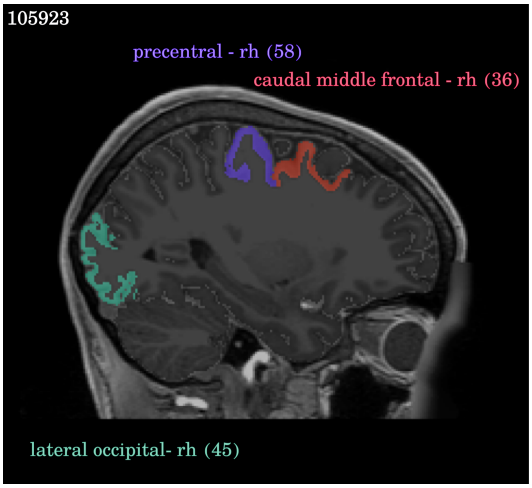

Figure 5.16: Regions set as priors, as expected to be active during a visuomotor task: lateral occipital cortex, precentral and caudal middle frontal gyrus. Note that the regions are homotopic and that this slice only shows the right hemisphere (subject 105923).

all interconnected) the number of initial permutations is $P(6,2) = 30$. However, some region pairs are not structurally connected. Based on the neuroanatomy, the following fibers are expected to appear between them

- Association fibers (axons connecting areas within the same cerebral hemisphere): lateral occipital $\leftrightarrow$ precentral, lateral occipital $\leftrightarrow$ caudal middle frontal. This gives a total of 4 sets of fibers (2 sets per hemisphere).
- U-fibers (short association fibers, between adjacent gyri of the brain): precentral $\leftrightarrow$ caudal middle frontal; giving 2 sets in total.
- Commissural fibers (connecting the two hemispheres of the brain)
    - between the homotopic brain regions i.e. same regions in two hemispheres (e.g. precentral left $\leftrightarrow$ precentral right). For 3 regions there are 3 sets of such fibers.
    - between different regions from two hemispheres. These connections only exist in precentral $\leftrightarrow$ caudal middle frontal. There are no fibers between lateral occipital region in one hemisphere and motor regions (precentral/caudal middle frontal) in the contralateral hemisphere. Therefore there are 2 sets in total.

This means there are up to 11 *undirected* region edges (11 sets of fiber bundles) that can appear anatomically in a subject (i.e. $N_{ED} = 22$ directed edges). So for such case, the maximal number of reconstructions would be at most $\frac{22 \cdot 23}{2} = 253$. Figure 5.17 depicts the streamlines between these 6 active regions for 2 subjects. The reason why we illustrate this for 2 subjects is only to show that the structural connectivity profile is never identical for different subjects. The regional connectivity profile, however, *should* be the same or very similar across subjects for a coarse atlas such as Desikan-Killiany. We chose 10 HCP subjects who had at least 9 (out of 11 maximally) undirected regional connections i.e. sets of streamlines.

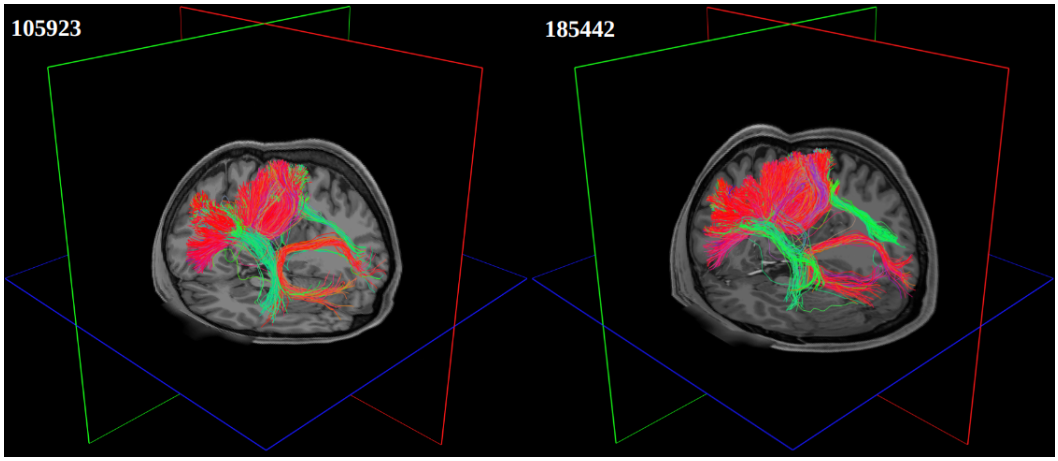

Figure 5.17: Streamlines between 6 active regions (lateral occipital, precentral and caudal middle frontal in both hemispheres) for 2 subjects, 105923 and 185442. The structural connectivity profile is never identical for different subjects.

When it comes to CIMIP_OML results of motor task data, firstly we show in Figure 5.18 a visual representation of updates in the CIMIP_OML algorithm, i.e. the cost evolution and the corresponding network motifs. Since we noticed that the cost function for some subjects does not have a prominent minimal value (the red star), we also show the costs that are 1 % higher than the minimal (the orange stars in Fig. 5.18). Secondly, in Figure 5.19 we shows the cost evolution for 2 subjects, for left and right hand movements. The drawback of this algorithm is the danger of getting trapped in a local minima. In the Alg. 1, we wrote for simplicity that the stopping criteria is $F(\hat{\boldsymbol{j}}_{\boldsymbol{p}^*}^{new}) < F(\hat{\boldsymbol{j}}_{p^*})$. However, the stopping criteria in the implementation is in fact $|F(\hat{\boldsymbol{j}}_{p^*}) - F(\hat{\boldsymbol{j}}_{\boldsymbol{p}^*}^{new})| > 1$, which was set to avoid continuing the optimization for a difference behind the decimal points. This leads to the drawback that suboptimal solutions are possible. Yet, this is also a compromise with the computation time, due to the fact that the reconstructions are costly in terms of time and resources.

Thirdly, we show these reconstructions on the brain for the same 2 subjects, in Figures 5.21 and 5.22. We can see in both cases that the visual response appears ∼100-150ms after the visual stimulus in the occipital lobe, but some weaker activity remains in those areas even later, around ∼200ms. Even though activations in the motor areas contralateral to the hand movement appear (more prominently in subject 185442 than 105923), ipsilateral activity emerges as well. While in most subjects the visual response was followed by a motor response, the pattern of activation is not *identical* across all subjects.

That is why, lastly, we show group results for 10 subjects, for both left and right hand task in Figure 5.20. We counted the most frequent edges in the optimal and near-optimal motifs in 10 subjects, for right and left hand tasks. Near-optimal motifs are the ones that gave a cost 1% higher than the minimal one. Note that there

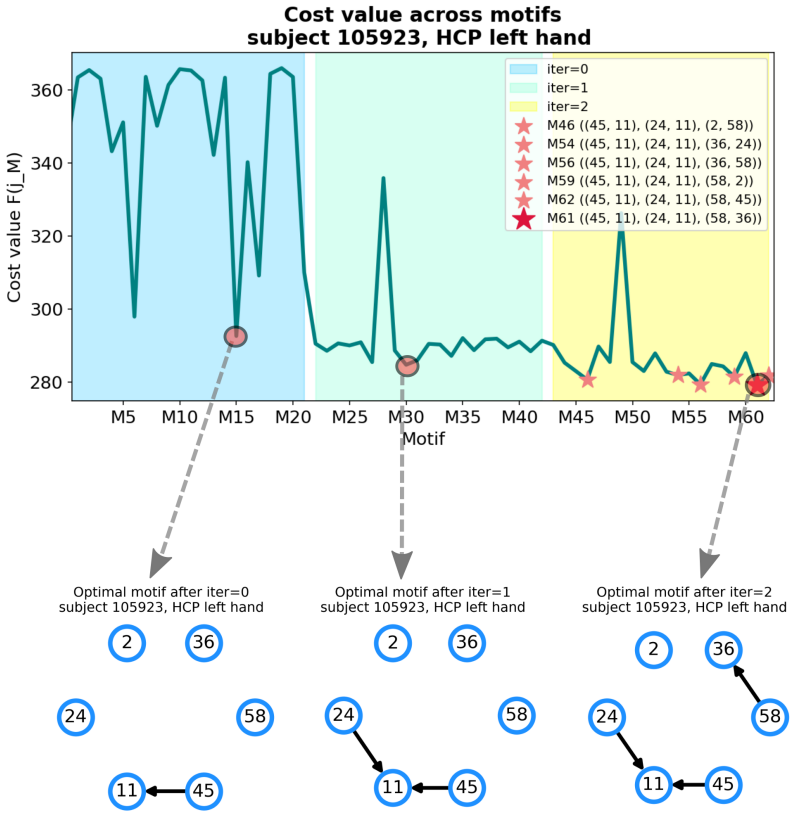

Figure 5.18: Visual representation of updates of the CIMIP_OML algorithm. Cost value across different motifs for a left hand task, subject 105923. The lowest cost value in each iteration (in blue, green and yellow areas) actually corresponds to a motif portrayed below, that gave that cost. Region edges are added iteratively as long as the cost decreases.

is a potential bias due to the fact that in some subjects, there are no near-optimal motifs according to this criteria, while in some subjects there are multiple. Below we illustrate the edges weighted by their occurrences. Interestingly, we see for both hand tasks that the "strongest" (i.e. most frequent) edges are the ones corresponding to interhemispheric interactions. For the left hand task, the most prominent region edges are from lateral occipital right (45) to left (11) and from precentral right (58) to caudal middle frontal left (2). The functional connections between the lateral occipital regions seem to be strong and emerge as well for the right hand task, which is in agreement with previous studies [Martuzzi *et al.* 2006, Murray *et al.* 2001]. These results (in particular for the left hand) are consistent with previous studies [Stephan *et al.* 2007, Nowicka *et al.* 1996] as during particularly lateralized tasks, the information transfer is expected to be asymmetrically enhanced from the non-specialized to the specialized hemisphere to ensure most efficient processing. Yet, for the right hand, more regional edges have similar weights than in the case of the left hand task. This lack of symmetry for the 2 hand movements could possibly be explained by the fact that most the people are right-handed, which could be guiding the increased number of functional connections for right hand movements. Also, it is interesting

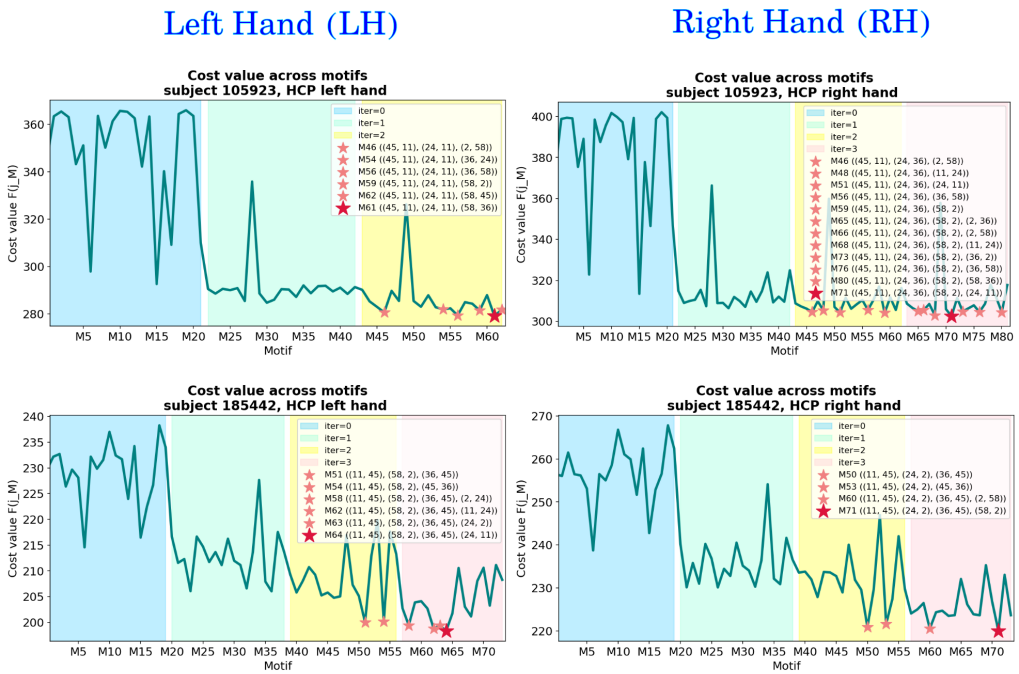

Figure 5.19: Cost evolution for subject 105923 and 185442. The red star indicates the minimum cost, while the orange stars indicate the costs that are 1 % higher than the minimal.

that for some edges, their opposite-directional counterpart is also found. This is not so surprising because every brain region is reciprocally connected and brain activity is inherently cyclic [Valdes-Sosa *et al.* 2011]. Nevertheless, these are only preliminary results. We analyzed the data on a rather small cohort of 10 subjects. More subjects need to be included for conclusive and convincing results. Moreover, the regularization parameter was chosen empirically based on previous reconstructions and due to computational limitations. For example, the motif search for 1 subject and 1 movement, could take up to 90h, depending on the number of iterations i.e. how quickly it reaches the stopping criteria. It would be interesting to test these reconstructions across a range of values of regularization parameters. However, that is left for future studies.

5.6 Limitations

There are a few limitations of CIMIP_OML approach such as

(1) The necessity to define active regions (network of interest) *a priori*
While visuomotor tasks have been widely studied before, it would be an obstacle to study tasks where the regional network is not clearly defined or if there is a big variability in results obtained by previous studies, that would require the choice of a higher number of prior regions. It would also be interesting

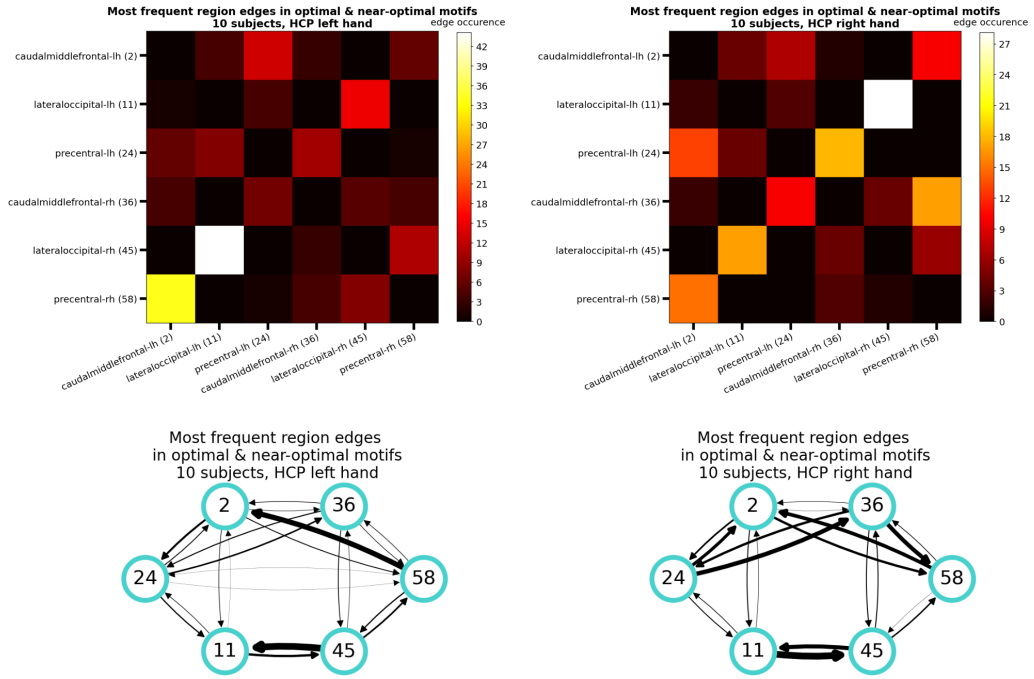

Figure 5.20: Most frequent region edges in 10 subjects, for both hand movements.

to include prior knowledge from other modalities such as fMRI. However conventional methods, such as the general linear model, require the knowledge of the task paradigm to estimate the contribution of each voxel's time course to the given task. Recently a novel approach has been proposed [Costantini *et al.* 2022] to deconvolve fMRI images and recover the brain activity from fMRI signals without prior knowledge. Nonetheless, including data from another modality would increase the complexity of the preprocessing pipeline and data storage requirements. Still, it would be a compelling avenue to explore in the future.

(2) Combinatorial optimization
The second limitation is the combinatorial optimization, which can be rather costly in terms of resources. Combinatorial optimization is the process of searching for maxima (or minima) of an objective function whose domain is a discrete but large configuration space (as opposed to an N-dimensional continuous space). Even if we know the network of interest, its size is a significant constraint, since the number of needed reconstructions increases polynomially with the number of regions.

(3) Possibility of being trapped in a local minima
As we already mentioned, there is a danger of being trapped in a local minima resulting in a suboptimal solution, according to the given criteria. A way

to overcome this issue would be to for example do a brute-force search, i.e. test all possible network motifs, which would be extremely computationally demanding.

(4) Possibility of imprecise delay estimates
The assumption of a constant information transmission speed across the brain is a limitation of our hypothesis. However, it is not inherent to our approach since only the values in the delay matrix would change if we for example considered bundle specific diameters (ergo different delays). In reality, the axonal diameters in the white matter are not constant [Liewald *et al.* 2014, Innocenti *et al.* 2014] so using a distribution of values may be more realistic. Tractography methods can approximate the macroscopic trajectory of axons, by searching for pathways whose fibre orientation estimates derived in each voxel from dMRI are maximally coherent [Jeurissen *et al.* 2019]. Every streamline represents a coherent set of axons coursing together. Even though many tracking algorithms have been developed, none of the existing methods can provide information about the axon diameter of the individual reconstructed fiber bundles. Several dMRI biophysical models have been proposed in the literature to obtain information about axon diameter at the voxel level such as AxCaliber [Assaf *et al.* 2008] and ActiveAx [Alexander *et al.* 2010]. AxCaliber allows the estimates of axon diameter distributions but it requires diffusion MRI signal to be be acquired perpendicular to the axons main orientation (i.e. it requires prior knowledge on the bundle orientations). ActiveAx does not require any prior knowledge on axon orientatios, but it provides estimates of the *mean* axon diameter, and not the full distribution. In general, most of the similar methods suffer from several limitations [Barakovic *et al.* 2021]. Firstly, their estimation is performed voxel-wise and independently in each imaging voxel, which neglects the fact that axons are continuous 3D structures. Secondly, most of these methods rely on the assumption of a single axon population inside a voxel and fail to handle complex fiber configurations such as crossing and fanning. It was estimated [Jeurissen *et al.* 2014] that such voxels comprise up to 90 % of all white matter voxels, leading to biased model estimated since they suffer from significant overestimation of the axon diameters [Alexander *et al.* 2010]. Thirdly, the accuracy of the estimates highly depends on the strength of the diffusion gradients on the MRI systems, which, in typical clinical practises is not high enough [Drakesmith *et al.* 2019]. All these limitations make quantification of axon diameters rather challenging. Recently, a novel microstructure-informed tractography approach has been proposed [Barakovic *et al.* 2021] to resolve axon diameter index estimates at the streamline level. It enables characterization of an invariant value of axon diameter index per streamline in the human brains, thus making the estimates invariant along trajectories. Although we acknowledge the existence of voxel-wise techniques to estimate axon diameter distributions, it was far outside the scope of this thesis and is left for future studies.

5.7 Conclusion

In this Chapter, we first mentioned the limitations of the Laplacian operator that operates on the whole graph, favours smooth solutions across all connections, for all delays, regardless of the connections directions. To alleviate these issues on the reconstructions, we addressed the following aspects: (1) the impact of restraining the source space to a network of interest, (2) the impact of directionality in the information transfer and (3) the impact of estimation of transmission speed. Secondly, we reflected back on the findings in the state-of-the-art regarding visuomotor tasks: the brain ares that have been shown to be active during such tasks and the networks they belong to, needed to integrate the processing of visual information, motor planning and execution, as well as the interplay between these regions. Thirdly, we introduced CIMIP_OML, an algorithm that (1) searches for an optimal network motif - an optimal pattern of interaction between different regions and (2) reconstructs the source activity given the found motif. We kept the idea to include transmission delays supported by dMRI to enforce temporal smoothness between time courses or structurally connected sources, while also addressing the issues of the Laplacian operator. Fourthly, we showed the found optimal motifs and the source estimates obtained with them, for both simulated and real data. We also compared our reconstruction results with 3 different state-of-the-art methods and CIMIP approaches proposed in Chapter 4. Lastly, we mentioned some limitations of the proposed approach and highlighted some future perspectives.

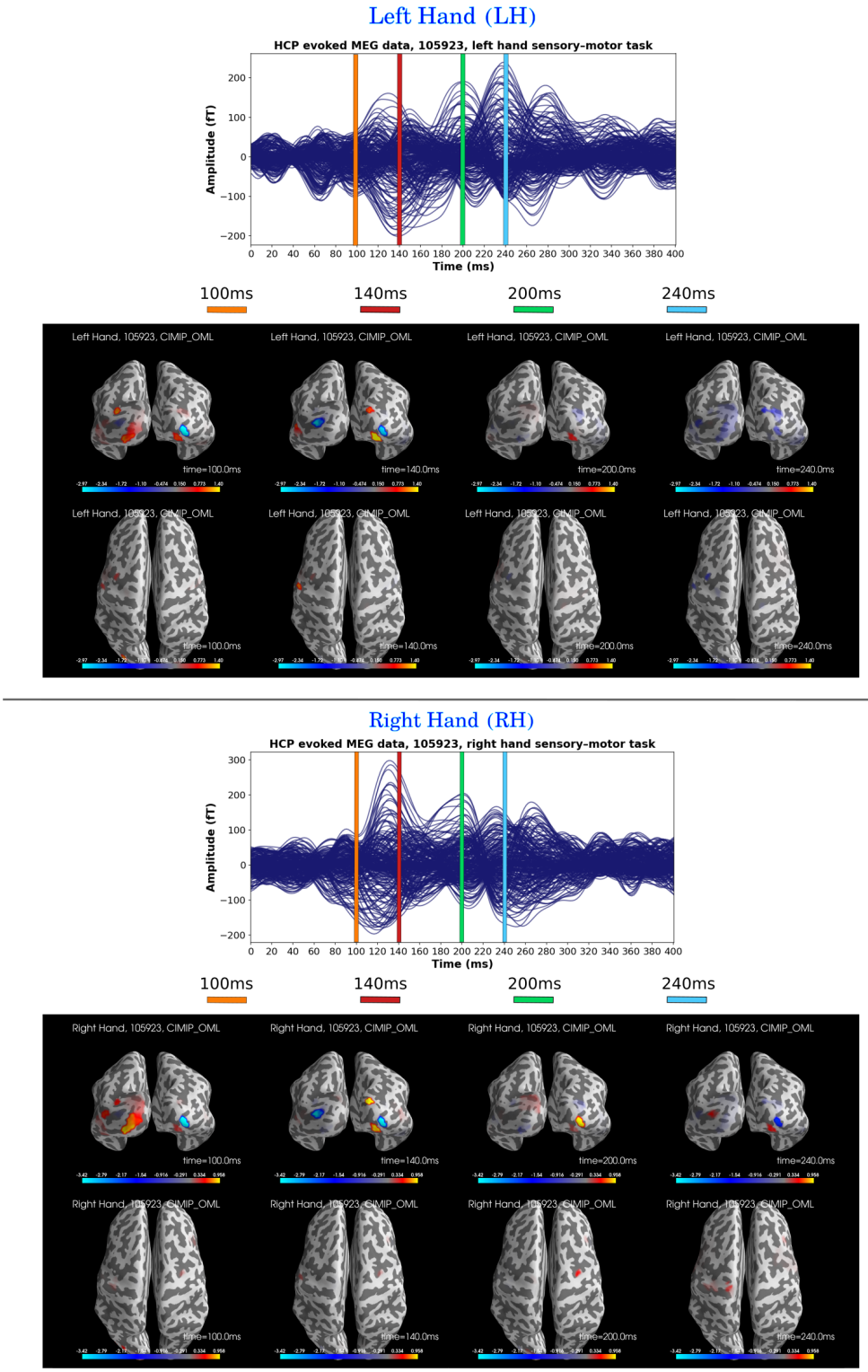

Figure 5.21: HCP MEG data for left and right hand tasks with CIMIP_OML reconstructions, respectively, subject 105923.

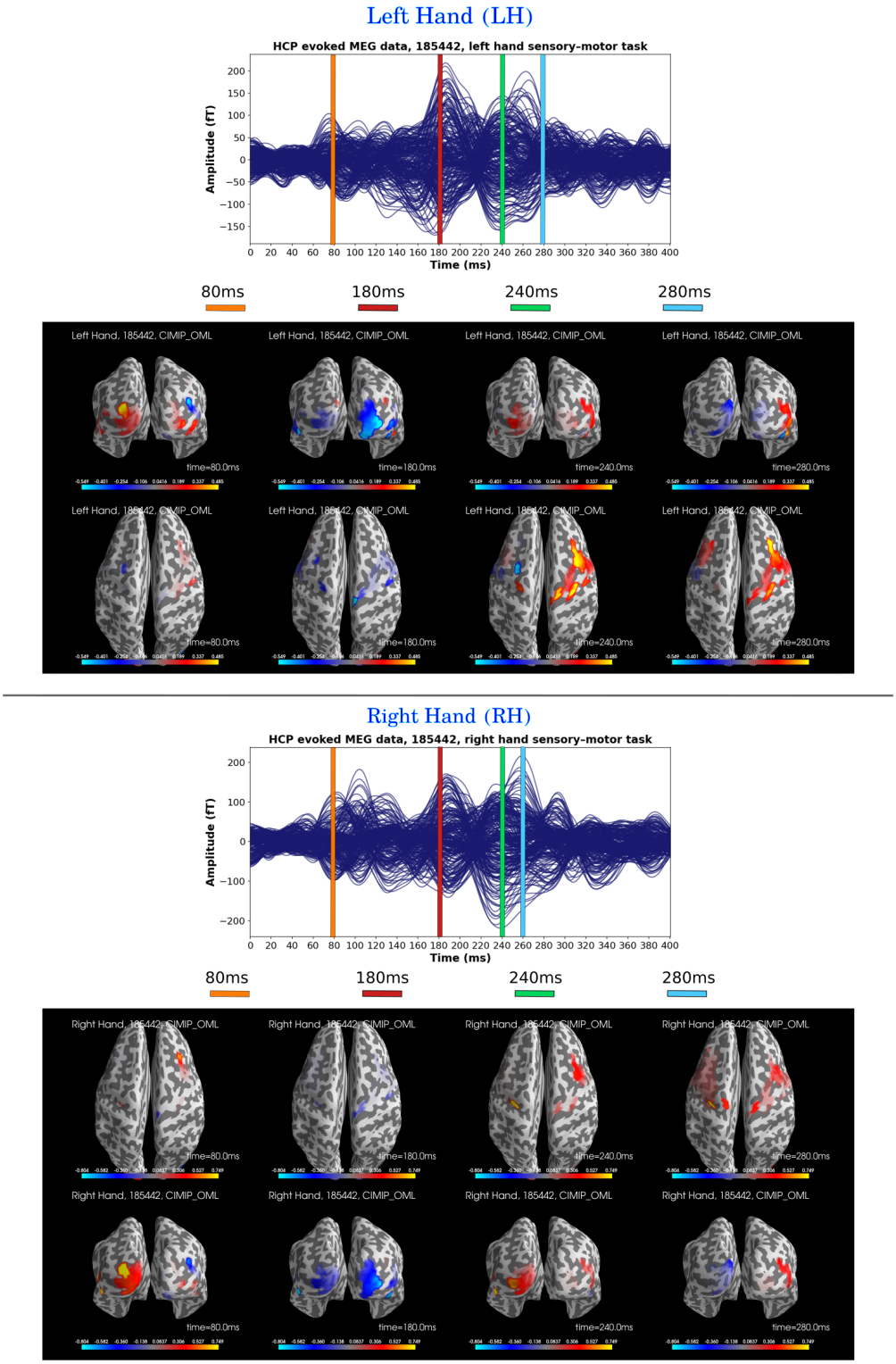

Figure 5.22: HCP MEG data for left and right hand tasks with CIMIP_OML reconstructions, respectively, subject 185442.

Chapter 6

Conclusion

A fundamental role in shaping the rich temporal structure of functional connectivity in the brain at multiple time scales is played by the structural connectivity [Sporns 2011, Honey *et al.* 2007] which places constraints on which functional interactions occur in the network. Diffusion MRI enables the assessment of neural tissue architecture and structural connectivity, while M/EEG provides information about the brain activity with a rich temporal resolution, allowing to track fast processes in the human brain at the millisecond scale. Therefore, it is more than enticing to combine structural and functional brain imaging data with these *in vivo* and non-invasive modalitites, to explore brain activity in terms of large-scale neural dynamics. We have proposed three main contributions in this thesis.

1. Multimodal preprocessing pipeline and a framework for simulating cortical activity

Despite the appeal of using multimodal data to explore new avenues in brain structure and function, the actual process of its integration can be quite cumbersome. This is mostly due to the various coordinate systems and units the data are acquired and expressed, and the different transforms needed to bring the data from one system to another. In this work, the data we used were in 5 different coordinate systems, and quite heterogeneous: structural, functional, acquired and/or represented as 3D volumes, 2D surfaces, 1D time series, on a sphere and on a graph, in millimeters and in meters, milliseconds and seconds, in femtoteslas and nanoampere-meters...Yet, its integration was an essential process that lead us to one part of our **first contribution**: a **multimodal preprocessing pipeline** for integration of structural MRI, dMRI and MEG data into a same framework. It is an imperative first step, requiring cautious quality control since, if done improperly, discredits all further analysis.
However, it is important to highlight that, despite our best efforts, imperfections are possible in the data itself and at different steps of the pipeline. Firstly, MEG data, as all measurements, can be corrupted with noise. Secondly (though this is not necessarily a drawback) is the fact that we parcellated the cortex according to Desikan-Killiany atlas. Recall from Section 1.2.4 that the brain can be subdivided based on different assumptions about cytoarchitectonic, anatomical, functional and structural criteria. So representation in terms of this atlas is just one of many possibilities. Third point worth mentioning is that we considered only the cortex of the brain, while subcortical structures also exist, and the information can be routed

through them [Marieb & Hoehn 2007]. Nevertheless, recall from Section 1.5.3 that with MEG, in general, it is hard to detect deep sources in the brain. Hence, principally the cortical sources contribute to the signal that MEG captures. This is why we, as well as most M/EEG inverse techniques in the literature, consider the surface-based source space [Dale & Sereno 1993]. The fourth point relates to structural connectivity mapping. The issues in this case are related to tractography, which remains ill-posed. This will be discussed below, in the general limitations.

In the second part of this contribution, we proposed a **simulation procedure of source-level brain activity**. It was a prerequisite for quantitative validation of source reconstruction methods we proposed in our second and third contribution, and of those of state-of-the-art. We exploited the use of MAR models to formulate this framework, which also encompasses the delays derived from dMRI. Quantifying the performance of distributed source methods is not trivial and still lacks a well-established consensus [Grova *et al.* 2006, Samuelsson *et al.* 2021]. This is why we used 3 different error metrics for evaluation: the peak-to-peak error, center-of-gravity error and area under the ROC curve (AuC) score.
Since the exact nature of information transfer in the brain remains an open question in neuroscience (and is discussed in more details in the general limitations), we want to highlight that simulations were done under certain hypotheses. The activity was simulated as a Directed Acyclic Graph (DAG) because we wanted to mimic the expected activity during visuomotor tasks, in which Evoked Response Potentials (ERP) emerge. For visuomotor task paradigms, a network of *a few* brain regions is expected to be active during their execution [Martuzzi *et al.* 2006]. It was shown that ERP oscillations die away within $500ms$ [Brookings *et al.* 2009]. So, following the assumption that only a few regions are typically significantly active during such tasks, we simulated the brain activity for several subnetworks of active regions as a DAG (or a graph path). The activity resembling an ERP was propagated between sources in the active regions that share a long-range connection, with appropriate delays and with a constant amplitude. In addition, the activity of each node is spread to its adjacent neighbours. Yet, brain regions are reciprocally connected and brain activity is inherently cyclic [Valdes-Sosa *et al.* 2011]. Therefore, if we wanted to study, for example, resting-state brain activity, we would have to extend this approach to include cyclic activity.

2. Connectivity-Informed M/EEG Inverse Problem

In the methods regularizing the dynamics of M/EEG, **transmission delays** are almost always neglected despite the fact that the information in the brain does not propagate instantaneously. In our **second contribution**, we proposed of a novel framework for solving the M/EEG inverse problem called Connectivity-Informed M/EEG Inverse Problem (**CIMIP**). Prior transmission delays supported by dMRI were included to enforce temporal smoothness between time courses of connected

sources in a network-based framework. We proposed 3 different variations of the CIMIP regularization matrix and explained the similar, yet slightly different hypotheses behind them. We incorporated a Laplacian operator into the regularization, that operates on a time-dependent connectivity graph. We showed results for simulated and real data and compared them with 3 different state-of-the-art reconstruction methods. Yet, it seemed that the potential benefits of adding delays supported by long-range connectivity was not fully exploited. The limitations of the CIMIP method seemed to be principally due to the nature of the Laplacian operator which is (1) isotropic across space, (2) isotropic across delays and (3) agnostic to directionality. This means it acts on the whole graph, favours smooth solutions across all connections, for all delays, without taking account of the directionality in the information transfer.

3. Optimal Masked Laplacian

We wanted to investigate patterns of brain activity during visuomotor tasks, during which only a subset of regions typically get significantly activated. This led us to our **third contribution**, an extension of the CIMIP approach that addresses the aforementioned limitations of the Laplacian, named **CIMIP_OML** ("Optimal Masked Laplacian"). We restricted the full source space network to a network of regions of interest and tried to find how the information is transferred between them. To describe the interactions between nodes in a directed graph, we used the concept of *network motifs*. Apart from restraining the source space to a network of interest, we examine the impact of directionality in the information transfer and the impact of delay estimation. We proposed CIMIP_OML an algorithm which:

(1) Searches for an optimal network motif i.e. an optimal pattern of interaction between different regions which are assumed to be known.
(2) Reconstructs the source activity given the found motif. We kept the idea to include transmission delays supported by dMRI to enforce temporal smoothness between time courses or structurally connected sources, while also addressing the issues of the Laplacian operator.

We show the optimal motifs found with CIMIP_OML as well as associated source estimates, for both simulated and real data. We again compared our reconstruction results with 3 state-of-the-art methods, as well as with the CIMIP approach. In addition, we showed the impact of under- or overestimation of transmission speed (and consequently the delays) on the errors in the reconstruction. For simulated data, *if* the correct (simulated) motif is found, the spatial pattern is recovered accurately. Yet, even though CIMIP_OML does not always perfectly recover simulated network motifs, it still considerably outperforms all other reconstruction methods in terms of CoG error and AuC score. Regarding CIMIP_OML reconstructions of motor task data, we obtained interesting results. Firstly, while in most subjects the visual response was followed by a motor response, the pattern of activation was not

identical across all subjects. This is why we showed group results. We counted the most frequent edges in the optimal and near-optimal motifs across subjects, for both hand tasks. Interestingly, in both cases, the most frequent edges that emerge across subjects are the ones corresponding to interhemispheric interactions. This is more prominent for the left hand task and is consistent with previous studies [Stephan *et al.* 2007, Nowicka *et al.* 1996] where the information transfer is expected to be asymmetrically enhanced from the non-specialized to the specialized hemisphere, for more efficient processing during execution of lateralized tasks. Yet, we see an asymmetry for the right hand task, where more regional edges have similar weights than in the case of the left hand. This lack of symmetry could possibly be explained by the fact that most people are right-handed, which could be guiding the increased number of functional connections for right hand movements. However, we acknowledge the cohort of 10 subjects is small for significant conclusions. Although promising results are obtained for both simulated and real data, there are a few limitations of the CIMIP_OML approach such as (1) the need of *a priori* definiton of network of interest, (2) combinatorial optimization, (3) possibility of suboptimal solutions and (4) possibility of imprecise delay estimates (though this is not inherent to this approach but rather a limitation of our hypothesis on information transmission speed).

General limitations

Let us address some general limitations across different aspects of the thesis.

1. **Ill-posedness of tractography**
   Recall from Section 1.6.3 that tractography still remains an ill-posed problem and that even advanced fiber-tracking approaches will still be subject to modeling errors [Jeurissen *et al.* 2014]. Some of the reasons for this are (1) the reliability of estimation of the local geometry of the fiber orientations, (2) different integration schemes yielding different results, (3) changeable seeds locations from which the streamlines are propagated, (4) variability in track termination and track acceptance criteria etc.
2. **Possibility of imprecise delay estimates**
   The underlying assumption across the thesis, both in simulation and reconstruction, is that the information transmission speed is constant across the fiber bundles in the brain. In reality, the axonal diameters in the white matter are not constant [Innocenti *et al.* 2014] so using a distribution of values may be more realistic. Yet, this is a limitation of our hypothesis we acknowledged from the very beginning. However, it is not inherent to our approach since only the values in the delay matrix would change if we, for example, considered bundle specific diameters. None of the existing tracking methods can provide information about the *axon diameter* of the individual reconstructed fiber bundles except from some very recent techniques [Barakovic *et al.* 2021].

Multiple dMRI biophysical models were proposed to obtain information about axon diameter at the voxel level such as AxCaliber [Assaf *et al.* 2008] and ActiveAx [Alexander *et al.* 2010]. Nevertheless, most of them suffer from limitations such as (1) performing voxel-wise estimation and neglecting the fact that axons are continuous 3D structures, (2) assuming a single axon population inside a voxel and thus failing to handle complex fiber configurations such as crossing and fanning, which can comprise of up to 90 % of all white matter voxels [Jeurissen *et al.* 2014] etc. Furthermore, issues arise regarding the acquisition itself, both in terms of (1) voxel resolution and (2) gradient strength. Micrometer voxel resolution at the level of individual axons remains unrealistic due to the current hardware limitations, impractically longer scan times, and the decrease in the resulting SNR leading to unreliable data [Jones *et al.* 2013, Jeurissen *et al.* 2019]. The strength of the diffusion gradients on the MRI systems largely determines the accuracy of the microstrucural estimates and in typical clinical practises is not high enough [Drakesmith *et al.* 2019].

Open questions

Open questions mainly refer to the mechanisms behind the **information transfer** in the brain, which still remain a challenge in neurosience. More specifically, if you recall from Chapter 4, in this macroscopic context there are a few open questions:

1. **What is the number of streamlines used for information transfer?**
   Even if we know that neural signals were transmitted from e.g. region A to region B, there are multiple sources that connect them. Currently, there is neither invasive or non-invasive technique to infer *which* and *how many* structural connections are used for information transfer in the human brain.
2. **How the number of streamlines influences the amplitude of neural activity?**
   It is well known that action potentials need to have minimal amplitude in order to be transmitted. Up to our knowledge, on the macroscale level, it still unclear if signal attenuation happens during information transfer and how it is related to the number of connections used for it. That is, if a node distributes its activity to many other nodes, does the amplitude in all of them remain the same or it is divided across them. If divided, what are the properties of such a distribution and what does it depend on? It is not fully clear if signal amplitudes attenuate when they propagate from one brain area to the other one. As we mentioned already, intrasurgical ECoG studies [Filipiak *et al.* 2021] showed that N1 amplitudes decrease with streamline *length*. Yet, in their study transmission delays measures were based on propagation of Cortico-Cortical Evoked Potentials induced with intrasurgical direct electrical stimulation. This differs from our case since we did not stimulate the brain and we did not use ECoG.

3. **The impact of connectivity strength**
   Recall from Section 3.6 that the structural connectivity (SC) matrix was made by binarizing the streamline count matrix. Such SC matrix only represents the presence or absence of a long-range connection and does not assess any notion of structural connection *strength*. The strength of the biological connectivity within the brain spans over several order of magnitudes [Bassett & Bullmore 2017] and a low number of streamlines in the streamline count matrix does not necessarily correspond to a false negative connection. dMRI-based tractography is not quantitative per-se, so, *ideally*, it should be complemented in order to associate to each streamline the corresponding connectivity strength. Tractography filtering techniques have been developed as post-processing methods on an existing tractogram, aiming to assign to each streamline a quantitative marker of the connectivity strength. A notable example is SIFT2 [Smith *et al.* 2012] which associates weighting factors to each streamline, which can be interpreted as the mean cross sectional area along the streamline. However, it is questionable how this would impact the velocity and how (if) it could tell us which connections were actually used for the information transfer. Also, these methods come with limitations such as that they can change the topology of brain networks, and thus alter network metrics both in the pathological and the healthy brains [Frigo *et al.* 2020].

Perspectives

There are several perspectives for future studies. Firstly, it would be interesting to try more extensive simulation using cyclic graphs, to validate more the robustness of CIMIP_OML. Secondly, it would be useful to test our algorithm across multiple tractograms obtained with different tracking algorithms, since, as we mentioned, probabilistic tractography algorithms are not completely reproducible [Maier-Hein *et al.* 2017] and they will always lead to slight variations, even for the same algorithm, within the same subject. It would also be intriguing to explore other task paradigms (such as working memory task, language processing task,...) and see if the obtained network motifs comply with the literature and, perhaps, provide some new insights into neural underpinnings and brain mechanisms elicited by brain newtorks involved in these tasks. Another interesting idea would be to include prior knowledge on networks of interest from other modalities like fMRI. A novel approach has recently been proposed [Costantini *et al.* 2022] to deconvolve fMRI images and recover brain activity from fMRI signals without prior knowledge. Yet, including new data from another modality would increase the complexity of the preprocessing pipeline and data storage requirements. Still, it would be a compelling avenue to explore in the future. Further, it would be useful to encompass some notion of connectivity strength into the structural connectome. Lastly, one of the ultimate goals would be to include some estimates of axon diameters, despite the current limitations, which would provide more reliable delay estimates.

To conclude, the aim of this thesis was to reconstruct cortical activity from M/EEG data using transmission delays estimated from dMRI in a network-based framework and provide new insights on large-scale neural dynamics. After the integration of multimodal neuroimaging data and simulation of source-level brain activity, we tackled the M/EEG inverse problem in a network-based framework where transmission delays coming from dMRI were used as prior information. Further, we restricted the full source space network to a network of regions of interest and proposed an algorithm that, first, aims to find the optimal pattern of interactions between regions and second, reconstruct source-level brain activity given that pattern. We examined visuomotor brain networks and hopefully shed new light on the dynamic and rich spatiotemporal interplay between the regions that constitute them.

List of publications

- I. Kojčić, T. Papadopoulo, R. Deriche, and S. Deslauriers-Gauthier. Including transmission delays supported by dMRI into linear M/EEG inverse methods with an application to visuomotor brain networks. *(Journal paper in preparation.)*

- I. Kojčić, T. Papadopoulo, R. Deriche, and S. Deslauriers-Gauthier. Incorporating tramsission delays from long-range connectivity into MEG source reconstruction, 2021 IEEE 18th International Symposium on Biomedical Imaging (ISBI), April 2021, Nice, France

- I. Kojčić, T. Papadopoulo, R. Deriche, and S. Deslauriers-Gauthier. Connectivity-informed MEEG inverse problem, GRAIL 2020: MICCAI Workshop on GRaphs in biomedicAl Image anaLysis, October 2020, Lima, Peru

- I. Kojčić, T. Papadopoulo, R. Deriche, and S. Deslauriers-Gauthier. Connectivity-informed spatio-temporal MEG source reconstruction: Simulation results using a MAR model, Colloque Line Garnero, October 2019, Paris, France

- I. Kojčić, T. Papadopoulo, R. Deriche, and S. Deslauriers-Gauthier. Connectivity-informed solution for spatio-temporal M/EEG source reconstruction, First meeting of NeuroMod Institute, July 2019, Fréjus, France

Bibliography

[Abe & Hanakawa 2009] Mitsunari Abe and Takashi Hanakawa. *Functional coupling underlying motor and cognitive functions of the dorsal premotor cortex.* Behavioural brain research, vol. 198, no. 1, pages 13–23, 2009. (Cited on pages 9 and 151.)

[Adde *et al.* 2005] Geoffray Adde, Maureen Clerc, Renaud Keriven*et al. Imaging methods for MEG/EEG inverse problem.* International Journal of Bioelectromagnetism, vol. 7, no. 2, pages 111–114, 2005. (Cited on page 55.)

[Alarcon *et al.* 1994] G Alarcon, CN Guy, CD Binnie, SR Walker, RD Elwes and CE Polkey. *Intracerebral propagation of interictal activity in partial epilepsy: implications for source localisation.* Journal of Neurology, Neurosurgery & Psychiatry, vol. 57, no. 4, pages 435–449, 1994. (Cited on page 17.)

[Alexander *et al.* 2010] Daniel C Alexander, Penny L Hubbard, Matt G Hall, Elizabeth A Moore, Maurice Ptito, Geoff JM Parker and Tim B Dyrby. *Orientationally invariant indices of axon diameter and density from diffusion MRI.* Neuroimage, vol. 52, no. 4, pages 1374–1389, 2010. (Cited on pages 157 and 165.)

[Alimi *et al.* 2020] Abib Alimi, Samuel Deslauriers-Gauthier, Felix Matuschke, Andreas Müller, Sascha EA Muenzing, Markus Axer and Rachid Deriche. *Analytical and fast fiber orientation distribution reconstruction in 3D-polarized light imaging.* Medical image analysis, vol. 65, page 101760, 2020. (Cited on page 27.)

[Amblard *et al.* 2004] Cécile Amblard, Ervig Lapalme and J-M Lina. *Biomagnetic source detection by maximum entropy and graphical models.* IEEE transactions on biomedical engineering, vol. 51, no. 3, pages 427–442, 2004. (Cited on page 59.)

[Arthur & Guyton 1982] M BROWN Arthur and MD Guyton. Medical physiology. WILEY, 1982. (Cited on pages 7 and 8.)

[Assaf *et al.* 2008] Yaniv Assaf, Tamar Blumenfeld-Katzir, Yossi Yovel and Peter J Basser. *AxCaliber: a method for measuring axon diameter distribution from diffusion MRI.* Magnetic Resonance in Medicine: An Official Journal of the International Society for Magnetic Resonance in Medicine, vol. 59, no. 6, pages 1347–1354, 2008. (Cited on pages 157 and 165.)

[Axer *et al.* 2011] Markus Axer, Katrin Amunts, David Grässel, Christoph Palm, Jürgen Dammers, Hubertus Axer, Uwe Pietrzyk and Karl Zilles. *A novel approach to the human connectome: ultra-high resolution mapping of fiber*

tracts in the brain. Neuroimage, vol. 54, no. 2, pages 1091–1101, 2011. (Cited on page 27.)

[Azevedo *et al.* 2009] Frederico AC Azevedo, Ludmila RB Carvalho, Lea T Grinberg, José Marcelo Farfel, Renata EL Ferretti, Renata EP Leite, Wilson Jacob Filho, Roberto Lent and Suzana Herculano-Houzel. *Equal numbers of neuronal and nonneuronal cells make the human brain an isometrically scaled-up primate brain.* Journal of Comparative Neurology, vol. 513, no. 5, pages 532–541, 2009. (Cited on page 3.)

[Baillet & Garnero 1997] Sylvain Baillet and Line Garnero. *A Bayesian approach to introducing anatomo-functional priors in the EEG/MEG inverse problem.* IEEE transactions on Biomedical Engineering, vol. 44, no. 5, pages 374–385, 1997. (Cited on pages xii, 39, 45, 55 and 85.)

[Baillet *et al.* 2001] Sylvain Baillet, John C Mosher and Richard M Leahy. *Electromagnetic brain mapping.* IEEE Signal processing magazine, vol. 18, no. 6, pages 14–30, 2001. (Cited on pages 15, 16, 21, 40, 60, 62, 63, 68, 80 and 85.)

[Baillet 2017] Sylvain Baillet. *Magnetoencephalography for brain electrophysiology and imaging.* Nature neuroscience, vol. 20, no. 3, page 327, 2017. (Cited on pages 17 and 18.)

[Barakovic *et al.* 2021] Muhamed Barakovic, Gabriel Girard, Simona Schiavi, David Romascano, Maxime Descoteaux, Cristina Granziera, Derek K Jones, Giorgio M Innocenti, Jean-Philippe Thiran and Alessandro Daducci. *Bundle-specific axon diameter index as a new contrast to differentiate white matter tracts.* Frontiers in neuroscience, page 687, 2021. (Cited on pages 157 and 164.)

[Basser *et al.* 1994] Peter J Basser, James Mattiello and Denis LeBihan. *Estimation of the effective self-diffusion tensor from the NMR spin echo.* Journal of Magnetic Resonance, Series B, vol. 103, no. 3, pages 247–254, 1994. (Cited on pages 24 and 26.)

[Bassett & Bullmore 2017] Danielle S Bassett and Edward T Bullmore. *Small-world brain networks revisited.* The Neuroscientist, vol. 23, no. 5, pages 499–516, 2017. (Cited on pages 131 and 166.)

[Bassett & Sporns 2017] Danielle S Bassett and Olaf Sporns. *Network neuroscience.* Nature neuroscience, vol. 20, no. 3, pages 353–364, 2017. (Cited on page 34.)

[Battaglia-Mayer *et al.* 2015] Alexandra Battaglia-Mayer, Simone Ferrari-Toniolo and Federica Visco-Comandini. *Timing and communication of parietal cortex for visuomotor control.* Current opinion in neurobiology, vol. 33, pages 103–109, 2015. (Cited on pages 82 and 92.)

[Bazil *et al.* 2007] Carl W. Bazil, Gregory L. Sahlem and Derek J. Chong. *Chapter 17 - Electroencephalography.* In Teri J. Barkoukis and Alon Y. Avidan, editors, Review of Sleep Medicine (Second Edition), pages 321 – 330. Butterworth-Heinemann, second edition édition, 2007. (Cited on page 17.)

[Beck & Teboulle 2009] Amir Beck and Marc Teboulle. *A fast iterative shrinkage-thresholding algorithm for linear inverse problems.* SIAM journal on imaging sciences, vol. 2, no. 1, pages 183–202, 2009. (Cited on page 53.)

[Becker & Hervais-Adelman 2020] Robert Becker and Alexis Hervais-Adelman. *Resolving the Connectome, Spectrally-Specific Functional Connectivity Networks and Their Distinct Contributions to Behavior.* Eneuro, vol. 7, no. 5, 2020. (Cited on page 130.)

[Becker *et al.* 2014] Hanna Becker, Laurent Albera, Pierre Comon, Rémi Gribonval and Isabelle Merlet. *Fast, variation-based methods for the analysis of extended brain sources.* In 2014 22nd European Signal Processing Conference (EUSIPCO), pages 41–45. IEEE, 2014. (Cited on page 55.)

[Becker *et al.* 2015] Hanna Becker, Laurent Albera, Pierre Comon, Rémi Gribonval, Fabrice Wendling and Isabelle Merlet. *Brain-source imaging: From sparse to tensor models.* IEEE Signal Processing Magazine, vol. 32, no. 6, pages 100–112, 2015. (Cited on page 40.)

[Becker *et al.* 2017] Hanna Becker, Laurent Albera, Pierre Comon, J-C Nunes, Rémi Gribonval, Julien Fleureau, Philippe Guillotel and Isabelle Merlet. *SISSY: An efficient and automatic algorithm for the analysis of EEG sources based on structured sparsity.* NeuroImage, vol. 157, pages 157–172, 2017. (Cited on pages 45 and 55.)

[Belaoucha & Papadopoulo 2017] Brahim Belaoucha and Théodore Papadopoulo. *Spatial regularization based on dMRI to solve EEG/MEG inverse problem.* In 2017 39th Annual International Conference of the IEEE Engineering in Medicine and Biology Society (EMBC), pages 3608–3611. IEEE, 2017. (Cited on pages 45, 50, 58 and 85.)

[Belaoucha & Papadopoulo 2020] Brahim Belaoucha and Theodore Papadopoulo. *Structural connectivity to reconstruct brain activation and effective connectivity between brain regions.* Journal of Neural Engineering, 2020. (Cited on pages xii, 45, 58, 84 and 92.)

[Belaoucha *et al.* 2015] Brahim Belaoucha, Jean-Marc Lina, Maureen Clerc and Théodore Papadopoulo. *MEM-diffusion MRI framework to solve MEEG inverse problem.* In 2015 23rd European Signal Processing Conference (EUSIPCO), pages 1875–1879. IEEE, 2015. (Cited on pages xii, 58, 59 and 92.)

[Belaoucha 2017] Brahim Belaoucha. *Using diffusion MR information to reconstruct networks of brain activations from MEG and EEG measurements.* PhD thesis, Université Côte d'Azur, 2017. (Cited on pages 19 and 22.)

[Belge *et al.* 2002] Murat Belge, Misha E Kilmer and Eric L Miller. *Efficient determination of multiple regularization parameters in a generalized L-curve framework.* Inverse problems, vol. 18, no. 4, page 1161, 2002. (Cited on page 98.)

[Bénar *et al.* 2006] Christian-G Bénar, Christophe Grova, Eliane Kobayashi, Andrew P Bagshaw, Yahya Aghakhani, Francois Dubeau and Jean Gotman. *EEG–fMRI of epileptic spikes: concordance with EEG source localization and intracranial EEG.* Neuroimage, vol. 30, no. 4, pages 1161–1170, 2006. (Cited on pages 17 and 39.)

[Biggs *et al.* 1986] Norman Biggs, E Keith Lloyd and Robin J Wilson. Graph theory, 1736-1936. Oxford University Press, 1986. (Cited on page 104.)

[Bollobás & Bollobas 1998] Béla Bollobás and Bela Bollobas. Modern graph theory, volume 184. Springer Science & Business Media, 1998. (Cited on page 104.)

[Brodman 1909] K Brodman. Vergleichende lokalisationslehre der grosshirnrinde, in ihren prinzipien dargestellt auf grund des zellenbaues. Barth Leipzig, 1909. (Cited on page 12.)

[Brookings *et al.* 2009] Ted Brookings, Stephanie Ortigue, Scott Grafton and Jean Carlson. *Using ICA and realistic BOLD models to obtain joint EEG/fMRI solutions to the problem of source localization.* Neuroimage, vol. 44, no. 2, pages 411–420, 2009. (Cited on pages 57, 85 and 162.)

[Bullmore & Sporns 2009] Ed Bullmore and Olaf Sporns. *Complex brain networks: graph theoretical analysis of structural and functional systems.* Nature reviews neuroscience, vol. 10, no. 3, pages 186–198, 2009. (Cited on pages 32, 33, 34 and 134.)

[Buzsáki & Draguhn 2004] György Buzsáki and Andreas Draguhn. *Neuronal oscillations in cortical networks.* science, vol. 304, no. 5679, pages 1926–1929, 2004. (Cited on pages 55 and 130.)

[Buzsáki *et al.* 2012] György Buzsáki, Costas A Anastassiou and Christof Koch. *The origin of extracellular fields and currents—EEG, ECoG, LFP and spikes.* Nature reviews neuroscience, vol. 13, no. 6, pages 407–420, 2012. (Cited on pages 51, 83 and 130.)

[Caminiti *et al.* 2013] Roberto Caminiti, Filippo Carducci, Claudia Piervincenzi, Alexandra Battaglia-Mayer, Giuseppina Confalone, Federica Visco-Comandini, Patrizia Pantano and Giorgio M Innocenti. *Diameter, length,*

speed, and conduction delay of callosal axons in macaque monkeys and humans: comparing data from histology and magnetic resonance imaging diffusion tractography. Journal of Neuroscience, vol. 33, no. 36, pages 14501–14511, 2013. (Cited on page 82.)

[Castellanos *et al.* 2002] J Longina Castellanos, Susana Gómez and Valia Guerra. *The triangle method for finding the corner of the L-curve.* Applied Numerical Mathematics, vol. 43, no. 4, pages 359–373, 2002. (Cited on page 95.)

[Catani & De Schotten 2012] Marco Catani and Michel Thiebaut De Schotten. Atlas of human brain connections. Oxford University Press, 2012. (Cited on pages 4 and 5.)

[Chambolle 2004] Antonin Chambolle. *An algorithm for total variation minimization and applications.* Journal of Mathematical imaging and vision, vol. 20, no. 1, pages 89–97, 2004. (Cited on pages 54 and 55.)

[Chang *et al.* 2011] Edward F Chang, Erik Edwards, Srikantan S Nagarajan, Noa Fogelson, Sarang S Dalal, Ryan T Canolty, Heidi E Kirsch, Nicholas M Barbaro and Robert T Knight. *Cortical spatio-temporal dynamics underlying phonological target detection in humans.* Journal of cognitive neuroscience, vol. 23, no. 6, pages 1437–1446, 2011. (Cited on pages 51 and 83.)

[Chung & Graham 1997] Fan RK Chung and Fan Chung Graham. Spectral graph theory. Number 92. American Mathematical Soc., 1997. (Cited on page 105.)

[Clerc & Papadopoulo 2008] Maureen Clerc and Théo Papadopoulo. *Inverse problems in functional brain imaging.* Reference material for the MVA Master, vol. 2, 2008. (Cited on pages 15 and 21.)

[Cohen 2014] Mike X Cohen. Analyzing neural time series data: theory and practice. MIT press, 2014. (Cited on page 61.)

[Cohen 2017] Michael X Cohen. *Where does EEG come from and what does it mean?* Trends in neurosciences, vol. 40, no. 4, pages 208–218, 2017. (Cited on pages 16, 55 and 61.)

[Costantini *et al.* 2022] Isa Costantini, Rachid Deriche and Samuel Deslauriers-Gauthier. *An Anisotropic 4D Filtering Approach to Recover Brain Activation From Paradigm-Free Functional MRI Data.* Frontiers in Neuroimaging, vol. 1, page 815423, 2022. (Cited on pages 55, 156 and 166.)

[Craddock *et al.* 2013] R Cameron Craddock, Saad Jbabdi, Chao-Gan Yan, Joshua T Vogelstein, F Xavier Castellanos, Adriana Di Martino, Clare Kelly, Keith Heberlein, Stan Colcombe and Michael P Milham. *Imaging human connectomes at the macroscale.* Nature methods, vol. 10, no. 6, pages 524–539, 2013. (Cited on page 32.)

[Dale & Sereno 1993] Anders M Dale and Martin I Sereno. *Improved localization of cortical activity by combining EEG and MEG with MRI cortical surface reconstruction: a linear approach.* Journal of cognitive neuroscience, vol. 5, no. 2, pages 162–176, 1993. (Cited on pages 21, 40, 68 and 162.)

[Dale *et al.* 2000] Anders M Dale, Arthur K Liu, Bruce R Fischl, Randy L Buckner, John W Belliveau, Jeffrey D Lewine and Eric Halgren. *Dynamic statistical parametric mapping: combining fMRI and MEG for high-resolution imaging of cortical activity.* Neuron, vol. 26, no. 1, pages 55–67, 2000. (Cited on pages 45, 51 and 57.)

[Darvas *et al.* 2004] Felix Darvas, D Pantazis, E Kucukaltun-Yildirim and RM Leahy. *Mapping human brain function with MEG and EEG: methods and validation.* NeuroImage, vol. 23, pages S289–S299, 2004. (Cited on pages 16, 18, 22, 99 and 100.)

[Daubechies *et al.* 2004] Ingrid Daubechies, Michel Defrise and Christine De Mol. *An iterative thresholding algorithm for linear inverse problems with a sparsity constraint.* Communications on Pure and Applied Mathematics: A Journal Issued by the Courant Institute of Mathematical Sciences, vol. 57, no. 11, pages 1413–1457, 2004. (Cited on page 53.)

[Daunizeau *et al.* 2005] Jean Daunizeau, Christophe Grova, Jérémie Mattout, Guillaume Marrelec, Diego Clonda, Bernard Goulard, Mélanie Pélégrini-Issac, J-M Lina and Habib Benali. *Assessing the relevance of fMRI-based prior in the EEG inverse problem: a Bayesian model comparison approach.* IEEE Transactions on Signal Processing, vol. 53, no. 9, pages 3461–3472, 2005. (Cited on page 57.)

[Davenport *et al.* 2012] Mark A Davenport, Marco F Duarte, Yonina C Eldar and Gitta Kutyniok. *Introduction to compressed sensing.*, 2012. (Cited on page 52.)

[de Pasquale *et al.* 2012] Francesco de Pasquale, Stefania Della Penna, Abraham Z Snyder, Laura Marzetti, Vittorio Pizzella, Gian Luca Romani and Maurizio Corbetta. *A cortical core for dynamic integration of functional networks in the resting human brain.* Neuron, vol. 74, no. 4, pages 753–764, 2012. (Cited on page 34.)

[Deecke *et al.* 1969] Lüder Deecke, Peter Scheid and Hans H Kornhuber. *Distribution of readiness potential, pre-motion positivity, and motor potential of the human cerebral cortex preceding voluntary finger movements.* Experimental brain research, vol. 7, no. 2, pages 158–168, 1969. (Cited on pages 8, 9, 123 and 134.)

[Deriche 2016] Rachid Deriche. *Computational Brain Connectivity Mapping: A Core Health and Scientific Challenge.* Medical Image Analysis, vol. 33, 06 2016. (Cited on page xi.)

[Descoteaux *et al.* 2008] Maxime Descoteaux, Rachid Deriche, Thomas R Knosche and Alfred Anwander. *Deterministic and probabilistic tractography based on complex fibre orientation distributions.* IEEE transactions on medical imaging, vol. 28, no. 2, pages 269–286, 2008. (Cited on page 30.)

[Descoteaux 1999] Maxime Descoteaux. *High angular resolution diffusion imaging (HARDI).* Wiley encyclopedia of electrical and electronics engineering, pages 1–25, 1999. (Cited on pages 24, 26 and 27.)

[Desikan *et al.* 2006] Rahul S Desikan, Florent Ségonne, Bruce Fischl, Brian T Quinn, Bradford C Dickerson, Deborah Blacker, Randy L Buckner, Anders M Dale, R Paul Maguire, Bradley T Hyman*et al. An automated labeling system for subdividing the human cerebral cortex on MRI scans into gyral based regions of interest.* Neuroimage, vol. 31, no. 3, pages 968–980, 2006. (Cited on pages 12, 13, 68, 80 and 113.)

[Deslauriers-Gauthier *et al.* 2019] Samuel Deslauriers-Gauthier, Jean-Marc Lina, Russell Butler, Kevin Whittingstall, Guillaume Gilbert, Pierre-Michel Bernier, Rachid Deriche and Maxime Descoteaux. *White matter information flow mapping from diffusion MRI and EEG.* NeuroImage, vol. 201, page 116017, 2019. (Cited on pages xii, 10, 45, 58, 59, 82, 92 and 150.)

[Deslauriers-Gauthier *et al.* 2020] Samuel Deslauriers-Gauthier, Isa Costantini and Rachid Deriche. *Non–invasive inference of information flow using diffusion MRI, functional MRI, and MEG.* Journal of Neural Engineering, vol. 17, no. 4, page 045003, 2020. (Cited on pages 10, 45, 58, 59 and 92.)

[Despotović *et al.* 2013] Ivana Despotović, Ewout Vansteenkiste and Wilfried Philips. *A realistic volume conductor model of the neonatal head: methods, challenges and applications.* In 2013 35th Annual International Conference of the IEEE Engineering in Medicine and Biology Society (EMBC), pages 3303–3306. IEEE, 2013. (Cited on page 22.)

[Destrieux *et al.* 2010] Christophe Destrieux, Bruce Fischl, Anders Dale and Eric Halgren. *Automatic parcellation of human cortical gyri and sulci using standard anatomical nomenclature.* Neuroimage, vol. 53, no. 1, pages 1–15, 2010. (Cited on pages 12 and 13.)

[Dinh *et al.* 2021] Christoph Dinh, John Gustaf Wilhelm Samuelsson, Alexander Hunold, Matti Hämäläinen and Sheraz Khan. *Contextual MEG and EEG Source Estimates Using Spatiotemporal LSTM Networks.* Frontiers in Neuroscience, vol. 15, page 119, 2021. (Cited on pages 55 and 56.)

[Dong *et al.* 2016] Xiaowen Dong, Dorina Thanou, Pascal Frossard and Pierre Vandergheynst. *Learning Laplacian matrix in smooth graph signal representations.* IEEE Transactions on Signal Processing, vol. 64, no. 23, pages 6160–6173, 2016. (Cited on page 139.)

[Donoghue & Sanes 1994] John P Donoghue and Jerome N Sanes. *Motor areas of the cerebral cortex.* Journal of clinical neurophysiology: official publication of the American Electroencephalographic Society, vol. 11, no. 4, pages 382–396, 1994. (Cited on page 8.)

[Drakesmith *et al.* 2019] Mark Drakesmith, Robbert Harms, Suryanarayana Umesh Rudrapatna, Greg D Parker, C John Evans and Derek K Jones. *Estimating axon conduction velocity in vivo from microstructural MRI.* NeuroImage, vol. 203, page 116186, 2019. (Cited on pages 81, 150, 157 and 165.)

[Eckhorn & Reitboeck 1990] R Eckhorn and HJ Reitboeck. *Stimulus-specific synchronization in cat visual cortex and its possible role in visual pattern recognition.* In Synergetics of cognition, pages 99–111. Springer, 1990. (Cited on page 55.)

[Efron *et al.* 2004] Bradley Efron, Trevor Hastie, Iain Johnstone and Robert Tibshirani. *Least angle regression.* The Annals of statistics, vol. 32, no. 2, pages 407–499, 2004. (Cited on page 52.)

[Einstein 1905a] Albert Einstein. *Über die von der molekularkinetischen Theorie der Wärme geforderte Bewegung von in ruhenden Flüssigkeiten suspendierten Teilchen.* Annalen der physik, vol. 4, 1905. (Cited on page 24.)

[Einstein 1905b] Albert Einstein. *Zur elektrodynamik bewegter körper.* Annalen der physik, vol. 4, 1905. (Cited on page 93.)

[Engel *et al.* 1990] Andreas K Engel, Peter König, Charles M Gray and Wolf Singer. *Stimulus-dependent neuronal oscillations in cat visual cortex: inter-columnar interaction as determined by cross-correlation analysis.* European Journal of Neuroscience, vol. 2, no. 7, pages 588–606, 1990. (Cited on page 55.)

[Engemann & Gramfort 2015] Denis A Engemann and Alexandre Gramfort. *Automated model selection in covariance estimation and spatial whitening of MEG and EEG signals.* NeuroImage, vol. 108, pages 328–342, 2015. (Cited on page 47.)

[Essen 1997] David C van Essen. *A tension-based theory of morphogenesis and compact wiring in the central nervous system.* Nature, vol. 385, no. 6614, pages 313–318, 1997. (Cited on page 4.)

[Ferguson *et al.* 1994] AS Ferguson, Xu Zhang and Gerhard Stroink. *A complete linear discretization for calculating the magnetic field using the boundary element method.* IEEE transactions on biomedical engineering, vol. 41, no. 5, pages 455–460, 1994. (Cited on pages 23 and 69.)

[Filipiak *et al.* 2021] Patryk Filipiak, Fabien Almairac, Théodore Papadopoulo, Denys Fontaine, Lydiane Mondot, Stéphane Chanalet, Rachid Deriche, Maureen Clerc and Demian Wassermann. *Towards linking diffusion MRI*

based macro-and microstructure measures with cortico-cortical transmission in brain tumor patients. NeuroImage, vol. 226, page 117567, 2021. (Cited on pages 82, 92, 130 and 165.)

[Fischl & Dale 2000] Bruce Fischl and Anders M Dale. *Measuring the thickness of the human cerebral cortex from magnetic resonance images.* Proceedings of the National Academy of Sciences, vol. 97, no. 20, pages 11050–11055, 2000. (Cited on page 67.)

[Fischl 2012] Bruce Fischl. *FreeSurfer.* Neuroimage, vol. 62, no. 2, pages 774–781, 2012. (Cited on page 67.)

[Fletcher & Reeves 1964] Reeves Fletcher and Colin M Reeves. *Function minimization by conjugate gradients.* The computer journal, vol. 7, no. 2, pages 149–154, 1964. (Cited on page 113.)

[Fornito *et al.* 2013] Alex Fornito, Andrew Zalesky and Michael Breakspear. *Graph analysis of the human connectome: promise, progress, and pitfalls.* Neuroimage, vol. 80, pages 426–444, 2013. (Cited on pages 32, 35, 36 and 103.)

[Fox & Raichle 2007] Michael D Fox and Marcus E Raichle. *Spontaneous fluctuations in brain activity observed with functional magnetic resonance imaging.* Nature reviews neuroscience, vol. 8, no. 9, pages 700–711, 2007. (Cited on pages 21 and 83.)

[Franzone *et al.* 1985] P Colli Franzone, L Guerri, Bruno Taccardi and C Viganotti. *Finite element approximation of regularized solutions of the inverse potential problem of electrocardiography and applications to experimental data.* Calcolo, vol. 22, no. 1, pages 91–186, 1985. (Cited on page 93.)

[Frässle *et al.* 2021] Stefan Frässle, Zina M Manjaly, Cao T Do, Lars Kasper, Klaas P Pruessmann and Klaas E Stephan. *Whole-brain estimates of directed connectivity for human connectomics.* NeuroImage, vol. 225, page 117491, 2021. (Cited on pages 9, 10, 123, 134 and 151.)

[Friedman *et al.* 2007] Jerome Friedman, Trevor Hastie, Holger Höfling and Robert Tibshirani. *Pathwise coordinate optimization.* The annals of applied statistics, vol. 1, no. 2, pages 302–332, 2007. (Cited on page 53.)

[Frigo *et al.* 2020] Matteo Frigo, Samuel Deslauriers-Gauthier, Drew Parker, Abdol Aziz Ould Ismail, Junghoon John Kim, Ragini Verma and Rachid Deriche. *Diffusion MRI tractography filtering techniques change the topology of structural connectomes.* Journal of Neural Engineering, vol. 17, no. 6, page 065002, 2020. (Cited on pages 131 and 166.)

[Frigo 2021] Matteo Frigo. *Computational Brain Connectivity Mapping: From Multi-Compartment Modeling To Network Topology Via Tractography Filtering.* PhD thesis, Université Côte d'Azur, 2021. (Cited on page 28.)

[Friston *et al.* 1995] Karl J Friston, G Tononi, O Sporns and GM Edelman. *Characterising the complexity of neuronal interactions.* Human Brain Mapping, vol. 3, no. 4, pages 302–314, 1995. (Cited on page 33.)

[Friston *et al.* 2003] Karl J Friston, Lee Harrison and Will Penny. *Dynamic causal modelling.* Neuroimage, vol. 19, no. 4, pages 1273–1302, 2003. (Cited on page 35.)

[Friston *et al.* 2013] Karl Friston, Rosalyn Moran and Anil K Seth. *Analysing connectivity with Granger causality and dynamic causal modelling.* Current opinion in neurobiology, vol. 23, no. 2, pages 172–178, 2013. (Cited on page 35.)

[Friston 1994] Karl J Friston. *Functional and effective connectivity in neuroimaging: a synthesis.* Human brain mapping, vol. 2, no. 1-2, pages 56–78, 1994. (Cited on page 34.)

[Friston 2002] Karl Friston. *Beyond phrenology: what can neuroimaging tell us about distributed circuitry?* Annual review of neuroscience, vol. 25, no. 1, pages 221–250, 2002. (Cited on pages 32, 33, 34 and 135.)

[Fuchs *et al.* 1999] Manfred Fuchs, Michael Wagner, Thomas Köhler and Hans-Aloys Wischmann. *Linear and nonlinear current density reconstructions.* Journal of clinical Neurophysiology, vol. 16, no. 3, pages 267–295, 1999. (Cited on pages 44 and 54.)

[Fukushima *et al.* 2015] Makoto Fukushima, Okito Yamashita, Thomas Knösche and Masa-aki Sato. *MEG source reconstruction based on identification of directed source interactions on whole-brain anatomical networks.* Neuroimage, vol. 105, pages 408–427, 2015. (Cited on pages xii, 45, 58, 82, 84, 85, 92 and 150.)

[Gallardo Diez 2018] Guillermo Alejandro Gallardo Diez. *Construction et comparaison de parcellisations structurelles cérébrale par imagerie de diffusion.* PhD thesis, Université Côte d'Azur (ComUE), 2018. (Cited on pages 4 and 12.)

[Gallardo *et al.* 2018] Guillermo Gallardo, William Wells III, Rachid Deriche and Demian Wassermann. *Groupwise structural parcellation of the whole cortex: A logistic random effects model based approach.* NeuroImage, vol. 170, pages 307–320, 2018. (Cited on pages 12 and 13.)

[Glasser *et al.* 2013] Matthew F Glasser, Stamatios N Sotiropoulos, J Anthony Wilson, Timothy S Coalson, Bruce Fischl, Jesper L Andersson, Junqian Xu, Saad Jbabdi, Matthew Webster, Jonathan R Polimeni*et al.* *The minimal preprocessing pipelines for the Human Connectome Project.* Neuroimage, vol. 80, pages 105–124, 2013. (Cited on page 70.)

[Glasser *et al.* 2016] Matthew F Glasser, Timothy S Coalson, Emma C Robinson, Carl D Hacker, John Harwell, Essa Yacoub, Kamil Ugurbil, Jesper Andersson, Christian F Beckmann, Mark Jenkinson*et al. A multi-modal parcellation of human cerebral cortex*. Nature, vol. 536, no. 7615, pages 171–178, 2016. (Cited on pages 12, 13 and 33.)

[Goldstein & Osher 2009] Tom Goldstein and Stanley Osher. *The split Bregman method for L1-regularized problems*. SIAM journal on imaging sciences, vol. 2, no. 2, pages 323–343, 2009. (Cited on page 53.)

[Golub *et al.* 1979] Gene H Golub, Michael Heath and Grace Wahba. *Generalized cross-validation as a method for choosing a good ridge parameter*. Technometrics, vol. 21, no. 2, pages 215–223, 1979. (Cited on pages 93 and 98.)

[Gorodnitsky *et al.* 1995] Irina F Gorodnitsky, John S George and Bhaskar D Rao. *Neuromagnetic source imaging with FOCUSS: a recursive weighted minimum norm algorithm*. Electroencephalography and clinical Neurophysiology, vol. 95, no. 4, pages 231–251, 1995. (Cited on pages 45 and 52.)

[Gramfort *et al.* 2012] Alexandre Gramfort, Matthieu Kowalski and Matti Hämäläinen. *Mixed-norm estimates for the M/EEG inverse problem using accelerated gradient methods*. Physics in Medicine & Biology, vol. 57, no. 7, page 1937, 2012. (Cited on pages 45, 51, 53, 55, 56, 58 and 101.)

[Gramfort *et al.* 2013] Alexandre Gramfort, Daniel Strohmeier, Jens Haueisen, Matti S Hämäläinen and Matthieu Kowalski. *Time-frequency mixed-norm estimates: Sparse M/EEG imaging with non-stationary source activations*. NeuroImage, vol. 70, pages 410–422, 2013. (Cited on pages 53 and 56.)

[Gramfort *et al.* 2014] Alexandre Gramfort, Martin Luessi, Eric Larson, Denis A Engemann, Daniel Strohmeier, Christian Brodbeck, Lauri Parkkonen and Matti S Hämäläinen. *MNE software for processing MEG and EEG data*. Neuroimage, vol. 86, pages 446–460, 2014. (Cited on pages 68 and 69.)

[Gramfort 2009] Alexandre Gramfort. *Mapping, timing and tracking cortical activations with MEG and EEG: Methods and application to human vision*. PhD thesis, Ecole nationale supérieure des telecommunications-ENST, 2009. (Cited on page 16.)

[Granger 1969] Clive WJ Granger. *Investigating causal relations by econometric models and cross-spectral methods*. Econometrica: journal of the Econometric Society, pages 424–438, 1969. (Cited on page 35.)

[Gray 1878] Henry Gray. Anatomy of the human body, volume 8. Lea & Febiger, 1878. (Cited on pages 2, 3 and 5.)

[Grech *et al.* 2008] Roberta Grech, Tracey Cassar, Joseph Muscat, Kenneth P Camilleri, Simon G Fabri, Michalis Zervakis, Petros Xanthopoulos, Vangelis

Sakkalis and Bart Vanrumste. *Review on solving the inverse problem in EEG source analysis.* Journal of neuroengineering and rehabilitation, vol. 5, no. 1, page 25, 2008. (Cited on pages 40 and 99.)

[Grova *et al.* 2006] Christophe Grova, Jean Daunizeau, J-M Lina, Christian G Bénar, Habib Benali and Jean Gotman. *Evaluation of EEG localization methods using realistic simulations of interictal spikes.* Neuroimage, vol. 29, no. 3, pages 734–753, 2006. (Cited on pages 23, 40, 59, 85, 99, 100 and 162.)

[Guevara Alvez 2011] Pamela Beatriz Guevara Alvez. *Inference of a human brain fiber bundle atlas from high angular resolution diffusion imaging.* PhD thesis, Paris 11, 2011. (Cited on page 6.)

[Hämäläinen & Ilmoniemi 1994] Matti S Hämäläinen and Risto J Ilmoniemi. *Interpreting magnetic fields of the brain: minimum norm estimates.* Medical & biological engineering & computing, vol. 32, no. 1, pages 35–42, 1994. (Cited on pages xii, 45, 47, 48, 50, 113 and 142.)

[Hamalainen & Sarvas 1989] Matti S Hamalainen and Jukka Sarvas. *Realistic conductivity geometry model of the human head for interpretation of neuromagnetic data.* IEEE transactions on biomedical engineering, vol. 36, no. 2, pages 165–171, 1989. (Cited on pages 19, 21, 22, 23 and 69.)

[Hammond *et al.* 2013] David K Hammond, Benoit Scherrer and Simon K Warfield. *Cortical graph smoothing: a novel method for exploiting DWI-derived anatomical brain connectivity to improve EEG source estimation.* IEEE transactions on medical imaging, vol. 32, no. 10, pages 1952–1963, 2013. (Cited on pages xii, 45, 57, 96, 97, 98, 106, 113, 115, 116, 119 and 142.)

[Hansen & O'Leary 1993] Per Christian Hansen and Dianne Prost O'Leary. *The use of the L-curve in the regularization of discrete ill-posed problems.* SIAM journal on scientific computing, vol. 14, no. 6, pages 1487–1503, 1993. (Cited on pages 93, 94, 95, 96 and 98.)

[Hansen 1992] Per Christian Hansen. *Analysis of discrete ill-posed problems by means of the L-curve.* SIAM review, vol. 34, no. 4, pages 561–580, 1992. (Cited on pages 93 and 94.)

[Hansen 1999] Per Christian Hansen. *The L-curve and its use in the numerical treatment of inverse problems.* 1999. (Cited on pages 49, 50, 93, 94 and 95.)

[Hauk & Stenroos 2014] Olaf Hauk and Matti Stenroos. *A framework for the design of flexible cross-talk functions for spatial filtering of EEG/MEG data: DeFleCT.* Human brain mapping, vol. 35, no. 4, pages 1642–1653, 2014. (Cited on page 62.)

[Hauk *et al.* 2019] Olaf Hauk, Matti Stenroos and Matthias Treder. *Towards an objective evaluation of EEG/MEG source estimation methods: The Linear Tool Kit.* BioRxiv, page 672956, 2019. (Cited on page 99.)

[Herculano-Houzel 2009] Suzana Herculano-Houzel. *The human brain in numbers: a linearly scaled-up primate brain.* Frontiers in human neuroscience, page 31, 2009. (Cited on pages xi, 3 and 12.)

[Hodgkin & Huxley 1952] Alan L Hodgkin and Andrew F Huxley. *A quantitative description of membrane current and its application to conduction and excitation in nerve.* The Journal of physiology, vol. 117, no. 4, page 500, 1952. (Cited on pages 15 and 92.)

[Honey *et al.* 2007] Christopher J Honey, Rolf Kötter, Michael Breakspear and Olaf Sporns. *Network structure of cerebral cortex shapes functional connectivity on multiple time scales.* Proceedings of the National Academy of Sciences, vol. 104, no. 24, pages 10240–10245, 2007. (Cited on pages 34 and 161.)

[Horowitz *et al.* 2015] Assaf Horowitz, Daniel Barazany, Ido Tavor, Moran Bernstein, Galit Yovel and Yaniv Assaf. *In vivo correlation between axon diameter and conduction velocity in the human brain.* Brain Structure and Function, vol. 220, no. 3, pages 1777–1788, 2015. (Cited on pages 81 and 150.)

[Horwitz 2003] Barry Horwitz. *The elusive concept of brain connectivity.* Neuroimage, vol. 19, no. 2, pages 466–470, 2003. (Cited on pages 34 and 35.)

[Huppertz *et al.* 2001] Hans-Jürgen Huppertz, Eberhard Hof, Joachim Klisch, Mirko Wagner, Carl Hermann Lücking and Rumyana Kristeva-Feige. *Localization of interictal delta and epileptiform EEG activity associated with focal epileptogenic brain lesions.* Neuroimage, vol. 13, no. 1, pages 15–28, 2001. (Cited on pages 17, 39 and 53.)

[Hämäläinen *et al.* 1993] Matti Hämäläinen, Riitta Hari, Risto Ilmoniemi, Jukka Knuutila and Olli V. Lounasmaa. *Magnetoencephalography: Theory, instrumentation, and applications to noninvasive studies of the working human brain.* Rev. Mod. Phys., vol. 65, pages 413–, 1993. (Cited on pages 15, 16, 18 and 39.)

[Im *et al.* 2003] Chang-Hwan Im, Kwang-Ok An, Hyun-Kyo Jung, Hyukchan Kwon and Yong-Ho Lee. *Assessment criteria for MEG/EEG cortical patch tests.* Physics in Medicine & Biology, vol. 48, no. 15, page 2561, 2003. (Cited on page 99.)

[Innocenti *et al.* 2014] Giorgio M Innocenti, Alessandro Vercelli and Roberto Caminiti. *The diameter of cortical axons depends both on the area of origin and target.* Cerebral Cortex, vol. 24, no. 8, pages 2178–2188, 2014. (Cited on pages 81, 82, 92, 134, 150, 157 and 164.)

[Ionta 2021] Silvio Ionta. *Visual neuropsychology in development: anatomo-functional brain mechanisms of action/perception binding in health and disease*. Frontiers in Human Neuroscience, vol. 15, page 282, 2021. (Cited on pages 10, 11, 135 and 151.)

[Jaeger & Jung 2015] Dieter Jaeger and Ranu Jung. Encyclopedia of computational neuroscience. Springer New York, 2015. (Cited on page 16.)

[Jatoi *et al.* 2014] Munsif Ali Jatoi, Nidal Kamel, Aamir Saeed Malik, Ibrahima Faye and Tahamina Begum. *A survey of methods used for source localization using EEG signals*. Biomedical Signal Processing and Control, vol. 11, pages 42–52, 2014. (Cited on pages 17 and 40.)

[Jbabdi & Johansen-Berg 2011] Saad Jbabdi and Heidi Johansen-Berg. *Tractography: where do we go from here?* Brain connectivity, vol. 1, no. 3, pages 169–183, 2011. (Cited on pages 34 and 106.)

[Jbabdi *et al.* 2007] Saad Jbabdi, Mark W Woolrich, Jesper LR Andersson and TEJ Behrens. *A Bayesian framework for global tractography*. Neuroimage, vol. 37, no. 1, pages 116–129, 2007. (Cited on page 30.)

[Jeurissen *et al.* 2014] Ben Jeurissen, Jacques-Donald Tournier, Thijs Dhollander, Alan Connelly and Jan Sijbers. *Multi-tissue constrained spherical deconvolution for improved analysis of multi-shell diffusion MRI data*. NeuroImage, vol. 103, pages 411–426, 2014. (Cited on pages 27, 28, 29, 31, 70, 157, 164 and 165.)

[Jeurissen *et al.* 2019] Ben Jeurissen, Maxime Descoteaux, Susumu Mori and Alexander Leemans. *Diffusion MRI fiber tractography of the brain*. NMR in Biomedicine, vol. 32, no. 4, page e3785, 2019. (Cited on pages 27, 30, 31, 157 and 165.)

[Jirsa *et al.* 2002] Viktor K Jirsa, Kelly J Jantzen, Armin Fuchs and JA Scott Kelso. *Spatiotemporal forward solution of the EEG and MEG using network modeling*. IEEE transactions on medical imaging, vol. 21, no. 5, pages 493–504, 2002. (Cited on pages 21 and 83.)

[Jones *et al.* 2013] Derek K Jones, Thomas R Knösche and Robert Turner. *White matter integrity, fiber count, and other fallacies: the do's and don'ts of diffusion MRI*. Neuroimage, vol. 73, pages 239–254, 2013. (Cited on pages 27 and 165.)

[Karahanoğlu *et al.* 2013] Fikret Işık Karahanoğlu, César Caballero-Gaudes, François Lazeyras and Dimitri Van De Ville. *Total activation: fMRI deconvolution through spatio-temporal regularization*. Neuroimage, vol. 73, pages 121–134, 2013. (Cited on page 55.)

[Khrennikov *et al.* 2018] Andrei Khrennikov, Irina Basieva, Emmanuel M Pothos and Ichiro Yamato. *Quantum probability in decision making from quantum information representation of neuronal states.* Scientific reports, vol. 8, no. 1, pages 1–8, 2018. (Cited on page 15.)

[Kim *et al.* 2007] Seung-Jean Kim, Kwangmoo Koh, Michael Lustig, Stephen Boyd and Dimitry Gorinevsky. *An interior-point method for large-scale ℓ_1-regularized least squares.* IEEE journal of selected topics in signal processing, vol. 1, no. 4, pages 606–617, 2007. (Cited on page 52.)

[Kohler *et al.* 2006] Th Kohler, M Wagner, M Fuchs, H-A Wischmann, R Drenckhahn and A Theissen. *Depth normalization in MEG/EEG current density imaging.* In Proceedings of 18th Annual International Conference of the IEEE Engineering in Medicine and Biology Society, volume 2, pages 812–813. IEEE, 2006. (Cited on pages 45 and 50.)

[Kojčić *et al.* 2020] Ivana Kojčić, Théodore Papadopoulo, Rachid Deriche and Samuel Deslauriers-Gauthier. *Connectivity-informed M/EEG inverse problem.* In GRAIL 2020-MICCAI Workshop on GRaphs in biomedicAl Image anaLysis, 2020. (Cited on pages 92 and 109.)

[Kojčić *et al.* 2021] Ivana Kojčić, Théodore Papadopoulo, Rachid Deriche and Samuel Deslauriers-Gauthier. *Incorporating transmission delays supported by diffusion MRI in MEG source reconstruction.* In 2021 IEEE 18th International Symposium on Biomedical Imaging (ISBI), pages 64–68. IEEE, 2021. (Cited on pages 92 and 109.)

[Kolb & Whishaw 1998] Bryan Kolb and Ian Q Whishaw. *Brain plasticity and behavior.* Annual review of psychology, vol. 49, no. 1, pages 43–64, 1998. (Cited on page 36.)

[Kust Küst 2003] Jutta Kust Küst. *Corpus Callosum.* In Michael J. Aminoff and Robert B. Daroff, editors, Encyclopedia of the Neurological Sciences, pages 771–774. Academic Press, New York, 2003. (Cited on pages 10 and 135.)

[Kybic *et al.* 2005] J. Kybic, M. Clerc, T. Abboud, O. Faugeras, R. Keriven and T. Papadopoulo. *A common formalism for the Integral formulations of the forward EEG problem.* IEEE Transactions on Medical Imaging, vol. 24, no. 1, pages 12–28, 2005. (Cited on pages 23, 40 and 69.)

[Lamus *et al.* 2012] Camilo Lamus, Matti S Hämäläinen, Simona Temereanca, Emery N Brown and Patrick L Purdon. *A spatiotemporal dynamic distributed solution to the MEG inverse problem.* NeuroImage, vol. 63, no. 2, pages 894–909, 2012. (Cited on pages 45, 55, 56, 84, 85, 99 and 100.)

[Larson-Prior *et al.* 2013] Linda J Larson-Prior, Robert Oostenveld, Stefania Della Penna, G Michalareas, F Prior, Abbas Babajani-Feremi, J-M Schoffe-

len, Laura Marzetti, Francesco de Pasquale, F Di Pompeo*et al.* *Adding dynamics to the Human Connectome Project with MEG.* Neuroimage, vol. 80, pages 190–201, 2013. (Cited on pages 66, 71 and 72.)

[Lavrov *et al.* 2021] Igor Lavrov, Timur Latypov, Elvira Mukhametova, Brian Lundstrom, Paola Sandroni, Kendall Lee, Bryan Klassen and Matt Stead. *Pre-motor versus motor cerebral cortex neuromodulation for chronic neuropathic pain.* Scientific reports, vol. 11, no. 1, pages 1–12, 2021. (Cited on pages 135 and 151.)

[Le Bihan & Breton 1985] Denis Le Bihan and EJCAS Breton. *Imagerie de diffusion in vivo par résonance magnétique nucléaire.* Comptes rendus de l'Académie des sciences. Série 2, Mécanique, Physique, Chimie, Sciences de l'univers, Sciences de la Terre, vol. 301, no. 15, pages 1109–1112, 1985. (Cited on page 25.)

[Le Bihan *et al.* 2001] Denis Le Bihan, Jean-François Mangin, Cyril Poupon, Chris A Clark, Sabina Pappata, Nicolas Molko and Hughes Chabriat. *Diffusion tensor imaging: concepts and applications.* Journal of Magnetic Resonance Imaging: An Official Journal of the International Society for Magnetic Resonance in Medicine, vol. 13, no. 4, pages 534–546, 2001. (Cited on page 24.)

[Le Bihan 2020] Denis Le Bihan. *On time and space in the brain: A relativistic pseudo-diffusion framework.* Brain Multiphysics, vol. 1, page 100016, 2020. (Cited on pages 92 and 93.)

[Lei *et al.* 2015] Xu Lei, Taoyu Wu and Pedro Valdes-Sosa. *Incorporating priors for EEG source imaging and connectivity analysis.* Frontiers in neuroscience, vol. 9, page 284, 2015. (Cited on page 40.)

[Li *et al.* 2016] Ying Li, Jing Qin, Stanley Osher and Wentai Liu. *Graph fractional-order total variation EEG source reconstruction.* In 2016 38th Annual International Conference of the IEEE Engineering in Medicine and Biology Society (EMBC), pages 101–104. IEEE, 2016. (Cited on pages 45 and 55.)

[Liewald *et al.* 2014] Daniel Liewald, Robert Miller, Nikos Logothetis, Hans-Joachim Wagner and Almut Schüz. *Distribution of axon diameters in cortical white matter: an electron-microscopic study on three human brains and a macaque.* Biological cybernetics, vol. 108, no. 5, pages 541–557, 2014. (Cited on page 157.)

[Lin *et al.* 2006] Fa-Hsuan Lin, Thomas Witzel, Seppo P Ahlfors, Steven M Stufflebeam, John W Belliveau and Matti S Hämäläinen. *Assessing and improving the spatial accuracy in MEG source localization by depth-weighted minimum-norm estimates.* Neuroimage, vol. 31, no. 1, pages 160–171, 2006. (Cited on pages 45, 50, 51, 99 and 119.)

[Lütkepohl 2005] Helmut Lütkepohl. New introduction to multiple time series analysis. Springer Science & Business Media, 2005. (Cited on page 86.)

[Lynn & Bassett 2019] Christopher W Lynn and Danielle S Bassett. *The physics of brain network structure, function and control.* Nature Reviews Physics, vol. 1, no. 5, pages 318–332, 2019. (Cited on pages 33 and 134.)

[Maier-Hein *et al.* 2017] Klaus H Maier-Hein, Peter F Neher, Jean-Christophe Houde, Marc-Alexandre Côté, Eleftherios Garyfallidis, Jidan Zhong, Maxime Chamberland, Fang-Cheng Yeh, Ying-Chia Lin, Qing Ji*et al. The challenge of mapping the human connectome based on diffusion tractography.* Nature communications, vol. 8, no. 1, pages 1–13, 2017. (Cited on pages 31, 142 and 166.)

[Maksymenko 2019] Kostiantyn Maksymenko. *Novel algorithmic approaches for the forward and inverse M/EEG problems.* PhD thesis, COMUE Université Côte d'Azur (2015-2019), 2019. (Cited on page 19.)

[Malmivuo *et al.* 1997] Jaakko Malmivuo, Veikko Suihko and Hannu Eskola. *Sensitivity distributions of EEG and MEG measurements.* IEEE Transactions on Biomedical Engineering, vol. 44, no. 3, pages 196–208, 1997. (Cited on pages 16, 18 and 19.)

[Marieb & Hoehn 2007] Elaine Nicpon Marieb and Katja Hoehn. Human anatomy & physiology. Pearson education, 2007. (Cited on pages 7, 8 and 162.)

[Mårtensson *et al.* 2018] Gustav Mårtensson, Joana B Pereira, Patrizia Mecocci, Bruno Vellas, Magda Tsolaki, Iwona Kłoszewska, Hilkka Soininen, Simon Lovestone, Andrew Simmons, Giovanni Volpe*et al. Stability of graph theoretical measures in structural brain networks in Alzheimer's disease.* Scientific reports, vol. 8, no. 1, pages 1–15, 2018. (Cited on page 80.)

[Martuzzi *et al.* 2006] Roberto Martuzzi, Micah M Murray, Philippe P Maeder, Eleonora Fornari, Jean-Philippe Thiran, Stephanie Clarke, Christoph M Michel and Reto A Meuli. *Visuo-motor pathways in humans revealed by event-related fMRI.* Experimental brain research, vol. 170, no. 4, pages 472–487, 2006. (Cited on pages 9, 10, 123, 134, 135, 151, 154 and 162.)

[Matsuura & Okabe 1995] Kanta Matsuura and Yoichi Okabe. *Selective minimum-norm solution of the biomagnetic inverse problem.* IEEE Transactions on Biomedical Engineering, vol. 42, no. 6, pages 608–615, 1995. (Cited on pages 45 and 52.)

[Metz 1986] Charles E Metz. *ROC methodology in radiologic imaging.* Investigative radiology, vol. 21, no. 9, pages 720–733, 1986. (Cited on pages 100 and 102.)

[Meunier *et al.* 2010] David Meunier, Renaud Lambiotte and Edward T Bullmore. *Modular and hierarchically modular organization of brain networks.* Frontiers in neuroscience, vol. 4, page 200, 2010. (Cited on pages xi, 32 and 103.)

[Michel *et al.* 2011] Vincent Michel, Alexandre Gramfort, Gaël Varoquaux, Evelyn Eger and Bertrand Thirion. *Total variation regularization for fMRI-based prediction of behavior.* IEEE transactions on medical imaging, vol. 30, no. 7, pages 1328–1340, 2011. (Cited on page 55.)

[Milo *et al.* 2002] Ron Milo, Shai Shen-Orr, Shalev Itzkovitz, Nadav Kashtan, Dmitri Chklovskii and Uri Alon. *Network motifs: simple building blocks of complex networks.* Science, vol. 298, no. 5594, pages 824–827, 2002. (Cited on page 136.)

[Mori *et al.* 1999] Susumu Mori, Barbara J Crain, Vadappuram P Chacko and Peter CM Van Zijl. *Three-dimensional tracking of axonal projections in the brain by magnetic resonance imaging.* Annals of Neurology: Official Journal of the American Neurological Association and the Child Neurology Society, vol. 45, no. 2, pages 265–269, 1999. (Cited on page 30.)

[Morozov 2012] Vladimir Alekseevich Morozov. Methods for solving incorrectly posed problems. Springer Science & Business Media, 2012. (Cited on page 93.)

[Mosher & Leahy 1998] John C Mosher and Richard M Leahy. *Recursive MUSIC: a framework for EEG and MEG source localization.* IEEE Transactions on Biomedical Engineering, vol. 45, no. 11, pages 1342–1354, 1998. (Cited on page 63.)

[Mosher *et al.* 1992] John C Mosher, Paul S Lewis and Richard M Leahy. *Multiple dipole modeling and localization from spatio-temporal MEG data.* IEEE transactions on biomedical engineering, vol. 39, no. 6, pages 541–557, 1992. (Cited on pages 59 and 62.)

[Mosher *et al.* 1999] John C Mosher, Richard M Leahy and Paul S Lewis. *EEG and MEG: forward solutions for inverse methods.* IEEE Transactions on Biomedical Engineering, vol. 46, no. 3, pages 245–259, 1999. (Cited on pages 19, 21, 23 and 69.)

[Murray *et al.* 2001] Micah M Murray, John J Foxe, Beth A Higgins, Daniel C Javitt and Charles E Schroeder. *Visuo-spatial neural response interactions in early cortical processing during a simple reaction time task: a high-density electrical mapping study.* Neuropsychologia, vol. 39, no. 8, pages 828–844, 2001. (Cited on page 154.)

[Myers 2011] David G Myers. Psychology in everyday life. Macmillan, 2011. (Cited on page 2.)

[Napadow *et al.* 2013] Vitaly Napadow, James D Sheehan, Jieun Kim, Lauren T LaCount, Kyungmo Park, Ted J Kaptchuk, Bruce R Rosen and Braden Kuo. *The brain circuitry underlying the temporal evolution of nausea in humans.* Cerebral cortex, vol. 23, no. 4, pages 806–813, 2013. (Cited on pages 10, 11 and 151.)

[NiBabel 2021] NiBabel. *NiBabel-Coordinate systems and affines*, 2021. [Online; accessed 9-November-2021]. (Cited on pages 74 and 75.)

[Niedermeyer & Lopes da Silva 1995] Ernst Niedermeyer and F Electroencephalograpy Lopes da Silva. *Basic principles, clinical applications, and related fields.* In Electroencephalography, pages 1005–1009. Urban and Schwarzenberg, Baltimore and Munich, 1995. (Cited on pages 15, 16 and 39.)

[Nocedal & Wright 2006] Jorge Nocedal and Stephen J Wright. *Conjugate gradient methods.* Numerical optimization, pages 101–134, 2006. (Cited on page 113.)

[Nowicka *et al.* 1996] A Nowicka, A Grabowska and E Fersten. *Interhemispheric transmission of information and functional asymmetry of the human brain.* Neuropsychologia, vol. 34, no. 2, pages 147–151, 1996. (Cited on pages 154 and 164.)

[Nunez *et al.* 2006] Paul L Nunez, Ramesh Srinivasan*et al.* Electric fields of the brain: the neurophysics of eeg. Oxford University Press, USA, 2006. (Cited on pages 21 and 83.)

[Oostenveld 2021] Robert Oostenveld. *How are the different head and MRI coordinate systems defined?*, 2021. [Online; accessed 9-November-2021]. (Cited on page 78.)

[Ou *et al.* 2009] Wanmei Ou, Matti S Hämäläinen and Polina Golland. *A distributed spatio-temporal EEG/MEG inverse solver.* NeuroImage, vol. 44, no. 3, pages 932–946, 2009. (Cited on pages 45, 53, 55 and 56.)

[O'Donnell & Westin 2011] Lauren J O'Donnell and Carl-Fredrik Westin. *An introduction to diffusion tensor image analysis.* Neurosurgery Clinics, vol. 22, no. 2, pages 185–196, 2011. (Cited on pages 24 and 26.)

[Park & Friston 2013] Hae-Jeong Park and Karl Friston. *Structural and functional brain networks: from connections to cognition.* Science, vol. 342, no. 6158, page 1238411, 2013. (Cited on page 35.)

[Pascual-Marqui *et al.* 1994] Roberto D Pascual-Marqui, Christoph M Michel and Dietrich Lehmann. *Low resolution electromagnetic tomography: a new method for localizing electrical activity in the brain.* International Journal of psychophysiology, vol. 18, no. 1, pages 49–65, 1994. (Cited on pages xii, 45, 50, 56, 105, 113 and 142.)

[Pascual-Marqui *et al.* 2002] Roberto Domingo Pascual-Marqui*et al.* *Standardized low-resolution brain electromagnetic tomography (sLORETA): technical details.* Methods Find Exp Clin Pharmacol, vol. 24, no. Suppl D, pages 5–12, 2002. (Cited on pages 45 and 51.)

[Pascual-Marqui *et al.* 2011] Roberto D Pascual-Marqui, Dietrich Lehmann, Martha Koukkou, Kieko Kochi, Peter Anderer, Bernd Saletu, Hideaki Tanaka, Koichi Hirata, E Roy John, Leslie Prichep*et al.* *Assessing interactions in the brain with exact low-resolution electromagnetic tomography.* Philosophical Transactions of the Royal Society A: Mathematical, Physical and Engineering Sciences, vol. 369, no. 1952, pages 3768–3784, 2011. (Cited on pages 45 and 51.)

[Pascual-Marqui 1999] Roberto Domingo Pascual-Marqui. *Review of methods for solving the EEG inverse problem.* International journal of bioelectromagnetism, vol. 1, no. 1, pages 75–86, 1999. (Cited on page 40.)

[Pascucci *et al.* 2020] David Pascucci, Maria Rubega and Gijs Plomp. *Modeling time-varying brain networks with a self-tuning optimized Kalman filter.* PLoS computational biology, vol. 16, no. 8, page e1007566, 2020. (Cited on page 58.)

[Pascucci *et al.* 2021] David Pascucci, Maria Rubega, Joan Rué-Queralt, Sebastien Tourbier, Patric Hagmann and Gijs Plomp. *Structure supports function: informing directed and dynamic functional connectivity with anatomical priors.* bioRxiv, 2021. (Cited on page 58.)

[Philippe *et al.* 2013] Anne-Charlotte Philippe, Maureen Clerc, Théodore Papadopoulo and Rachid Deriche. *Cortex parcellation via diffusion data as prior knowledge for the MEG inverse problem.* In 2013 IEEE 10th International Symposium on Biomedical Imaging, pages 994–997. IEEE, 2013. (Cited on pages 45, 50 and 58.)

[Phillips *et al.* 2002] Christophe Phillips, Michael D Rugg and Karl J Friston. *Anatomically informed basis functions for EEG source localization: combining functional and anatomical constraints.* NeuroImage, vol. 16, no. 3, pages 678–695, 2002. (Cited on page xii.)

[Polak & Ribiere 1969] Elijah Polak and Gerard Ribiere. *Note sur la convergence de méthodes de directions conjuguées.* ESAIM: Mathematical Modelling and Numerical Analysis-Modélisation Mathématique et Analyse Numérique, vol. 3, no. R1, pages 35–43, 1969. (Cited on page 113.)

[Proix *et al.* 2016] Timothée Proix, Andreas Spiegler, Michael Schirner, Simon Rothmeier, Petra Ritter and Viktor K Jirsa. *How do parcellation size and short-range connectivity affect dynamics in large-scale brain network models?* Neuroimage, vol. 142, pages 135–149, 2016. (Cited on page 57.)

[Purves *et al.* 2019] Dale Purves, George J Augustine, David Fitzpatrick, William Hall, Anthony-Samuel LaMantia and Leonard White. Neurosciences. De Boeck Supérieur, 2019. (Cited on pages 4 and 13.)

[Robinson *et al.* 2006] Peter A Robinson, Peter M Drysdale, Heila Van der Merwe, Elizabeth Kyriakou, MK Rigozzi, Biljana Germanoska and CJ Rennie. *BOLD responses to stimuli: dependence on frequency, stimulus form, amplitude, and repetition rate.* Neuroimage, vol. 31, no. 2, pages 585–599, 2006. (Cited on pages 72 and 85.)

[Rubinov & Sporns 2010] Mikail Rubinov and Olaf Sporns. *Complex network measures of brain connectivity: uses and interpretations.* Neuroimage, vol. 52, no. 3, pages 1059–1069, 2010. (Cited on pages 32, 33 and 34.)

[Rudin *et al.* 1992] Leonid I Rudin, Stanley Osher and Emad Fatemi. *Nonlinear total variation based noise removal algorithms.* Physica D: nonlinear phenomena, vol. 60, no. 1-4, pages 259–268, 1992. (Cited on page 54.)

[Sakkalis 2011] Vangelis Sakkalis. *Review of advanced techniques for the estimation of brain connectivity measured with EEG/MEG.* Computers in biology and medicine, vol. 41, no. 12, pages 1110–1117, 2011. (Cited on page 35.)

[Samuelsson *et al.* 2021] John G Samuelsson, Noam Peled, Fahimeh Mamashli, Jyrki Ahveninen and Matti S Hämäläinen. *Spatial fidelity of MEG/EEG source estimates: A general evaluation approach.* Neuroimage, vol. 224, page 117430, 2021. (Cited on pages 54, 99 and 162.)

[Sanz Leon *et al.* 2013] Paula Sanz Leon, Stuart A Knock, M Marmaduke Woodman, Lia Domide, Jochen Mersmann, Anthony R McIntosh and Viktor Jirsa. *The Virtual Brain: a simulator of primate brain network dynamics.* Frontiers in neuroinformatics, vol. 7, page 10, 2013. (Cited on page 83.)

[Sarvas 1987] Jukka Sarvas. *Basic mathematical and electromagnetic concepts of the biomagnetic inverse problem.* Physics in Medicine & Biology, vol. 32, no. 1, page 11, 1987. (Cited on pages 16, 19, 20, 22 and 43.)

[Schieber 2001] Marc H Schieber. *Constraints on somatotopic organization in the primary motor cortex.* Journal of neurophysiology, vol. 86, no. 5, pages 2125–2143, 2001. (Cited on page 8.)

[Schmahmann *et al.* 2009] Jeremy D Schmahmann, Jeremy Schmahmann and Deepak Pandya. Fiber pathways of the brain. OUP USA, 2009. (Cited on pages 12 and 70.)

[Schmidt 1986] Ralph Schmidt. *Multiple emitter location and signal parameter estimation.* IEEE transactions on antennas and propagation, vol. 34, no. 3, pages 276–280, 1986. (Cited on page 62.)

[Schmitt *et al.* 2001] Uwe Schmitt, Alfred K Louis, Felix Darvas, Helmut Buchner and Manfred Fuchs. *Numerical aspects of spatio-temporal current density reconstruction from EEG-/MEG-data.* IEEE transactions on medical imaging, vol. 20, no. 4, pages 314–324, 2001. (Cited on pages 45 and 55.)

[Ségonne *et al.* 2004] Florent Ségonne, Anders M Dale, Evelina Busa, Maureen Glessner, David Salat, Horst K Hahn and Bruce Fischl. *A hybrid approach to the skull stripping problem in MRI.* Neuroimage, vol. 22, no. 3, pages 1060–1075, 2004. (Cited on page 69.)

[Silva *et al.* 1991] Laurie R Silva, Yael Amitai and Barry W Connors. *Intrinsic oscillations of neocortex generated by layer 5 pyramidal neurons.* Science, vol. 251, no. 4992, pages 432–435, 1991. (Cited on page 55.)

[SlicerWiki 2021] SlicerWiki. *Coordinate systems — Slicer Wiki,*, 2021. [Online; accessed 9-November-2021]. (Cited on page 73.)

[Smith *et al.* 2012] Robert E Smith, Jacques-Donald Tournier, Fernando Calamante and Alan Connelly. *Anatomically-constrained tractography: improved diffusion MRI streamlines tractography through effective use of anatomical information.* Neuroimage, vol. 62, no. 3, pages 1924–1938, 2012. (Cited on pages 32, 70, 131 and 166.)

[Sporns *et al.* 2005] Olaf Sporns, Giulio Tononi and Rolf Kötter. *The human connectome: a structural description of the human brain.* PLoS computational biology, vol. 1, no. 4, page e42, 2005. (Cited on pages xi and 34.)

[Sporns 2011] Olaf Sporns. *The human connectome: a complex network.* Annals of the New York Academy of Sciences, vol. 1224, no. 1, pages 109–125, 2011. (Cited on pages xii, 33, 34, 103 and 161.)

[Steinmetz *et al.* 2000] Peter N Steinmetz, A Roy, PJ Fitzgerald, SS Hsiao, KO Johnson and Ernst Niebur. *Attention modulates synchronized neuronal firing in primate somatosensory cortex.* Nature, vol. 404, no. 6774, pages 187–190, 2000. (Cited on page 55.)

[Steinsträter *et al.* 2010] Olaf Steinsträter, Stephanie Sillekens, Markus Junghoefer, Martin Burger and Carsten H Wolters. *Sensitivity of beamformer source analysis to deficiencies in forward modeling.* Human brain mapping, vol. 31, no. 12, pages 1907–1927, 2010. (Cited on page 62.)

[Stejskal & Tanner 1965] Edward O Stejskal and John E Tanner. *Spin diffusion measurements: spin echoes in the presence of a time-dependent field gradient.* The journal of chemical physics, vol. 42, no. 1, pages 288–292, 1965. (Cited on pages 24 and 25.)

[Stephan *et al.* 2007] Klaas E Stephan, John C Marshall, Will D Penny, Karl J Friston and Gereon R Fink. *Interhemispheric integration of visual processing*

during task-driven lateralization. Journal of Neuroscience, vol. 27, no. 13, pages 3512–3522, 2007. (Cited on pages 10, 154 and 164.)

[Stephan *et al.* 2010] Klaas Enno Stephan, Will D Penny, Rosalyn J Moran, Hanneke EM den Ouden, Jean Daunizeau and Karl J Friston. *Ten simple rules for dynamic causal modeling*. Neuroimage, vol. 49, no. 4, pages 3099–3109, 2010. (Cited on page 36.)

[Strang 2011] Gilbert Strang. *18.06SC Linear Algebra*. Massachusetts Institute of Technology: MIT OpenCourseWare, page https://ocw.mit.edu, 2011. (Cited on pages 42, 43 and 46.)

[Swets 1988] John A Swets. *Measuring the accuracy of diagnostic systems*. Science, vol. 240, no. 4857, pages 1285–1293, 1988. (Cited on page 102.)

[Tadel *et al.* 2011] François Tadel, Sylvain Baillet, John C Mosher, Dimitrios Pantazis and Richard M Leahy. *Brainstorm: a user-friendly application for MEG/EEG analysis*. Computational intelligence and neuroscience, vol. 2011, 2011. (Cited on page 83.)

[Tibshirani 1996] Robert Tibshirani. *Regression shrinkage and selection via the lasso*. Journal of the Royal Statistical Society: Series B (Methodological), vol. 58, no. 1, pages 267–288, 1996. (Cited on page 52.)

[Tikhonov 1943] Andrey Nikolayevich Tikhonov. *On the stability of inverse problems*. In Dokl. Akad. Nauk SSSR, volume 39, pages 195–198, 1943. (Cited on page 47.)

[Tononi *et al.* 1994] Giulio Tononi, Olaf Sporns and Gerald M Edelman. *A measure for brain complexity: relating functional segregation and integration in the nervous system*. Proceedings of the National Academy of Sciences, vol. 91, no. 11, pages 5033–5037, 1994. (Cited on pages xii, 33 and 34.)

[Tournier *et al.* 2004] J-Donald Tournier, Fernando Calamante, David G Gadian and Alan Connelly. *Direct estimation of the fiber orientation density function from diffusion-weighted MRI data using spherical deconvolution*. Neuroimage, vol. 23, no. 3, pages 1176–1185, 2004. (Cited on page 29.)

[Tournier *et al.* 2007] J-Donald Tournier, Fernando Calamante and Alan Connelly. *Robust determination of the fibre orientation distribution in diffusion MRI: non-negativity constrained super-resolved spherical deconvolution*. Neuroimage, vol. 35, no. 4, pages 1459–1472, 2007. (Cited on page 29.)

[Tournier *et al.* 2012] J-Donald Tournier, Fernando Calamante and Alan Connelly. *MRtrix: diffusion tractography in crossing fiber regions*. International journal of imaging systems and technology, vol. 22, no. 1, pages 53–66, 2012. (Cited on page 30.)

[Tournier *et al.* 2019] J-Donald Tournier, Robert Smith, David Raffelt, Rami Tabbara, Thijs Dhollander, Maximilian Pietsch, Daan Christiaens, Ben Jeurissen, Chun-Hung Yeh and Alan Connelly. *MRtrix3: A fast, flexible and open software framework for medical image processing and visualisation.* NeuroImage, page 116137, 2019. (Cited on page 70.)

[Tuch 1999] David S Tuch. *High angular resolution diffusion imaging of the human brain.* In Proceedings of the 7th Annual Meeting of ISMRM, Philadelphia, 1999, volume 321, 1999. (Cited on page 27.)

[Tudor *et al.* 2005] Mario Tudor, Lorainne Tudor Car and Katarina Ivana Tudor. *Hans berger (1873-1941) - The history of electroencephalography.* Acta medica Croatica : casopis Hravatske akademije medicinskih znanosti, vol. 59, pages 307–13, 2005. (Cited on page 17.)

[Tzourio-Mazoyer *et al.* 2002] Nathalie Tzourio-Mazoyer, Brigitte Landeau, Dimitri Papathanassiou, Fabrice Crivello, Octave Etard, Nicolas Delcroix, Bernard Mazoyer and Marc Joliot. *Automated anatomical labeling of activations in SPM using a macroscopic anatomical parcellation of the MNI MRI single-subject brain.* Neuroimage, vol. 15, no. 1, pages 273–289, 2002. (Cited on pages 12 and 13.)

[Uutela *et al.* 1999] Kimmo Uutela, M Hämäläinen and Erkki Somersalo. *Visualization of magnetoencephalographic data using minimum current estimates.* NeuroImage, vol. 10, no. 2, pages 173–180, 1999. (Cited on pages 45 and 52.)

[Valdes-Sosa *et al.* 2011] Pedro A Valdes-Sosa, Alard Roebroeck, Jean Daunizeau and Karl Friston. *Effective connectivity: influence, causality and biophysical modeling.* Neuroimage, vol. 58, no. 2, pages 339–361, 2011. (Cited on pages 155 and 162.)

[Van Essen *et al.* 2013] David C Van Essen, Stephen M Smith, Deanna M Barch, Timothy EJ Behrens, Essa Yacoub, Kamil Ugurbil, Wu-Minn HCP Consortium*et al. The WU-Minn human connectome project: an overview.* Neuroimage, vol. 80, pages 62–79, 2013. (Cited on pages 66 and 67.)

[Van Veen & Buckley 1988] Barry D Van Veen and Kevin M Buckley. *Beamforming: A versatile approach to spatial filtering.* IEEE assp magazine, vol. 5, no. 2, pages 4–24, 1988. (Cited on page 61.)

[Van Veen *et al.* 1997] Barry D Van Veen, Wim Van Drongelen, Moshe Yuchtman and Akifumi Suzuki. *Localization of brain electrical activity via linearly constrained minimum variance spatial filtering.* IEEE Transactions on biomedical engineering, vol. 44, no. 9, pages 867–880, 1997. (Cited on page 62.)

[Varela *et al.* 2001] Francisco Varela, Jean-Philippe Lachaux, Eugenio Rodriguez and Jacques Martinerie. *The brainweb: phase synchronization and large-*

scale integration. Nature reviews neuroscience, vol. 2, no. 4, pages 229–239, 2001. (Cited on page 34.)

[Wang *et al.* 1992] J-Z Wang, Samuel J Williamson and Lloyd Kaufman. *Magnetic source images determined by a lead-field analysis: the unique minimum-norm least-squares estimation.* IEEE Transactions on Biomedical Engineering, vol. 39, no. 7, pages 665–675, 1992. (Cited on page 47.)

[Watts & Strogatz 1998] Duncan J Watts and Steven H Strogatz. *Collective dynamics of 'small-world'networks.* Nature, vol. 393, no. 6684, page 440, 1998. (Cited on page 32.)

[Weiten 2021] Wayne Weiten. Psychology: Themes and variations. Cengage Learning, 2021. (Cited on page 14.)

[Westner *et al.* 2022] Britta U Westner, Sarang S Dalal, Alexandre Gramfort, Vladimir Litvak, John C Mosher, Robert Oostenveld and Jan-Mathijs Schoffelen. *A unified view on beamformers for M/EEG source reconstruction.* NeuroImage, vol. 246, page 118789, 2022. (Cited on page 62.)

[Wideman 2003] Graham Wideman. *Understanding FreeSurfer Coordinates*, 2003. [Online; accessed 9-November-2021]. (Cited on page 76.)

[Wilson & Cowan 1972] Hugh R Wilson and Jack D Cowan. *Excitatory and inhibitory interactions in localized populations of model neurons.* Biophysical journal, vol. 12, no. 1, pages 1–24, 1972. (Cited on pages 33 and 84.)

[Wolters *et al.* 2004] Carsten H Wolters, Lars Grasedyck and Wolfgang Hackbusch. *Efficient computation of lead field bases and influence matrix for the FEM-based EEG and MEG inverse problem.* Inverse problems, vol. 20, no. 4, page 1099, 2004. (Cited on page 23.)

[Wong & Wang 2006] Kong-Fatt Wong and Xiao-Jing Wang. *A recurrent network mechanism of time integration in perceptual decisions.* Journal of Neuroscience, vol. 26, no. 4, pages 1314–1328, 2006. (Cited on page 84.)

[Xie *et al.* 2021] Wen-Jie Xie, Yang Yong, Na Wei, Peng Yue and Wei-Xing Zhou. *Identifying states of global financial market based on information flow network motifs.* The North American Journal of Economics and Finance, vol. 58, page 101459, 2021. (Cited on page 136.)

[Yeo *et al.* 2011] BT Thomas Yeo, Fenna M Krienen, Jorge Sepulcre, Mert R Sabuncu, Danial Lashkari, Marisa Hollinshead, Joshua L Roffman, Jordan W Smoller, Lilla Zöllei, Jonathan R Polimeni*et al. The organization of the human cerebral cortex estimated by intrinsic functional connectivity.* Journal of neurophysiology, 2011. (Cited on pages 9, 10 and 151.)

[Zeynep 2012] Akalin Acar Zeynep. *Forward and Inverse Problem of EEG*. Swartz Center for Computational Neuroscience, 2012. Presentation slides. (Cited on page 20.)

[Zhi *et al.* 2022] Da Zhi, Maedbh King, Carlos R Hernandez-Castillo and Jörn Diedrichsen. *Evaluating brain parcellations using the distance-controlled boundary coefficient*. Human Brain Mapping, 2022. (Cited on page 12.)

[Zivot & Wang 2006] Eric Zivot and Jiahui Wang. *Vector autoregressive models for multivariate time series*. Modeling Financial Time Series with S-Plus®, pages 385–429, 2006. (Cited on page 86.)